frontiers | Research Topics

Advances in haptic feedback for neurorobotics applications

Edited by
Guanghua Xu, Min Li, Yang Zheng, Chenyun Dai,
Emanuele Lindo Secco and Pengwen Xiong

Published in
Frontiers in Neuroscience

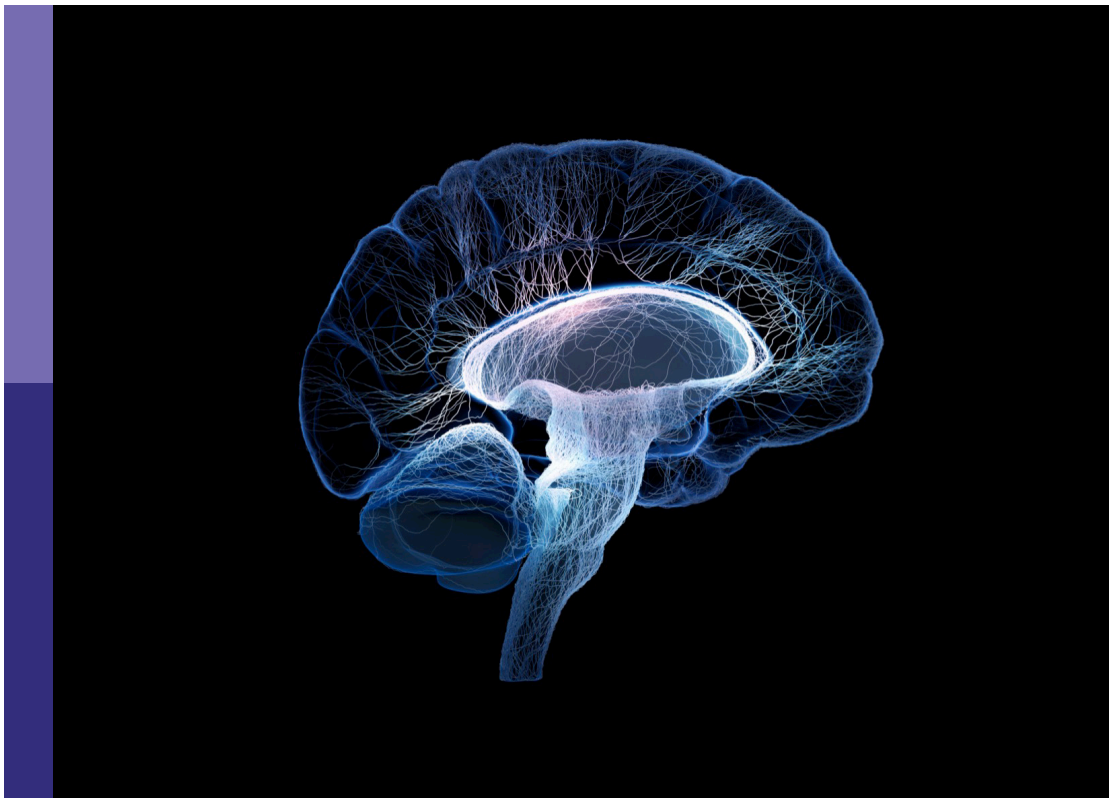

ISSN 1664-8714
ISBN 978-2-8325-2243-1
DOI 10.3389/978-2-8325-2243-1

About Frontiers

Frontiers is more than just an open access publisher of scholarly articles: it is a pioneering approach to the world of academia, radically improving the way scholarly research is managed. The grand vision of Frontiers is a world where all people have an equal opportunity to seek, share and generate knowledge. Frontiers provides immediate and permanent online open access to all its publications, but this alone is not enough to realize our grand goals.

Frontiers journal series

The Frontiers journal series is a multi-tier and interdisciplinary set of open-access, online journals, promising a paradigm shift from the current review, selection and dissemination processes in academic publishing. All Frontiers journals are driven by researchers for researchers; therefore, they constitute a service to the scholarly community. At the same time, the *Frontiers journal series* operates on a revolutionary invention, the tiered publishing system, initially addressing specific communities of scholars, and gradually climbing up to broader public understanding, thus serving the interests of the lay society, too.

Dedication to quality

Each Frontiers article is a landmark of the highest quality, thanks to genuinely collaborative interactions between authors and review editors, who include some of the world's best academicians. Research must be certified by peers before entering a stream of knowledge that may eventually reach the public - and shape society; therefore, Frontiers only applies the most rigorous and unbiased reviews. Frontiers revolutionizes research publishing by freely delivering the most outstanding research, evaluated with no bias from both the academic and social point of view. By applying the most advanced information technologies, Frontiers is catapulting scholarly publishing into a new generation.

What are Frontiers Research Topics?

Frontiers Research Topics are very popular trademarks of the *Frontiers journals series*: they are collections of at least ten articles, all centered on a particular subject. With their unique mix of varied contributions from Original Research to Review Articles, Frontiers Research Topics unify the most influential researchers, the latest key findings and historical advances in a hot research area.

Find out more on how to host your own Frontiers Research Topic or contribute to one as an author by contacting the Frontiers editorial office: frontiersin.org/about/contact

Advances in haptic feedback for neurorobotics applications

Topic editors

Guanghua Xu — Xi'an Jiaotong University, China
Min Li — Xi'an Jiaotong University, China
Yang Zheng — Xi'an Jiaotong University, China
Chenyun Dai — Fudan University, China
Emanuele Lindo Secco — Liverpool Hope University, United Kingdom
Pengwen Xiong — Nanchang University, China

Citation

Xu, G., Li, M., Zheng, Y., Dai, C., Secco, E. L., Xiong, P., eds. (2023). *Advances in haptic feedback for neurorobotics applications*. Lausanne: Frontiers Media SA. doi: 10.3389/978-2-8325-2243-1

Table of contents

frontiers | Frontiers in Neuroscience

TYPE Editorial
PUBLISHED 11 April 2023
DOI 10.3389/fnins.2023.1189749

OPEN ACCESS

EDITED AND REVIEWED BY
Michela Chiappalone,
University of Genoa, Italy

*CORRESPONDENCE
Min Li
✉ min.li@mail.xjtu.edu.cn
Emanuele Lindo Secco
✉ seccoe@hope.ac.uk
Yang Zheng
✉ yzheng@mail.xjtu.edu.cn

SPECIALTY SECTION
This article was submitted to Neuroprosthetics, a section of the journal Frontiers in Neuroscience

RECEIVED 20 March 2023
ACCEPTED 28 March 2023
PUBLISHED 11 April 2023

CITATION
Li M, Secco EL, Zheng Y, Dai C, Xiong P and Xu G (2023) Editorial: Advances in haptic feedback for neurorobotics applications. *Front. Neurosci.* 17:1189749. doi: 10.3389/fnins.2023.1189749

Editorial: Advances in haptic feedback for neurorobotics applications

Min Li[1]*, Emanuele Lindo Secco[2]*, Yang Zheng[1]*, Chenyun Dai[3], Pengwen Xiong[4] and Guanghua Xu[1]

[1]Institute of Engineering & Medicine Interdisciplinary Studies, School of Mechanical Engineering, Xi'an Jiaotong University, Xi'an, China, [2]School of Mathematics Computer Science & Engineering, Liverpool Hope University, Liverpool, United Kingdom, [3]Center for Biomedical Engineering, School of Information Science and Technology, Fudan University, Shanghai, China, [4]School of Advanced Manufacturing, Nanchang University, Nanchang, Jiangxi, China

KEYWORDS

neural-machine interfaces, neurorobotics, motion intention decoding, haptic sensing, haptic feedback

Editorial on the Research Topic
Advances in haptic feedback for neurorobotics applications

Neuro-robots and neural-machine interfaces have shown to offer a set of solutions and benefits on a variety of disciplines, including assistive and rehabilitative devices for individuals with motor dysfunction, telerobotics, and good Human robot interaction with prosthetics.

Typically, the interaction between these systems and the end-user is performed by detecting the human intention through the acquisition of physiological parameters or action, such as, for example, the ElectroEncephaloGram (EEG), the ElectroCardioGram (ECG), the ElectroMyoGram (EMG), ElectroOculoGram (EOG), or the movement of a limb.

In this context we have launched this novel Research Topic on *"Advances in haptic feedback for neurorobotics applications"* where, in particular, we want to focus on the human-machine interaction from a haptics viewpoint.

The reason why we have introduced Haptic feedback is twofold: first, we believe that is crucial to have robotics-designs which are *human-centered*, i.e., they are defined, developed, and improved around the subject and the end-user. Secondly, but not less important, we also strongly believe that *Haptic Feedback* is at present still under-estimated and not sufficiently investigated as a real-time and intuitive mean between the robotic device and the human being.

Accordingly, our call has received a nice set of answers and the Research Topic has collected the interest of more than 60 authors around the word, presenting an intriguing set of human-centered original researches.

Novel motion intention decoding methods and algorithms

Introducing novel motion intention decoding methods and exploring novel algorithms with good robustness and the reliability is a very important aspect of this Research Topic. Li et al. presented *"A novel EEG decoding method for a facial-expression-based BCI system using the combined convolutional neural network and genetic algorithm"* where they showed that their Facial-Expression-based BCI system provides superior performance vs. traditional methods.

Gesture recognition can also be used for motion intention decoding. Ruan et al. looked at how PhotoPlethysmoGraphy signals may improve gesture recognition vs. human-computer interaction performed by means of wearable devices and they presented wrist- and finger-related gesture recognition based on *"Principal component analysis of photoplethysmography signals for improved gesture recognition"*.

Zhang et al. looked at motion intention decoding in human-robot interaction from a further perspective and they presented a Personalized Speed Adaptation method where EEG and EOG capture operator's mental state, and then regulate robot's speed according to this mental state. To the best of our knowledge, this paper is the first *"Feasibility study of personalized speed adaptation method based on mental state for teleoperated robots"*.

Haptic feedback modalities

Haptic feedback modalities are another important direction of this Research Topic. Electro-tactile feedback is a common haptic feedback modality for prosthesis. The dexterous movements of the upper limbs are inseparable from proprioceptive feedback. Han et al. showed how prosthetic sensory feedback could benefit of the *"Substitutive proprioception feedback of a prosthetic wrist by electro-tactile stimulation"* in experiments with five able-bodied subjects and two amputee subjects. Vibrotactile feedback is another common haptic feedback modality for prosthesis.

How to choose the location of tactile feedback in amputee users is an important question to be answered. Morand et al. proposed a *"FeetBack–Redirecting touch sensation from a prosthetic hand to the human foot"* where a vibrotactile insole was set up in order to vibrate according to the sensed force of prosthetic fingers while subjects manipulate fragile and heavy objects, providing a novel approach vs. tactile sensation in myoelectric prosthetics.

In a similar context, Pardo et al. investigated vibrotactile sensation of the arm-shoulder region in *"Vibrotactile mapping of the upper extremity: absolute perceived intensity is location-dependent; perception of relative changes is not,"* providing an overview of the sensory bandwidth that can be achieved with vibrotactile stimulation of the human arm. The result may help in the design of vibrotactile feedback interfaces (displays) for the hand/arm/shoulder-region.

Evaluating other possible haptic feedback modalities rather than commonly-used ones is another research direction. Mayer et al. looked at the *"Temporal and spatial characteristics of bone conduction as non-invasive haptic sensory feedback for upper-limb prosthesis"*, highlighting this approach's potential as a non-invasive feedback modality for upper-limb prostheses.

Control strategies

In order to improve the utility and user experience of neuro-robots, robust closed-loop control with respect to disturbance is needed. On the *"EMG feedback outperforms force feedback in the presence of prosthesis control disturbance"*, Tchimino et al. showed that EMG feedback may provide better performance vs. force feedback in human-prosthesis interaction.

Another interesting contribution for this direction was coming from Bruni et al., where the authors validate an *"Object stiffness recognition and vibratory feedback without ad-hoc sensing on the Hannes prosthesis by means of a machine learning approach."* The experimental results proved that the proposed strategy allowed able-bodied subjects and amputees to recognize the objects' stiffness accurately and quickly.

To sum up, this Research Topic aims to highlight the most advanced achievements in motion intention decoding, haptic sensing, and haptic feedback for Neural-Machine Interface (NMI)-based neurorobotics research, which can be applied for teleoperation, human robot interaction with prosthetics, assistive and rehabilitative robots, and other relevant circumstances. The novel neural decoding methods, novel haptic feedback modalities, and new control strategies reported in this Research Topic should inspire and guide the future direction of this field.

Author contributions

ES and ML: writing. YZ, GX, CD, and PX: modification. All authors contributed to the article and approved the submitted version.

Conflict of interest

The authors declare that the research was conducted in the absence of any commercial or financial relationships that could be construed as a potential conflict of interest.

Publisher's note

frontiers | Frontiers in Neuroscience

TYPE Original Research
PUBLISHED 02 September 2022
DOI 10.3389/fnins.2022.976437

OPEN ACCESS

EDITED BY
Pengwen Xiong,
Nanchang University, China

REVIEWED BY
Mathias Vukelić,
Fraunhofer Institute for Industrial Engineering, Germany
William David Casebeer,
Lockheed Martin, United States

*CORRESPONDENCE
Xiaodong Zhang
xdzhang@mail.xjtu.edu.cn

SPECIALTY SECTION
This article was submitted to Neuroprosthetics, a section of the journal Frontiers in Neuroscience

RECEIVED 23 June 2022
ACCEPTED 29 July 2022
PUBLISHED 02 September 2022

CITATION
Zhang T, Zhang X, Lu Z, Zhang Y, Jiang Z and Zhang Y (2022) Feasibility study of personalized speed adaptation method based on mental state for teleoperated robots. *Front. Neurosci.* 16:976437. doi: 10.3389/fnins.2022.976437

Feasibility study of personalized speed adaptation method based on mental state for teleoperated robots

Teng Zhang[1], Xiaodong Zhang[1,2]*, Zhufeng Lu[1], Yi Zhang[1], Zhiming Jiang[1] and Yingjie Zhang[1]

[1]School of Mechanical Engineering, Xi'an Jiaotong University, Xi'an, China, [2]Shaanxi Key Laboratory of Intelligent Robot, Xi'an Jiaotong University, Xi'an, China

The teleoperated robotic system can support humans to complete tasks in high-risk, high-precision and difficult special environments. Because this kind of special working environment is easy to cause stress, high mental workload, fatigue and other mental states of the operator, which will reduce the quality of operation and even cause safety accidents, so the mental state of the people in this system has received extensive attention. However, the existence of individual differences and mental state diversity is often ignored, so that most of the existing adjustment strategy is out of a match between mental state and adaptive decision, which cannot effectively improve operational quality and safety. Therefore, a personalized speed adaptation (PSA) method based on policy gradient reinforcement learning was proposed in this paper. It can use electroencephalogram and electro-oculogram to accurately perceive the operator's mental state, and adjust the speed of the robot individually according to the mental state of different operators, in order to perform teleoperation tasks efficiently and safely. The experimental results showed that the PSA method learns the mapping between the mental state and the robot's speed regulation action by means of rewards and punishments, and can adjust the speed of the robot individually according to the mental state of different operators, thereby improving the operating quality of the system. And the feasibility and superiority of this method were proved. It is worth noting that the PSA method was validated on 6 real subjects rather than a simulation model. To the best of our knowledge, the PSA method is the first implementation of online reinforcement learning control of teleoperated robots involving human subjects.

KEYWORDS

personalized, teleoperated robots, biosignals, reinforcement learning, mental state, EEG and EOG

Introduction

As a branch of the field of robotics, teleoperated robotic systems have received extensive attention from academia and industry due to their advantages such as remote operation and operation in hazardous environments. In this system, the operator guides the robot movement to perform the task. In the process of the robot performing a task, the operator, as a part of the system, can learn the task execution status through information perception or feedback, and can also control the robot by sending commands. Teleoperated robotic systems are mostly used in special operations such as deep-sea exploration, space operations, detoxification and detonation and precision surgery (Nuño et al., 2011; Zhai and Xia, 2016). Due to the characteristics of high risk, high precision and high difficulty in this field, the amount of information that operators need to process has increased dramatically, resulting in higher mental workload and mental pressure. Studies have shown that higher mental workload and mental pressure will cause rapid mental fatigue, decreased vigilance, stress reaction, and increase people's errors and frustration (Zhang T. et al., 2019). On the contrary, too low mental workload and mental pressure will cause a waste of human resources or cause disgust. These adverse mental states will lead to errors in information acquisition, analysis, and decision-making, which will further lead to the decline of job performance and even lead to safety problems caused by human accidents (Wilson, 2005; Catelani et al., 2021).

To overcome this problem, various adjustment methods have been proposed. As early as in the 1990s, an adaptive automation method was first proposed. Parasuraman (1993), Scerbo et al. (2003), Kaber et al. (2016) scholars published a series of papers to discuss adaptive automation concept and theoretical issues. It is defined as an automated human-computer interaction system design method that can change the level of automation by users and systems. This method can dynamically adjust the automation level or working mode at any time according to the operator's mental state to match the operator's needs and mental state (such as the mental workload state, fatigue state, etc.), thus achieving the purpose of improving the operation performance and reducing human errors (Parasuraman, 1993; Scerbo et al., 2003; Kaber et al., 2016).

In recent years, adjustment methods based on physiological signal detection has been widely accepted with its unique advantages. Firstly, neurophysiological measures could be obtained continuously and online. Secondly, the neurophysiological ones may be recorded continuously without using overt responses (i.e., additional tasks) and may provide a direct measure of the operator's mental (covert) activities. Also, neurophysiological measures have good resolution and form a good complementarity with performance measures (Di Flumeri et al., 2015). Finally, neurophysiological measures can be used not only to trigger the adjustment system but also to highlight why adjustment method is important for enhancing safety in high-risk and high-demanding tasks (Arico et al., 2016). From the late 1990s to the recent years, most of the studies have proved the positive effect of adjustment method in improving the system performance and subjective feeling using electroencephalogram (EEG), functional near-infrared spectroscopy (*fNIRS*), electro-oculogram (EOG), and heart rate variability (HRV) physiological parameters (Freeman et al., 1999; Di Flumeri et al., 2019; Li et al., 2019; Zhang X. et al., 2019; Wu E. Q. et al., 2021).

Among all these studies, EEG-based adjustment method is getting much attention. Parasuraman and Wilson (2008) proposed an adjustment system based on EEG detection, which can realize real-time detection of the operator's mental state and dynamically assign task attributes and levels between machine and human according to mental state, thus effectively improving task performance. Jia et al. (2014) proposed an adjustment system for teleoperated robot tasks, which can detect the mental state according to the EEG of the operator and adjust the running parameters of the robot in real-time according to the mental state. The robot's speed is increased and the response time is decreased when the operator is in an excellent mental state; on the contrary, when the operator is in a bad mental state, the robot's speed is reduced and the response time is improved. Therefore, the adjustment system effectively improves control accuracy and security (Jia et al., 2014). Yang and Zhang (2013) used the fuzzy modeling method to establish an operator mental state estimation and prediction model based on EEG. Once the operator is found to be in a high-risk mental state, the model will immediately adjust its task load or remind the operator to take some measures to make the operator's task match with its current mental state (Yang and Zhang, 2013). Pietro Arico used the passive brain-computer interface technology to detect the operator's mental workload in the realistic air traffic control environment and took it as the indicator to trigger the adjustment system. Meanwhile, the technology's effectiveness was verified in the realistic air traffic management system (Arico et al., 2016).

Although adjustment technology, especially EEG detection-based adjustment method, has achieved remarkable results, it is undeniable that there are still challenges to be solved. Firstly, due to the existence of individual differences, the relationship between mental state and operational quality is also different (Jia et al., 2012), and as the user's operational skills improve, the relationship between mental state and operational quality will also change. This puts the conventional method based on static and fixed adjustment strategies into a predicament, because it does not have the ability of individual adjustment, and at the same time, it cannot change the adjustment strategy with the improvement of the operator's skills. Secondly, most studies predetermine the "good or bad" characteristics of mental states, therefore, the task becomes more complicated when the "good" mental state is detected and less complicated when the "bad"

mental state is detected. What makes this subjectivity wrong is the ignorance of mental states' diversity, which is particularly strong across individuals and across time. Also, because the brain is in a highly dynamic and non-linear environment, mental states and behaviors are not one-to-one correspondence, but many-to-one, one-to-many or mixed cross correspondence (Abbass et al., 2014). As a result, most of the existing adjustment strategy is out of a match between mental state and adaptive decision, which cannot effectively improve operational quality and safety. Thirdly, the stability and robustness of adjustment systems based on EEG detection alone need to be improved, and adjustment systems for the fusion of multiple bioelectrical signals are the trend of development (Laurent et al., 2013; Wu W. et al., 2021).

To address these three problems, by introducing the idea of policy gradient reinforcement learning (Mnih et al., 2015) and combining the advantages of EEG and EOG, a personalized speed adaptation (PSA) method was proposed. Then, its feasibility was verified by designing a teleoperation experiment. Prominently, The PSA method belongs to a "human-in-the-loop" reinforcement learning framework, it is an interactive learning technology, which uses the interaction between the agent and the environment, and records each reward and punishment as personalized feedback to update the adjustment strategy. Compared with the methods based on static and fixed adjustment strategies, it has better dynamic adaptability. Secondly, reinforcement learning problems are usually normalized as Markov decision process (MDP), so this makes the PSA model have the natural characteristics of modeling mapping sequences (Arulkumaran et al., 2017), which can fully characterize the sequence features and capture the individual characteristics of operators. Moreover, the setting of the exploration mechanism can make the agent more fully explore the state and action space, which improves the diversity of results to a certain extent. Thirdly, since this type of model often aims to maximize the cumulative reward of the system, that is, the long-term feedback of the user's operational quality is the optimization goal to update the adjustment strategy, so it can adapt to the development trend of the operator's personalization. Finally, for a "human-in-the-loop" reinforcement learning training process, it's arguably better for the algorithm to learn certain repetitive subsequences of actions (or patterns of actions) and store them in a rule-based fashion. Once an action pattern has been shown to be successful in multiple instances of a task context, it can be applied in similar other task contexts. This reinforcement learning convergence strategy can cope well with dynamic task environments (Wen et al., 2020; van Zoelen et al., 2021). It is worth noting that the mental state in this article does not refer to a specific discrete state, but a continuous state, which is mainly evaluated by the two indicators of arousal and valence in the dimension theory of psychology (Russell, 2003). The arousal represents the neurophysiological activation level of the subject, and the lower the degree of arousal, the stronger the degree of fatigue in the mental state, and vice versa. The valence indicates the positive or negative of the subject's emotional state, and the lower the degree of valence, the stronger the negative degree in the mental state, and vice versa. Changes in the operator's mental state in these two dimensions (indicators) will lead to changes in the quality of the operation. For example, as the degree of arousal decreases, that is, the degree of fatigue of the operator increases, the quality of the operation will be degraded or even human error will occur (Chuang et al., 2018). As the valence decreases, that is, the degree of negative mental state of the operator increases, the quality of the operation decreases (Jin et al., 2017). Moreover, the advantage of this setting using continuous indicators to evaluate mental state is that the influence of the diversity of mental states on operational quality can be fully considered. In addition, the PSA method has the following three advantages: (1) The PSA method is an end-to-end learning method that learns the mapping between mental states and robot speed regulation instructions through rewards and punishments, and does not need to explicitly identify which specific mental state it is, thus overcoming the above challenge 2. (2) The PSA method is individually trained for each operator, and with the increase of usage time, each operator's personalized interaction habits, skill growth, etc., will optimize the PSA model parameters, thereby overcoming the above challenges 1. (3) The PSA method utilizes multimodal bioelectrical signals combining EEG and EOG in mental state perception, and fuses them on the feature layer, thereby overcoming the above challenges 3.

The major contributions of the paper can be summarized in three aspects. Firstly, according to the characteristics of the tele-robot system and the advantages of human and computer, a dual-loop human- machine information solution interaction mechanism was designed. By introducing the idea of policy gradient reinforcement learning, a mental state-based PSA model was constructed. Secondly, the PSA algorithm was developed which includes three steps, which are multimodal bioelectrical signal data preprocessing, mental state feature extraction and model efficient training. Finally, due to the high cost of data acquisition and labor-intensive problems in the "human-in-the-loop" reinforcement learning method (Nielsen et al., 2015; Alamdari et al., 2020), this paper collects a large number of experimental data with real human participation by designing two experimental paradigms of teleoperation robots with engineering value. The data not only proves the effectiveness of the PSA method, but also provides valuable knowledge and experience for future adjustment system design. The remaining of this paper is organized as follows. Section "Methodologies" describes PSA models and methods. Section "Materials and experiments" presents experimental materials, experimental paradigms, and data processing procedures. The results are presented in Section "Results." Remarks and discussions are presented in Section "Discussion," followed by the conclusion in Section "Conclusion."

Methodologies

We first designed a dual-loop human-computer information interaction mechanism according to the characteristics of the teleoperated robot system and the respective advantages of humans and computers. Secondly, by introducing the idea of policy gradient reinforcement learning, the PSA framework that could individually adjust the speed of the robot according to the mental state of different operators was constructed. Thirdly, the PSA problem was formulated and analyzed, and a mathematical model was established. Finally, the convergence criteria of the PSA model were defined.

Personalized speed adaptation framework

The PSA method proposes a dual-loop human machine information interaction mechanism composed of the active control loop and the personalized regulation loop, as shown in **Figure 1**. In the active control loop, the operator sent control instruction to the robot through the control device, and supervised the running state of the robot through visual and auditory information, thus adjusting control instruction in real-time, and correcting sudden errors. In order to solve the problem that the operator's mental state leaded to poor operational quality or even danger, a personalized regulation loop was designed on the basis of the active control loop. By introducing the idea of policy gradient reinforcement learning, the operator's brain was innovatively used as the environmental element, the control algorithm (CA) as the agent element, the mental state as the state element, the speed adjustment instruction as the action element, and the operational quality as the reward element. Then, an end-to-end PSA model was established, which took as input the multimodal bioelectrical signals composed of EEG and EOG that reflect the operator's mental state, and used the robot's personalized speed adjustment instructions as the output. This model had been trained for many times to establish a mapping relationship between the operator's mental state and the speed of the robot. It could adjust the speed of the robot individually according to different mental states, in order to improve the operational quality and system safety.

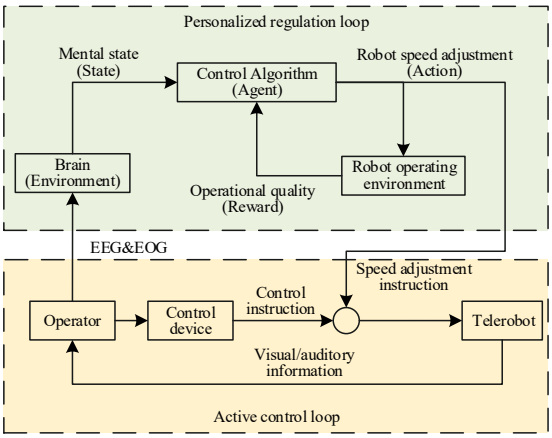

FIGURE 1
The figure shows the overall framework of the personalized speed adaptation (PSA) method.

Personalized speed adaptation problem formulation

Markov decision process

In the personalized regulation loop, the idea of policy gradient reinforcement learning was introduced, and a reinforcement learning model composed of five elements: brain environment, mental state, action indicating the robot speed adjustment command, reward indicating operational quality and CA was built. More specifically, the study found that the mental state of the operator can be changed by the task and the behavior of the robot. For example, when a teleoperated robot performs a difficult task or when the robot makes a mistake, it will trigger the human brain alert (McIntire et al., 2013). When teleoperation tasks are complex and take a long time to perform, brain fatigue can occur due to high mental workload (Warm et al., 2008). When the teleoperation task is too single and simple, it will lead to a decrease in the concentration of the brain (Daly et al., 2017). Therefore, we assumed that the process conforms to a MDP (Chanel et al., 2020). The MDP framework is a convenient choice for planning under uncertainty. This famous stochastic control process is an elegant way to model and solve probabilistic planning problems. Once the possible actions and mental states have been identified, the goal of the problem is defined using a reward function that evaluates the utility of a state-action pair. This makes possible to define the utility of an action sequence as the expected sum of the rewards obtained over time given an initial state. The optimal sequence of actions is the one that maximizes such an expected sum of rewards.

Monte Carlo sampling

Unlike reinforcement learning models that know the reward by performing a single-step operation, the PSA model needs to perform a multi-step operation task before getting the reward. At the same time, since the state transition probability and reward function of the model are unknown, the model belongs to the category of multi-step, model-free reinforcement learning. Therefore, we started from Monte Carlo sampling (Speagle, 2020) to design the PSA model. In the case of model-free reinforcement learning, the first problem encountered by the policy iteration algorithm is that the policy cannot be

evaluated. This is due to the fact that the model is unknown and cannot do full probability expansion. At this point, the state of the transition and the reward obtained can only be observed by performing the selected action in the environment. Inspired by the *K*-armed bandit, a straightforward alternative to policy evaluation is to "sample" multiple times and then find the average cumulative reward as an approximation of the expected cumulative reward. This is called Monte Carlo reinforcement learning and is also a key point in designing the PSA model (Andrieu et al., 2003).

Policy gradient

The policy gradient method is to directly simulate the policy with a neural network. The input of the neural network is the current corresponding state of the agent, and the output is the corresponding action (or action selection probability). The training of the model is actually a process of continuous exploration directly in the policy space to find the optimal policy (neural network parameters). This method works by modeling the policy function and then using gradient descent to update the parameters of the network. It does not have an actual loss function in reinforcement learning, and its purpose is to maximize the expected value of the cumulative reward, so the expected value of the cumulative reward is used as the loss function. The formula is as follows:

$$\nabla J(\theta) = E_{\tau \sim p_\theta(\tau)}[R(\tau) \nabla \ln p_\theta(\tau)] \tag{1}$$

where $R(\tau)$ represents the reward for sampling trajectory τ. $p_\theta(\tau)$ refers to the probability of sampling trajectory τ in the case of given neural network parameters θ. For those cases of high-dimensional or continuous state space, after obtaining the value function through the learning based on the value function, when formulating the strategy, it is necessary to compare the value corresponding to various actions. In this way, if the dimension of the action space is high or continuous, it is necessary to compare an action with the maximum value function from it, and this process becomes impractical. However, the policy gradient method can be directly applied to reinforcement learning scenarios in high-dimensional or continuous action spaces. Therefore, this paper chose to design the PSA model based on the policy gradient framework.

Formally, the MDP model of PSA was defined as a tuple (*S*, *A*, *P*, *R*), where:

- *S* is the set of states, this paper represents the set of mental states *s*;
- *A* is the set of actions, this paper represents the set of robot speed adjustment instructions *a*;
- *P* is the transition function, which defines the policy *p* of reaching the state $s_i \in S$ given that the action $a \in A$ is performed in state $s_i - 1 \in S$;
- *R* is the reward function that values any state-action pair, this paper represents the operational quality function;

Personalized speed adaptation method

According to the framework of policy gradient reinforcement learning, starting from the principle of Monte Carlo sampling, the PSA model was designed. Among them, the multi-step sampling process is shown in **Figure 2**. Starting from any initial mental state s_1, a certain policy p is used for sampling, and the policy is executed for i steps and the trajectory τ is obtained. This process can be represented by the following formula (Zhang et al., 2021):

$$\left.\begin{aligned} p_\theta(\tau) &= p(s_1)\, p_\theta(c_1|s_1)\, p(s_2|s_1, c_1)\, p_\theta(c_2|s_2) \\ &\quad p(s_3|s_2, c_2) \cdots p_\theta(c_t|s_t)\, p(s_{t+1}|s_t, c_t) \\ &= p(s_1) \prod_{t=1}^{T} p_\theta(c_t|s_t)\, p(s_{t+1}|s_t, c_t) \end{aligned}\right\} \tag{2}$$

where s_i $(i = 1,\ldots..,k)$ represents the mental state at the moment i (hereinafter referred to as the state). a_i $(i = 1,\ldots..,k)$ represents the robot's speed adjustment action at the moment i (hereinafter referred to as the action). $p_\theta(\tau)$ refers to the probability of sampling trajectory τ in the case of given neural network parameters θ. $p(s_1)$ is the probability of the initial state s_1. $p_\theta(a_i|s_i)$ is the probability of taking action a_i given the current state s_i. $p(s_{i+1}|s_i, a_i)$ refers to the probability of returning the next state s_{i+1} based on the conditional probability after taking the current state s_i and action a_i. For a certain sampling trajectory τ, the corresponding reward can be obtained. Different rewards can be obtained by optimizing the PSA model. The actions taken by the PSA model and the appearance of a certain state are random. The ultimate goal is to find a policy neural network with the maximum cumulative expected reward $\bar{R}_\theta$, and according to Formula (1), the objective function is shown as follows:

$$\bar{R}_\theta = \sum_\tau R(\tau) p_\theta(\tau) \tag{3}$$

where $R(\tau)$ represents the reward for sampling trajectory τ. To calculate the maximum value of the objective function and the corresponding neural network parameter θ, the gradient descent method was adopted. The formula of the gradient $\nabla \bar{R}_\theta$ of the objective function is shown as follows:

$$\nabla \bar{R}_\theta \approx \frac{1}{N} \sum_{n=1}^{N} R\left(\tau^{(n)}\right) \nabla \ln p_\theta\left(\tau^{(n)}\right) \tag{4}$$

where n is the number of sampling. N is the total number of samples. From Formulas (2), (4), the following formula can be obtained:

$$\nabla \bar{R}_\theta \approx \frac{1}{N} \sum_{n=1}^{N} \sum_{i=1}^{k} R\left(\tau^{(n)}\right) \nabla \ln p_\theta\left(a_i^{(n)}|s_i^{(n)}\right) \tag{5}$$

To make the reward value $R(\tau)$ not affected by the randomness of sampling, a baseline b was introduced in this paper.

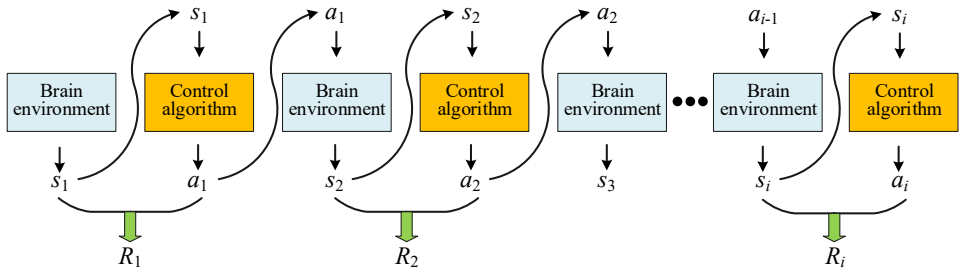

FIGURE 2
Schematic diagram of Monte Carlo sampling in the PSA model.

Therefore, the gradient formula is optimized as follows:

$$\left.\begin{aligned}\nabla \bar{R}_\theta &\approx \tfrac{1}{N}\sum_{n=1}^{N}\sum_{i=1}^{k}(R\left(\tau^{(n)}\right)-b)\nabla \ln p_\theta\left(a_i^{(n)}|s_i^{(n)}\right)\\ b &\approx E[R(\tau)]\end{aligned}\right\} \quad (6)$$

In Formula (6), the mental state s_i was represented by the feature vector of the collected bioelectric signals, and see Section "Mental state feature extractor" for the detailed formula. The action a_i representing the robot speed regulation command was obtained from the output value of the neural network. The reward R represented the operational quality, which was obtained according to the task quality score, and see Section "Personalized speed adaptation model trainer" for the detailed formula. Finally, the gradient descent method was used to update the parameter of the neural network θ. The detailed update process is shown in **Figure 3**.

$$\theta=\theta+\nabla\overline{R}_\theta \quad (7)$$

Personalized speed adaptation model training convergence criteria

The PSA approach is a "human-in-the-loop" reinforcement learning architecture that often exists in a dynamic task environment with no fixed optimal solution, where unpredictable events may require policy changes. In such an environment, conventional convergence rules are not a good criterion for performance evaluation because the agent needs to continuously learn and adapt. For a "human-in-the-loop" reinforcement learning training process, it's arguably better for the algorithm to learn certain repetitive subsequences of actions (or patterns of actions) and store them in a rule-based fashion. Once an action pattern has been shown to be successful in multiple instances of a task context, it can be applied in similar other task contexts (Wen et al., 2020; van Zoelen et al., 2021). Therefore, we believed that research on reinforcement learning of "human-in-the-loop" should not use conventional convergence criteria as a criterion for whether a model is valid, but should focus on whether a successful action pattern emerges, and its sustainability. Therefore, we updated the PSA model convergence evaluation method, which was evaluated by two indicators: reward and operator's subjective evaluation. When the fluctuation of the reward is maintained in a relatively small range, and the action level at this time is consistent with the action level expected by the operator's subjective evaluation. That is to say, the operator is neither strenuous (it will not consume too much mental workload because the difficulty is too high), nor boring (it will not lose the sense of participation or reduce the attention because the task is too easy), we believe that the model training has reached convergence at this time.

Materials and experiments

Participants and experimental setup

Six healthy participants took part in this study (the age range was 23−32, 1 female). All participants reported normal or corrected-to-normal vision and had no previous experience with the PSA system. Written informed consent was obtained from each participant before the experiment. The Institutional Review Board of Xi'an Jiaotong University approved the proposed experiment, and all experiments were conducted following the Declaration of Helsinki.

The PSA experimental system mainly included three subsystems: the bioelectrical signals acquisition subsystem, computer subsystem, and interactive subsystem. The bioelectrical signals acquisition subsystem was mainly responsible for acquiring, amplifying, and transmitting EEG and EOG signals to the computer subsystem. EEG&EOG-W32 model device manufactured by Neuracle Technology Co., Ltd., was used, the sampling frequency was 1000 Hz, and the communication method was WiFi. The device consisted of 30 EEG measuring electrodes, 2 EOG measuring electrodes, 1 reference electrode (REF) and 1 ground electrode (GND). The impedance level of all measuring electrodes were kept below 10 kΩ in each experiment. The electrodes' distribution conformed to international 10−20 standards (**Figure 4**). The

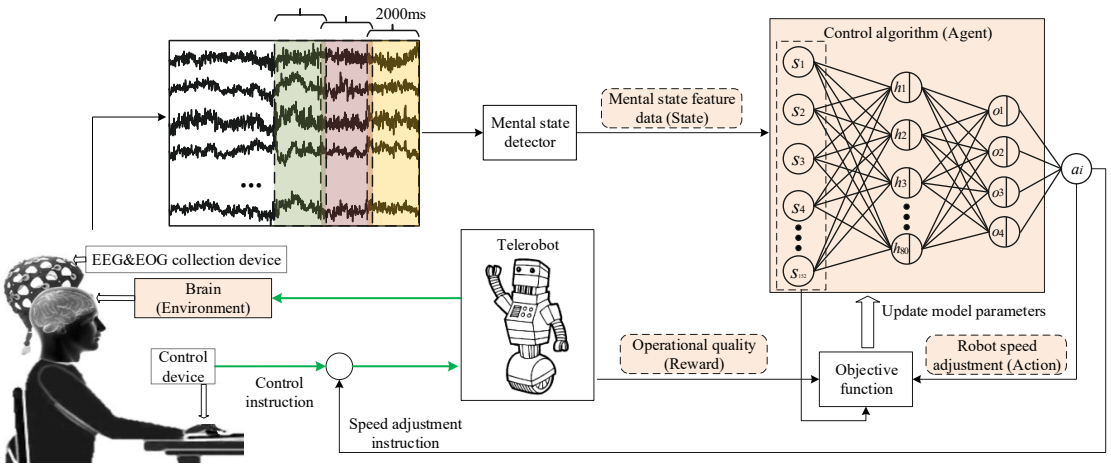

FIGURE 3
The figure shows the update process of the PSA model.

computer subsystem included two modules, the first one was the PSA module, which was responsible for real-time processing of bioelectrical signals (EEG and EOG), detecting the operator's mental state, and generating speed adjustment instructions for the robot. This module used MATLAB 2019b and PYTHON3.6. The second was the task simulator module, which was responsible for generating the task environment. This module uses PYTHON3.6. TCP/IP communication was used between the two modules. A microprocessor with Intel (R) Core (TM) i5-5600 CPU was employed in the computer. The interactive subsystem (this refers to the mouse) was used to realize the human-computer interaction function. An overview of the system is illustrated in Figure 5. When the operator controlled the robot through the mouse to perform tasks, the EEG and EOG were collected and transmitted to the computer in real-time. Then, the computer detected the operator's mental state and sent the speed adjustment instruction adaptively. Specifically, the EEG and EOG cap worn by the operator collected EEG and EOG data in real time while performing the task and sent it to the computer. The computer sequentially performed preprocessing (see section "Multimodal bioelectrical signal preprocessor" for details), feature extraction (see section "Mental state feature extractor") and PSA model processing (see section "Personalized speed adaptation model trainer") on these data. Then generated a speed adjustment instruction and sent it to the robot. MATLAB 2019b was used in the data preprocessing and feature extraction steps, and PYTHON 3.6 was used in the PSA model processing steps.

Experimental task

By analyzing the common characteristics of the telerobot tasks, we abstracted two virtual tasks, namely trajectory tracking and target positioning. Trajectory tracking could simulate tele-operated EOD robots to perform explosive transfer tasks, tele-operated detection robots to perform submarine inspection tasks, and tele-operated AGV robots to perform cargo transfer tasks, etc. Target positioning could simulate the remote-operated weapon system to perform targeting tasks, and the remote-operated aircraft to perform rendezvous and docking tasks with the space station. The specific contents of these two experimental tasks are as follows.

Figure 6A shows the screen of the trajectory tracking task, in which the blue block represents the mobile robot, and the red dotted line represents the preset trajectory. The operator could control the robot to perform the trajectory tracking task through the mouse. Specifically, the operator only needed to move the mouse (without clicking any button), and dragged the robot to move along the preset trajectory. The robot's position was coupled to the mouse coordinate system. The trajectory of the robot's movement in each round was recorded by the computer, and the deviation between it and the preset trajectory was calculated. When the robot moved from the starting point to the endpoint, it was regarded as having completed a round of trajectory tracking task. The trajectory deviation and task completion time were recorded to evaluate the trajectory tracking task's operational quality (the calculation formula is as shown in section "Personalized speed adaptation model trainer"). To increase the diversity of experimental trajectories, three difficulty levels of horizontal straight, slope, and curve were designed; Figure 6B shows the screen of the target positioning task, in which the red center is the bullseye, and the white rectangle is the sight (it can also be considered a robot). The operator could control the sight to perform the target positioning task through the mouse. Specifically, the operator only needed to move the mouse (without clicking any button), and dragged the sight to track the

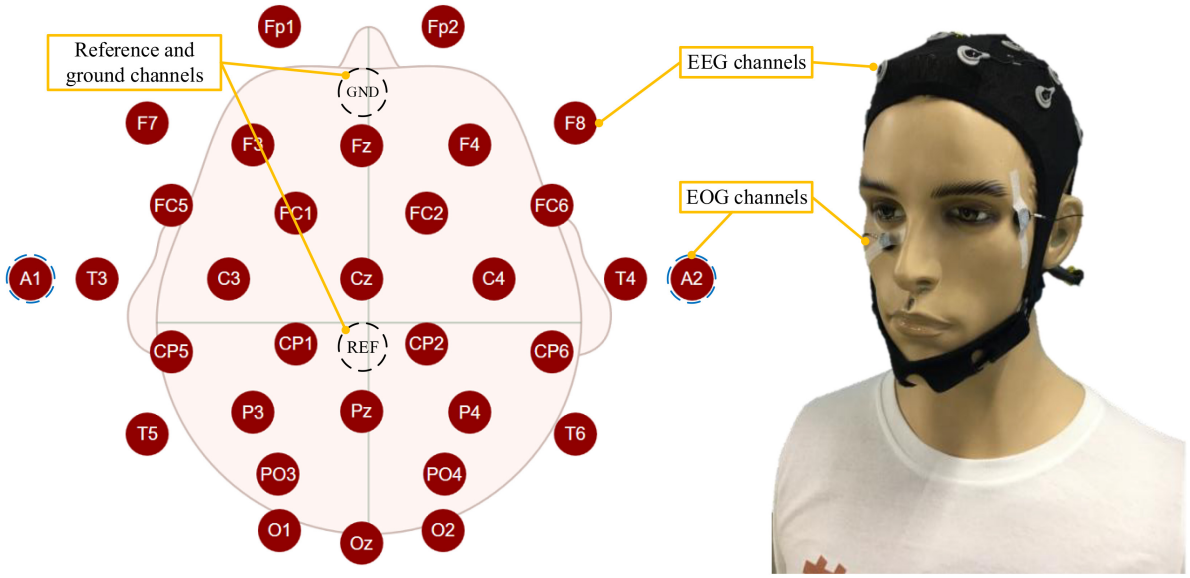

FIGURE 4
The figure shows the distribution of EEG and EOG electrodes and how the participant wore them.

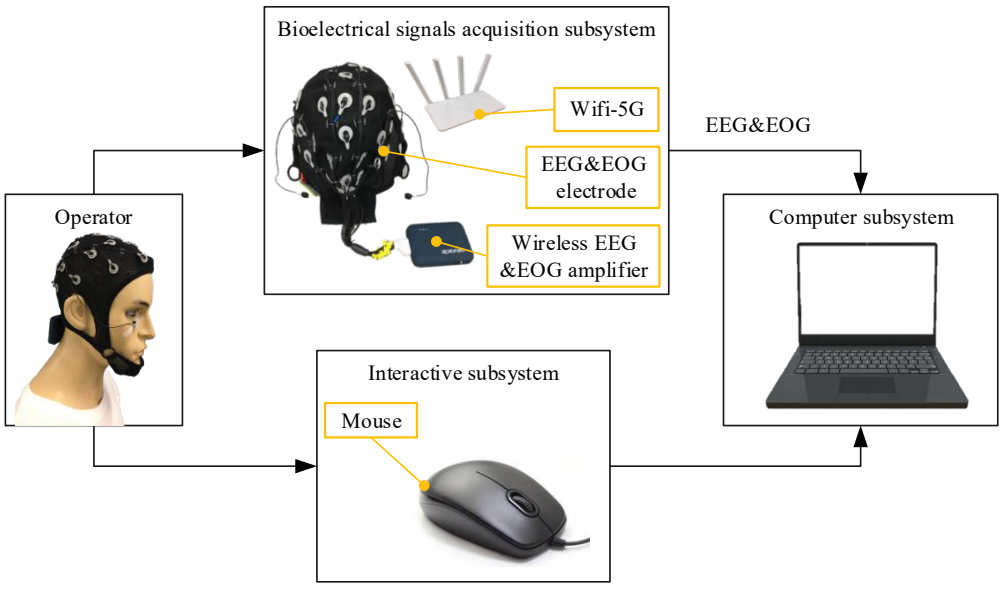

FIGURE 5
The figure shows the overview of the PSA experimental system.

target. When the rectangular frame of the sight fully enclosed the target's ring and was locked for a while, the target positioning mission was considered successful. The task completion time was recorded to evaluate the operational quality (the calculation formula is as shown in section "Personalized speed adaptation model trainer") of the target positioning task. The bullseye moved randomly to the next position after each round. The control instructions of the robot were controlled by the operator through the mouse, and the speed adjustment instructions were continuously adjusted by the CA in the PSA model according to the changes in the operator's mental state. The robot combined the two instructions to perform the tasks. In the task, the operator continuously adjusted the control instruction by observing the robot's running state. Meanwhile, the CA adjusts the robot's speed adjustment instruction in real-time by detecting the mental state of the human brain.

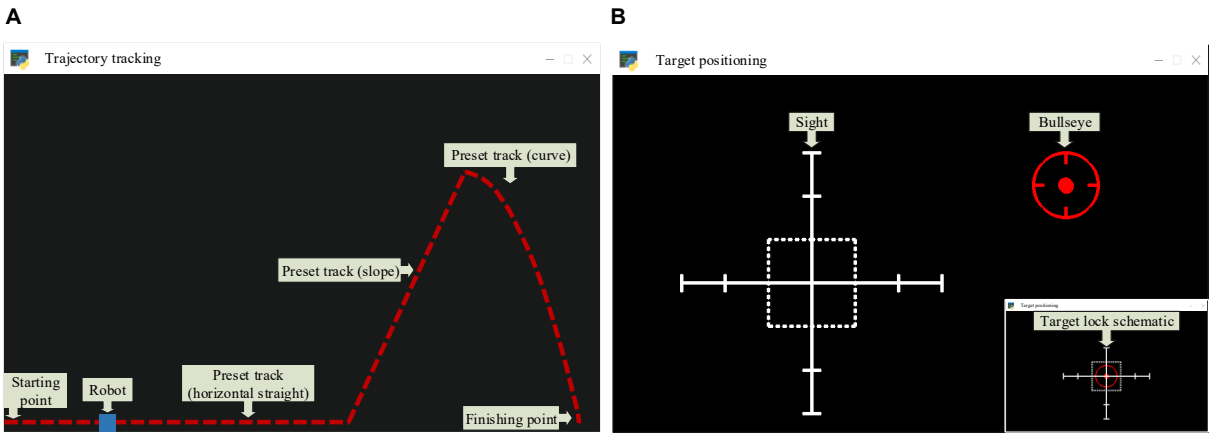

FIGURE 6
(A) The trajectory tracking task requires the operator to control the robot to move from the starting point to the finishing point. The higher the fitting degree of the trajectory and the robot's preset trajectory, and the shorter the task completion time, the higher the operational quality will be. Besides, three stimulation conditions were set in the experimental task, namely positive mental state stimulation, negative mental state stimulation, and nervous state stimulation. These stimulation conditions were also set in the target positioning task. **(B)** The target positioning task requires the operator to control the sight to track the bullseye. The shorter the time to complete the task, the higher the operational quality will be.

Experimental scenarios and procedures

In the experimental task of controlling the robot, the participants were asked to sit quietly in front of the computer screen and control the robot or the sight on the screen to perform trajectory tracking or target positioning tasks by mouse, and the experimental scenarios are shown in Figure 7. The experimental tasks were divided into three sessions, namely training session, testing session and control session, and the experimental procedures are shown in Figure 8. Firstly, the training session was used to train PSA model parameters. In the training session, the experiment was performed for 18 rounds. The first 3 rounds were used to practice trajectory tracking and target positioning tasks to prevent different operational proficiency from affecting the experimental results. The last 15 rounds were formal experiments, with 1 min rest time in the middle of every 5 rounds. Secondly, the testing session was used to test the effect of the PSA method. And the trained PSA model parameters were imported into the PSA model in the testing session. In the testing session, the experiment was performed for 15 rounds. Thirdly, the control session was used to provide reference. The conventional method was used in the control session (i.e., this method relies on a warning threshold to trigger an adjustment strategy (Stanney et al., 2009). A warning threshold for whether to enable the adjustment strategy was preset. Then, if the output value of the mental state detector was greater than the warning threshold, the adjustment strategy will be initiated to adjust the speed of the robot; otherwise, the adjustment strategy was not activated. More specifically, when the output value of the mental state detector was higher than the warning threshold, the speed of the robot was reduced. Conversely, when the output value of the mental state detector returned to normal, that is, when it was lower than the warning threshold, the speed of the robot was restored. It is a fixed, non-personalized method of adjustment). In the control session, the experiment was performed for 15 rounds. The effectiveness and superiority of the PSA method were analyzed through the comparison between the testing session and the control session. At the end of each experimental session, the subjects were asked to answer several subjective questionnaire questions. It took about 2 h for each subject to complete the experiment of 3 sessions in total, and the whole experiment lasted 6 days to complete.

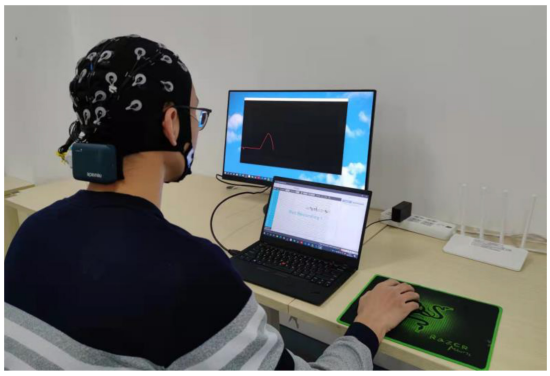

FIGURE 7
The figure shows the experimental scenario.

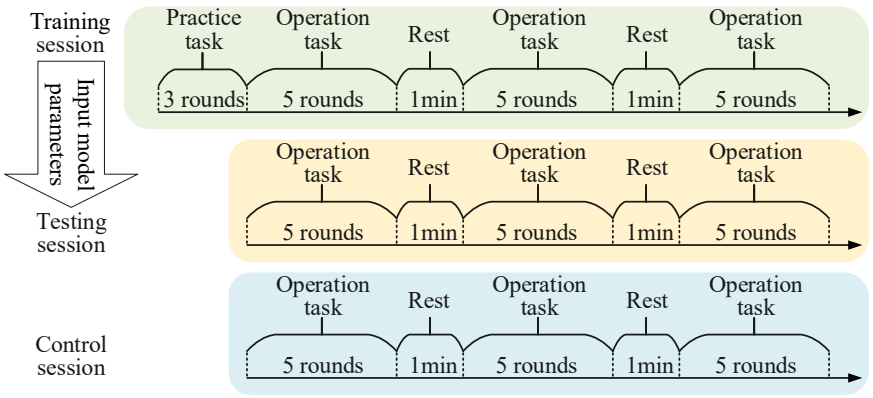

FIGURE 8
The figure shows the experimental procedure.

Moreover, to increase the diversity of mental states in sampled data, two main measures were adopted. Firstly, three kinds of stimulation conditions were set in the experimental task, namely positive mental state stimulation: a positive text prompt of "Performance is very good" would appear randomly on the screen; negative mental state stimulation: a negative text prompt "Performance is very bad" would appear randomly on the screen; nervous state stimulation: a text prompt of "The Key round" would appear randomly on the display screen, accompanied by the audio prompt of a countdown. Secondly, by setting up the rest time of the experiment, the mental state of fatigue and non-fatigued could be increased. By analyzing the questionnaires of the participants, the settings of these two measures increased the diversity of mental states during the experiment to a certain extent (see section "Changes in mental state during teleoperation experiments" for details).

Data processing

Data processing mainly includes three steps of multimodal bioelectrical signal (EEG and EOG) preprocessing, mental state feature extraction, and efficient model training. The detailed processing flow is shown in **Figure 9**.

Multimodal bioelectrical signal preprocessor

To feed real-time EEG and EOG into the PSA model, the last 1 min long signal in the computer memory was extracted at each round. A time window of 2000 ms duration was designed for sliding sampling, and 50 sets of raw data were generated. Then, the data was preprocessed, which mainly includes three steps. Firstly, baseline drift in raw EEG and EOG signals was eliminated by the fitted baseline method. The purpose was to eliminate the effects of baseline drift in technical artifacts. The detailed operation method was to fit the trend term by the least squares method, and then subtracted the trend term from the original data. Secondly, the 4th order Butterworth bandpass filter was used to process the two original signals, retaining the EEG of 0.5−45.0 Hz and the EOG of 0.1−30 Hz, respectively. Since EOG also contained mental state information, it was an effective signal in this study, so no artifact processing operation was required for it. Finally, the sampling frequencies of EEG and EOG were down-sampled to 256 Hz and 128 Hz, respectively, thereby reducing the amount of data and improving the calculation speed.

Mental state feature extractor

We first introduced the feature extraction method of EEG, which mainly included three steps: (1) Obtained rhythm waves in different frequency bands through wavelet transform. (2) Calculated the four features of sample entropy (*SE*), differential entropy (*DE*), band power (*BP*) and band energy (*BE*) for rhythmic waves of various frequency bands. (3) Calculated the mutual information (*MI*) value between each feature and arousal (or valence) to judge the validity of the feature (it should be noted that the third step was to compare the pros and cons of the four features, which was not required in the actual algorithm running). The following is a detailed introduction. Firstly, the EEG was decomposed and reconstructed using the wavelet basis function of fifth-order vanishing interval Daubechies, and five kinds of rhythmic waves were generated. Their frequency bands are δ (0.5−3 Hz), θ (4−7 Hz), α (8−15 Hz), β (16−31 Hz), and γ (>32 Hz), respectively (Hipp et al., 2011; Dimitrakopoulos et al., 2018). The wavelet transform formula is as follows:

$$x_j = AC_j + \sum_{j=1}^{L} DC_j \tag{8}$$

where x_j represents EEG of the jth frequency band; L represents the number of decomposition layers; AC_j represents the approximate component of the jth frequency band; DC_j represents the detailed components of different scales of the jth frequency band. Secondly, *SE* features, *DE* features, *BP* features,

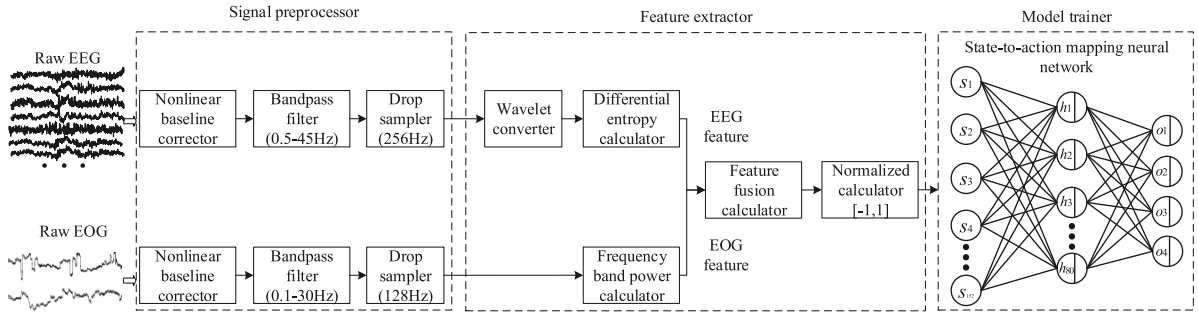

FIGURE 9
Flow chart of data preprocessing steps.

and *BE* features of 5 rhythmic waves from 30 EEG channels were calculated. Studies had found that as the mental state changes, the information complexity of EEG was also changing (García-Martínez et al., 2016; Xu et al., 2019; Ahammed and Ahmed, 2020). For example, when the degree of fatigue increases, the ability of the central nervous system to inhibit brain neural activity may increase, resulting in a decrease in the disordered degree of thinking in the cerebral cortex, thereby reducing the information complexity of EEG (Wang et al., 2011). For another example, Deli and Fry studied positive and negative mental states from the perspective of thermodynamics, and believed that the positive state is in an endothermic cycle (Reversed Carnot cycle), which is a process of absorbing energy from the environment and increasing entropy; In contrast, the negative state is in an exothermic cycle (Carnot cycle), a process that releases energy into the environment and reduces entropy (Deli and Kisvarday, 2020). This also leads to changes in the information complexity of EEG. Therefore, this paper selected representative *SE* and *DE* features for analysis. The *SE* is defined as the negative natural logarithm of the conditional probability that the two subsequences are similar when the pair of subsequences of length m are similar after adding one sample point in each order. It can be used to describe the self-similarity and complexity of a sequence (Cuesta-Frau et al., 2017). The lower the *SE* value, the higher the self-similarity of the sequence and the lower the complexity, and the calculation formula of *SE* is as follows (Li et al., 2018):

$$SE(U, v, \eta) = -\ln \frac{B^{v+1}(\eta)}{B^{v}(\eta)} \tag{9}$$

where U is the sequence length. v is the length of continuous subsequence. η is the distance error threshold to judge the similarity of two subsequences. $B^{v}(\eta)$ represents the logarithm of the continuous subsequence with length m satisfies the similarity condition r in the sequence. The parameters m and r can be determined by cross-validation results on the training set. In this paper, $m = 2$, $r = 0.2^{*}std$, where std is the data's standard deviation. Besides, *DE* could also be used to measure the complexity of temporal sequence signals (García-Martínez et al., 2016). For a fixed-length EEG sequence, the calculation formula of *DE* can be approximated as (Shi et al., 2013):

$$\left.\begin{array}{l} DE(x) = -\int_{x} f(x)\ln(f(x))dx \approx \\ -\int_{-\infty}^{\infty}\left\{\frac{1}{\sqrt{2\pi\sigma^2}}\exp\left[-\frac{(x-\mu)^2}{2\sigma^2}\right]\ln \right. \\ \left.\left(\frac{1}{\sqrt{2\pi\sigma^2}}\exp\left[-\frac{(x-\mu)^2}{2\sigma^2}\right]\right)\right\}dx = \\ \frac{1}{2}\ln\left(2\pi\sigma^2\right)+\frac{1}{2} \\ \sigma^2 = \frac{1}{L}\sum_{j=1}^{L} x_j^2 \end{array}\right\} \tag{10}$$

where $f(x)$ is the probability density function of time series. μ and σ represent the mean and standard deviation of the Gaussian, respectively. In addition, the study found that the frequency domain characteristics of EEG could also characterize mental state. Therefore, this paper selected two features, *BP* (Liu F. et al., 2021) and *BE* (Matei and Matei, 2021), respectively. Finally, *MI* was used to analyze the amount of mental state information contained in the four EEG features, so as to select the optimal feature. *MI* between these four features (*SE*, *DE*, *BP*, and *BE*) and the valence (or arousal) in dimension theory were calculated separately. In probability theory and information theory, *MI* of two random variables is a measure of the interdependence of variables (Peng et al., 2005). In this paper, the *MI* of X_F and Y_L, two random variables representing features and valence (or arousal), respectively, is defined as:

$$MI(X_{\mathrm{F}};\, Y_{\mathrm{L}}) = \sum_{y_{\mathrm{L}}\in Y_{\mathrm{L}}}\sum_{x_{\mathrm{F}}\in X_{\mathrm{F}}} p(x_{\mathrm{F}}, y_{\mathrm{L}})\log\left(\frac{p(x_{\mathrm{F}}, y_{\mathrm{L}})}{p(x_{\mathrm{F}})p(y_{\mathrm{L}})}\right) \tag{11}$$

where $p(x_{\mathrm{F}}, y_{\mathrm{L}})$ is the joint probability distribution function of X_F and Y_L. $p(x_{\mathrm{F}})$ and $p(y_{\mathrm{L}})$ are the marginal probability distribution functions of X_F and Y_L, respectively. Study found *DE* could effectively characterize mental state (Zheng and Lu, 2015; Zheng et al., 2019; Liu S. et al., 2021) (see section "Analysis of mental state features" for details), hence, it was selected as an EEG feature to represent mental state in the following study. There were 30 EEG channels, and the EEG of each channel was decomposed into 5 rhythmic waves, so the features data of EEG had a total of 150 dimensions.

Then, we introduced the feature extraction method of EOG. It was found that the low-frequency components of EOG increased while the high-frequency components decreased when the arousal level was low (Ma et al., 2014). Therefore, the power ratios (*PR*) of low-frequency components and high-frequency components in the signals were selected as the EOG features representing mental states. The calculation formula is as follows:

$$PR = \frac{pl(x)}{ph(x)} \tag{12}$$

where $pl(x)$ and $ph(x)$ represent the power of low-frequency component (0−1.5 Hz) and high-frequency component (1.5−30 Hz), respectively (Magosso et al., 2007; Gao et al., 2012). There were 2 EOG channels, so the features data of EOG had a total of 2 dimensions. In summary, the EEG and EOG features data were combined and normalized to form 152-dimensional characteristic data representing the operator's mental state.

Personalized speed adaptation model trainer

To consider the algorithm accuracy and response speed, a three-layer fully connected state-to-action mapping neural network (SAMNN) was established in the PSA model. The input of the network was mental state s_i and the output was robot speed adjustment instruction a_i. There were 152 neurons in the input layer, 80 neurons in the hidden layer, and 4 neurons in the output layer, representing 4 dimensionless speed levels. Tanh activation function (LeCun et al., 2012) was adopted in the hidden layer. The reason was that (1) the network had only one hidden layer, and under the premise of enjoying the advantages of the Tanh activation function, there was no need to worry about the hidden danger of gradient vanishing (Wang et al., 2019). At the same time, (2) the problem of permanent neuron death by using the ReLU activation function was avoided (Nair and Hinton, 2010). Softmax function (Liang et al., 2017) was used for the output layer. The higher the value of the output neuron, the higher the probability of the corresponding action being selected, and vice versa. Then, *s*, *a*, and *R* was input to the objective function [Formula (6)], and the SAMNN parameters were updated according to the adaptive moment estimation method (ADAM) (Kingma and Ba, 2014), Among them, the exponential decay rate for the 1st moment estimates was set to 0.9, and the exponential decay rate for the 2nd moment estimates was set to 0.999. The learning rate was set to 0.001. Each round was an episode, each episode would generate 50 sets of data pairs, and the batch size was 50. The SAMNN parameter was updated once every episode until the model converged.

It is important to note that the reinforcement learning model's performance is directly affected by the convergence property (Mnih et al., 2015). Therefore, to enhance the convergence performance of the PSA model, shorten the convergence process and improve data utilization, before the online training of the PSA model, the DEAP (Koelstra et al., 2012) dataset was first used to pre-train the SAMNN. The input was feature data representing the mental state, which was from the DEAP dataset. The output was 4 categories representing High valence and High arousal, High valence and Low arousal, Low valence and High arousal, and Low valence and Low arousal, respectively. After 10,000 epoch training, the loss function value was 0.001. It should be noted that before the main model training starts, the pre-trained model parameters need to be imported into the main training model.

In addition, it should be noted that the reward *R* in the PSA model [that is, the *R* in Formula (6)] needed to be calculated according to the specific task, which represented the operational quality. The trajectory tracking reward R_t was evaluated by two indicators of robot trajectory quality and task completion time. The target positioning task reward R_p was evaluated by the indicator of task completion time. The calculation formula is as follows:

$$\left.\begin{array}{l} R_{\mathrm{t}} = \frac{1}{\sum_{m=1}^{M} |Y_m - O_m|} + \frac{g}{t} \\ R_{\mathrm{p}} = \frac{g}{t} \qquad \text{if} \quad t \geq T \end{array}\right\} \tag{13}$$

where *Y* represents the trajectory of the robot. *O* represents the target trajectory. *t* is the time to complete each round. *g* is the time gain coefficient. *M* represents the total number of steps of the whole trajectory, and *T* represents the time threshold of the sight continuously aiming at the bullseye.

Results

Analysis of mental state features

In order to find EEG features that can stably and effectively represent mental state, we used the DEAP dataset to calculate the average of the four EEG features (*SE*, *DE*, *BP*, and *BE*) described above, and the *MI* between these four averages and valence. The higher the *MI*, the more mental state information was contained in the feature data, and vice versa. For a more intuitive display, for each feature, the *MI* of each rhythmic wave in 30 EEG channels was calculated separately, and the brain topographic map was drawn according to the *MI* value. **Figure 10A** shows the *MI* brain topography between *SE* and valence for the five rhythmic waves. By contrast, it was found that *MI* decreased with increasing rhythmic wave frequency. **Figure 10B** shows the *MI* brain topography between *DE* and valence for the five rhythmic waves. By comparison, it was found that the *MI* not only did not show an obvious decreasing trend, but also all channels remained at a relatively high level (the average was 0.85), which indicated that the *DE* features contained more information of mental state and had a high stability. **Figures 10C,D** show *MI* brain topography between *BP*, *BE*, and valence for the five rhythmic waves, respectively. Both *MI* values showed a low level (average values were 0.4, 0.3, respectively), and the volatility between each rhythm wave

was large, and the volatility between each channel was also large. Comprehensive comparison found that the *MI* value of the *DE* feature data was the highest and the stability was strong. At the same time, the study found that the *MI* between these four features and arousal also had the same regularity. To sum up, the *DE* feature contained the most mental state information, and the PSA method achieved the expected effect in the experiment, which also proved the reliability of this phenomenon. Therefore, *DE* features were selected as EEG features to represent mental states.

Changes in mental state during teleoperation experiments

In order to analyze the change characteristics of the subjects' mental state during the experiment, we integrated the data recorded by the subjective evaluation scale to generate **Table 1**. The fatigue level of all subjects changed during the experiment. All subjects except subject 2 experienced changes in their stress level. Except for subjects 4 and 6, the positive and negative mental states of the other subjects changed. It showed that by setting the task difficulty and auxiliary stimulation conditions, the subjects could be induced to induce different mental state. Comprehensive analysis found that subject 1, subject 3, and subject 5 had changes in the degree of fatigue, stress and positive/negative states. Compared with other subjects, these three subjects were more likely to have mental state fluctuations, which was also a manifestation of individual differences.

Taking subject 3 to perform the trajectory tracking task as an example, we recorded his EEG in three states of normal, fatigue and stress during the experiment, and calculated the *DE* feature of the EEG in 30 channels, and then drawn the brain topography according to *DE* value. Firstly, by comparing the brain topographic maps of the fatigue (**Figure 11B**) and normal state (**Figure 11A**), it was found that the *DE* value decreased when the subject moved from the normal state to the fatigue state, indicating that the complexity of the EEG was reduced. This is in line with previous studies, where one explanation is that fatigue induces the inhibition of cerebral cortical activity by the central nervous system, resulting in a reduced degree of disorder in the EEG of the cerebral cortex (Liu et al., 2010; Wang et al., 2011; Xu et al., 2019). In addition, in the fatigue state, the *DE* values of the occipital lobe, part of the parietal lobe and the prefrontal lobe region decreased to a greater extent (the regions indicated by the arrows in **Figure 11B**), indicating that these regions are closely related to the processing of the fatigue state. And this phenomenon had also been confirmed in previous studies (Chuang et al., 2018; Ma et al., 2019; Liu et al., 2020). Secondly, by comparing the brain topographic maps in the stress state (**Figure 11C**) and the normal state (**Figure 11A**), it was found that the *DE* values in both temporal lobes increased in the stress state (the regions indicated by the arrows in **Figure 11C**). This phenomenon is consistent with previous studies, and one explanation is that the temporal lobe is involved in the processing of stress states, which are closely related to stress states (Hosseini and Naghibi-Sistani, 2011; Lucassen et al., 2014; Choi et al., 2015; Katmah et al., 2021).

Without loss of generality, the average properties of all subjects' mental states while performing the trajectory tracking task were analyzed. Taking the fatigue state as an example, the reason is that in the experiment, each subject reported that the fatigue state appeared. We recorded the EEG when all subjects reported fatigue during the experiment, calculated the *DE* characteristics of the EEG in 30 channels separately, and plotted a line graph based on their mean and standard deviation. **Figure 12** shows that, relative to the normal state, the *DE* value of the fatigue state is reduced, especially in the occipital region, part of the parietal region and the prefrontal region, which is also consistent with the phenomenon in **Figure 11B**. The generality of EEG features in the fatigue state was demonstrated. To sum up, by analyzing the EEG characteristics of the subjects when they appeared in various mental states during the experiment, and it was found that the same phenomenon existed in previous studies, which proved that the subjects would produce different mental states during the experiment.

Feasibility analysis of personalized speed adaptation

To demonstrate the feasibility of the PSA method, we recorded the operational quality of each subject at the early (the first 3 rounds) and late (the last 3 rounds) training stages, normalized the data, and plotted it into boxplots (**Figure 13**). In the two experimental tasks, the operational quality of each subject in the late training stage was significantly improved compared with the early training stage. A total of 36 data pairs were formed by recording the operational quality data of all subjects at the early and late stages of training. Statistical analysis using two-sample *T*-test found that there was a significant difference in the operational quality between the two periods, as shown in **Figure 14A**. It showed that in the training process of the PSA model, CA gradually learned the mapping relationship between each subject's mental state and the robot's speed adjustment instructions, and could adjust the robot's speed in real time according to the mental state, thereby improving the operational quality. In addition, in the trajectory tracking task, the interquartile range (IQR) value of each subject (except subject 5) at the later stage of training was lower than that at the early stage of training. In the target positioning task, the IQR value of each subject (except subject 3) was lower in the late training period compared to the early training period. At the same time, **Figure 14A** shows that in both experimental tasks, the standard deviation of the operational quality data in the later stage of training is smaller than that in the early stage of training.

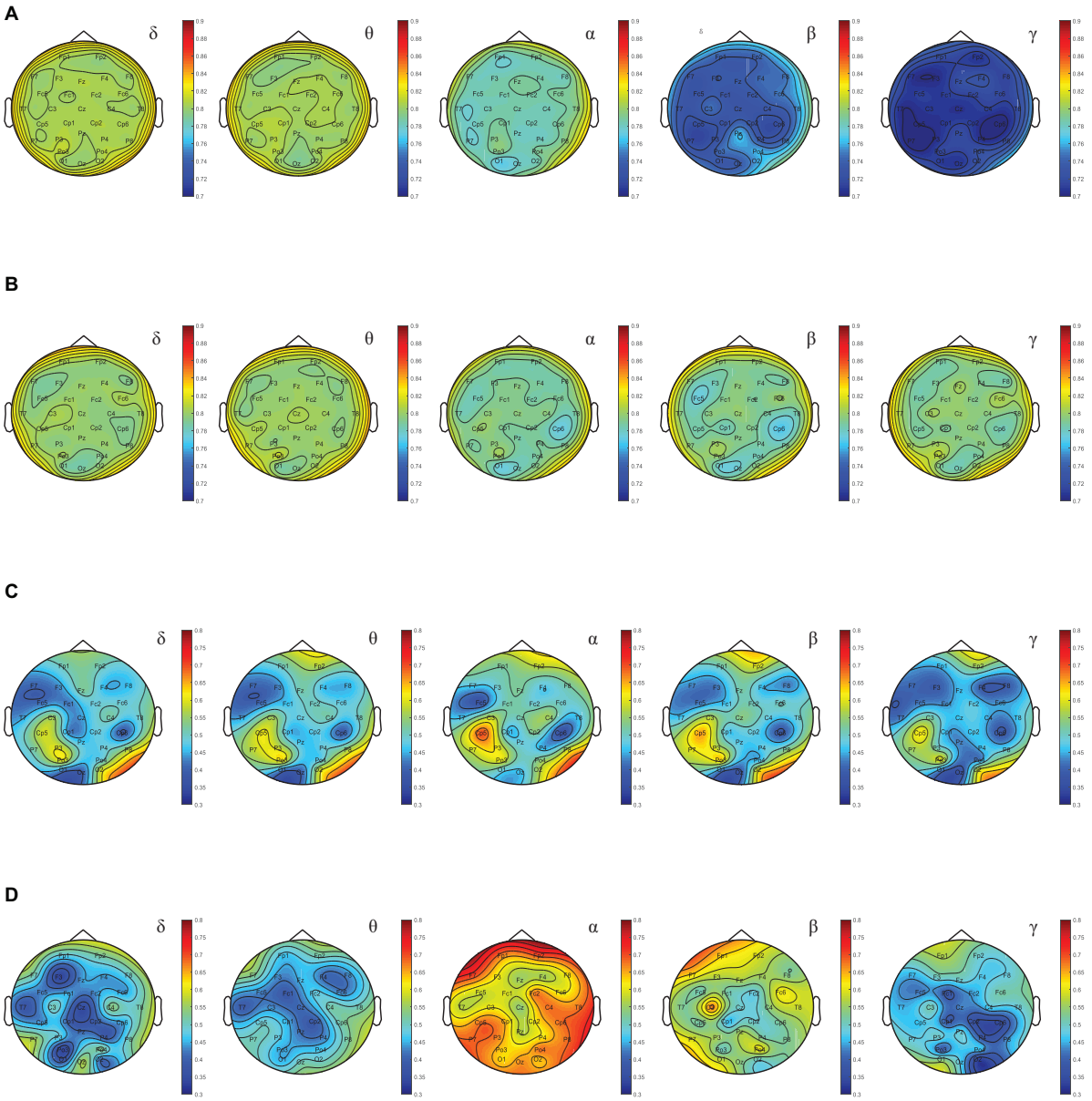

FIGURE 10
(A) Brain topography based on *MI* between *SE* and valence. **(B)** Brain topography based on *MI* between *DE* and valence. **(C)** Brain topography based on *MI* between *BP* and valence. **(D)** Brain topography based on *MI* between *BE* and valence.

TABLE 1 Subjective evaluation results of mental state during the experiment.

	Has fatigue level changed?	Has the stress level changed?	Have positive and negative mental states changed?
Subject1	Yes	Yes	Yes
Subject2	Yes	No	Yes
Subject3	Yes	Yes	Yes
Subject4	Yes	Yes	No
Subject5	Yes	Yes	Yes
Subject6	Yes	Yes	No

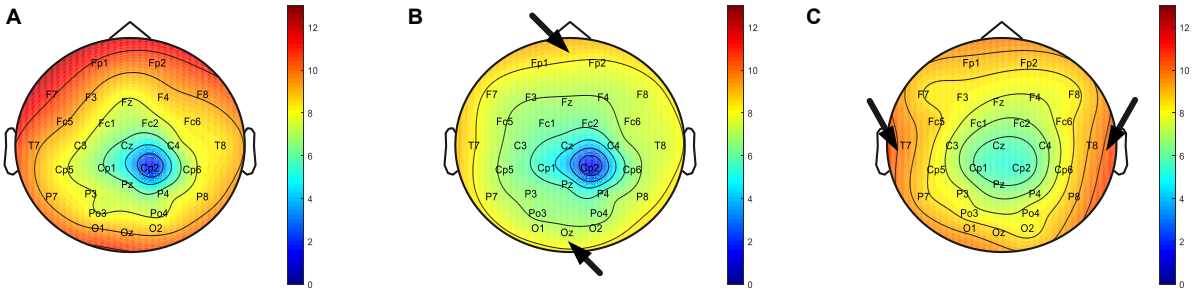

FIGURE 11
(A) Brain topography in normal state. **(B)** Brain topography in fatigue state. **(C)** Brain topography during stress state.

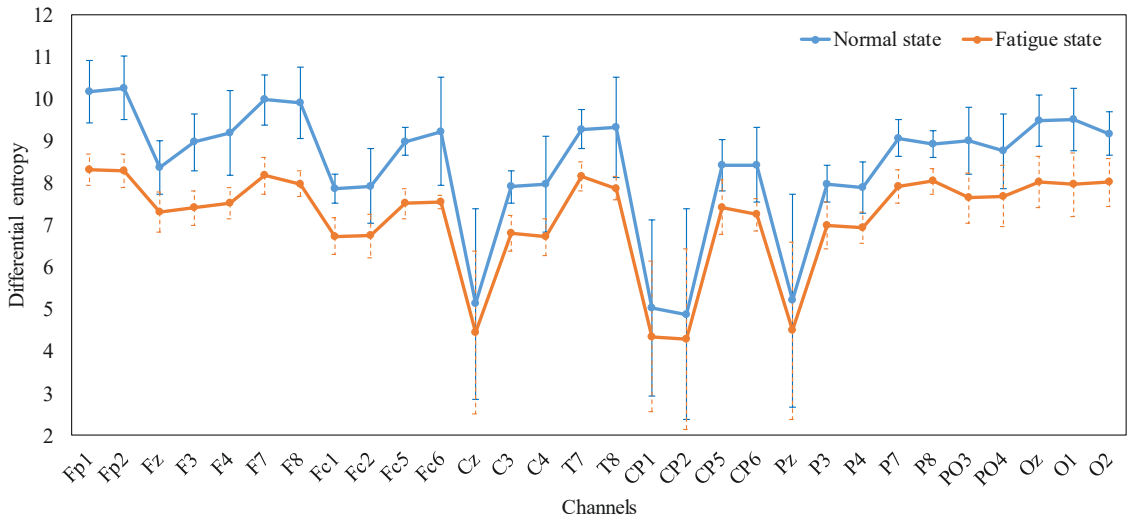

FIGURE 12
Line graph of the average *DE* characteristics of all subjects in normal and fatigue states, respectively.

Both phenomena illustrated that after training, the PSA model gradually converges and the stability gradually improves. Taken together, the feasibility of the PSA method was demonstrated by these phenomena.

Superiority analysis of personalized speed adaptation

In order to demonstrate the superiority of the PSA method, we choose the current conventional adjustment method based on mental state and the PSA method for comparison, that is, the comparison between the control session and testing session experiments. In the control and test groups of each experimental task, the operational quality data of 6 subjects who performed 15 rounds of the task were recorded, forming a total of 90 data pairs. The mean and standard deviation of these data were calculated, respectively, and then a contrast histogram was drawn. Figure 14B shows that the average operational quality of the PSA method is better than that of the conventional method in both experimental tasks. And the statistical analysis by the two-sample *T*-test found that there was a significant difference in the mean between the two. In conclusion, the validation of 6 subjects in two independent experimental tasks showed that the PSA method was superior to conventional mental state-based adjustment methods. Furthermore, since the feasibility and superiority of the PSA method could be verified on two experimental tasks with different levels of difficulty and task modes, it was proved that the PSA method has good universality.

Personalized analysis of personalized speed adaptation

Through the analysis of the robot speed adjustment instructions (actions) output by the trained PSA model for each subject, it was found that the PSA method had been individually adjusted according to the mental state of different subjects.

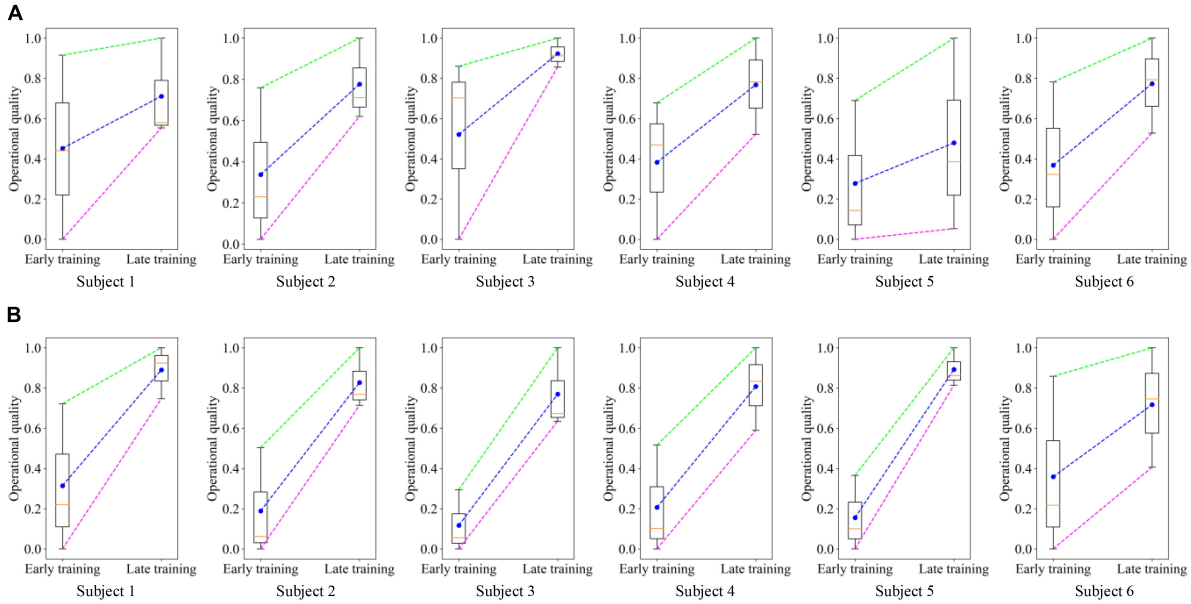

FIGURE 13
Boxplots were drawn based on the operational quality of all subjects in the early (the first 3 rounds) and late (the last 3 rounds) stages of PSA model training. The dots in the figure represent the mean value, and the horizontal line represents the median. **(A)** Trajectory tracking task. **(B)** Target positioning task.

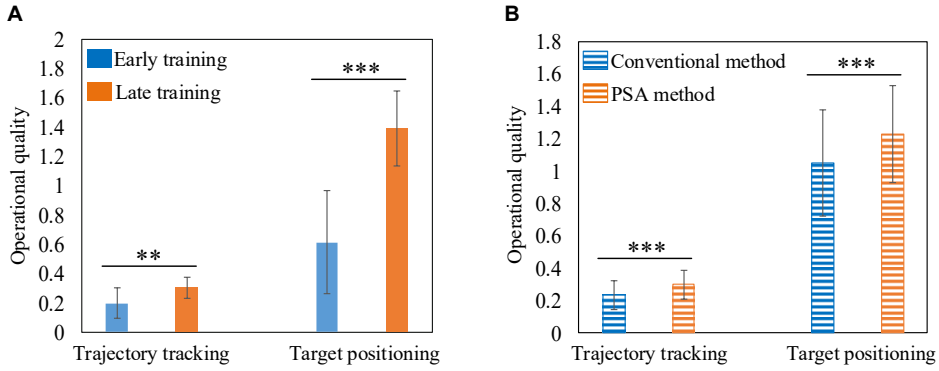

FIGURE 14
(A) The comparison histogram of operational quality between early and late training. **(B)** The comparison histogram of operational quality between the conventional method and the PSA method. **Represents $p < 0.01$, and *** represents $p < 0.001$.

Referring to previous studies on the classification of operators (or drivers) style (Sadrpour et al., 2014; Gilman et al., 2015; Wang et al., 2020), we divided the subjects into aggressive and conservative types according to the speed of the robot controlled. Subject 1 and 5 belonged to the aggressive style, and the other 4 subjects belonged to the conservative style. Taking the trajectory tracking task as an example, we plotted the distribution histogram and fitting curve of the robot speed data controlled by the aggressive and conservative subjects during the task (**Figure 15**). **Figure 15A** shows that the robot controlled by the aggressive subjects has a wide range of X-axis velocity distribution (0∼9.0), the mean value of the velocity distribution is 1.22, and the standard deviation is 1.17; and the Y-axis velocity distribution range is also wide (−5.0∼4.0), the mean value of the velocity distribution is 0.09, and the standard deviation is 1.28. It showed that the aggressive subjects paid more attention to the sense of control when manipulating the robot, and there would be more rapid acceleration and deceleration. However, **Figure 15B** shows that the robot controlled by conservative subjects has a narrow range of X-axis velocity distribution (−0.3∼2.7), the mean value of velocity distribution is 0.38, and the standard deviation is 0.32; and the Y-axis velocity

distribution range is also narrow (−2.1∼1.8), with a mean value of 0.03 and a standard deviation of 0.41. It showed that conservative subjects paid more attention to the stability when manipulating the robot and avoid rapid acceleration and deceleration. Through this phenomenon, it was fully proved that the PSA method can perceive the differences between operators and make individual adjustments to the robot speed according to the mental state.

Visual analysis of personalized speed adaptation

In order to observe the effectiveness and superiority of the PSA method in the two experimental tasks more intuitively, the trajectories of subject 1 when controlling the robot (and sight) to perform the task in the testing session and the control session were recorded 5 times, respectively, as shown in **Figures 16**, **17**. In the trajectory tracking task, it can be seen from the relatively fluctuating trajectories of the control session that the mobile robot frequently loses the trajectory target (**Figure 16A**), so the operator needs to constantly adjust the control instructions. Not only does this lead to longer time spent on the entire task, but it also increases mental workload and negative emotions. For the testing session using the PSA method, the fit of the mobile robot's motion trajectory and the target trajectory is better than that of the control session, and the phenomenon of missing targets is reduced (**Figure 16B**). From the relatively smooth motion trajectories, it could be seen that the operator could control the mobile robot's travel trajectory compliantly, and did not need to adjust the control commands frequently, and the operation was more accurate and efficient. This phenomenon also exists in the target positioning task, especially when the sight is getting closer and closer to the bullseye, the trajectories of the control session shows that the sighting frequently loses the position of the bullseye. The trajectories at the 5 bullseye positions are like a mess of ropes, as indicated by the arrows in **Figure 17A**. This not only results in longer time spent on the entire task, but also increases the operator's mental workload and negative emotions. For the testing session using the PSA method, the trajectories show that the sight can quickly locate and lock the bullseye, no matter whether it is close to the trajectories of the bullseye stage, or the trajectories of the locking stage of the bullseye has been improved (**Figure 17B**). This showed that the operator could accurately control the sight, and did not need to adjust the control commands frequently for repeated positioning, and the operation was more accurate and efficient.

Without loss of generality, we listed the performance of all subjects in the test and control sessions. In the trajectory tracking task, **Table 2** shows that the operational quality of each subject (except subject 6) under the PSA method is better than that of the conventional method, and in the target positioning task, the operational quality of each subject under the PSA method is also better than that of the conventional method. Moreover, in both experimental tasks, the mean operational quality of the PSA method was also superior to that of the conventional method, thus proving the general applicability of the PSA method.

Discussion

This paper aims to study the feasibility of the PSA method based on mental state for teleoperated robots. The PSA model based on policy gradient reinforcement learning was established, and related algorithms were developed and verified by experiments on real subjects instead of simulation models. The following sections focus on personalization, rapid reinforcement learning, and the scalability of the method in application areas. Then, the existing limitations and future work are prospected.

Personalization

Due to the huge number of teleoperators involved in various fields of operation, different operators have obvious differences in age, personality, psychological state, and proficiency, as well as the inherent complexity of the operator's mental state and behavior. As a result, the differential representation of the operating habits and qualities of different operators has become a difficult problem. In the adjustment strategy design of the conventional teleoperated robot system, the method of adapting to the operator's behavior through parameter calibration is difficult to meet the individual needs of a large number of operators. Different from the conventional subjective (i.e., biased by developer experience) and fixed adjustment methods, the PSA method is objective and flexible (Sogaard et al., 2019; Tang et al., 2019; Wen et al., 2020). The first reason is that the PSA method is designed based on a reinforcement learning architecture, which can obtain feedback rewarded with operational quality through the interaction between the CA and the brain environment, to capture the mapping between various mental states and robot speed regulation commands in real time. Then, the mapping between the various mental states and the robot's speed-regulating commands is captured in real time. In this way, a personalized "human-in-the-loop" teleoperated robot system model is dynamically established. It can better solve the problems that are difficult to overcome by conventional methods. For example, **Figure 15** shows that under the adjustment of the PSA method, the distribution of the speed (action) data of the robot controlled by the subjects has changed, indicating that the method has established a personalized adjustment strategy for each subject. Not only that, as the operating time increases, the operator's cognitive level and

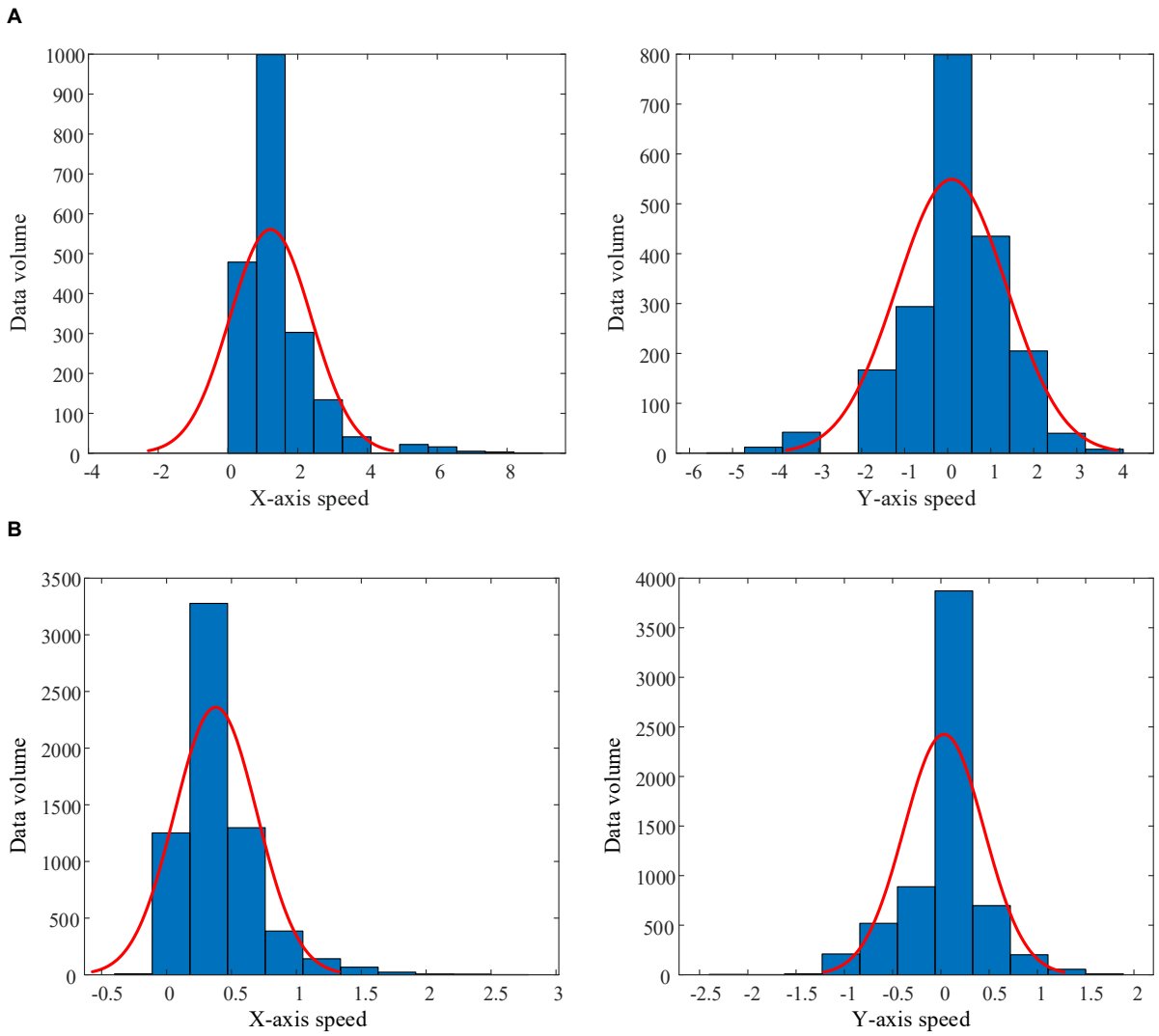

FIGURE 15
Histograms and fitting curves of the speed distributions of the robots controlled by aggressive style and conservative style subjects. **(A)** Aggressive style subject. **(B)** Conservative style subject.

operation skills of the system are also continuously improved, and the operation habits are also changed. The second reason is that the CA (agent) in the PSA model collects more and more personalized, comprehensive information about the operator. Based on this data, model parameters are continuously optimized and adjusted, allowing each teleoperated robotic system to evolve toward a personalized direction. Therefore, the teleoperated robot system equipped with the PSA method also has the ability of lifelong learning and continuous evolution.

Rapid reinforcement learning

Personalized speed adaptation is a reinforcement learning method based on "human-in-the-loop," which includes a typical online interactive learning process and has unique advantages, such as personalization, evolution, and better dynamic adaptability. However, due to the difficulty in ensuring the convergence and training efficiency of the "human-in-the-loop" reinforcement learning model, most of the current research is mostly carried out on simulated human models. For example, Wu et al. (2022) established a robot knee tracking control method based on "human-in-the-loop" reinforcement learning, which was verified in a so-called realistic human-robot system simulator. To the best of our knowledge, there is little research and experimental validation on human models, and even less in the field of teleoperated robotics. One reason is that the human brain is an element in the model, which increases the model's complexity and uncertainty. As Xuesen Qian pointed out, the living system, especially people with

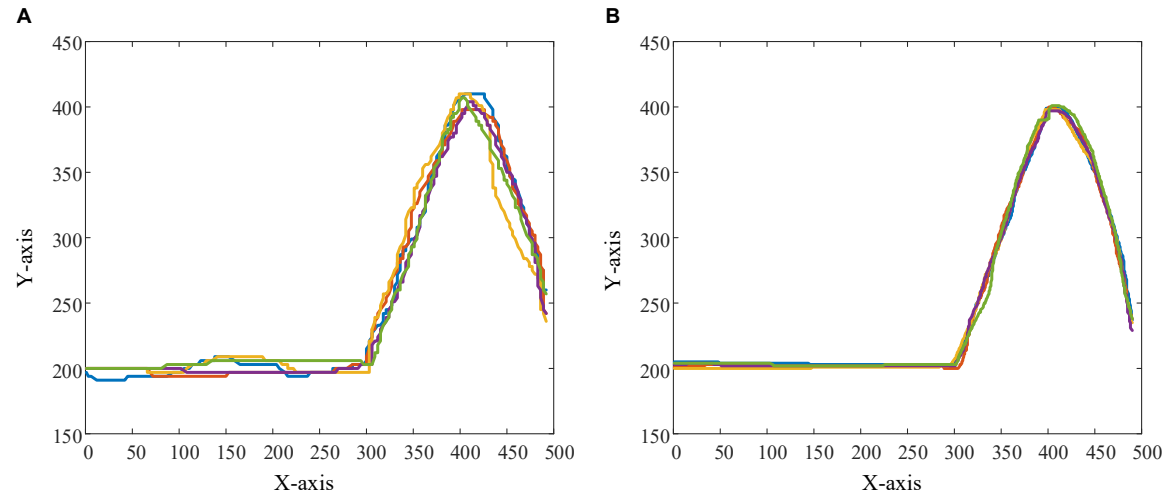

FIGURE 16
The figure shows the trajectories of the mobile robot in the trajectory tracking task. **(A)** Robot trajectories in the control session. **(B)** Robot trajectories in the testing session.

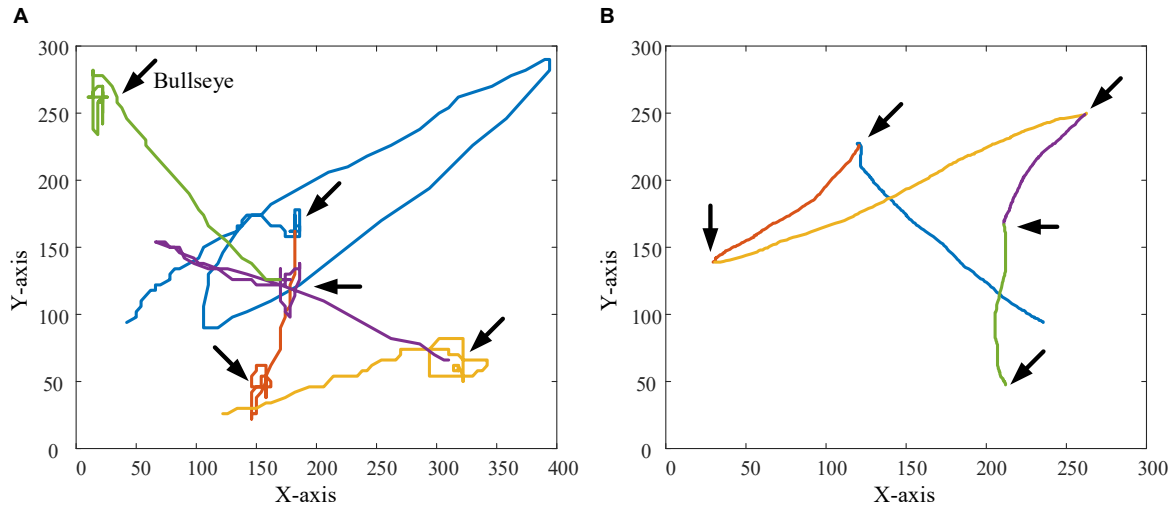

FIGURE 17
The figure shows the trajectories of the sight in the target positioning task. The position indicated by the arrow in the figure is the bullseye position. **(A)** The trajectories of the sight in the control session. **(B)** The trajectories of the sights in the testing session.

advanced psychological activities, is an open and complex giant system. In this case, the control actions are essentially infinitely flexible (Sheridan, 2011). Another reason is that such methods have high data acquisition costs and labor-intensive problems. In this paper, the following efforts are made to solve the problem of rapid learning of the "human-in-the-loop" reinforcement learning model: In terms of algorithms, (1) by setting pre-training, the existing data sets were used to accelerate the learning process of online tasks. (2) By reducing the dimensional space of state and action, the network structure of SAMNN was simplified and the difficulty of network training was reduced. In terms of experimental paradigm, (1) the diversity of samples was increased by setting stimulation conditions in the experiment. (2) A reasonable number of experimental rounds was designed after many attempts. The study found that too many experiment times will reduce the experimental experience of the subjects, but too few experiment times often cannot achieve convergence. It has to be admitted that there are some subjects who can achieve convergence after several attempts. To sum up, after various efforts, the PSA model achieved rapid learning with the participation of real people. However, this work still needs to be further improved, and the next step will be to explore the

TABLE 2 Operational quality of all subjects.

	Trajectory tracking task		Target positioning task	
	Operational quality under conventional method	Operational quality under PSA method	Operational quality under conventional method	Operational quality under PSA method
Subject1	0.18	**0.26**	1.14	**1.41**
Subject2	0.23	**0.31**	1.19	**1.23**
Subject3	0.18	**0.29**	0.72	**1.05**
Subject4	0.31	**0.32**	0.98	**1.20**
Subject5	0.25	**0.36**	1.14	**1.26**
Subject6	**0.25**	0.24	1.13	**1.21**
Average	0.23 ± 0.05	0.30 ± 0.04	1.03 ± 0.18	$\mathbf{1.23 \pm 0.10}$

Bold text indicates better values.

following aspects: (1) Introduce a meta-learning strategy, meta-learning is to use past knowledge and experience to guide the learning of new tasks, so that the network has the ability to learn to learn, and it is one of the commonly used methods to solve the few-shot learning problem. Theoretically, the meta-reinforcement learning algorithm can enable the agent to learn new skills from a small amount of experience. Although there are some drawbacks, it is a way to try (Rakelly et al., 2019). (2) Introduce the bootstrapped policy gradient rapid reinforcement learning strategy. The bootstrapped policy gradient method can introduce prior knowledge into the policy gradient to improve sample efficiency. Its core idea is to update the sum probability of a series of related actions in the gradient estimation sample, rather than the sum probability of a single action (Zhang and Goh, 2021; Zhang et al., 2021).

Implications of the results

In this paper, only the speed parameter of the robot was selected as the adjustment variable for research, and exciting results were obtained. The research shows that on the basis of the PSA method, other parameters can be selected as adjustment variables according to the characteristics of the specific teleoperating system and the robot. Furthermore, the PSA method can realize not only the adjustment of a single parameter, but also the coupled adjustment of multiple parameters. It should be noted that when a single parameter is adjusted, the complexity of the teleoperated robot system is relatively easy to determine, but when multiple parameters are adjusted in coupling, the complexity of the system will increase dramatically due to the coupling relationship between the parameters.

The PSA method has been verified in the two tasks of trajectory tracking and target positioning. These two tasks are abstracted according to the common characteristics of the tasks of the teleoperated robot system, and do not depend on any specific teleoperated robot system. Therefore, the PSA method can be well extended to a variety of teleoperated robotic systems. For example, in the field of manipulating special operation robots, such as remote-operated fire-fighting robots, maintenance robots, surgical robots, and space station maintenance robots (Bucolo et al., 2022). The set adjustment parameters can be the response time of the robot system, the speed and acceleration of the moving parts of the robot, and the coupling parameters between them, etc. At the same time, it also has application prospects in other fields, such as information matching and recommendation fields, such as education and training, web page information recommendation (Lan and Baraniuk, 2016; Mizgajski and Morzy, 2019). The set adjustment parameter can be the difficulty level of the task (or event).

Limitations and future work

The core of the PSA method based on the reinforcement learning framework is to learn the mapping from the mental state (state) to the robot speed regulation instruction (action), which is an end-to-end learning method. Its advantage is that it has the learning ability of non-linear mapping, and it does not need to abstract the rules of the teleoperated robot process, nor to establish a mathematical model between EEG indicators and behavioral performance, thus avoiding the cumulative bias introduced by oversimplifying the study subjects. However, it has to be admitted that its learning process is "black box" and has poor interpretability (special research in this area can be carried out in the next step). Even so, this still cannot hide the unique advantages of the PSA method.

The mental states in this study can be defined in many ways, with different meanings in different disciplines. This paper draws on the definition method of dimension theory in psychology, because it evaluates mental state on a continuous dimension through indicators such as design valence and arousal. The evaluation criteria can fully take into account the characteristics of the diversity of mental states. In the

future, the mental state detector in the PSA method can be specially designed and improved for specific fields. A specific, single mental state can be selected for more targeted research. For example, to study the influence of mental fatigue on the teleoperation robot system, it is only necessary to replace the feature extraction method in the mental state detector. The PSA method can realize the function of special customization and rapid transplantation, so as to adapt to the teleoperated robot system with special requirements.

In related fields such as teleoperated robots and car driving, the driving styles of operators (or drivers) are mostly divided into conservative and aggressive types according to driving habits and the speed of the robot (or car) being driven (Sadrpour et al., 2014; Gilman et al., 2015; Wang et al., 2020). Referring to research findings in related fields, we divided the subjects into aggressive and conservative types according to the speed of the robot controlled. However, it has to be admitted that there are still some limitations. Firstly, the existing research on driving style has not formed a unified conceptual framework, and there is no general scheme for the classification of driving style (Sagberg et al., 2015). Secondly, in the field of teleoperation, the theoretical basis for the classification of driving styles and objective group differentiation methods need further exploration.

In this paper, there was no special method for removing electromyogenic artifacts in signal processing, but filtering (retaining the maximum frequency of EEG to 45 Hz) was used to reduce the influence of electromyogenic artifacts as much as possible (Hipp and Siegel, 2013). At the same time, it can ensure the efficient running of the algorithm to meet the requirements of online training for the speed of the algorithm. However, it has to be admitted that when the frequency band of EEG is less than 45 Hz, it is still unable to remove all electromyogenic artifacts. After balancing the advantages and disadvantages of various aspects, we designed this processing method suitable for the working conditions of this paper. In the future, we need to deepen research from two perspectives: (1) Develop a more efficient electromyogenic artifact removal method that is suitable for our online training. (2) Further quantitatively evaluate the advantages and disadvantages between the developed electromyogenic artifact removal method and the low-frequency EEG preservation method, such as the degree of electromyogenic artifact elimination, the degree of effective signal mis injury, and the algorithm running rate.

This paper selects 6 subjects to participate in the online experiment, the main reasons are as follows: Different from other methods that need to verify cross-individual characteristics, they use a large number of subjects to verify their cross-individual accuracy, robustness and stability, however, the focus of the PSA method is on the study of individualized adjustment for the mental state of different operators, not only does not involve cross-individual verification, but instead focuses on the differences between individuals. In the experimental validation involving 6 subjects, it has been observed that the PSA method has carried out personalized regulation for aggressive style and conservative style subjects. And at the same time, it also avoids the drawback that the overall sample is too large to blur the characteristics of the data. In addition, the effect of the PSA method in a single subject is robust and has significant differences. Therefore, this paper used 6 subjects for experimental verification (Fischer and Whitney, 2014).

Conclusion

Aiming at the problem that the poor mental state of the teleoperator causes the quality of the operation to decline, or even dangerous, the PSA model based on policy gradient reinforcement learning was established in this paper. This model had a dual-loop human-computer information interaction mechanism, which could give full play to the advantages of humans and computers. At the same time, the PSA algorithm was developed, which could extract the *DE* feature of EEG and the *PR* feature of EOG, and performed feature-level fusion to obtain a data matrix that effectively characterizes the mental state. In addition, by fusing the perceptron based on artificial neural network and the decision maker based on reinforcement learning, the function of individually adjusting the speed of the robot according to the mental state of different users was realized. Experiments were carried out on 6 real subjects instead of simulation models. The results showed that the method could accurately perceive the mental state of the operator when performing the task, and the speed of the robot was individually adjusted according to the mental state of different operators, which effectively improved the operational quality and realized the efficient and safe execution of teleoperation tasks. Aiming at the problem of performance degradation of teleoperated robotic systems caused by human factors, this research result may inspire a new control framework. Compared with the conventional methods based on user behavior model mining, a series of methods based on this framework have better personalization and dynamic adaptability.

Data availability statement

The raw data supporting the conclusions of this article will be made available by the authors, without undue reservation.

Ethics statement

The studies involving human participants were reviewed and approved by the Institutional Review Board of Xi'an Jiaotong University. The patients/participants provided their

written informed consent to participate in this study. Written informed consent was obtained from the individual(s) for the publication of any potentially identifiable images or data included in this article.

Author contributions

TZ proposed and did the research and wrote the manuscript. XZ proposed the research idea, supervised the work, and revised the manuscript. ZL organized and carried out the experiments. YiZ assisted in processing experimental data. ZJ assisted in collecting experimental data. YnZ revised the manuscript. All authors contributed to the article and approved the submitted version.

Funding

This work was supported in part by the National Key Research and Development Program of China (No. 2017YFB1300303), and partially supported by grants from the Science and Technology Supporting Xinjiang Project (No. 2020E0259).

Conflict of interest

The authors declare that the research was conducted in the absence of any commercial or financial relationships that could be construed as a potential conflict of interest.

Publisher's note

All claims expressed in this article are solely those of the authors and do not necessarily represent those of their affiliated organizations, or those of the publisher, the editors and the reviewers. Any product that may be evaluated in this article, or claim that may be made by its manufacturer, is not guaranteed or endorsed by the publisher.

References

Abbass, H. A., Tang, J., Amin, R., Ellejmi, M., and Kirby, S. (2014). Augmented cognition using real-time EEG-based adaptive strategies for air traffic control. *Proc. Hum. Factors Ergonom. Soc. Annual Meet.* 58, 230–234. doi: 10.1177/1541931214581048

Ahammed, K., and Ahmed, M. U. (2020). Quantification of mental stress using complexity analysis of EEG signals. *Biomed. Eng. Appl. Basis Commun.* 32:2050011.

Alamdari, N., Lobarinas, L., and Kehtarnavaz, N. (2020). Personalization of hearing aid compression by human-in-the-loop deep reinforcement learning. *IEEE Access* 8, 203503–203515. doi: 10.1109/ACCESS.2020.3035728

Andrieu, C., de Freitas, N., Doucet, A., and Jordan, M. I. (2003). An introduction to MCMC for machine learning. *Mach. Learn.* 50, 5–43. doi: 10.1023/A:1020281327116

Arico, P., Borghini, G., Di Flumeri, G., Colosimo, A., Bonelli, S., Golfetti, A., et al. (2016). Adaptive automation triggered by EEG-Based mental workload index: a passive brain-computer interface application in realistic air traffic control environment. *Front. Hum. Neurosci.* 10:539. doi: 10.3389/fnhum.2016.00539

Arulkumaran, K., Deisenroth, M. P., Brundage, M., and Bharath, A. A. (2017). Deep reinforcement learning: a brief survey. *IEEE* 34, 26–38. doi: 10.1109/MSP.2017.2743240

Bucolo, M., Bucolo, G., Buscarino, A., Fiumara, A., Fortuna, L., and Gagliano, S. (2022). Remote ultrasound scan procedures with medical robots: towards new perspectives between medicine and engineering. *Appl. Bionics. Biomech.* 2022:1072642. doi: 10.1155/2022/1072642

Catelani, M., Ciani, L., Guidi, G., and Patrizi, G. (2021). An enhanced SHERPA (E-SHERPA) method for human reliability analysis in railway engineering. *Reliabil. Eng. System Safety* 215:107866.

Chanel, C., Roy, R. N., Dehais, F., and Drougard, N. (2020). Towards mixed-initiative human-robot interaction: assessment of discriminative physiological and behavioral features for performance prediction. *Sensors* 20:296. doi: 10.3390/s20010296

Choi, Y., Kim, M., and Chun, C. (2015). Measurement of occupants' stress based on electroencephalograms (EEG) in twelve combined environments. *Building Environ.* 88, 65–72. doi: 10.1016/j.buildenv.2014.10.003

Chuang, C., Cao, Z., King, J., Wu, B., Wang, Y., and Lin, C. (2018). Brain electrodynamic and hemodynamic signatures against fatigue during driving. *Front. Neurosci.* 12:181. doi: 10.3389/fnins.2018.00181

Cuesta-Frau, D., Miro-Martinez, P., Jordan, N. J., Oltra-Crespo, S., and Molina, P. A. (2017). Noisy EEG signals classification based on entropy metrics. performance assessment using first and second generation statistics. *Comput. Biol. Med.* 87, 141–151. doi: 10.1016/j.compbiomed.2017.05.028

Daly, T., Murphy, J., Anglin, K., Szalma, J., Acree, M., Landsberg, C., et al. (2017). "Moving vigilance out of the laboratory: dynamic scenarios for UAS operator vigilance training," in *Augmented Cognition. Enhancing Cognition and Behavior in Complex Human Environments. AC 2017. Lecture Notes in Computer Science*, eds D. Schmorrow and C. Fidopiastis (Cham: Springer International Publishing).

Deli, E., and Kisvarday, Z. (2020). The thermodynamic brain and the evolution of intellect: the role of mental energy. *Cogn. Neurodynamics* 14, 743–756. doi: 10.1007/s11571-020-09637-y

Di Flumeri, G., Borghini, G., Aricò, P., Colosimo, A., Pozzi, S., Bonelli, S., et al. (2015). "On the use of cognitive neurometric indexes in aeronautic and air traffic management environments," in *Symbiotic Interaction. Symbiotic 2015. Lecture Notes in Computer Science*, eds B. Blankertz, G. Jacucci, L. Gamberini, A. Spagnolli, and J. Freeman (Cham: Springer International Publishing).

Di Flumeri, G., De Crescenzio, F., Berberian, B., Ohneiser, O., Kramer, J., Aricò, P., et al. (2019). Brain-Computer interface-based adaptive automation to prevent out-of-the-loop phenomenon in air traffic controllers dealing with highly automated systems. *Front. Hum. Neurosci.* 13:296. doi: 10.3389/fnhum.2019.00296

Dimitrakopoulos, G. N., Kakkos, I., Dai, Z., Wang, H., Sgarbas, K., Thakor, N., et al. (2018). Functional connectivity analysis of mental fatigue reveals different network topological alterations between driving and vigilance tasks. *IEEE Trans. Neural. Syst. Rehabil. Eng.* 26, 740–749. doi: 10.1109/TNSRE.2018.2791936

Fischer, J., and Whitney, D. (2014). Serial dependence in visual perception. *Nat. Neurosci.* 17, 738–743.

Freeman, F. G., Mikulka, P. J., Prinzel, L. J., and Scerbo, M. W. (1999). Evaluation of an adaptive automation system using three EEG indices with a visual tracking task. *Biol. Psychol.* 50, 61–76. doi: 10.1016/s0301-0511(99)00002-2

Gao, C., Lv, B., and Ma, J. (2012). A new method of extracting vigilant feature from electrooculography using wavelet packet transform. *Chinese J. Biomed. Eng.* 31, 641–648.

García-Martínez, B., Martínez-Rodrigo, A., Zangróniz Cantabrana, R., Pastor García, J., and Alcaraz, R. (2016). Application of entropy-based metrics to identify emotional distress from electroencephalographic recordings. *Entropy* 18, 221–221. doi: 10.3390/e18060221

Gilman, E., Keskinarkaus, A., Tamminen, S., Pirttikangas, S., Röning, J., and Riekki, J. (2015). Personalised assistance for fuel-efficient driving. *Transportation Res. Part C Emerg. Technol.* 58, 681–705. doi: 10.1016/j.trc.2015.02.007

Hipp, J. F., Engel, A. K., and Siegel, M. (2011). Oscillatory synchronization in large-scale cortical networks predicts perception. *Neuron* 69, 387–396. doi: 10.1016/j.neuron.2010.12.027

Hipp, J. F., and Siegel, M. (2013). Dissociating neuronal gamma-band activity from cranial and ocular muscle activity in EEG. *Front. Hum. Neurosci.* 7:338. doi: 10.3389/fnhum.2013.00338

Hosseini, S. A., and Naghibi-Sistani, M. B. (2011). Classification of emotional stress using brain activity. *Appl. Biomed. Eng.* 7, 32–41.

Jia, Y., Xi, N., Liu, S., Wang, Y., Li, X., and Bi, S. (2014). Quality of teleoperator adaptive control for telerobotic operations. *Int. J. Robotics Res.* 33, 1765–1781. doi: 10.1177/0278364914556124

Jia, Y., Xi, N., Wang, Y., and Li, X. (2012). "Online identification of quality of teleoperator (QoT) for performance improvement of telerobotic operations," in *Proceedings of the 2012 IEEE International Conference on Robotics and Automation*, (Saint Paul, MN).

Jin, J., Xuejun, J., Zhen, Z., Yong, C., and Hanjun, Y. (2017). Study on functional state of operators during simulated space tasks. *Manned Spaceflight* 23, 123–129.

Kaber, D. B., Wright, M. C., Prinzel, L. J., and Clamann, M. P. (2016). Adaptive automation of human-machine system information-processing functions. *Hum. Factors* 47, 730–741. doi: 10.1518/001872005775570989

Katmah, R., Al-Shargie, F., Tariq, U., Babiloni, F., Al-Mughairbi, F., and Al-Nashash, H. (2021). A review on mental stress assessment methods using EEG signals. *Sensors* 21:5043. doi: 10.3390/s21155043

Kingma, D. P., and Ba, J. (2014). "Adam: a method for stochastic optimization," in *Proceedings of the 2015 International Conference on Learning Representations*, (San Diego, CA).

Koelstra, S., Muhl, C., Soleymani, M., Lee, J., Yazdani, A., Ebrahimi, T., et al. (2012). DEAP: a database for emotion analysis;using physiological signals. *IEEE Trans. Affect. Comp.* 3, 18–31. doi: 10.1109/t-affc.2011.15

Lan, A. S., and Baraniuk, R. G. (2016). "A contextual bandits framework for personalized learning action selection," in *Paper Presented at 9th International Conference on Educational Data Mining, EDM*, (Raleigh, NC).

Laurent, F., Valderrama, M., Besserve, M., Guillard, M., Lachaux, J., Martinerie, J., et al. (2013). Multimodal information improves the rapid detection of mental fatigue. *Biomed. Signal Process. Control* 8, 400–408. doi: 10.1016/j.bspc.2013.01.007

LeCun, Y. A., Bottou, L., Orr, G. B., and Müller, K. (2012). *Efficient BackProp*. Berlin: Springer.

Li, M., Liang, Z., He, B., Zhao, C., Yao, W., Xu, G., et al. (2019). Attention-Controlled assistive wrist rehabilitation using a low-cost EEG sensor. *IEEE Sensors J.* 19, 6497–6507. doi: 10.1109/JSEN.2019.2910318

Li, R., Zhang, X., Lu, Z., Liu, C., Li, H., Sheng, W., et al. (2018). An approach for brain-controlled prostheses based on a facial expression paradigm. *Front. Neurosci.* 12:943. doi: 10.3389/fnins.2018.00943

Liang, X., Wang, X., Lei, Z., Liao, S., and Li, S. Z. (2017). "Soft-Margin softmax for deep classification," in *Proceedings of the ICONIP*, (Cham: Springer International Publishing).

Liu, F., Fuh, J. L., Peng, C. K., and Yang, A. C. (2021). Phenotyping neuropsychiatric symptoms profiles of alzheimer's disease using cluster analysis on EEG power. *Front. Aging Neurosci.* 13:623930. doi: 10.3389/fnagi.2021.623930

Liu, J., Zhang, C., and Zheng, C. (2010). EEG-based estimation of mental fatigue by using KPCA-HMM and complexity parameters. *Biomed. Signal Proc. Control* 5, 124–130. doi: 10.1016/j.bspc.2010.01.001

Liu, S., Wang, X., Zhao, L., Zhao, J., Xin, Q., and Wang, S. (2021). Subject-Independent emotion recognition of EEG signals based on dynamic empirical convolutional neural network. *IEEE/ACM Trans. Comp. Biol. Bioinform.* 18, 1710–1721. doi: 10.1109/TCBB.2020.3018137

Liu, Y., Lan, Z., Cui, J., Sourina, O., and Müller-Wittig, W. (2020). Inter-subject transfer learning for EEG-based mental fatigue recognition. *Adv. Eng. Inform.* 46:101157. doi: 10.1016/j.aei.2020.101157

Lucassen, P. J., Pruessner, J., Sousa, N., Almeida, O. F., Van Dam, A. M., Rajkowska, G., et al. (2014). Neuropathology of stress. *Acta Neuropathol.* 127, 109–135.

Ma, J., Shi, L., and Lu, B. (2014). An EOG-based vigilance estimation method applied for driver fatigue detection. *Neurosci. Biomed. Eng.* 2, 41–51.

Ma, Y., Chen, B., Li, R., Wang, C., Wang, J., She, Q., et al. (2019). Driving fatigue detection from EEG using a modified PCANet method. *Comput. Intell. Neurosci.* 2019:4721863. doi: 10.1155/2019/4721863

Magosso, E., Ursino, M., Provini, F., and Montagna, P. (2007). Wavelet analysis of electroencephalographic and electro-oculographic changes during the sleep onset period. *Annu. Int. Conf. IEEE Eng. Med. Biol. Soc.* 2007:4006–4010. doi: 10.1109/IEMBS.2007.4353212

Matei, R., and Matei, D. (2021). *Frequency Analysis of EEG Signals Using Band Energy Distribution*. Iasi: IEEE, doi: 10.1109/EHB52898.2021.9657648

McIntire, L., McKinley, R. A., McIntire, J., Goodyear, C., Nelson, J., and Estrada, A. X. (2013). Eye metrics: an alternative vigilance detector for military operators. *Military Psychol.* 25, 502–513. doi: 10.1037/mil0000011

Mizgajski, J., and Morzy, M. (2019). Affective recommender systems in online news industry: how emotions influence reading choices. *User Model. User-Adapted Interact.* 29, 345–379.

Mnih, V., Kavukcuoglu, K., Silver, D., Rusu, A. A., Veness, J., Bellemare, M. G., et al. (2015). Human-level control through deep reinforcement learning. *Nature* 518, 529–533. doi: 10.1038/nature14236

Nair, V., and Hinton, G. E. (2010). "Rectified linear units improve restricted boltzmann machines," in *Proceedings of the 27th International Conference on Machine Learning*, (Haifa).

Nielsen, J. B. B., Nielsen, J., and Larsen, J. (2015). Perception-Based personalization of hearing aids using gaussian processes and active learning. *IEEE/ACM Trans. Audio Speech Lang. Proc.* 23, 162–173. doi: 10.1109/TASLP.2014.2377581

Nuño, E., Basañez, L., and Ortega, R. (2011). Passivity-based control for bilateral teleoperation: a tutorial. *Automatica* 47, 485–495.

Parasuraman, R. (1993). "Effects of adaptive function allocation on human performance," in *Human Factors and Advanced Aviation Technologies*, eds D. J. Garland and J. A. Wise (Daytona Beach, FL: Embry-Riddle Aeronautical University Press), 147–157.

Parasuraman, R., and Wilson, G. F. (2008). Putting the brain to work: neuroergonomics past. *Present Future Hum. Factors* 50, 468–474. doi: 10.1518/001872008X288349

Peng, H., Long, F., and Ding, C. (2005). Feature selection based on mutual information: criteria of max-dependency, max-relevance, and min-redundancy. *IEEE Trans. Pattern Anal. Mach. Intell.* 27, 1226–1238. doi: 10.1109/TPAMI.2005.159

Rakelly, K., Zhou, A., Quillen, D., Finn, C., and Levine, S. (2019). "Efficient off-policy meta-reinforcement learning via probabilistic context variables," in *Proceedings of the 36th International Conference on Machine Learning*, (Berkeley CA).

Russell, J. A. (2003). Core affect and the psychological construction of emotion. *Psychol. Rev.* 110, 145–172. doi: 10.1037/0033-295x.110.1.145

Sadrpour, A., Jin, J., and Ulsoy, A. G. (2014). "The role of operator style on mission energy requirements for tele-operated unmanned ground vehicles," in *Proceedings of the American Control Conference*, (Portland, OR: IEEE).

Sagberg, F., Selpi, G. F., Piccinini, B., and Engström, J. (2015). A review of research on driving styles and road safety. *Hum. Factors* 57, 1248–1275. doi: 10.1177/0018720815591313

Scerbo, M. W., Freeman, F. G., and Mikulka, P. J. (2003). A brain-based system for adaptive automation. *Theoretical Issues Ergon. Sci.* 4, 200–219. doi: 10.1080/1463922021000020891

Sheridan, T. B. (2011). Adaptive automation, level of automation, allocation authority, supervisory control, and adaptive control: distinctions and modes of adaptation. *IEEE Trans. Systems Man Cybernetics Systems Hum.* 41, 662–667. doi: 10.1109/TSMCA.2010.2093888

Shi, L., Jiao, Y., and Lu, B. (2013). Differential entropy feature for EEG-based vigilance estimation. *Conf. Proc.* 2013:6627.

Sogaard, J. N., Hau, O., Bagger, N. J., Bundgaard, N. T., and Vase, L. S. (2019). Perceptual effects of adjusting hearing-aid gain by means of a machine-learning approach based on individual user preference. *Trends Hear.* 23:2331216519847413. doi: 10.1177/2331216519847413

Speagle, J. S. (2020). DYNESTY: a dynamic nested sampling package for estimating Bayesian posteriors and evidences. *Monthly Notices R. Astronom. Soc.* 493, 3132–3158. doi: 10.1093/mnras/staa278

Stanney, K. M., Schmorrow, D. D., Johnston, M., Fuchs, S., Jones, D., Hale, K. S., et al. (2009). Augmented cognition: an overview. *Rev. Hum. Factors Ergonom.* 5, 195–224. doi: 10.1518/155723409X448062

Tang, X., Chen, Y., Li, X., Liu, J., and Ying, Z. (2019). A reinforcement learning approach to personalized learning recommendation systems. *Br. J. Math. Stat. Psychol.* 72, 108–135. doi: 10.1111/bmsp.12144

van Zoelen, E. M., Van Den Bosch, K., and Neerincx, M. A. (2021). Becoming team members: identifying interaction patterns of mutual adaptation for human-robot co-learning. *Front. Robot. AI* 8:692811. doi: 10.3389/frobt.2021.692811

Wang, P., Chen, M., Fan, Z., Gao, J., and Zhang, L. (2011). Analysis of multiparameter electroencephalogram based on wavelet packet for mental fatigue. *Ji Suan Ji Gong Cheng Yu Ying Yong* 47, 144–147. doi: 10.3778/j.issn.1002-8331.2011.30.039

Wang, X., Qin, Y., Wang, Y., Xiang, S., and Chen, H. (2019). ReLTanh: an activation function with vanishing gradient resistance for SAE-based DNNs and its application to rotating machinery fault diagnosis. *Neurocomputing* 363, 88–98. doi: 10.1016/j.neucom.2019.07.017

Wang, X., Wu, C., Xue, J., and Chen, Z. (2020). A method of personalized driving decision for smart car based on deep reinforcement learning. *Information* 11:295. doi: 10.3390/info11060295

Warm, J. S., Parasuraman, R., and Matthews, G. (2008). Vigilance requires hard mental work and is stressful. *Hum. Factors* 50, 433–441. doi: 10.1518/001872008X312152

Wen, Y., Si, J., Brandt, A., Gao, X., and Huang, H. H. (2020). Online reinforcement learning control for the personalization of a robotic knee prosthesis. *IEEE Trans. Cybern.* 50, 2346–2356. doi: 10.1109/TCYB.2019.2890974

Wilson, G. F. (2005). Operator functional state assessment for adaptive automation implementation. *Proc. SPIE-Int. Soc. Optical Eng.* 5797, 100–104. doi: 10.1117/12.601806

Wu, E. Q., Deng, P., Qiu, X., Tang, Z., Zhang, W., Zhu, L., et al. (2021). Detecting fatigue status of pilots based on deep learning network using EEG signals. *IEEE Trans. Cogn. Dev. Systems* 13, 575–585. doi: 10.1109/TCDS.2019.2963476

Wu, R., Yao, Z., Si, J., and Huang, H. (2022). Robotic knee tracking control to mimic the intact human knee profile based on actor-critic reinforcement learning. *IEEE/CAA J. Automatica Sinica* 9, 19–30. doi: 10.1109/JAS.2021.1004272

Wu, W., Wu, Q. M. J., Sun, W., Yang, Y., Yuan, X., Zheng, W., et al. (2021). A regression method with subnetwork neurons for vigilance estimation using EOG and EEG. *IEEE Trans. Cogn. Dev. Systems* 13, 209–222. doi: 10.1109/TCDS.2018.2889223

Xu, X., Gu, H., Yan, S., Pang, G., and Gui, G. (2019). Fatigue EEG feature extraction based on tasks with different physiological states for ubiquitous edge computing. *IEEE Access* 7, 73057–73064. doi: 10.1109/ACCESS.2019.2920014

Yang, S., and Zhang, J. (2013). An adaptive human-machine control system based on multiple fuzzy predictive models of operator functional state. *Biomed. Signal Proc. Control.* 8, 302–310. doi: 10.1016/j.bspc.2012.11.003

Zhai, D., and Xia, Y. (2016). Adaptive control for teleoperation system with varying time delays and input saturation constraints. *IEEE Trans. Industrial Electron.* 63, 6921–6929. doi: 10.1109/TIE.2016.2583199

Zhang, T., Zhang, X., Zhang, Y., Lu, Z., and Li, H. (2019). *Effects of User Fatigue Mental State on the Facial-expression Paradigm of BCI*. Beijing: IEEE.

Zhang, T., Zhang, X., Zhang, Y., Lu, Z., Zhu, W., and Jiang, Y. (2021). A precise control method for brain-computer cooperation with deep reinforcement learning. *J. Xi'an Jiaotong University* 2021, 1–9.

Zhang, X., Xu, Z., Ravi, A., Pearce, S., and Jiang, N. (2019). "A hybrid BCI approach to detect brain switch in action observation by utilizing convolution neural network," in *2019 IEEE International Conference on Systems, Man and Cybernetics (SMC)*, (Piscataway, NJ: IEEE).

Zhang, Y., and Goh, W. (2021). Personalized task difficulty adaptation based on reinforcement learning. *User Model. User-adapted Interact.* 31, 753–784. doi: 10.1007/s11257-021-09292-w

Zheng, W., and Lu, B. (2015). Investigating critical frequency bands and channels for EEG-Based emotion recognition with deep neural networks. *IEEE Trans. Autonomous Mental Dev.* 7, 162–175. doi: 10.1109/TAMD.2015.2431497

Zheng, W., Zhu, J., and Lu, B. (2019). Identifying stable patterns over time for emotion recognition from EEG. *IEEE Trans. Affect. Comp.* 10, 417–429. doi: 10.1109/TAFFC.2017.2712143

frontiers | Frontiers in Neuroscience

TYPE Original Research
PUBLISHED 13 September 2022
DOI 10.3389/fnins.2022.988535

OPEN ACCESS

EDITED BY
Min Li,
Xi'an Jiaotong University, China

REVIEWED BY
Jiahui Pan,
South China Normal University, China
Yin Liang,
Beijing University of Technology, China
Jiahui Yu,
Zhejiang University, China

*CORRESPONDENCE
Rui Li
liruizixing@163.com
Weiping Liu
liuwp@fmmu.edu.cn

SPECIALTY SECTION
This article was submitted to Neuroprosthetics, a section of the journal Frontiers in Neuroscience

RECEIVED 07 July 2022
ACCEPTED 17 August 2022
PUBLISHED 13 September 2022

CITATION
Li R, Liu D, Li Z, Liu J, Zhou J, Liu W, Liu B, Fu W and Alhassan AB (2022) A novel EEG decoding method for a facial-expression-based BCI system using the combined convolutional neural network and genetic algorithm. *Front. Neurosci.* 16:988535. doi: 10.3389/fnins.2022.988535

A novel EEG decoding method for a facial-expression-based BCI system using the combined convolutional neural network and genetic algorithm

Rui Li[1,2]*, Di Liu[1], Zhijun Li[1], Jinli Liu[1], Jincao Zhou[1], Weiping Liu[2]*, Bo Liu[1], Weiping Fu[1] and Ahmad Bala Alhassan[3]

[1]School of Mechanical and Instrumental Engineering, Xi'an University of Technology, Xi'an, China, [2]Xi'an People's Hospital, Xi'an, China, [3]Department of Electrical and Information Technology, King Mongkut's University of Technology, Bangkok, Thailand

Multiple types of brain-control systems have been applied in the field of rehabilitation. As an alternative scheme for balancing user fatigue and the classification accuracy of brain–computer interface (BCI) systems, facial-expression-based brain control technologies have been proposed in the form of novel BCI systems. Unfortunately, existing machine learning algorithms fail to identify the most relevant features of electroencephalogram signals, which further limits the performance of the classifiers. To address this problem, an improved classification method is proposed for facial-expression-based BCI (FE-BCI) systems, using a convolutional neural network (CNN) combined with a genetic algorithm (GA). The CNN was applied to extract features and classify them. The GA was used for hyperparameter selection to extract the most relevant parameters for classification. To validate the superiority of the proposed algorithm used in this study, various experimental performance results were systematically evaluated, and a trained CNN-GA model was constructed to control an intelligent car in real time. The average accuracy across all subjects was 89.21 ± 3.79%, and the highest accuracy was 97.71 ± 2.07%. The superior performance of the proposed algorithm was demonstrated through offline and online experiments. The experimental results demonstrate that our improved FE-BCI system outperforms the traditional methods.

KEYWORDS

brain computer interface, convolutional neural network (CNN), genetic algorithm, EEG, facial expression

Introduction

Brain–computer interface (BCI) systems serve as a communication link between humans and peripheral equipment. This technology has been shown to improve the lives of numerous patients suffering from various neurological disorders, including amyotrophic lateral sclerosis and spinal cord injuries (Abiri et al., 2019; Edelman et al., 2019). Over the past few decades, the development of signal acquisition and decoding

technology has led to the development of various rehabilitation applications, including neuro-prosthesis (Li et al., 2018a), wheelchairs (Pinheiro et al., 2018), quadcopters (Yan et al., 2020), and robotic arms (Cao et al., 2021).

Several types of brain-controlled systems have been studied; these can be classified into spontaneous and evoked BCI systems (Zhang et al., 2020a). Motor imagery (MI)-based BCI is an important spontaneous BCI system that has been extensively investigated. Reust and his colleagues employed an MI-BCI system corresponding to human hand movement to control two robotic hands; this approach achieved a 95% classification accuracy overall (Reust et al., 2018). Another novel mental imagery system developed by the University of Montreal employed a multimodal BCI system to control the single-step and forward walking status using an immersive virtual reality avatar (Alchalabi et al., 2021).

Numerous BCI studies have focused on evoked BCI systems, such as steady-state visually evoked potentials (SSVEP)- and P300-based BCI systems (Zhang et al., 2021). Zhao et al. demonstrated the feasibility of a new stimulation paradigm that makes full use of peripheral vision, and they used the Manhattan distance for final detection in their research (Zhao et al., 2021). A modified SSVEP-BCI speller with dual-frequency and phase-modulation paradigms was designed at Tsinghua University. It obtained an accuracy of 96% *via* multivariate synchronization index analysis (Yan et al., 2021). P300 BCIs have also been used in a variety of applications for disabled people (Allison et al., 2020; Shukla et al., 2021). A reliable authentication system (based on the P300-BCI system) for protecting against online fraud was designed by Rathi's group. In their study, the optimal performance was observed when using a quadratic discriminant analysis algorithm (Rathi et al., 2021).

To summarize, the merit of spontaneous BCI systems is their stable and rapid responses. However, the long training time and inter-user variability limit further study. Evoked BCI systems achieve high recognition accuracies with low training times; however, this type of BCI system relies entirely upon stimulator design. To solve these obstacles, numerous efforts have been made to develop a novel BCI system in the past few years.

Recently, another type of BCI system based on affective computing was developed. Prof. Lu was the first to report on an emotion-based BCI system; this used a stable electroencephalogram (EEG) decoding algorithm to recognize different emotions (Zheng et al., 2019). Prof. Pan and his colleagues reported a novel facial expression detection method based upon two-decision-level fusion using a sum rule combined production rule (Huang et al., 2017). They subsequently developed a Mindlink-Eumpy software toolbox to classify facial expression information by integrating the EEG signals; this was feasible and efficient (Li et al., 2021). Another representative study was reported by the East China University of Science and Technology, which demonstrated that the presentation of different facial images to subjects could successfully evoke event-related potentials (Jin et al., 2012). In 2018, the present authors used real facial expressions instead of flashing facial images to elicit EEG signals. The experimental results demonstrate the validity of the proposed facial-expression-based BCI (FE-BCI) system (Li et al., 2018b).

Considering all the above, the major challenge in improving the performance of existing BCI systems is the EEG classification accuracy. Most BCI studies have used traditional machine learning or pattern recognition methods to identify relevant information for EEG classification (Zhang et al., 2020b). For example, independent component analysis (ICA) and multivariate empirical mode decomposition (MEMD) are typically used for artifact removal. The wavelet transform (WT) is commonly used for feature extraction and linear discriminant analysis. Back propagation neural network (BPNN)-based classifiers are frequently employed to identify different EEG signals. The EEG decoding method based on spatial information is also widely used in BCI systems to ensure recognition performance. Zhao et al. used combined space–time–frequency features to decode EEG signals. In this study, a deep ConvNet model that combined time-frequency transformations, spatial filtering, and classification was used (Zhao et al., 2019). The University of Glasgow developed a novel space-by-time decomposition method based upon non-negative matrix factorization, to decode single-trial EEG signals (Delis et al., 2016). Nanyang Technological University proposed another space-based EEG decoding method. The time-frequency common spatial pattern method was used to solve the problem of poor classification and robustness in MI-BCI systems (Mishuhina and Jiang, 2021). Jia et al. published one of the most recent studies based on the spatial EEG decoding method, and they employed time-contained spatial filtering to extract spatial and temporal information for EEG multi-classification tasks (Jia et al., 2021).

Unfortunately, these methods are limited by their reliance upon prior experimental knowledge and their low processing capacities for large EEG datasets. These drawbacks also reduce the reliability of BCI systems and further degrade their performance. Following innovations in algorithm development, novel neural network architectures for deep learning have offered the benefits of a smaller reliance upon prior expert knowledge, and automatic feature optimization has recently been employed for decoding EEG signals (Craik et al., 2020). Tang et al. employed a traditional convolutional neural network (CNN) to classify EEG signals from left- and right-hand movements (Tang et al., 2017). Xu et al. used topographically represented energy calculations alongside a novel CNN model to extract time–frequency features from four types of MI tasks. This method improves classification accuracy (Xu et al., 2020). Kwak et al. explored an improved CNN model to distinguish the band power features from different SSVEPs using only two channels (Kwak et al., 2017). Xie et al. combined long short-term memory (LSTM) generative adversarial networks and a multi-output

convolutional neural network for MI classification, and their experimental results indicated its favorable performance (Xie et al., 2021). Yu et al. reported a novel adaptive skeleton-based neural network that combined an attentional LSTM network with a 3D convolution, to identify human actions or interactions (Yu et al., 2021b). Moreover, they proposed an LSTM-based network-integrated temporal attention mechanism for spatial human-robot interactions (Yu et al., 2021a). Although these methods can effectively improve the classification accuracy in most MI-BCI systems, the parameters of the CNN model still depend on the researcher's empirical understanding, which leads to poor robustness across different scenarios. Many existing deep learning methods manually set arbitration coefficients or fusion rules according to specific tasks and the researcher's experience.

While GA algorithms have been widely used for CNN parameter optimization in image classification (Sun et al., 2020) or text processing (Liu et al., 2021), the response of EEG signals is entirely different from the 2D image or text information. EEG signals have their unique time-frequency characteristics, and their response from different paradigms is entirely different. So decoding of EEG signals needs a specific architecture of the CNN model and parameter setting guidelines. In particular, although the CNN model-based EEG decoding methods have been studied, only a few works have focused on the FE-BCI system, especially for decoding EEG signals under different expressions.

Despite the number of successful methods available for developing an emotion-based BCI system, it remains challenging to address the dependence of BCI upon the performance of stimulus sources, to thereby ensuring its recognition accuracy. Thus, there remains a need to develop a novel paradigm and expert algorithm that can efficiently identify EEG signals for FE-BCI systems.

The primary objective of this study was to address the dependence of FE-BCI upon the stimulus source and overcome the limitations of long training times and inter-user variability. In this study, an FE-BCI system with four facial expressions (left smirking, right smirking, furrowing brow, and raising brow) was constructed and then used to control an intelligent car. The EEG signals of the proposed FE-BCI system were recorded from the prefrontal and motor cortices. To further optimize the FE-BCI performance, the EEG decoding algorithm constructed using the CNN model combined GA was applied to select the optimal hyperparameter value for the constructed neural network. From our experimental verifications, the main contributions of this work can be summarized as follows:

First, to balance between user fatigue and the classification accuracy of traditional BCI systems, an FE-BCI system identifying four different facial expressions is proposed. It provides an additional option to solve the obstacle between BCI performance and its stimulus reliance. The selected EEG signals from the four different facial expressions are accurately recognized.

Second, to address the issues of the EEG recognition accuracy for different facial expressions, a novel EEG decoding algorithm based upon the CNN model is designed to automatically extract the discriminative features of expression-based EEG signals.

Third, in view of the disadvantages of traditional enumeration methods for hyperparameter value selection, a hyperparameter optimization method based upon the GA algorithm is embedded into the CNN model by setting this model as a fitness function. The CNN model combined with GA is an effective way to optimize the decoding results of EEG signals, further enhancing the overall capabilities of the FE-BCI system.

The remainder of this paper is organized as follows. In Section Materials and methods, the relevant studies and details of the proposed method are presented. The experimental results are analyzed and discussed in Sections Result analysis and Discussion, respectively. The final section concludes this paper.

Materials and methods

Related work

With the rapid development of affective computing, emotion recognition has gradually become an important factor when designing natural and friendly human–machine interactions (Svetla and Dimitar, 2015). The mechanisms of emotion states have attracted considerable interest in different research fields (e.g., the physiology, representation, recognition of emotions according to different physiological signals, and their application to affective BCI systems) (Mühl et al., 2014). However, it remains a challenge to distinguish brain responses to different emotional states, owing to spontaneous brain activity (Olderbak et al., 2014). Recent studies have discovered that numerous activities can express emotional states, such as facial expressions, speech, and gestures (Schuller et al., 2005; D'Mello and Graesser, 2009).

Among these factors, facial expressions serve as an effective external feature for depicting emotional states; this has inspired considerable discussion (Wood et al., 2016). Earl et al. reported that brain activity in the prefrontal cortex is related to emotion processing. Friedman and Thayer also demonstrated that changes in facial expressions could produce corresponding brain activity in the prefrontal cortex (Friedman and Thayer, 1991). Moreover, facial expressions are also body movements; thus, they respond to brain activity in the motor cortex (Ross et al., 2016). To summarize, brain activity arising from the prefrontal and motor cortices and attributable to facial expressions can enhance differences when estimating emotion states. Our previous study (Li et al., 2018b) analyzed the mechanisms of facial expressions and further demonstrated that EEG signals from the prefrontal and motor cortices can be discriminated to represent stable emotions. One of the aims

of affective neuroscience is to include human emotions in BCI systems. Therefore, facial expressions that represent human emotions can be used in BCI systems. Our previous study also constructed a recognition model based on a traditional machine learning algorithm to distinguish EEG signals arising from different facial expressions; however, the performance of the established FE-BCI system can be further improved. Hence, a new calculation model is proposed in this study. More details regarding the experimental setting and algorithm construction can be found in the following section.

Subjects and data acquisition

In this study, 16 healthy subjects from 22 to 30 years old (two females and 14 males) participated in the experiment. None of the patients had a history of neurological diseases or any previous experience with the proposed facial expression experiment. Before the experiment, each participant signed a written informed consent form. The Institutional Review Board of the Xi'an University of Technology approved the proposed experiment, and all experiments were conducted in accordance with the Declaration of Helsinki. More details of sample size estimation can be found in Section Statistical analysis.

A NeuSen-W64 (Figure 1A) with 64 channels was used to record the EEG signal, and all channel distributions adopted the International Standard 10-20 Electrode Location System. Eight electrodes (FC5, FC6, F7, F8, FZ, C3, C4, and CPz) from the prefrontal and motor cortices were selected to record EEG data. AFz and CPz electrodes were the reference and grounding electrodes, respectively. The electrode distribution and the locations of the selected channels are shown in Figure 1B. During EEG data acquisition, the impedances of all electrodes were maintained below 5 KΩ.

Experimental procedure

According to the facial expression mechanisms, the EEG signals from four facial expressions were collected: furrowing brow, left smirking, right smirking, and raising brow. The subjects were required to keep their bodies stable to prevent noise interference in the EEG signals. The experiment was performed in two steps. The purpose of the offline experiment was to evaluate the efficiency of the proposed CNN-GA and verify the distinguishability of EEG signals under different expressions. The online experiment was to investigate the feasibility of an improved FE-BCI system. For the offline experiment, each facial expression experiment consisted of ten sessions, and each session included six trials. In each trial, the subjects were asked to maintain one of the four selected expressions for 4 s. To avoid mental fatigue, each trial began with a 2 s preparation time and a 2 s rest time when each trial finished. Subjects were allowed a 10-min break when they completed one session. The offline experimental time series is shown in Figure 2A, and the structure of the FE-BCI system is shown in Figure 2B.

The online experiment consisted of six sessions. In each session, the subject was asked to perform one of the four selected facial expressions of their own volition, to control an intelligent car return to the starting position after tracking three targets on four laps: Round 1–4. For the sake of sample balance and its practicality, the start position is distributed in Round 1, Target 1 in Round 4, Target 2 in Round 3, and Target 3 in Round 2. In each session, it contained "change lane to the left" three times, "change lane to the right" three times, "accelerate" five times, and "decelerate" four times. The online experimental process was divided into four stages.

STEP 1: Move the intelligent car from the start position to Target 1. This step includes right-hand lane changes to Rounds 2 and 3, acceleration, deceleration, and another right-hand lane changes to Round 4.

STEP 2: Move the intelligent car from Target 1 to Target 2; this involves acceleration, deceleration, and a left-hand lane change to Round 3.

STEP 3: Move the intelligent car from Target 2 to Target 3; this includes acceleration, deceleration, and a left-hand lane change to Round 2.

STEP 4: Move the intelligent car from Target 3 to the start position; this involves acceleration, deceleration, a left-hand lane change to Round 1, and acceleration to the start position.

The time series for the online experiment matched that of the offline experiment. During the online experiment, left smirking (LS) and right smirking (RS) were used to move the intelligent car 30° to the left and right, respectively. Furrowing brow (FB) and raising brow (RB) were used to produce 0.05 m/s acceleration and deceleration, respectively.

In this study, we used offline EEG data as a training database to construct the improved CNN model, and the online data were used to investigate the generalizability of the proposed method.

Data analysis

Artifact removal algorithm

Brain activity from the scalp is fairly weak: its magnitude is usually in the range of 10–50 μV. Hence, artifacts from the surroundings can easily damage the performance of the BCI system. Depending on the mechanism of signal generation, the artifacts can be classified into power-frequency noise and physiological noise (Mowla et al., 2015).

The Butterworth filter can be applied as an effective linear filter to remove power-frequency noise. Hence, a five-order Butterworth filter with a frequency band of 0.5–45 Hz was initially applied. Subsequently, a noise-assisted MEMD method

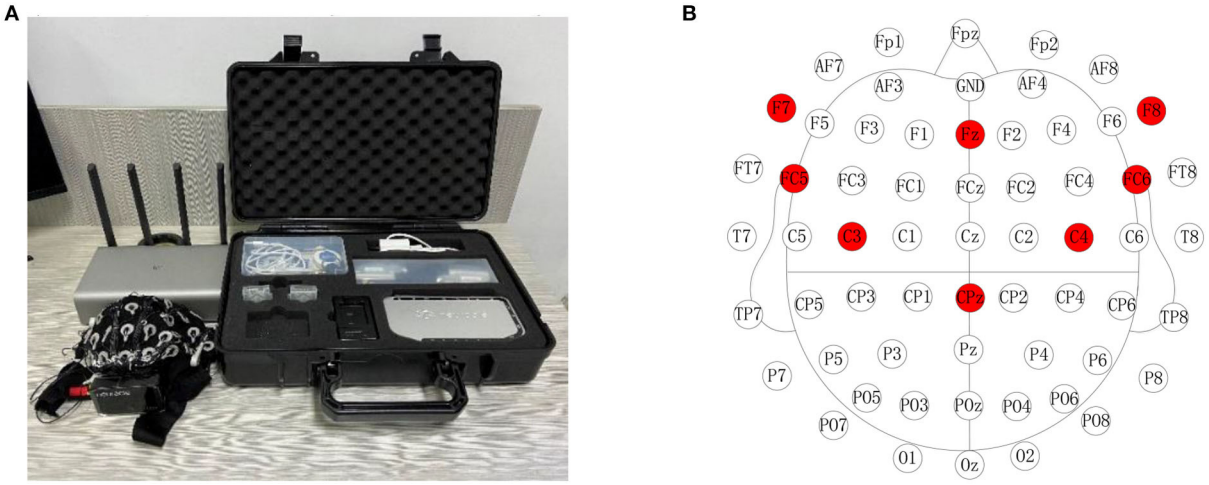

FIGURE 1
NeuSen-W64 EEG recording system and channel locations. **(A)** NeuSen-W64 EEG recording system. **(B)** Selected eight-channel configuration in NeuSen-W64.

with highly localized time-frequency representations and self-adaptation was implemented to remove electromyogram (EMG) and electrooculogram (EOG) artifacts (Chen et al., 2018). In this method, the noise-assisted MEMD was employed to decompose the raw EEG signal; then, the sample entropy value of each intrinsic mode function was estimated to detect and remove physiological artifacts. Further details regarding the artifact removal algorithm have been presented in our previous study (Li et al., 2018b).

Convolutional neural network algorithm

Deep learning was first introduced by Hinton and Salakhutdinov (2006); it consists of a sequence of convolutions and subsampling layers, in contrast to traditional artificial neural network methods (Craik et al., 2020). CNNs are a representative deep learning algorithm; they offer faster network training, superior conservation of information throughout the hierarchical process, and prevention of overfitting in the built network. These benefits allow the CNN classifier to automatically learn the appropriate features from the EEG data while maintaining its translation invariance and data hierarchy (Xiao and Fang, 2021).

The CNN model in this study consists of several layers, such as convolutional, pooling, dropout, and batch normalization, as well as a fully connected layer. When designing the CNN, the size of the input data and its output results should be taken into consideration. In our study, the input matrix fed into the CNN was $8 \times 4{,}000$, where the row corresponds to the eight selected EEG channels and the column indicates the sampling point of 4 s. Because the CNN was used to discriminate the EEG data from four different facial expression tasks, the output layer was designed to have four outputs.

The second component of CNNs is the convolutional layer, which is crucial in facilitating automatic feature learning. In this study, three 2D convolutional layers were designed to perform advanced EEG feature extraction. In each convolutional layer, a convolutional filter whose width matched the dimensions of the input data and whose kernel size of 3×3 was applied, to extract the correlation of EEG signals in the adjacent channel and preserve its spatial information. *Via* the convolution of each layer, a two-dimensional feature mapping (combining enhanced information regarding the original EEG data from different facial expression tasks) was acquired.

An important hyperparameter in the convolution layer is the number of kernels, which can sizably reduce the number of weight parameters. To solve the problem of under-fitting (i.e., a small number of convolution kernels) and over-fitting (i.e., a redundancy of convolution kernels), the number of kernel convolutions was adaptively optimized using a GA. More details on the GA can be found in Section Genetic algorithm for hyperparameter optimization.

The pooling layer was inserted after the convolutional layer, to receive the compression feature map matrix from all selected channels and temporal values (Kwon and Im, 2021). The objective of the pooling layer is to improve the statistical efficiency of the network and improve its invariance (and subsequently its robustness). To further reduce the size of the feature map and the number of network parameters, a max pooling layer was used to downsample the feature map and store important information, using a receptive field window size of 2×2.

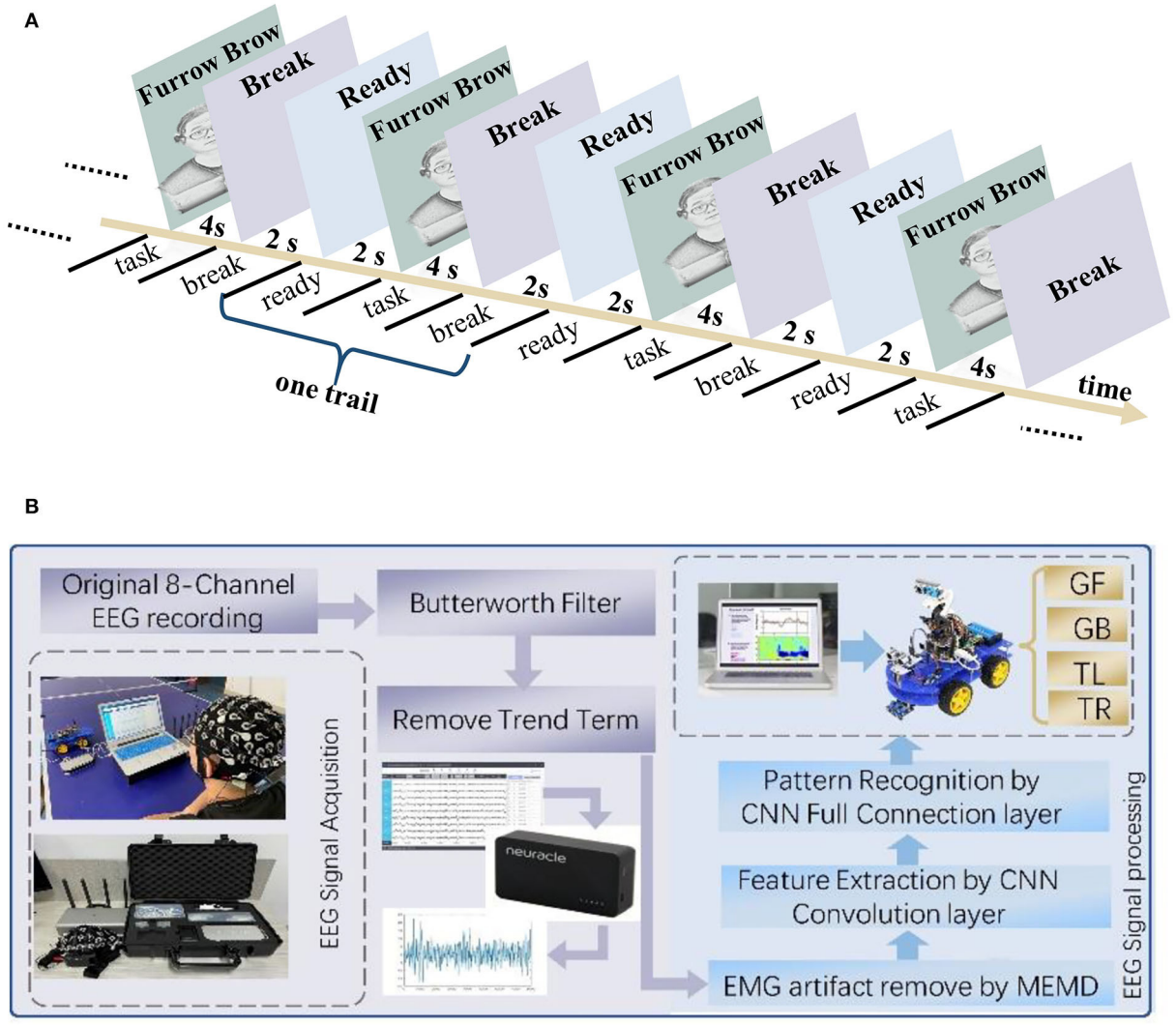

FIGURE 2
FE-BCI system and its experimental protocol. **(A)** Experimental protocol for the offline experiment. **(B)** Scheme of FE-BCI system for an intelligent car.

Subsequently, three fully connected layers followed by pooling layers were used to connect all advanced features and then classify them. The first fully connected layer receives a one-dimensional feature vector and outputs the weighted sum of the features to the second fully connected layer. The number of output neurons in the third layer matched the number of facial expression categories to be classified.

Considering the calculation speed, risk of overfitting, and unsaturated and sparse datasets, the drop-out technique was applied to the fully connected layer, and rectilinear linear unit (ReLU) and Softmax activation functions were applied to each layer, to improve the performance of the proposed CNN models (Stieger et al., 2021). The architecture of the proposed CNN model is illustrated in Figure 3.

As in traditional CNN models, the hyperparameter settings (e.g., the learning rate, batch size, and number of neurons) significantly influences the CNN model performance. Appropriate hyperparameter selections can optimize the performance of the neural network model and further resolve the overfitting problem. Hence, in this study, the GA optimization method was implemented in the constructed CNN model. Two hyper-parameters describing the number of convolution kernels and neurons in the fully connected layer were dynamically optimized *via* the GA evolutionary process. The remaining value of hyperparameters for CNN was the batch

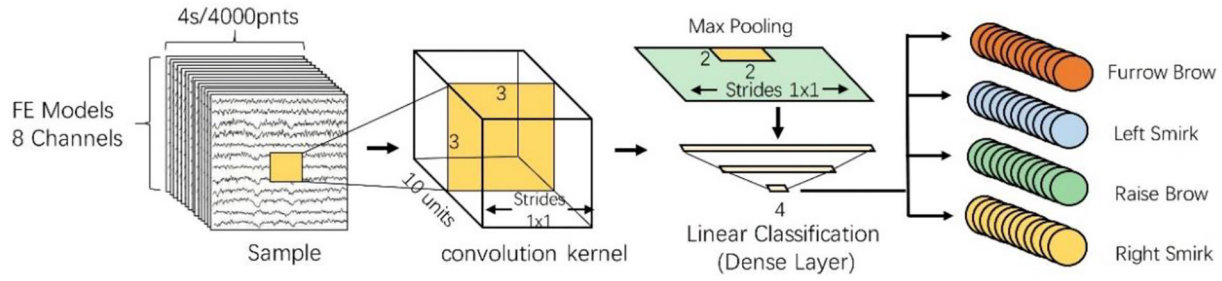

FIGURE 3
Architecture of the proposed CNN model.

size of 16, the learning rate of 0.001, the number of iterations of 100, and the loss function was a cross-entropy loss function.

Genetic algorithm for hyperparameter optimization

The hyperparameter optimization of neural networks is a persistent issue. When a neural network is constructed, the key to achieving an efficient model performance is adjusting the hyperparameters, because the performance is highly sensitive to these parameters. When the model complexity increases, the number of hyperparameters increases, and the combination of hyperparameters increases accordingly. It is difficult to determine the exact optimal values of the neural network hyperparameters. At present, mainstream hyperparameter optimization methods include grid search, Bayesian optimization, evolutionary computation, and neural architecture search.

The main advantage of GA is its excellent global search ability, which can quickly search out the whole solution in the solution space without any prior knowledge of the system. Moreover, its characteristic of paralleling process conducts a variety of routes to find optimal results that avoid falling into the fast-falling trap of the optimal local solution. Most important, the superior performance of the GA method is its social ability, which makes it easier to link with other algorithms (Chang and Yang, 2019).

In this study, a neural network hyperparameter optimization method based on a GA was proposed. GA was first introduced by Holland (2000). It was inspired by the Darwinian theory of survival and the fitness mechanism in nature (Rui et al., 2019). A GA method is a population-based search algorithm whereby each individual in a population represents a set of hyperparameter solutions. Each individual is a set of genes, where each gene represents a hyperparameter. Different gene combinations determine the fitness value of the neural network (i.e., the classification accuracy of the CNN model). The fitness value also determines which individual can transmit its genes to their offspring (i.e., the value of the hyperparameter). A schematic of the GA is shown in Figure 4.

After the initial population is generated, the fitness of each individual is calculated, and the relationship between the fitness and hyperparameters is established. In this study, the hyperparameters describing the number of convolution kernels and neurons in the fully connected layer were encoded via a binary code. The encoding precision δ can be calculated as

$$\delta = \frac{u_{\max} - u_{\min}}{2^l - 1} \tag{1}$$

where l is the encoding length, and u_{max} and u_{min} are the upper and lower limits of the set hyperparameters, respectively.

The fitness of individuals indicates the applicability of the hyperparameter solutions to the model performance, and superior individuals can be obtained by selecting, crossing, and mutating three genetic operators. In the present study, the roulette method was used to select individuals. The probability $P(x_i)$ of each individual is represented as

$$P(x_i) = \frac{f(x_i)}{\sum_{j=1}^{N} f(x_j)} \tag{2}$$

where N is the population size, x_i is the i_{th} individual, and $f(x_i)$ is the fitness of the i_{th} individual.

Crossover operators are generated by two new individuals that exchange gene components between two chromosomes in a certain way. In this study, a multipoint crossover operator was used to pair individuals in the population. The mutation operator is an auxiliary method for generating new individuals; it determines the local search ability of the GA and maintains population diversity.

The entire process of the combined CNN–GA method is shown in Figure 5. The EEG signals were recorded from eight channels in the prefrontal and motor regions; hence, the input data for the CNN model were 8 × 4,000, where the rows denote channels and the columns are sampling points. The CNN model employed in our study consisted of three convolutional layers,

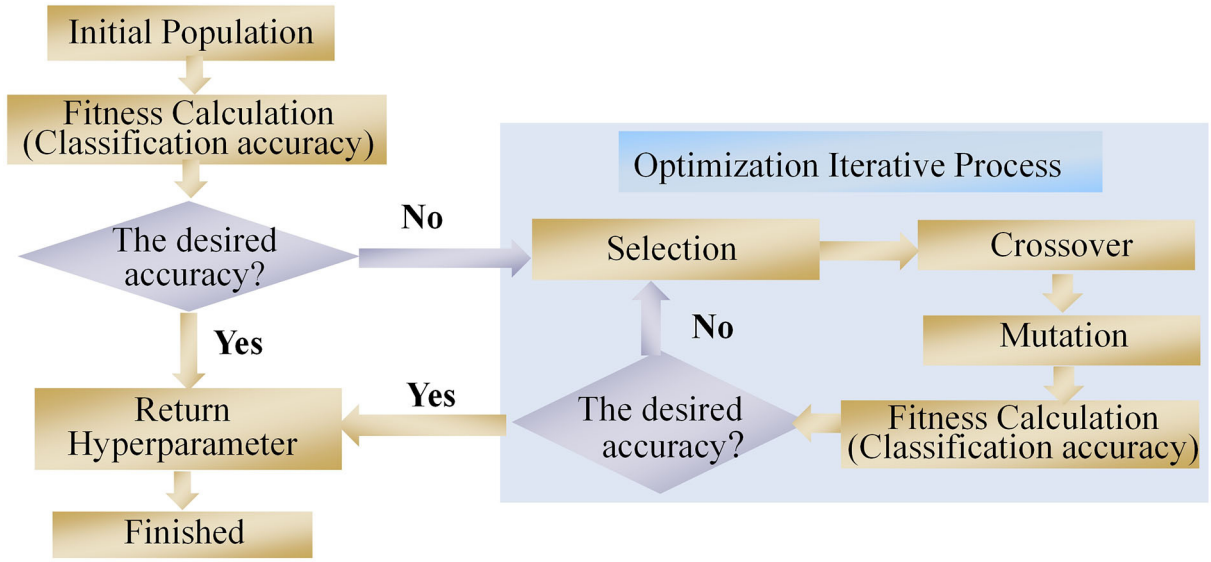

FIGURE 4
Architecture of the proposed GA.

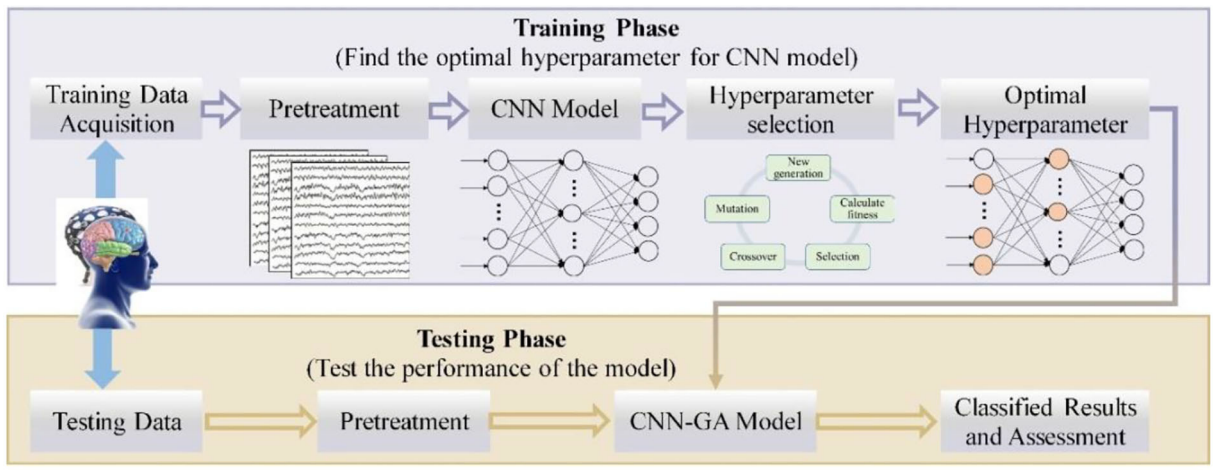

FIGURE 5
Scheme of the proposed CNN–GA algorithm.

one pooling layer, and three fully connected layers. Two batch normalization (BN) and one dropout were also used in the proposed CNN–GA model. Because the third fully connected layer is used to output the discrimination result from the four expression-based EEG signals, the number of neurons in this layer was four, and its activation function was selected as Softmax. The initial values for the CNN model parameters were a batch size of 16, a learning rate of 0.001, 100 iterations, and a cross-entropy loss function. The numbers of convolution kernels (in the three convolutional layers) and neurons (in the two fully connected layers) were set *via* GA optimization.

In this study, we designed the proposed CNN model as the fitness function. The numbers of convolution kernels and neurons in the fully connected layer were set as the hyperparameters to be optimized, and the classification accuracy was set as the fitness value in the GA. For the GA algorithm, an excessively large population will increase the time cost. However, too small a population will mean that the algorithm is likely to fall into a locally optimal solution. Based on the relevant literature (Katoch et al., 2020) and experimental analysis, the population size was set as 20 in this study. Because the accuracy of the EEG signals tended to stabilize after 20 iterations, the

number of GA iterations was set to 20. The ranges of the five hyperparameters were $u_{min} = \{1, 1, 1, 1, 1\}$ to $u_{max} = \{20, 20, 20, 512, 512\}$. Because the hyperparameters in this study were integers, the precision of their values was defined as {1, 1, 1, 1, 1}. The initial values of the hyperparameters were chosen automatically within these ranges. Due to the individual variability, each subject had its own hyperparameter value after optimation.

After optimizing the CNN hyperparameters *via* training data, the testing data were applied to evaluate the model performance using the subject's own classifier. To evaluate the performance of the proposed CNN–GA algorithm, five-fold cross-validation was used to estimate its recognition accuracy. This cross-validation was repeated four times. In each validation, four data subsets were used for training and one was used for testing. Five-fold cross-validation means that 240 offline samples are randomly divided into five equally sized subsets. Four subsets ($240/5 \times 4 = 192$ samples) were used for training the CNN–GA model, and the remaining subset ($240/5 = 48$ samples) was used to verify the performance of the trained model.

To further evaluate the feasibility of the proposed CNN–GA method, the traditional combined WT–BPNN method and a traditional CNN model were used as comparison algorithms. The WT decomposition level was set to 5, and the db-3 wavelet served as the WT basis function. The energy and variances of the wavelet coefficients were employed as the feature sets of expression-based EEG signals. The three-layer BPNN model (with one hidden layer) was constructed in a previous study. Because the BPNN inputted two WT coefficients from eight channels of each trial, the corresponding input layer of the BPNN had 16 nodes. The output layer had two nodes (to flag the results), and the hidden layer had 20 nodes. Apart from the hyperparameters (that needed to be optimized), the structure of the comparison CNN model and its remaining parameter values were consistent with those of the CNN–GA model. That is, the batch size was 16, the learning rate was 0.001, the number of iterations was 100, and the loss function was a cross-entropy loss function. According to previous studies regarding parameters selection (Craik et al., 2020), the number of convolution kernels in the three convolutional layers was set as 3, and the numbers of neurons in the two fully connected layers were 64 and 32, respectively.

Furthermore, the kappa value serves as a well-known evaluation index for investigating the performance of EEG classification algorithms; it expresses the agreement between the classification accuracy of p_0 and the expected consistency rate p_e for the same categories (Chicco et al., 2021). The kappa coefficient can be interpreted as an agreement measure to determine whether different categories are consistent with their prediction results. The kappa coefficient ranges between 0 and 1, where 0 is consistent (owing to randomness) and 1 is perfectly consistent. The coefficient is defined as

$$K = \frac{p_0 - p_e}{1 - p_e} \tag{3}$$

where p_0 is the classification accuracy and p_e indicates the expected consistency rate.

The formula for calculating the classification accuracy p_0 is defined as

$$p_0 = \frac{TP + TN}{TP + TN + FP + FN} \tag{4}$$

where TP is a true positive, FN is a false negative, FP is a false positive, and TN is a true negative.

P_e is the expected agreement rate, which is the consistency rate attributable to chance. P_e is the accuracy under statistically independent observers, which can be computed *via*

$$p_e = \frac{(TP + FN) \times (TN + FN) + (TN + FP) \times (TP + FP)}{N^2} \tag{5}$$

where N is the number of samples in the dataset.

Statistical analysis

In this study, the difference in classification accuracies between the three EEG decoding methods (CNN, CNN–GA, and combined WT–BPNN) was assessed using a Student's paired t-test and one-way analysis of variance (ANOVA), respectively. Based on the statistical theory, three parameters of significance level α, the expected effect size f, and the desired statistical power (1-β) determined the choice of the sample size and verified the significant differences among different methods (Desu and Raghavarao, 1990). The desired effect size was 0.9 ($f = 0.9$), significance threshold was set as 0.05 ($a = 0.05$) and desired statistical power (1-β) was 0.8. Furthermore, the Greenhouse–Geisser correction was applied for p-value adjustment. Using the statistical software G*Power of the given parameters setting and referring to some existing studies (Zheng et al., 2019; Shajil et al., 2020; Cao et al., 2021), the sample size is 16 subjects in this study.

Student's paired t-test is primarily used to test whether the same group of subjects differs significantly under two different conditions. We investigated the variability (for the same subjects) between the CNN and CNN–GA algorithms and between the CNN–GA and WT–BPNN methods. Because the t-test is only suitable for testing the variability between two conditions, ANOVA was used to investigate the significant differences when more than two conditions differed. Therefore, this method verifies the variability between the CNN, CNN–GA, and WT–BPNN algorithms.

Result analysis

In this section, the offline and online experimental results are presented. The main purpose of the offline experiment was to evaluate the efficiency of the proposed CNN–GA, whereas the online experiment was performed to investigate the feasibility of the improved FE–BCI system.

Offline experimental results

Before verifying the effectiveness of the CNN–GA method for all subjects, data from one representative subject, S2, were thoroughly analyzed. Other participants reported similar results. Figure 6A depicts the decoding trends of the CNN–GA classifier and CNN for S2. The two algorithms exhibited similar trends after 20 epochs. However, several differences were observed during the training and testing stages. Figure 6B compares the stability and model loss between the CNN and CNN–GA classifiers. The improved CNN–GA model outperformed the traditional CNN algorithm, and its predicted targets varied slightly in both the training and testing stages, with CNN–GA loss values (after 20 epochs) of 1.024 and 1.456, respectively. The loss values of the CNN model were comparatively higher (at 1.683 and 2.457, respectively) under the same conditions. The analyzed results indicated that the hyperparameter optimization strategy could significantly improve the CNN performance.

To further analyze the performance of the CNN–GA algorithm in the FE-BCI system, the GA optimization process (with genetic offspring of size 20) and confusion matrices for CNN and CNN–GA were evaluated. Figure 7 shows the results for S2. Figure 7A depicts the process of hyperparameter optimization, where the *x*-axis indicates the population size, the *y*-axis indicates the generation size, and the *z*-axis indicates the accuracy across the different iterations. It is not difficult to find that the classification accuracy was gradually improved. After 15 iterations, the accuracy improved slightly, though the difference was not significant. This confirmed our previous hypothesis that it was feasible to improve the accuracy of the FE-BCI system using the GA optimization algorithm. The best hyperparameter optimization result for S2 is {15, 13, 6, 286, 68}. The first three numbers are the number of convolutional kernels, and the last two are the number of fully connected layer neurons.

As shown in Figure 7B, a confusion matrix was applied to demonstrate the superiority of the CNN–GA algorithm. The *x*- and *y*-axes denote the true and predicted values, respectively. Comparing the confusion matrices from the two methods, the overall accuracy was seen to be improved by 4%, which further demonstrates that the CNN–GA model can easily and accurately predict positive samples.

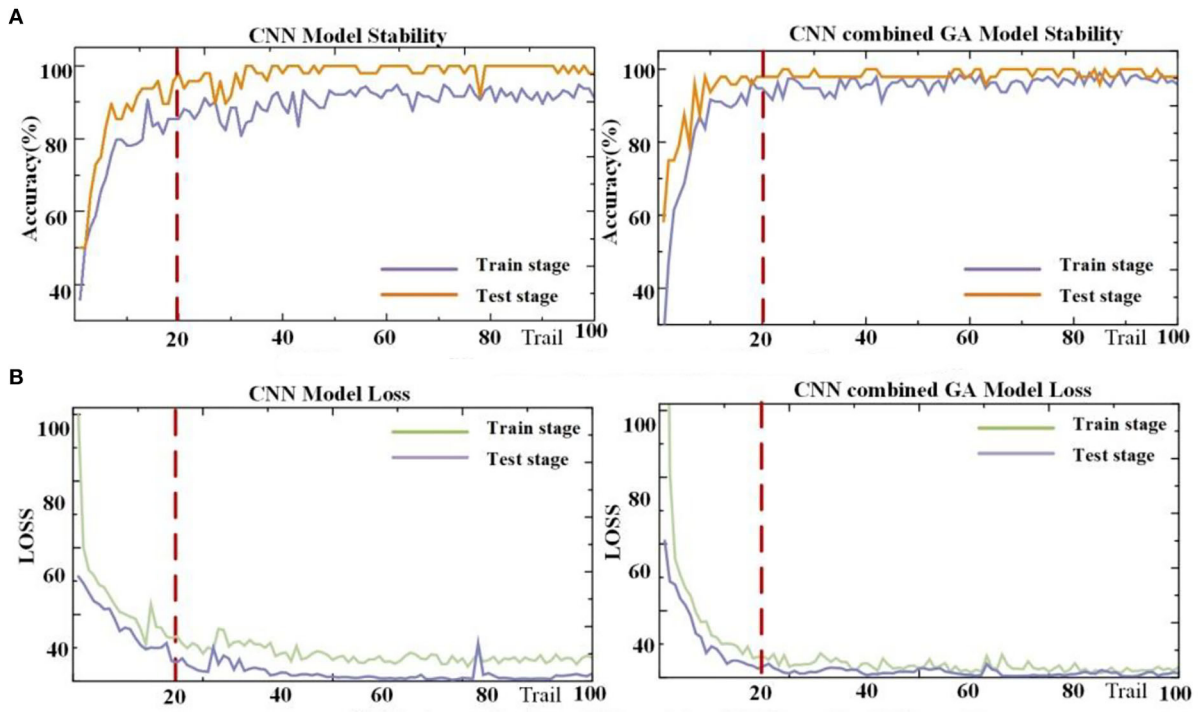

FIGURE 6
Performance from the CNN and CNN–GA algorithms. **(A)** The accuracy result from CNN model and CNN combined GA model. **(B)** The loss value from CNN model and CNN combined GA model.

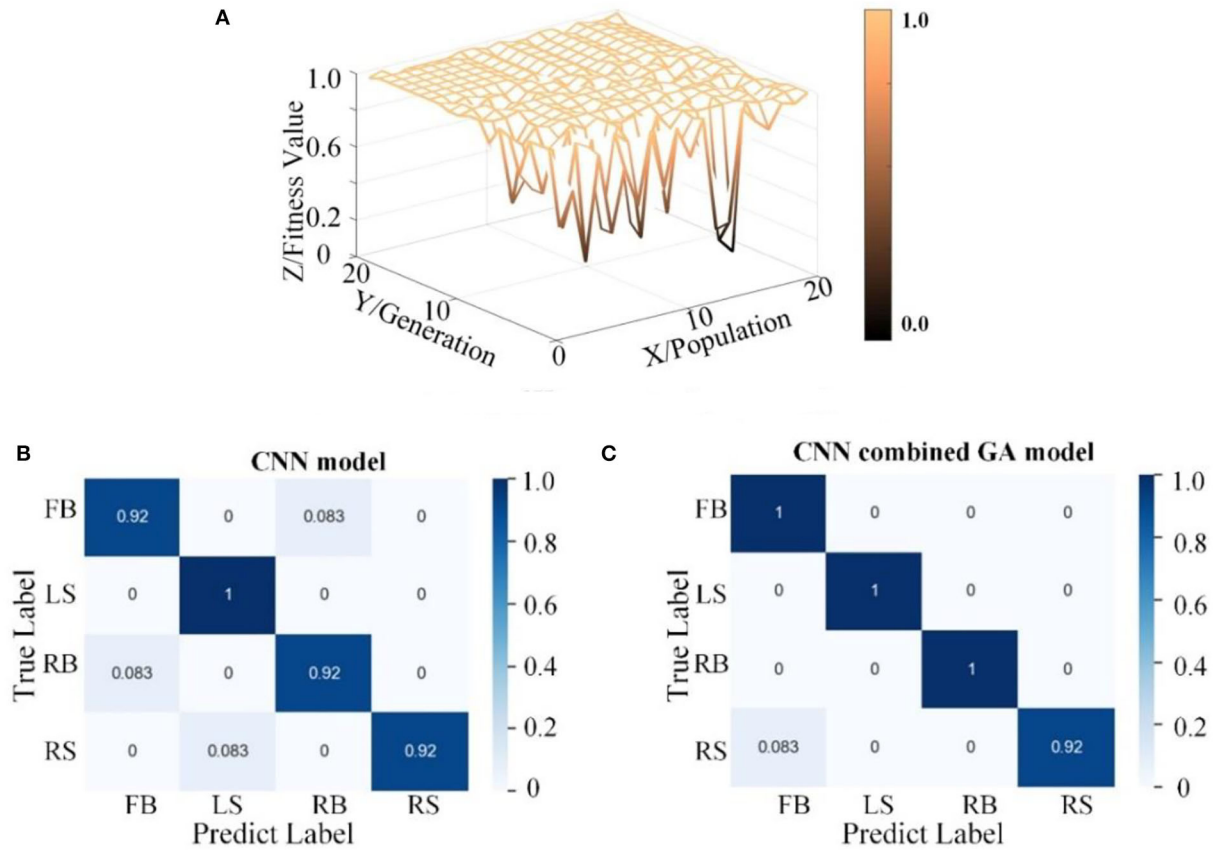

FIGURE 7
Hyperparameter optimization performance from the CNN combined GA. **(A)** The process of hyperparameter optimization by GA. **(B)** The confusion matrix from CNN and CNN combined GA.

The performances obtained from the spatiotemporal analysis showed that the CNN–GA model efficiently distinguished the EEG signals from different facial expressions. Table 1 further analyzes the testing classification for S2. The average accuracy for S2 in the two-round five-fold cross-validation was 97.71 ± 2.07%. The highest accuracy was 100% and the lowest was 93.75%.

To compare the optimization performances of the hyperparameters, the averaged classification accuracy and its standard deviation with and without GA optimization are listed in Table 2. The average accuracies achieved by CNN and CNN–GA for all subjects were 85.94 ± 6.51 and 89.21 ± 3.79%, respectively. The averaged kappa value increased from 0.816 to 0.856. The highest recognition accuracy was obtained for S2 (up to 97.71 ± 2.07%); the lowest accuracy was obtained for S4 (76.43 ± 7.13%). The proposed algorithm improved the average accuracy by 3.27%, and the standard deviation was reduced by 2.72% for all subjects. The recognition accuracy for S11 was significantly increased from 89.27 ± 6.53% to 94.79 ± 3.54%; this increased the accuracy by 5.52% and decreased its standard deviation by 2.99%. The average classification accuracy across eight subjects exceeded 91.25%.

To statistically compare the performances of the two classifiers, a paired t-test was conducted. The results showed a considerable difference between the two algorithms ($p < 0.05$). This also suggests that the hyperparameter optimization method can effectively optimize the classifier performance. Despite these general experimental results, inter-subject variability still occurred. This phenomenon may have been caused by attention attenuation or mental fatigue during repetitive facial tasks.

To determine the efficiency of the selected parameter-optimization method in the FE-BCI system, the classification accuracies of the traditional method and our proposed method are also compared in Table 3. The average accuracy under the CNN–GA method was 89.21 ± 3.79%; meanwhile, the overall average accuracy of the traditional WT-BPNN method was 81.60 ± 7.36%. The average accuracy increased by 7.61%, while its standard deviation decreased by 3.57%. The recognition accuracy for S7 increased significantly from 79.17 ± 9.17 to 91.25 ± 2.75%; this increased the

TABLE 1 Offline accuracies of the CNN–GA for S2.

	1	2	3	4	5	6	7	8	9	10	Mean
Acc (%)	97.92	100	97.92	95.83	93.75	95.83	97.92	100	100	97.92	97.71 ± 2.07

accuracy by 12.08% and reduced the standard deviation by 6.42%.

Furthermore, a statistical analysis was conducted using a paired *t*-test, to investigate whether the two algorithms had any significant differences. The results indicated a significant difference between the two methods, and the accuracy of CNN–GA outperformed that of the combined WT–BPNN ($P < 0.05$). The experimental results showed that the proposed optimization algorithm achieved a higher classification rate and superior robustness for all subjects.

To further investigate the performance of the proposed method, the classification results achieved by the three different methods are compared in Figure 8. The results verified that the performance of the CNN–GA surpassed that of the other two methods. One-way ANOVA was used to assess the performances under the three conditions, and significant differences were observed among the three conditions ($P < 0.05$). The experimental results further validated the efficiency of the proposed method for detecting the characteristics of EEG signals produced by different facial expressions.

The above results demonstrate that the optimization method proposed in this study is effective for decoding EEG signals for FE-BCI systems.

TABLE 2 Averaged accuracies for each subject under the CNN and CNN–GA methods.

Subject	CNN		CNN–GA	
	Test (%)	Kappa	Test (%)	Kappa
S1	84.90 ± 5.77	0.80	87.06 ± 4.51	0.83
S2	94.48 ± 3.90	0.93	97.71 ± 2.07	0.96
S3	80.52 ± 4.74	0.74	85.21 ± 4.92	0.80
S4	72.80 ± 6.22	0.61	76.43 ± 7.13	0.69
S5	88.75 ± 7.13	0.85	91.46 ± 5.27	0.89
S6	92.29 ± 6.93	0.90	96.88 ± 2.75	0.96
S7	86.77 ± 6.56	0.82	91.25 ± 2.75	0.88
S8	82.55 ± 6.22	0.77	86.09 ± 3.96	0.81
S9	83.13 ± 3.29	0.78	84.90 ± 2.27	0.80
S10	92.81 ± 16.29	0.92	95.83 ± 3.38	0.94
S11	89.27 ± 6.53	0.91	94.79 ± 3.54	0.93
S12	95.63 ± 6.34	0.94	96.77 ± 2.19	0.96
S13	78.54 ± 5.97	0.71	81.88 ± 3.39	0.76
S14	81.46 ± 6.08	0.75	83.52 ± 3.02	0.78
S15	81.15 ± 6.06	0.75	85.21 ± 4.87	0.80
S16	90.00 ± 6.07	0.87	93.02 ± 3.90	0.91
Avg ± Std	85.94 ± 6.51	0.816	89.21 ± 3.79	0.856

Online experimental results

The offline experimental results demonstrated the feasibility of the FE-BCI system, and the online experiment was designed to verify the practicality of the optimized FE-BCI system used for vehicle control. To preliminarily evaluate the online performance of the FE-BCI system for controlling an intelligent car, the success rate was calculated. During the online experiment, all subjects could cross Targets 1 to 3 and then return to the start position. Each session included three left-hand lane changes, three right-hand lane changes, five accelerations, and four decelerations. In the control stage, subjects were required to maintain the same facial expression for 1.5 s to generate a car movement decision; for the online task, this time window was set to 0.25 s. The intelligent car remained in the previous state until the new control commands had been generated three times in the same. Figure 9 shows the experimental scenario and a representative decision procedure from S2.

The task success rates for each subject are listed in Table 4. The average success rate across six sessions was 86.61 ± 6.06%, and the highest was 96.31 ± 2.71% from S10. The mean standard deviation during the online experiment was 6.06%, which further suggests the robustness of the proposed GA–CNN in applications.

Discussion

Existing disparities between the selectivity of BCI systems and their performance mean that there is plenty of room for improvement in current BCI systems. In this study, a novel FE-BCI system with an improved EEG decoding method combining a CNN with GA was proposed. The offline experimental results demonstrated that the improved deep learning method was able to significantly improve the model performance compared to the traditional method. The online experimental results verified the feasibility of the proposed FE-BCI system for practical applications. Notably, the improved FE-BCI system outperformed the conventional BCI system.

TABLE 3 Averaged accuracies of each subject under WT–BPNN and CNN–GA methods.

Subjects	Accuracy (%)			
	WT–BPNN		CNN–GA	
	Kappa	Test (%)	Kappa	Test (%)
S1	0.754	81.56 ± 6.77	0.828	87.06 ± 4.51
S2	0.874	90.42 ± 6.57	0.970	97.19 ± 2.81
S3	0.683	76.25 ± 8.18	0.803	85.21 ± 4.92
S4	0.613	70.94 ± 7.60	0.686	76.43 ± 7.13
S5	0.774	83.02 ± 8.64	0.886	91.46 ± 5.27
S6	0.879	90.94 ± 4.07	0.958	96.88 ± 2.75
S7	0.722	79.17 ± 9.17	0.883	91.25 ± 2.75
S8	0.739	80.42 ± 6.25	0.815	86.09 ± 3.96
S9	0.742	80.63 ± 6.04	0.799	84.90 ± 2.27
S10	0.803	85.21 ± 6.48	0.944	95.83 ± 3.38
S11	0.828	87.08 ± 8.78	0.931	94.79 ± 3.54
S12	0.833	87.50 ± 10.71	0.957	96.77 ± 2.19
S13	0.667	75.00 ± 7.34	0.758	81.88 ± 3.39
S14	0.690	76.77 ± 7.26	0.780	83.52 ± 3.02
S15	0.701	77.60 ± 7.26	0.803	85.21 ± 4.87
S16	0.776	83.23 ± 6.63	0.907	93.02 ± 3.90
Mean accuracy	0.755 ± 0.076	81.60 ± 7.36	0.857 ± 0.084	89.21 ± 3.79

Significance of the FE-BCI system

Emotion computation plays an important role in human communication and real-world applications. Although effective computation has attracted considerable interest in the past few years, the use of emotions in brain-controlled systems remains problematic. Research in the affective BCI field has focused on perception; numerous specific stimuli have been used to detect different emotions (e.g., emotional videos, images, and music). According to Jiang et al. different emotions can be evoked by a video's affective content and further applied in an emotion-based BCI system (Jiang et al., 2019).

Jin and his colleagues reported on a new emotion-detecting BCI system that employs a face-based image-induced paradigm (Cheng et al., 2017). In another study, Thammasan et al. studied a continuous music-emotion-recognition approach for the construction of affective BCI (Thammasan et al., 2016). However, it is difficult to detect the ground truth of human emotional states using these methods. Most importantly, these paradigms rely upon extra stimuli, which limits their real-world applications.

In contrast to traditional emotion discrimination techniques, it is more straightforward to recognize the emotional stage using different facial expressions. Facial expressions are the most common features of emotions and the most direct mechanism of emotional representation. Unfortunately, the inconsistency of emotion and expression still has been the main challenge for this type of emotion-based BCI system. Since the facial expression is a kind of body movement, the combination of EEG signals from the prefrontal and motor cortices could improve the robustness and credibility of techniques that exploit these signals. This way could also reduce the impact on the decoding accuracy of FE-BCI signals when expressions are inconsistent with emotions.

In our approach, EEG signals from the prefrontal and motor cortices were used to distinguish between different emotional states. Furthermore, a highly robust EEG recognition model was obtained by combining a CNN with a GA. To prove the effectiveness of the proposed FE-BCI system, Table 5 shows the results of representative EEG decoding algorithms for expression-based brain-computer interfaces system in the past few years. It can be seen that the decoding accuracy of the P300-based visually evoked BCI system was still relatively high (Cheng et al., 2017; Tian et al., 2018). The performance of this type of the FE-BCI system depends entirely on the design of the stimulator, which includes the size of the face picture, the space between two pictures, and the number of target appearances. In contrast, the method proposed in this study shows the superiority in the film video elicitation with WT- MLPNN and STFT combined Graph Regularized Extreme Learning Machine (Ozerdem and Polat, 2017; Zheng et al., 2019), music elicitation with Higuchi algorithm combined SVM (Thammasan et al., 2016), the pictures of facial expression elicitation (Huang et al., 2017) with mixed features and corresponding algorithms, and the previously proposed actual facial expression-based WT-BPNN decoding method (Toth and Arvaneh, 2017; Li et al., 2018b). This improvement will further extend the broader range of human-computer interaction. In contrast to previous studies, we used only eight-channel EEG signals, and the average accuracy was as high as 89.21 ± 3.79%. This will further extend the possibilities of human–computer interaction.

Efficacy of CNN–GA

Owing to the inherent signal quality limitations of non-invasive EEG signals, there remains a need to develop a novel EEG decoding algorithm that improves the precision of facial-expression-based BCI systems. Most conventional machine learning algorithms set these features manually; thus, they are highly dependent upon the experience of the researcher. However, irrelevant features reduce the classifier performance. Hence, selecting features relevant to the task will improve the classification performance. One advantage of CNN is the automatic extraction of discriminative features (Shajil et al., 2020; Kwon and Im, 2021). Learning hidden features and eliminating redundant information from the EEG signals will enhance the overall capability of BCI systems. Using the classification accuracy metric, Tables 3, 5 present a comparison

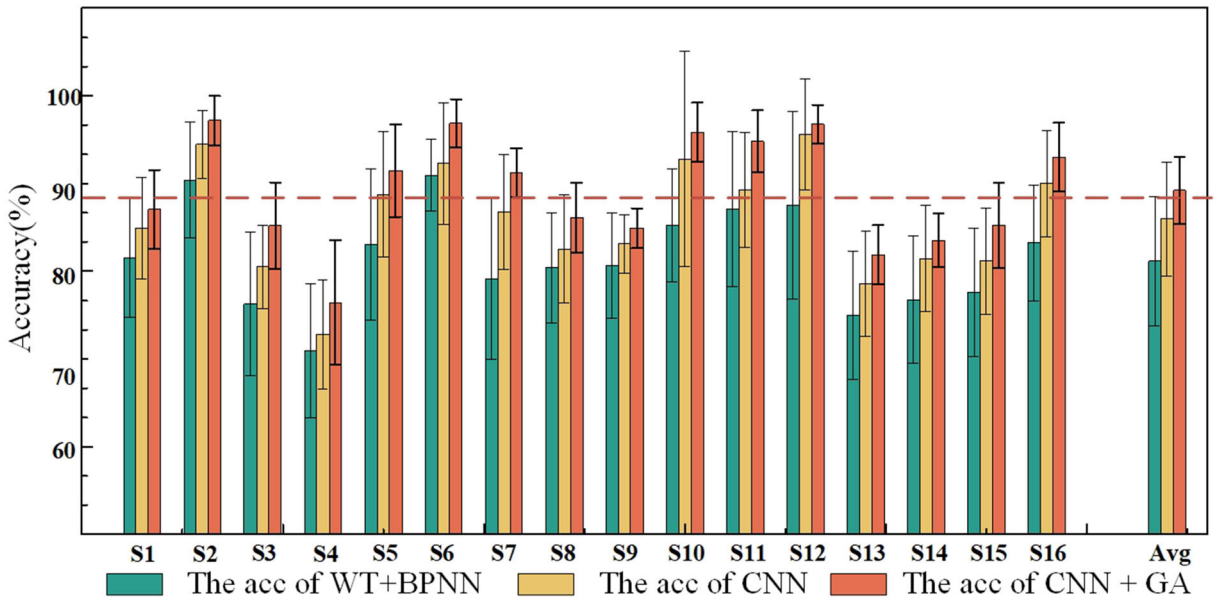

FIGURE 8
Offline classification accuracies and standard deviations under the three methods.

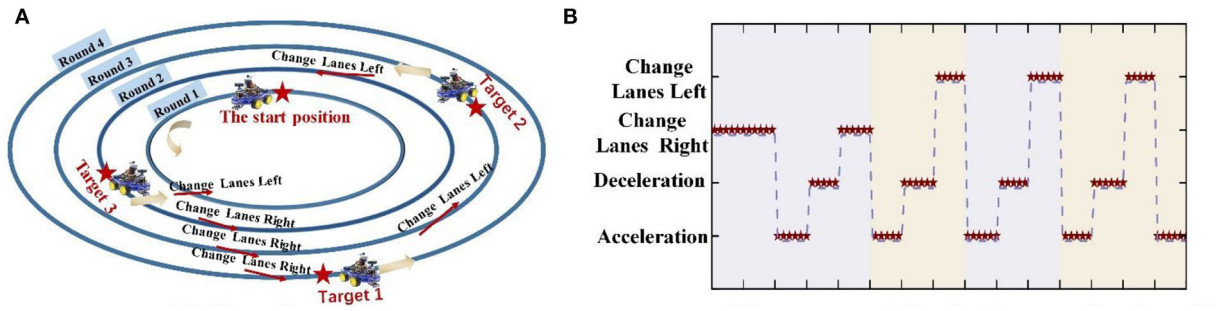

FIGURE 9
Online scenario and optimal recognition performance within a single session for S2. **(A)** The online scene. **(B)** One representative decision procedure from S2.

of the improved CNN and traditional methods. The proposed scheme outperformed other traditional feature extraction and classification methods. Hence, automatic learning of relevant features and eliminating redundant information from EEG signals could effectively improve the recognition accuracy of EEG signals under different expressing.

It is well-known that the performance of a neural network model is highly dependent upon its hyperparameters (Ali et al., 2019). However, most hyperparameter optimizations use the enumeration method to solve this problem. Unfortunately, the selection of inappropriate hyperparameters may result in a poor classification performance. In contrast to selecting hyperparameters using research experience, the proposed scheme sets important hyperparameters using the GA algorithm. GA has an excellent global search ability, which can quickly search out the best solution in the solution space without any prior knowledge. The GA's paralleling process uses numerous routes to find the optimal results. This characteristics ensures that the best solution was found while avoiding fast-falling trap of the optimal local solution (Rui et al., 2019). Most important, the superior performance of the GA method is its social ability, which makes it easier to link with other algorithms (Chang and Yang, 2019). Therefore, embedding the GA algorithm into the CNN model by setting this model as a fitness function is an effective way to optimize the decoding results of EEG signals. Table 2 presents a systematic comparison and qualitative evaluation of the proposed model with and without hyperparameter optimization. Superior accuracy was

TABLE 4 Averaged accuracies of each subject in the online task.

Subjects	Acc. (%)				
	Change left	Acceleration	Change right	Deceleration	Mean
S1	79.41	83.33	73.33	88.89	81.24 ± 6.55
S2	97.06	88.89	96.67	100	95.65 ± 4.75
S3	70.59	77.78	100	94.44	85.70 ± 13.81
S4	76.47	77.78	83.33	77.78	78.84 ± 3.06
S5	91.18	83.33	93.33	94.44	90.57 ± 5.01
S6	94.12	100	96.67	94.44	96.31 ± 2.71
S7	94.17	88.89	90.00	77.78	85.56 ± 6.76
S8	97.06	88.89	93.33	94.44	93.43 ± 3.41
S9	85.29	83.33	83.33	72.22	81.04 ± 5.95
S10	94.12	100	96.67	94.44	96.31 ± 2.71
S11	91.17	83.33	76.67	88.89	85.01 ± 6.46
S12	97.06	88.89	93.33	88.89	92.04 ± 3.95
S13	79.41	88.89	83.33	83.33	83.74 ± 3.90
S14	85.29	77.78	83.33	77.78	81.05 ± 3.85
S15	82.35	83.33	90.00	77.78	83.36 ± 5.04
S16	85.29	77.78	80.00	72.22	78.82 ± 5.41
Mean ± Std	87.50 ± 8.22	85.41 ± 6.37	88.33 ± 7.98	85.76 ± 8.83	86.61 ± 6.06

achieved compared to the CNN model. This experimental result verified that the GA-optimized hyperparameters improved the classification performance and further resolved the time-consumption problem of redundant information. These analytic results demonstrate that the CNN–GA EEG decoding model can produce a more interpretable model for exploring the information hidden in EEG signals. This should promote the development of a high-quality EEG decoding model.

Comparison with existing BCI systems

The practical performance of BCI systems is worth discussing. Existing challenges to the practical implementation of BCI systems include their accuracy, portability, and robustness. The MI-based BCI system is a representative BCI system used to improve the quality of life of disabled people. For example, Miao reported an MI-BCI system that helped stroke patients toward rehabilitation (Miao et al., 2021). However, this type of BCI system does not readily facilitate daily activities, owing to its low accuracy and limited commands. Recently, a great surge in SSVEP-based BCI systems has been observed in daily life applications. For example, Chen et al. produced a robotic arm control mechanism using an SSVEP system (Chen et al., 2021). Unfortunately, the performances of most existing strategies are highly dependent upon extra stimuli. This partially limits the mobility of the SSVEP–BCI system.

The development of the FE-BCI system provides an additional option for solving the tradeoff between BCI performance and stimulus reliance. Compared with the traditional BCI system, the EEG signals from real facial expressions can increase the portability of the FE-BCI system. EEG decoding algorithms also play a vital role in BCI systems. In this study, the combined CNN–GA model also ensured the accuracy of the FE-BCI system. Hence, the improved FE-BCI system is cost-effective, user-convenient, and more suitable for practical tasks.

Limitations and future work

Despite the superior performance of the improved FE-BCI system, certain aspects still need to be improved. One limitation of this study is that only healthy subjects were considered, and a relatively small number of subjects participated. In future studies, clinical applications involving certain patient groups and more subjects should be included. Moreover, enhancing the generalizability of the classifier and studying the asynchronous FE-BCI system should produce a better solution and provide a more flexible and realistic BCI system. There remains the motivation for finding more computationally and friendly metrics to investigate the consistency between emotions and expressions. Exploring a more advanced algorithm and effective criteria to reduce inter-subject variability will remain a challenge to be addressed in the future.

TABLE 5 Performance comparison of previous work based on the FE-BCI.

References	Modality	Stimulus	Method	Parameters	Acc (%)
Cheng et al. (2017)	EEG (P300)	P 300 evoked	Features extracted by calculating the percentiles of EEG; Classified by Bayesian linear discriminant analysis	Referring previous study	91.9
Tian et al. (2018)	EEG(N170)		N170 extracted by dimensionality reduction and normalization; Classified by L1-Regularized Logistic Regression		86.4
Thammasan et al. (2016)	EEG	Music	Features extracted by Higuchi algorithm; Classified by SVM	By experience	85.0
Ozerdem and Polat (2017)	EEG	Film chips	Features extracted by wavelet transform; classified by MLPNN	Referring previous study	77.14
Zheng et al. (2019)			Features extracted by STFT; classified by Graph Regularized Extreme Learning Machine		69.67
Huang et al. (2017)	Picture information EEG	Face pictures Facial expression	Picture feature extracted by AdaBoost and classified by neural network classifier EEG feature extracted by STFT and classified by SVM	Burte-Force Searching	82.75
Toth and Arvaneh (2017)	EEG Gyroscope	Facial expression	Feature extracted by FFT; classified by SVM-LDA-Bayesian	By experience	70.3
Li et al. (2018b)	EEG		Features extracted by wavelet transform; classified by BPNN		81.28
The proposed study			Features extracted and classified by CNN	By GA	89.21

Conclusion

This paper proposed a novel deep-learning-based EEG decoding method for an FE-BCI system, and the performance of the proposed CNN–GA model was evaluated systematically. The proposed method employed a CNN algorithm to decode EEG signals and a GA to select the optimal hyperparameters for the CNN model. To verify the model effectiveness, offline and online experiments were conducted. When using the CNN–GA algorithm in offline experiments, the averaged accuracies were increased from 85.94 ± 6.51 to 81.60 ± 7.36% (for the conventional CNN algorithm and traditional BPNN-based method, respectively) to 89.21 ± 3.79%. Moreover, the online experiment results demonstrated the practical applicability of the method, and the average accuracy was increased up to 86.61 ± 6.06%. Both the offline and online experimental results demonstrated the superiority of the proposed EEG decoding method in the FE-BCI system. In summary, the CNN–GA method is a significant achievement in the development of FE-BCI systems. Future work will aim to develop an asynchronous FE-BCI system using the CNN–GA model; this will further improve paralyzed patients' access to the real world.

Data availability statement

The raw data supporting the conclusions of this article will be made available by the authors, without undue reservation.

Ethics statement

The studies involving human participants were reviewed and approved by the Institutional Review Board of Xi'an University of Technology. All experiments were conducted in accordance with the of Helsinki. The patients/participants provided their written informed consent to participate in this study. Written informed consent was obtained from the individual(s) for the publication of any potentially identifiable images or data included in this article.

Author contributions

RL and DL organized the experiments and wrote the manuscript. ZL and JL did the research and revised the manuscript. WF and WL supervised the work and carried out the experiments. BL analyzed the data. JZ and AA modified the grammar of this article. All authors contributed to the article and approved the submitted version.

Funding

This research work was supported by the Natural Science Foundation of Shaanxi (Grant No. 2022JQ-402) and National Defense Science and Technology Foundation Strengthening Program Technology Field Fund Project (Grant No. 2020-JCJQ-JJ-367).

Conflict of interest

The authors declare that the research was conducted in the absence of any commercial or financial relationships that could be construed as a potential conflict of interest.

Publisher's note

All claims expressed in this article are solely those of the authors and do not necessarily represent those of their affiliated organizations, or those of the publisher, the editors and the reviewers. Any product that may be evaluated in this article, or claim that may be made by its manufacturer, is not guaranteed or endorsed by the publisher.

References

Abiri, R., Abiri, R., Borhani, S., Sellers, E. W., Jiang, Y., and Zhao, X. P. (2019), A comprehensive review of EEG-based brain-computer interface paradigms. *J. Neural Eng.* 16, 011001. doi: 10.1088/1741-2552/aaf12e

Alchalabi, B., Faubert, J., and Labbe, D. R. (2021). A multi-modal modified feedback self-paced BCI to control the gait of an avatar. *J. Neural. Eng.* 18, 056005. doi: 10.1088/1741-2552/abee51

Ali, L., Zhu, C., Zhou, M. Y., and Liu, Y. P. (2019). Early diagnosis of Parkinson's disease from multiple voice recordings by simultaneous sample and feature selection. *Expert Syst. Appl.* 137, 22–28. doi: 10.1016/j.eswa.2019.06.052

Allison, B. Z., Kubler, A., and Jin, J. (2020). 30+ years of P300 brain-computer interfaces. *Psychophysiology* 57, e13569. doi: 10.1111/psyp.13569

Cao, L. F., Li, G. Y., Xu, Y., Zhang, H., Shu, X. K., and Zhang, D. G. (2021). A brain-actuated robotic arm system using non-invasive hybrid brain-computer interface and shared control strategy. *J. Neural Eng.* 18, 046045. doi: 10.1088/1741-2552/abf8cb

Chang, H. L., and Yang, J. M. (2019). Genetic-based feature selection for efficient motion imaging of a brain–computer interface framework. *J. Neural Eng.* 15, 056020. doi: 10.1088/1741-2552/aad567

Chen, X., Xu, X. Y., Liu, A. P., McKeown, M. J., and Wang, Z. J. (2018). The use of multivariate EMD and CCA for denoising muscle artifacts from few-channel EEG recordings. *IEEE Trans. Instrum. Meas.* 67, 359–370. doi: 10.1109/TIM.2017.2759398

Chen, X. G., Huang, X. S., Wang, Y. J., and Gao, X. R. (2021). Combination of augmented reality based brain-computer interface and computer vision for high-level control of a robotic arm. *IEEE Trans. Neural Syst. Rehabil. Eng.* 28, 3140–3147. doi: 10.1109/TNSRE.2020.3038209

Cheng, J., Jin, J., and Wang, X. Y. (2017). Comparison of the BCI performance between the semitransparent face pattern and the traditional face pattern. *Comput. Intell. Neurosci.* 2017, 1323985. doi: 10.1155/2017/1323985

Chicco, D., Warrens, M. J., and Jurman, G. (2021). The matthews correlation coefficient (MCC) is more informative than Cohen's Kappa and Brier score in binary classification assessment. *IEEE Access* 9, 78368–78381. doi: 10.1109/ACCESS.2021.3084050

Craik, A., He, Y. T., and Contreras-Vidal, J. L. (2020). Deep learning for electroencephalogram (EEG) classification tasks: a review. *J. Neural Eng.* 16, 031001. doi: 10.1088/1741-2552/ab0ab5

Delis, I., Onken, A., Schyns, P. G., Panzeri, S., and Philiastides, M. G. (2016). Space-by-time decomposition for single-trial decoding of M/EEG activity. *Neuroimage* 133, 504–515. doi: 10.1016/j.neuroimage.2016.03.043

Desu, M., and Raghavarao, D. (1990). *Sample Size Methodology*. San Diego, CA: Academic Press.

D'Mello, S., and Graesser, A. (2009). Automatic detection of learner's affect from gross body language. *Appl. Art. Intell.* 23, 123–150. doi: 10.1080/08839510802631745

Edelman, B. J., Meng, J., Suma, D., Zurn, C., Nagarajan, E., Baxter, B. S., et al. (2019). Noninvasive neuroimaging enhances continuous neural tracking for robotic device control. *Sci. Robot.* 4, eaaw6844. doi: 10.1126/scirobotics.aaw6844

Friedman, B. H., and Thayer, J. F. (1991). Facial muscle activity and EEG recordings: redundancy analysis. *Electroencephalogr. Clin. Neurophysiol.* 79, 358–360. doi: 10.1016/0013-4694(91)90200-N

Hinton, G. E., and Salakhutdinov, R. R. (2006). Reducing the dimensionality of data with neural networks. *Science.* 313, 504–507. doi: 10.1126/science.1127647

Holland, J. H. (2000). Building blocks, cohort genetic algorithms, and hyperplane-defined functions. *Evolut. Comput.* 8, 373–391. doi: 10.1162/106365600568220

Huang, Y. R., Yang, J. H., Liao, P. K., and Pan, J. H. (2017). Fusion of facial expressions and EEG for multimodal emotion recognition. *Comput. Intell. Neurosci.* 2017, 2107451. doi: 10.1155/2017/2107451

Jia, X., Song, Y., Yang, L., and Xie, L. (2021). Joint spatial and temporal features extraction for multi-classification of motor imagery EEG. *Biomed. Signal Process. Control* 71, 103247. doi: 10.1016/j.bspc.2021.103247

Jiang, D. Z., Wu, K. C., Chen, D. C., Tu, G., Zhou, T., Garg, A., et al. (2019). A probability and integrated learning based classification algorithm for high-level human emotion recognition problems. *Measurement* 150, 107049. doi: 10.1016/j.measurement.2019.107049

Jin, J., Allison, B. Z., Kaufmann, T., Kubler, A., Zhang, Y., Wang, X. Y., et al. (2012). The changing face of P300 BCIs: a comparison of stimulus changes in a P300 BCI involving faces. *PLoS ONE* 7, e49688. doi: 10.1371/journal.pone.0049688

Katoch, S., Chauhan, S. S., and Kumar, V. (2020). A review on genetic algorithm: past, present, and future. *Multimed. Tools Appl.* 80, 8091–8126. doi: 10.1007/s11042-020-10139-6

Kwak, N. S., Muller, K. R., and Lee, S. W. (2017). A convolutional neural network for steady state visual evoked potential classification under ambulatory environment. *PLoS ONE* 12, e0172578. doi: 10.1371/journal.pone.0172578

Kwon, J., and Im, C. H. (2021). Subject-Independent functional near-infrared spectroscopy-based brain-computer interfaces based on convolutional neural networks. *Front. Hum. Neurosci.* 15, 646915. doi: 10.3389/fnhum.2021.646915

Li, R., Zhang, X. D., Li, H. Z., Zhang, L. M., Lu, Z., and Chen, J. (2018a). An approach for brain-controlled prostheses based on scene graph steady-state visual evoked potentials. *Brain Res.* 1692, 142–153. doi: 10.1016/j.brainres.2018.05.018

Li, R., Zhang, X. D., Lu, Z. F., Liu, C., Li, H. Z., Sheng, W. H., et al. (2018b). An approach for brain-controlled prostheses based on a

facial expression paradigm. *Front. Neurosci*. 12, 943. doi: 10.3389/fnins.2018.00943

Li, R. X., Liang, Y., Liu, X. J., Wang, B. B., Huang, W. X., Cai, Z. X., et al. (2021). MindLink-eumpy: an open-source python toolbox for multimodal emotion recognition. *Front. Hum. Neurosci*. 15, 621493. doi: 10.3389/fnhum.2021.621493

Liu, J., Shi, Q., Han, R. L., and Yang, J. (2021). A hybrid GA–PSO–CNN model for ultra-short-term wind power forecasting. *Energies* 14, 6500. doi: 10.3390/en14206500

Miao, Y. Y., Chen, S. G., Zhang, X. R., Jin, J., Xu, R., and Daly, I. (2021). BCI-Based rehabilitation on the stroke in sequela stage. *Neural Plast*. 2020, 8882764. doi: 10.1155/2020/8882764

Mishuhina, V., and Jiang, X. (2021). Complex common spatial patterns on time-frequency decomposed EEG for brain-computer interface. *Pattern Recognit*. 115, 107918. doi: 10.1016/j.patcog.2021.107918

Mowla, M. R., Ng, S. C., Zilany, M. S. A., and Paramesran, R. (2015). Artifacts-matched blind source separation and wavelet transform for multichannel EEG denoising. *Biomed. Signal Process. Control*. 22, 111–118. doi: 10.1016/j.bspc.2015.06.009

Mühl, C., Allison, B., and Nijholt, A. (2014). A survey of affective brain computer interfaces: principles, state-of-the-art, and challenges. *Brain Comp. Interfaces* 1, 66–84. doi: 10.1080/2326263X.2014.912881

Olderbak, S., Hildebrandt, A., Pinkpank, T., Sommer, W., and Wilhelm, O. (2014). Psychometric challenges and proposed solutions when scoring facial emotion expression codes. *Behav. Res. Methods* 46, 992–1006. doi: 10.3758/s13428-013-0421-3

Ozerdem, M. S., and Polat, H. (2017), Emotion recognition based on EEG features in movie clips with channel selection. *Brain Inform.* 4, 241–252. doi: 10.1007/s40708-017-0069-3

Pinheiro, O. R., Alves, L. R. G., and Souza, J. R. D. (2018). EEG signals classification_ motor imagery for driving an intelligent wheelchair. *IEEE Latin Am. Trans.* 16, 254–259 doi: 10.1109/TLA.2018.8291481

Rathi, N., Singla, R., and Tiwari, S. (2021). A novel approach for designing authentication system using a picture based P300 speller. *Cogn. Neurodyn*. 15, 805–824. doi: 10.1007/s11571-021-09664-3

Reust, A., Desai, J., and Gomez, L. (2018). "Extracting motor imagery features to control two robotic hands" in *IEEE International Symposium on Signal Processing and Information Technology* (Louisville, KY: IEEE), 118–122. doi: 10.1109/ISSPIT.2018.8642627

Ross, E. D., Gupta, S. S., Adnan, A. M., Holden, T. L., Havlicek, J., and Radhakrishnan, S. (2016). Neurophysiology of spontaneous facial expressions: I. Motor control of the upper and lower face is behaviorally independent in adults. *Cortex* 76, 28–42. doi: 10.1016/j.cortex.2016.01.001

Rui, F., M. A., Al-Absi, and Lee, H. J. (2019). "Introduce introduce a specific process of genetic algorithm through an example," in *International Conference on Information and Communication Technology Convergence* (Jeju: IEEE).

Schuller, B., Villar, R. J., Rigoll, G., and Lang, M. (2005). "Meta-classifiers in acoustic and linguistic feature fusion-based affect recognition," in *IEEE International Conference on Acoustics, Speech, and Signal Processing* (Philadelphia, PA: IEEE). doi: 10.1109/ICASSP.2005.1415116

Shajil, N., Mohan, S., Srinivasan, P., Arivudaiyanambi, J., and Murrugesan, A. A. (2020). Multiclass classification of spatially filtered motor imagery EEG signals using convolutional neural network for BCI based applications. *J. Med. Biol. Eng.* 40, 663–672. doi: 10.1007/s40846-020-00538-3

Shukla, P. K., Chaurasiya, R. K., and Verma, S. (2021). Performance improvement of P300-based home appliances control classification using convolution neural network. *Biomed. Signal Process. Control*. 63, 102220. doi: 10.1016/j.bspc.2020.102220

Stieger, J. R., Engel, S. A., Suma, D., and He, B. (2021). Benefits of deep learning classification of continuous noninvasive brain-computer interface control. *J. Neural Eng*. 18, 046082. doi: 10.1088/1741-2552/ac0584

Sun, Y. N., Xue, B., Zhang, M. J., Yen, G. G., and Lv, J. C. (2020). Automatically designing CNN architectures using the genetic algorithm for image classification. *IEEE Trans. Cybern*. 50, 3840–3854. doi: 10.1109/TCYB.2020.2983860

Svetla, R., and Dimitar, R. R. (2015). "Human-computer interface for communication and automated estimation of basic emotional states," in *IEEE International Conference on Computer* (Liverpool), 15681578.

Tang, Z. C., Li, C., and Sun, S. Q. (2017). Single-trial EEG classification of motor imagery using deep convolutional neural networks. *Optik* 130, 11–18. doi: 10.1016/j.ijleo.2016.10.117

Thammasan, N., Moriyama, K., Fukui, K., and Numao, M. (2016). Continuous music-emotion recognition based on electroencephalogram. *IEICE Trans. Inform. Syst.* E66D, 1234–1241. doi: 10.1587/transinf.2015EDP7251

Tian, Y., Zhang, H. L., Pang, Y., and Lin, J. Z. (2018). Classification for single-trial N170 during responding to facial picture with emotion. *Front. Comput. Neurosci.* 12, 68. doi: 10.3389/fncom.2018.00068

Toth, J., and Arvaneh, M. (2017). Facial expression classification using EEG and gyroscope signals. *IEEE Eng. Med. Biol. Soc*. 2017, 1018–1021. doi: 10.1109/EMBC.2017.8036999

Wood, A., Rychlowska, M., Korb, S., and Niedenthal, P. (2016). Fashioning the face: sensorimotor simulation contributes to facial expression recognition. *Trends Cogn. Sci*. 20, 227–240. doi: 10.1016/j.tics.2015.12.010

Xiao, X. L., and Fang, Y. E. (2021). Motor imagery EEG signal recognition using deep convolution neural network. *Front. Neurosci*. 15, 655599. doi: 10.3389/fnins.2021.655599

Xie, J. X., Siyu, C., Zhang, Y. Q., Gao, D. R., and Liu, T. J. (2021). Combining generative adversarial networks and multi-output CNN for motor imagery classification. *J. Neural Eng*. 18, 04026. doi: 10.1088/1741-2552/abecc5

Xu, M. Y., Yao, J. F., Zhang, Z. H., Li, R., Yang, B. R., Li, C. Y., et al. (2020). Learning EEG topographical representation for classification via convolutional neural network. *Pattern Recognit*. 105, 107390. doi: 10.1016/j.patcog.2020.107390

Yan, N., Wang, C., Tao, Y., Li, J. M., Zhang, K. X., Chen, T., et al. (2020). Quadcopter control system using a hybrid BCI based on off-line optimization and enhanced human-machine interaction. *IEEE Access* 8, 1160–1172. doi: 10.1109/ACCESS.2019.2961246

Yan, W. Q., Du, C. H., Luo, D., Wu, Y. C., Duan, N., Zheng, X. W., et al. (2021). Enhancing detection of steady-state visual evoked potentials using channel ensemble method. *J. Neural Eng*. 18, 046008. doi: 10.1088/1741-2552/abe7cf

Yu, J., Gao, H., Chen, Y., Zhou, Q. L., Liu, J., and Ju, Z. (2021b). Adaptive spatiotemporal representation learning for skeleton-based human action recognition. *IEEE Trans*. 1, 1. doi: 10.1109/TCDS.2021.3131253

Yu, J. H., Gao, H. W., Zhou, D. L., Liu, J. G., Gao, Q., and Ju, Z. J. (2021a). "Deep temporal model-based identity-aware hand detection for space human-robot interaction," in *IEEE Transactions On Cybernetics* (IEEE), 1–14. doi: 10.1109/TCYB.2021.3114031

Zhang, K., Xu, G. H., Du, C. H., Wu, Y. C., Zheng, X. W., and Zhang, S. C. (2021). Weak feature extraction and strong noise suppression for SSVEP-EEG based on chaotic detection technology. *IEEE Trans. Neural Syst. Rehabil. Eng*. 29, 862–871. doi: 10.1109/TNSRE.2021.3073918

Zhang, K., Xu, G. H., Han, Z. Z., Ma, K. Q., Zheng, X. W., Chen, L. T., et al. (2020a). Data augmentation for motor imagery signal classification based on a hybrid neural network. *Sensors* 20, 4485. doi: 10.3390/s20164485

Zhang, K., Xu, G. H., Zheng, X. W., Li, H. Z., Zhang, S. C., Yu, Y. H., et al. (2020b). Application of transfer learning in EEG decoding based on brain-computer interfaces: a review. *Sensors* 20, 6321. doi: 10.3390/s20216321

Zhao, D., Tang, F., Si, B., and Feng, X. (2019). Learning joint space–time–frequency features for EEG decoding on small labeled data. *Neural Netw*. 14, 67–77. doi: 10.1016/j.neunet.2019.02.009

Zhao, X., Wang, Z. Y., Zhang, M., and Hu, H. L. (2021). A comfortable steady state visual evoked potential stimulation paradigm using peripheral vision. *J. Neural Eng*. 18, 056021. doi: 10.1088/1741-2552/abf397

Zheng, W. L., Zhu, J. Y., and Lu, B. L. (2019). Identifying stable patterns over time for emotion recognition from EEG. *IEEE Trans. Affect. Comp*. 10, 417–429. doi: 10.1109/TAFFC.2017.2712143

frontiers | Frontiers in Neuroscience

TYPE Original Research
PUBLISHED 20 September 2022
DOI 10.3389/fnins.2022.952288

OPEN ACCESS

EDITED BY
Yang Zheng,
Xi'an Jiaotong University, China

REVIEWED BY
Marco Gazzoni,
Politecnico di Torino, Italy
Neha Thomas,
Johns Hopkins University,
United States

*CORRESPONDENCE
Jack Tchimino
itc@hst.aau.dk
Strahinja Dosen
sdosen@hst.aau.dk

SPECIALTY SECTION
This article was submitted to Neuroprosthetics, a section of the journal Frontiers in Neuroscience

RECEIVED 24 May 2022
ACCEPTED 22 August 2022
PUBLISHED 20 September 2022

CITATION
Tchimino J, Dideriksen JL and Dosen S (2022) EMG feedback outperforms force feedback in the presence of prosthesis control disturbance. *Front. Neurosci.* 16:952288. doi: 10.3389/fnins.2022.952288

EMG feedback outperforms force feedback in the presence of prosthesis control disturbance

Jack Tchimino*, Jakob Lund Dideriksen and Strahinja Dosen*

Neurorehabilitation Systems, Department of Health Science and Technology, Aalborg University, Aalborg, Denmark

Closing the prosthesis control loop by providing artificial somatosensory feedback can improve utility and user experience. Additionally, closed-loop control should be more robust with respect to disturbance, but this might depend on the type of feedback provided. Thus, the present study investigates and compares the performance of EMG and force feedback in the presence of control disturbances. Twenty able-bodied subjects and one transradial amputee performed delicate and power grasps with a prosthesis in a functional task, while the control signal gain was temporarily increased (high-gain disturbance) or decreased (low-gain disturbance) without their knowledge. Three outcome measures were considered: the percentage of trials successful in the first attempt (reaction to disturbance), the average number of attempts in trials where the wrong force was initially applied (adaptation to disturbance), and the average completion time of the last attempt in every trial. EMG feedback was shown to offer significantly better performance compared to force feedback during power grasping in terms of reaction to disturbance and completion time. During power grasping with high-gain disturbance, the median first-attempt success rate was significantly higher with EMG feedback (73.3%) compared to that achieved with force feedback (60%). Moreover, the median completion time for power grasps with low-gain disturbance was significantly longer with force feedback than with EMG feedback (3.64 against 2.48 s, an increase of 32%). Contrary to our expectations, there was no significant difference between feedback types with regards to adaptation to disturbances and the two feedback types performed similarly in delicate grasps. The results indicated that EMG feedback displayed better performance than force feedback in the presence of control disturbances, further demonstrating the potential of this approach to provide a reliable prosthesis-user interaction.

KEYWORDS

closed-loop control, somatosensory feedback, EMG feedback, vibrotactile stimulation, prosthetic hand, grasping force control, disturbance

Introduction

Upper limb loss has profound and lasting effects on the quality of life of those affected (Shahsavari et al., 2020). Amputees face significant challenges regarding the execution of daily tasks (Antfolk et al., 2013), returning to the workplace after their injury (Pomares et al., 2020; Shahsavari et al., 2020) and participating in social activities (Kristjansdottir et al., 2020; Shahsavari et al., 2020), while also potentially suffering from phantom limb pain (Esquenazi, 2002). Nowadays, myoelectric prostheses offer substantial restoration of lost hand functions; however, despite the ever-growing sophistication of these devices, users often find their control cumbersome and have difficulty accepting them as an integral part of their anatomy, resulting in high abandonment rates (Salminger et al., 2020).

Most commercial myoelectric prostheses are controlled using a direct proportional approach (Peerdeman et al., 2011; Roche et al., 2014), wherein the myoelectric signal is directly mapped to the velocity of prosthesis movement. It has been shown in the literature that closing the control loop by means of artificial somatosensory feedback enhances the performance and user experience of such control schemes, offering more precise control and sense of embodiment (Antfolk et al., 2013; Markovic et al., 2018a; Wilke et al., 2019; Bensmaia et al., 2020). Normally, somatosensory feedback is implemented by reading data from sensors embedded in prosthesis and conveying this information to the user by stimulating their residual limb mechanically or electrically (Jabban et al., 2022). Mechanical stimulation is delivered to the skin using vibration motors, rotational and linear actuators (Fu et al., 2019; Thomas et al., 2019; Abd et al., 2022). Alternatively, electrical stimulation can be delivered to the skin via non-invasive (Isakovic et al., 2019; Vargas et al., 2022) or invasive means, through peripheral nerve or even brain interfaces (Pasluosta et al., 2018). Different feedback variables have been used in the past to provide artificial exteroceptive and proprioceptive feedback, the most common of which was the grasping force (Brown et al., 2015; Fu and Santello, 2018; Fu et al., 2019; Vargas et al., 2022). More recently, electromyography (EMG) feedback, where the user is informed of the level of their muscle contraction (Dosen et al., 2015b; Schweisfurth et al., 2016; Engels et al., 2019; Tchimino et al., 2021) has been tested, demonstrating that this approach can facilitate predictive control of prosthesis grasping.

However, it is well known that the efficiency of such control strategies in clinical settings can be substantially impaired by the various sources of disturbance that perturb the control signals, which are largely absent from the rigorously controlled laboratory environment (Yang et al., 2019). A disturbance in the control signal will manifest itself as a different motor behavior in the prosthesis, posing a risk of damage to grasped objects (e.g., unintentional slipping or breaking). While the impact of such disturbances and the users' capability to adapt and compensate for them has been tested (Hahne et al., 2017), such an assessment has been seldomly performed regarding differing feedback approaches. In general, despite many feedback methods having been presented so far, using different feedback variables, stimulation techniques, and encoding methods, such approaches are rarely compared (Engels et al., 2019; Marasco et al., 2021). Such a comparison, however, is important, as it could be used to critically inform the selection and implementation of feedback interfaces.

An intrinsic characteristic of closed-loop control is that it should be more robust regarding disturbances and noise injected into the system. However, in the context of prosthesis control, the users' ability to react and compensate for the disturbance is likely affected by the specific type of feedback they receive. For example, EMG and force feedback are fundamentally different, therefore, it is reasonable to assume that the effectiveness of disturbance mitigation will also differ between them. In the case of EMG feedback, the user receives online information about their muscle contraction (prosthesis control input), even while the hand is in motion and not in contact with an object. This allows predictive force control, since the user can modulate or correct the generated EMG level even before the prosthesis grasps an object. Conversely, in the case of force feedback, the user must wait until the prosthesis makes contact with an object to assess the generated force and correct if necessary. Hence, it can be expected that EMG feedback would facilitate the compensation of control disturbances. In this case, the feedback would provide information on the control signal, thereby allowing the user to notice if the signal is disturbed and then modulate their muscle contraction in time, before the hand closes around the object and an erroneous force is applied.

The aim of this study was, therefore, to assess and compare the performance of prosthesis control when using EMG versus force feedback in the presence of control disturbances. The subjects were asked to perform a force matching task using a sensorized myoelectric prosthesis over a number of trials. In some of these trials, the myoelectric signal was amplified or attenuated, unbeknownst to the subjects.

We hypothesized that the subjects would perform better when using EMG feedback. More specifically, we assumed that they would be able better compensate for the disturbances as soon as they appeared; and that they would need fewer attempts to adapt to the disturbance in case they failed to compensate immediately. Lastly, a shorter completion time was expected when EMG feedback was used thanks to the real-time feedback flow.

Materials and methods

Subjects

Twenty healthy able-bodied subjects (28.5 ± 4.4 years), with no prior experience in myoelectric control, participated

in this study. The subjects were divided into two groups one of which performed the experiment using EMG feedback and the other using force feedback. In addition, one subject with left transradial amputation performed the experiment in both feedback conditions in two separate sessions. The amputee was 49 years old, had lost their arm 10 years prior and had been using a simple myoelectric prosthesis for 8 years. Prior to the present experiment, the amputee did not use a prosthesis equipped with artificial somatosensory feedback. The subjects signed an informed consent form before commencing the experiment, which was approved by the Research Ethics Committee of the Nordjylland Region (approval number N-20190036).

Experimental setup

The experimental setup for able-bodied subjects comprised the following components: (1) a multifunctional myoelectric prosthetic hand (Michelangelo hand, Otto Bock, Duderstadt, Germany), with proprietary controller, two dry EMG electrodes with embedded amplifiers (13E200, Otto Bock, Duderstadt, Germany) and a USB Bluetooth dongle, (2) four C3 vibrotactors and a control unit (Engineering Acoustics Inc., Casselberry, FL, United States), (3) a standardized box-and-blocks test, (4) a standard laptop (Lenovo ThinkPad P52, Intel Core i7 @2.60 GHz, 32 GB RAM), running Windows 10 Professional and an 18″ computer monitor. The able-bodied subjects carried the prosthesis on their right forearm using a specially made 3D printed mount (**Figure 1A**) and their wrist was immobilized with a thermoplastic orthopedic splint (ORLIMAN), to enforce isometric muscle contractions. The prosthesis was connected to the laptop via Bluetooth, using the USB dongle, while the tactor control unit was connected to the laptop via USB. The program that controlled the prosthesis and generated vibrotactile feedback was implemented in MATLAB Simulink 9.3, using the toolbox for closed-loop human-manual control (Dosen et al., 2015a).

The prosthesis controller sampled the EMG, computed the root mean square (RMS) in 100-ms windows, and sent the data to the laptop at a sampling frequency of 100 Hz. The electrodes were placed on the skin above the flexor carpi radialis and extensor carpi ulnaris muscles (**Figure 1A**), identified by palpation. The electrodes were attached to the skin with medical adhesive tape and an elastic band was placed around the forearm to ensure good electrode-skin contact and avoid electrode shift. If the EMG signal quality was poor, the electrodes were removed, a small amount of conductive gel was applied onto the skin to improve the electrode-skin interface and the electrodes were replaced.

The amputee subject was fitted with a custom-made socket, to which the Michelangelo hand was connected (**Figure 1B**). The socket was designed so that the electrodes were placed in the same position as in the socket normally used by the amputee.

The C3 tactors produce vibrations perpendicular to the skin, with adjustable gain and frequency. In this experiment, the frequency was set at 230 Hz, which corresponds to the maximum sensitivity of the Pacinian corpuscles (Gilman, 2002). The four tactors were placed equidistantly around the upper arm (**Figure 1**), approximately 5 cm proximal to the elbow, and were held in place with an elastic band. The biceps brachii was used as an anatomical landmark for the placement of the tactors. The tactors' gains were adjusted based on the sensation threshold (ST), determined for each subject (see section "Experimental protocol"). The tactors were placed around the upper arm of the amputee in the same configuration as in the able-bodied subjects.

The subjects stood in front of a desk, wearing the setup on their arm (**Figure 1**). The height of the desk was adjusted so that the subjects could execute the task comfortably, without fatiguing by lifting their arm too high. The box and blocks setup was placed on the desk in front of them and the computer monitor was positioned approximately 50 cm away from them.

The Michelangelo prosthesis supports velocity control over two degrees of freedom, namely hand opening/closing using two grasp types (palmar and lateral) and wrist rotation. In this experiment, the hand was configured to only open and close in palmar grasp. The command input to the prosthesis was a normalized myoelectric signal (ranging from 0 to 1). While the hand was in motion, this signal was proportional to the closing velocity and the grasping force generated upon contact (i.e., stronger contraction, faster closing, and higher force). After contact, a further increase in the prosthesis command input proportionally increased the force. The force was measured using sensors embedded in the hand, transmitted to the laptop at 100 Hz and normalized to the maximum force produced by the hand when it closed at the highest velocity. Importantly, the prosthesis was non-backdrivable and after contact responded only to an increase in the command input, while the grasping force remained unchanged if the myoelectric signal decreased. For instance, the subjects could relax their muscles and the prosthesis would still maintain the generated grasping force.

Closed-loop prosthesis control

The closed-loop control scheme implemented in this study is shown in **Figure 2**. The EMG RMS was normalized to 40% of the maximum voluntary contraction (MVC) and then low pass filtered using a second-order Butterworth filter with a cutoff frequency of 1 Hz. These parameter values were selected based on the results of our previous study (Tchimino et al., 2021), investigating the optimal calibration of EMG feedback. The normalized flexor signal was then mapped to the normalized closing velocity, where 0 indicated no movement and 1 corresponded to the maximum closing speed of the prosthesis. Hand opening was controlled using a simpler scheme, as it was

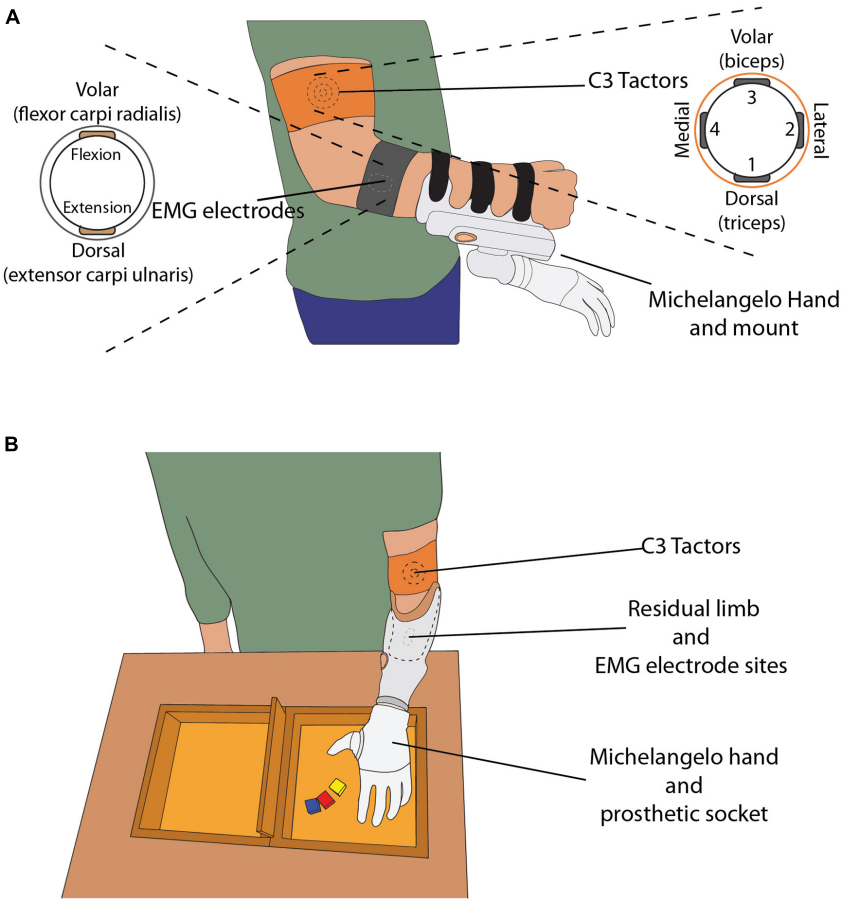

FIGURE 1
(A) The able-bodied subject wearing C3 tactors, EMG electrodes and the mount with the Michelangelo hand attached. The drawings on the left and right display the placement of the electrodes and tactors around the subject's arm, respectively. **(B)** The amputee subject wearing the custom-made socket, with the EMG electrodes embedded in the socket, and C3 tactors placed on their left upper arm. The box and blocks setup is placed on the table in front of the subject.

not relevant for the task (see section "Experimental protocol"). Specifically, when the normalized extensor signal surpassed a threshold of 0.4, the hand opened to its full aperture. The grasping force measured by the embedded force sensors was also normalized (0 – no force, 1 – maximum force).

Two feedback types were implemented: EMG and force feedback. Each subject received one of the two feedback types, depending on the experimental group to which they were assigned. For the feedback generation, the myoelectric and force signals were divided into five intervals and the feedback conveyed to the subject the discrete level of the signal, i.e., the interval in which the EMG/force lay at any moment (**Figure 2**). The threshold values for the intervals were {0.1, 0.2, 0.4, 0.65, and 0.95}. The thresholds were selected so that levels 1 to 4 were of increasing size to mitigate the larger variability of EMG arising from stronger muscle contractions (Ninu et al., 2014; Dosen et al., 2015b; Schweisfurth et al., 2016; Tchimino et al., 2021).

The feedback encoding scheme is shown in **Figure 2**. When the feedback signal (EMG or force) was in the dead zone (<0.1), no tactors were active. Each subsequent level was indicated by activating the corresponding tactor, while level 5 activated all four tactors simultaneously. Hence, the subject received vibrations that moved from the dorsal aspect of their upper arm to the lateral, volar, and medial aspects and finally all around the upper arm, as the level of the feedback signal increased. Discrete feedback in combination with spatial encoding has been shown to be an easy to understand, effective approach for closed-loop myoelectric control (Witteveen et al., 2012; Schweisfurth et al., 2016; De Nunzio et al., 2017; Markovic et al., 2018a,b; Tchimino et al., 2021).

The control of the Michelangelo hand using EMG and force feedback is illustrated in **Figures 3A,B**, respectively. In the case of EMG feedback, the subject received vibration as soon as they activated their muscles, and the hand started moving (**Figure 3A**). This allowed them to adjust their contraction level

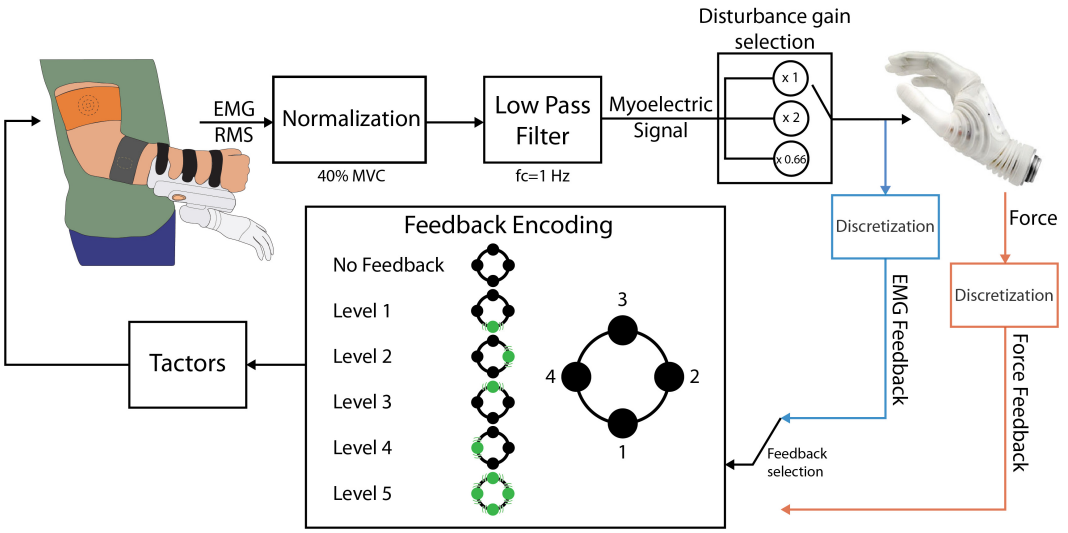

FIGURE 2
The closed-loop prosthesis control scheme. The electrodes outputted the RMS of the EMG, which was low-pass filtered and normalized to 40% of the MVC, resulting in the myoelectric (ME) control signal. The ME signal was sent to the prosthesis as a closing velocity or opening command. If EMG feedback was used, the ME signal was discretized into levels and conveyed back to the subject through the tactors. If force feedback was used, the force was discretized and fed back to the subject using the same encoding. The position and numbering of the tactors in this diagram is consistent with the one shown in **Figure 1**.

while the prosthesis was still in motion. Due to the proportional relation between the myoelectric signal, prosthesis closing velocity and grasping force, the subjects knew that the grasping force level produced by the prosthesis would correspond to the EMG feedback level that they received. Conversely, force feedback was only activated after the prosthesis had closed and applied force onto the object.

Disturbance scheme

The effect of control perturbations in myoelectric systems has been investigated in the past. Examples include the introduction of delays in the feedback delivery (Cipriani et al., 2014), injecting additive noise in the myoelectric signal (Hahne et al., 2017), artificial errors in visual feedback (Johnson et al., 2017), and electrode shift (Prahm et al., 2019). In the present study, the control disturbance was implemented by multiplying the prosthesis control signal by a gain, unbeknownst to the subjects (**Figure 2**, "disturbance gain selection" block) (Cipriani et al., 2014). Similarly to an approach implemented in Earley et al. (2017) and Earley et al. (2021), the gain of the myoelectric signal was doubled or reduced by 33% at the beginning of a disturbed trial. When the gain was doubled (high-gain disturbance), the system became more sensitive with respect to the nominal condition and the same muscle contraction now generated a stronger myoelectric signal. This, in turn, produced a faster closing of the prosthesis and a higher grasping force. Reducing the gain (low-gain disturbance) had the inverse effect, i.e., slower closing and lower force, with a larger contraction required to reach a specific EMG and force level. The subjects were not informed beforehand that any of the trials would be disturbed, as explained in the next section.

Experimental protocol

The subjects were first asked to rest their arm for 10 s while the baseline recording was performed. The mean value of the recorded signal (EMG RMS) was then subtracted from subsequent measurements. Afterward, the MVC was recorded for both flexors and extensors. The subject contracted each muscle maximally in three intervals of 5 s. The mean value of the recorded signal was computed in each interval and the MVC for each muscle was defined as the average of these three values.

Next, the sensation thresholds (ST) for the four C3 tactors were determined. Each tactor was activated in sequence and its gain, which corresponded to the vibration intensity, was slowly increased in steps of 2%. The gain at which the subject reported that they started feeling a vibration was defined as the ST. The gain of each tactor was subsequently set to ST + 0.4 × (MAX-ST), where MAX is the maximum gain (Tchimino et al., 2021). This value was selected as it elicited clear and localized vibrations, which were not intrusive.

The feedback training was then conducted, wherein the five levels of vibrotactile feedback were presented sequentially to the subjects, while the experimenter verbally indicated which tactors were active. A short session of reinforced learning followed,

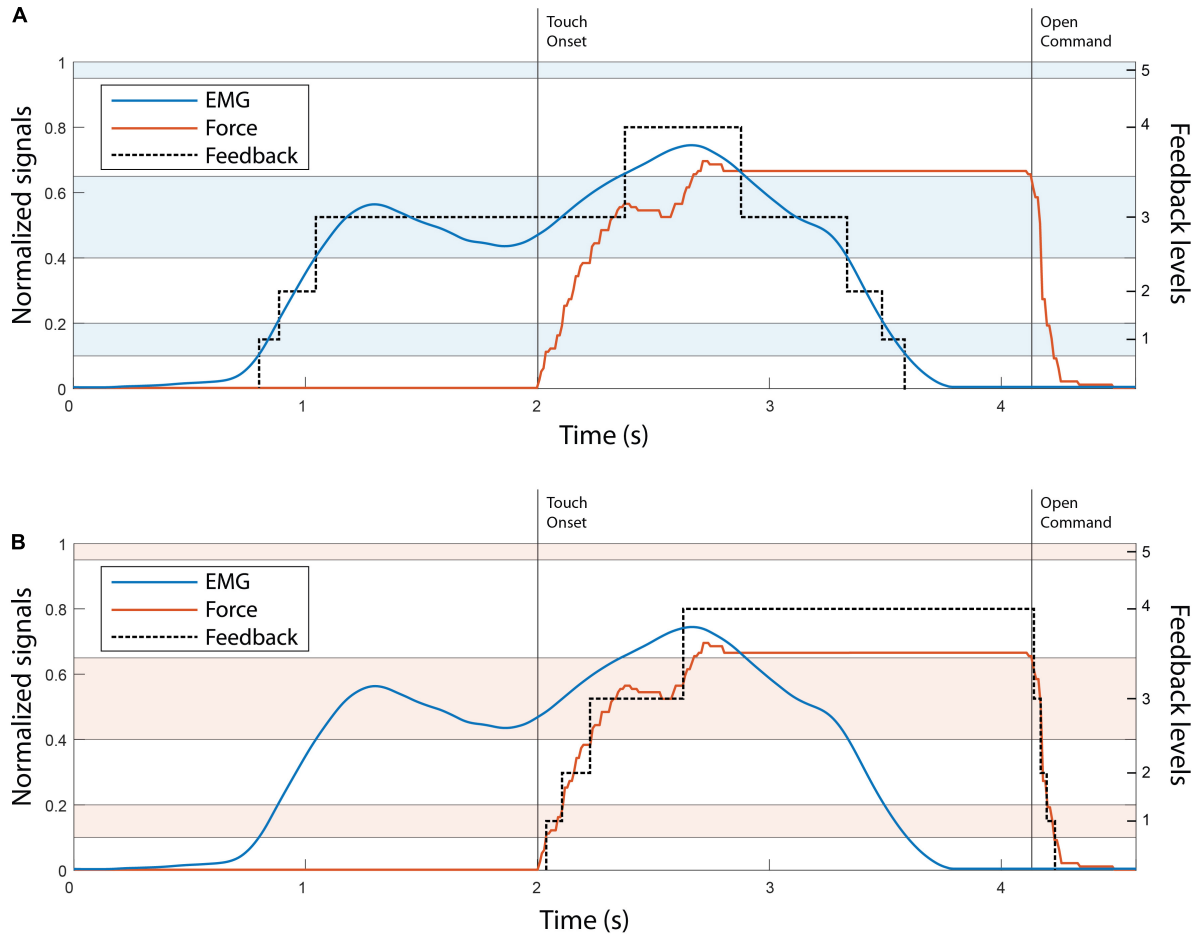

FIGURE 3
The illustration of EMG **(A)** and force **(B)** feedback. The EMG and force traces in both panels A, B are denoted with blue and red, respectively. The black dotted line in both plots indicates the feedback level. The alternating color bands are the EMG and force ranges. The touch onset and the moment that the open command was sent to the hand are denoted with vertical black lines. Note that levels 1–4 are of progressively larger size, to account for the higher EMG variability in stronger contractions.

where the stimulation patterns for levels 1–4 were delivered in a pseudorandom order and the subject was asked to identify each pattern. If the subject reported the wrong pattern, the experimenter provided the correct answer. Each pattern was presented 10 times in total. In the validation phase, the test was repeated, without the experimenter providing verbal feedback. If the identification rate was above 90%, the feedback training was deemed successful and if not, the procedure was repeated. Most subjects achieved a success rate of above 90% immediately after the first run, indicating that the feedback encoding was indeed simple to learn and interpret (Tchimino et al., 2021).

The subjects then performed the main experimental task. They used the prosthesis equipped with the vibrotactile feedback to perform a functional task inspired by the commonly used box and blocks test (Hebert and Lewicke, 2012; Raveh et al., 2018). The task included grasping wooden blocks with the prosthesis and transporting them from one compartment to the other (e.g., from the left to the right compartment). Once ten blocks were moved, the direction was changed (e.g., from the right to the left compartment). However, in this "sensorized" version of the test, the subjects were asked to grasp each block by exerting a specific grasping force level, indicated on the computer screen. The desired force levels were 2 and 4, which denoted delicate and power grasping, respectively. If the generated force level in a specific trial did not correspond to the target level, the subject repeated the trial. The experimenter also clarified that the forces could only be corrected upwards but not downwards (as the prosthesis was non-backdrivable).

When a trial was successful, a high-frequency beeping sound was generated by the computer. A lower-frequency sound indicated that the subject had failed, and the trial had to be repeated. The subjects were allowed a maximum of 10 attempts to successfully complete each trial. If they were successful in a smaller number of attempts or if they were still unsuccessful in

their 10th attempt, they proceeded to the next trial. All subjects managed to complete all the trials within the 10-attempt limit.

The subjects first performed a 100-trial training session (50 trials for each of force levels 2 and 4), to familiarize themselves with the setup and the task. At this stage, they could see their EMG signals on the monitor, as well as their current target force level, generated force, EMG level and remaining number of attempts. Before commencing, the experimenter verbally explained the setup, the prosthesis control and feedback scheme, and the task to be performed. Initially, the subjects were asked to perform the task while seated and with the prosthesis placed on the desk, so that they could focus on familiarizing themselves with the feedback. After approximately 25 successful trials, the prosthesis was mounted onto the subjects' arm and the subjects were asked to stand in front of the desk, facing the box and blocks kit and the monitor. They then performed the experimental task until they reached a total of 100 training trials.

After that, the subjects performed the main experiment, comprising three sets of 100 trials. Each set was performed in batches of 2 min, until a total of 100 trials was completed. There was a pause of approx. 30 s between the batches and a longer break between the sets. During the trials, the subjects could only see their target force, remaining attempts and a timer counting to zero from 120 s on the monitor. They were also instructed to complete as many successful trials as possible within a 2-minute batch. The time constraint was introduced to promote natural and intuitive control, while generating consistent movement profiles (Earley et al., 2017).

The first 100-trial run always included only non-disturbed trials to ensure that the subject was well trained in using the feedback and accomplishing the task in the nominal condition. The second and third runs included 30 disturbed trials (15 in each of the target levels) at a single disturbance gain (random order across the two sets). The order of the trials was pseudorandomized, with a constraint that two consecutive disturbed trials were separated by at least one non-disturbed trial. The sequence of the two disturbance gains was randomized among subjects, to minimize any training effects.

The able-bodied subjects performed the task with one of the feedback types (EMG or force), depending on the group to which they were allocated, while the amputee performed the experiment using both types. The amputee performed the two experimental sessions two days apart, first with force, then with EMG feedback. The experimental sessions lasted between 2 and 2.5 h.

Data analysis

The outcome measures were: (1) the first attempt success rate (SR) defined as the percentage of trials successful in the first attempt, (2) the average number of attempts in the trials that were unsuccessful in the first attempt, and (3) the average completion time of the successful (last) attempt in each trial. The latter was defined as the time from the moment the myoelectric control signal crossed the dead zone until the moment the maximum force was applied. The outcome measures were computed separately for the two types of disturbed trials (high- and low-gain disturbance), as well as for the non-disturbed trials.

The SR was deemed the most important measure, since an erroneous force potentially results in slippage or breakage of an object. In disturbed trials, this metric can be regarded as a measure of the subjects' *reaction* to the disturbance, i.e., their ability to compensate the disturbance as soon as it appears (in the first attempt).

The average number of attempts in trials that were unsuccessful in the first attempt is an indication of how effectively the feedback assisted the subjects in adjusting their control input (muscle contraction) across attempts. In disturbed trials, therefore, this can be regarded as a measure of *adaptation* to the control disturbance.

The metrics used in the analysis were computed for each subject and each gain using 30 disturbed trials at that gain. The baseline metrics were also computed, using 100 initial, non-disturbed trials. The results of the amputee subject were interpreted independently and were not considered in the statistical analysis.

Outliers were defined as values above or below 1.5 times the upper and lower quartiles, respectively. The data was tested for normality using the Lilliefors test. The outcome measures were compared between the two feedback types, using an unpaired t-test or a Mann-Whitney test, depending on the outcome of the normality test. The statistical toolbox of MathWorks MATLAB 2021a and IBM SPSS 27 were used for the statistical analysis. The results are reported in the text as "median {interquartile range}" and the threshold for significance was set at $p < 0.05$.

Results

Figure 4 displays the EMG and force traces in normal and disturbed trials with EMG and force feedback. In normal trials (plots A and D), the subjects produced an appropriate muscle contraction (level 2), which generated the desired force (also level 2) once the prosthesis closed around the object, accomplishing the task in a single attempt.

In the high-gain disturbed trials with force feedback (plot E, delicate grasping and plot F, power grasping), the subjects needed multiple attempts to adapt to the disturbance and complete the trial. With respect to the nominal case, the high gain increased the amplitude of the myoelectric signal generated in response to the same muscle contraction. Therefore, the myoelectric signals (gray lines) generated by the subjects were initially too high, in fact saturated, for both delicate (plot E) and power grasping (plot F). Consequently, the generated force

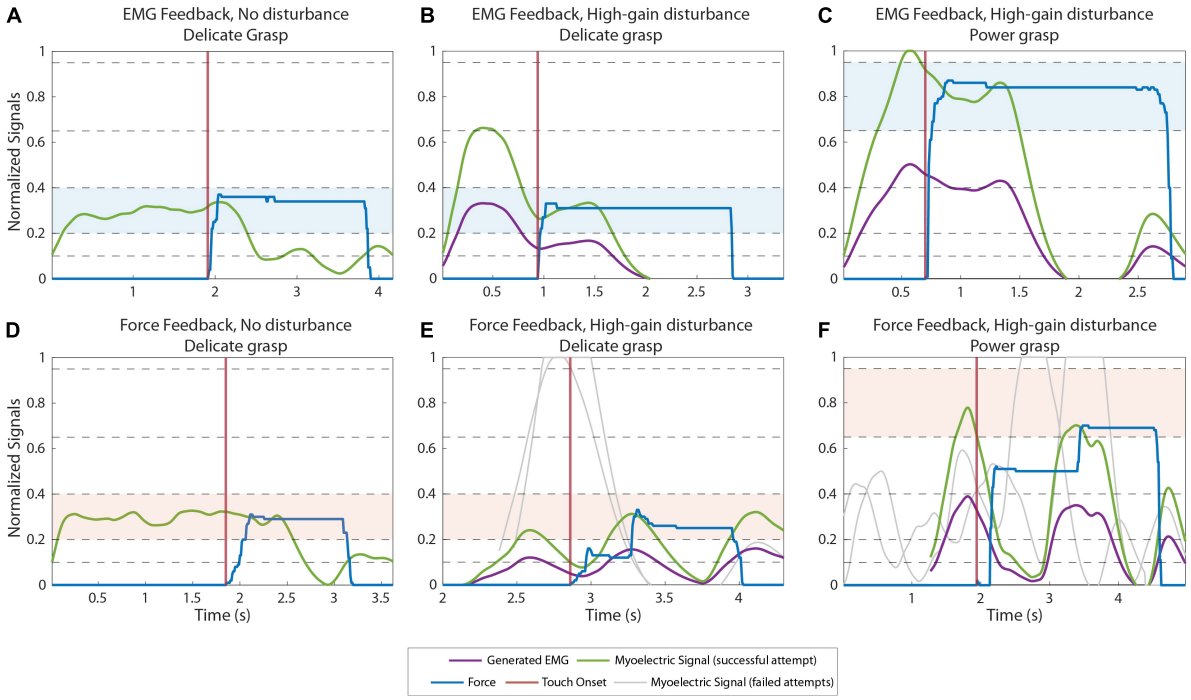

FIGURE 4
Example myoelectric (ME) and force traces recorded during normal **(A,D)** and high-gain disturbed **(B,C,E,F)** trials when using EMG feedback **(A–C)** and force feedback **(D–F)**. The green and blue lines correspond to the ME signal and the force applied in the last (successful) attempt in a trial, respectively. The purple lines are the ME signals produced by the subjects before the signal is multiplied by the disturbance gain. The gray lines are the ME signals generated in previous attempts of the same trial. The ME signals of all attempts are aligned on their respective contact points (when the prosthesis contacts the object), denoted by the vertical red lines. The target levels in each trial are highlighted with blue **(A–C)** and red **(D–F)** colored bands.

overshot the target (object "broken"). In subsequent attempts, the subjects gradually reduced their contraction levels, finally generating the appropriate contraction (green line), to reach the target force in the third attempt.

Conversely, with EMG feedback (Figures 4B,C) the subjects received online information about the generated control signal. Therefore, they immediately compensated for the overshoots caused by the high-gain disturbance by decreasing the muscle contraction with respect to that used in the nominal trials. Hence, they performed the task successfully already in the first attempt.

Figures 5A,B illustrate the power grasping trials with a low gain disturbance using EMG and force feedback respectively. In both cases, the subjects were successful in the first attempt. With reduced gain, the prosthesis closes more slowly for a given muscle contraction, creating a smaller grasp force. When using force feedback, therefore, the subjects initially undershot the force. After the hand made contact with the object, the subject received the feedback, realized that the force was too low and increased the muscle contraction until the desired force was achieved, resulting in a prolonged task duration (completion time of 3.85 s). With EMG feedback, on the contrary, the subject reacted similarly as in the high-gain case. They could immediately "feel" (via feedback) that the nominal contraction was not enough and then increased their contraction to level 4, effectively compensating for the decrease in gain. The task was, therefore, accomplished without force corrections and, hence, in a shorter time (completion time of 1.68 s).

Regarding the results in non-disturbed trials, EMG feedback outperformed force feedback slightly but significantly in terms of SR in power grasping (median {IQR} of 76% {10} against 71% {2.6}, p = 0.035) and number of attempts in delicate grasping (2.16 attempts {0.25} against 2.5 attempts {0.13}, p = 1.9e-6). However, force feedback resulted in significantly shorter completion time in delicate grasping (1.95 s {0.44} for force, against 2.37 s {0.46} for EMG feedback, p = 0.04). In all other cases, the difference in performance between the two feedback types was not significant.

The summary results for the SR in disturbed trials are displayed in Figure 6. The performance for EMG and force feedback were similarly high in both delicate and power grasping when a low-gain disturbance was introduced in the control signal. In the case of high-gain disturbance, however, the subjects performed significantly better (p = 0.044) in power grasping with EMG feedback (73.3% {26.7}) than with force

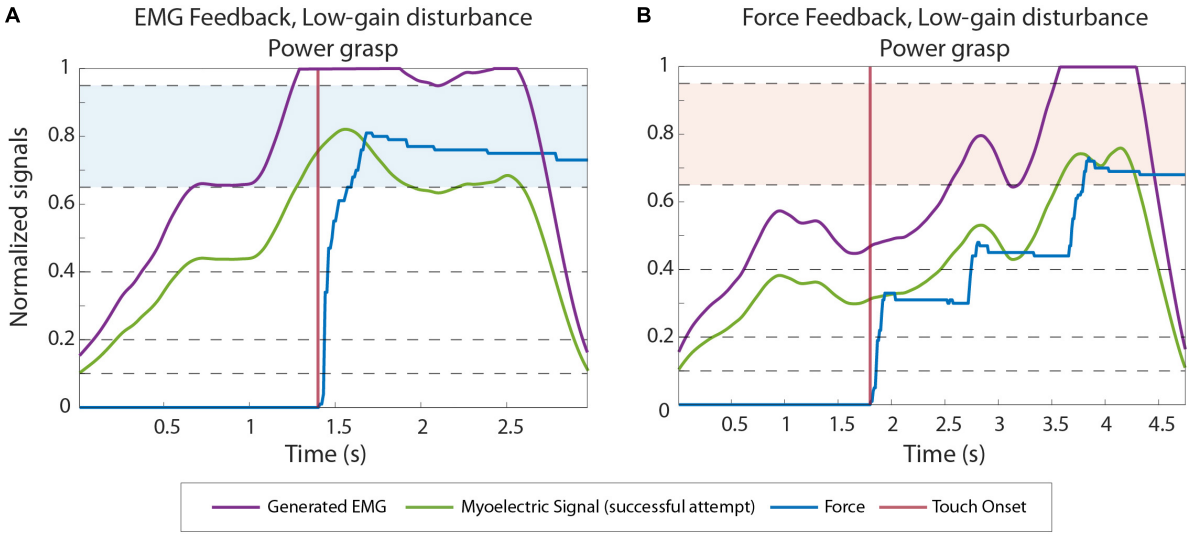

FIGURE 5
Example EMG and force traces recorded during low gain disturbed trials from subjects using EMG **(A)** and force feedback **(B)**. The green and blue lines correspond to the myoelectric (ME) signal and the force applied in the last (successful) attempt in a trial, respectively. The purple lines are the ME signals produced by the subjects before the signal is multiplied by the disturbance gain. The contact points (when the prosthesis contacts the object) are denoted by the vertical red lines. The target levels in each trial are highlighted with blue and red colored bands.

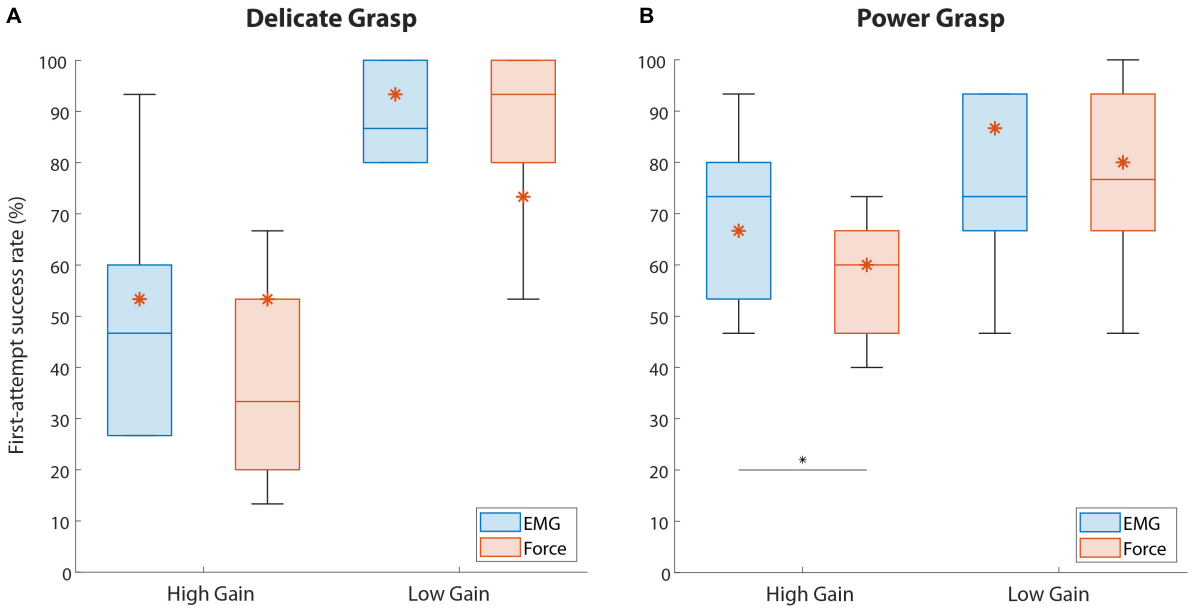

FIGURE 6
The percentage of trials successful in the first attempt (first-attempt SR), for both force targets. Boxplots **(A,B)** correspond to delicate and power grasps, respectively. The blue and red boxplots represent the summary performance with EMG and force feedback, respectively. The orange asterisks denote the performance of the amputee subject. The boxplots indicate the median (horizontal line), interquartile range (boxes), min/max values (whiskers), and outliers (circles). Statistically significant pairs are marked with horizontal bars (*$p < 0.05$). "High Gain" and "Low Gain" denote the disturbance conditions.

feedback (60% {20}). In delicate grasping, the median percentage for force feedback (33.3%) was also lower compared to EMG feedback (46.6%) but the difference was not significant.

The median number of repeated attempts ranged between 2 and 3 in all disturbed conditions, with no significant difference between the feedback types.

The results regarding the completion time of the last attempt in disturbed trials are shown in Figure 7. The completion time in delicate grasping was similar across all conditions (Figure 7A), with a median ranging between 1.9 and 2.5 s. In power grasping (Figure 7B), the results were similar for the two feedback types in the case of high-gain disturbance. However, in the low-gain disturbed trials the subjects using force feedback (3.64 s {0.73}) needed a significantly ($p = 0.046$) longer time to reach the target compared to those who used EMG feedback (2.48 s {1.66}).

The results regarding the amputee subject are denoted with asterisks in Figures 6, 7. Regarding the SR (Figure 6), the subject performed better with EMG feedback in three out of four conditions, with the largest difference in performance for delicate grasping and low-gain disturbance (93.3 against 73.3%). The SR for power grasping and high-gain disturbance was higher when EMG feedback was used (66.6 against 60%, Figure 6B) and the subject performed markedly faster in low-gain disturbed power grasp trials with EMG feedback (3.14 against 5.4 s, Figure 7B).

Discussion

This study compared the performance of prosthesis grasping in a force-matching task with EMG and force feedback when the prosthesis control signal was disturbed. The disturbed trials, which appeared unbeknownst to the subjects and were interspersed with normal trials, were characterized by a gain that amplified or attenuated the control signal, thereby substantially altering the response of the prosthesis to the subjects' muscle activity. Overall, the results imply the advantage of EMG over force feedback, albeit in fewer conditions than initially hypothesized.

We assumed that the prolonged training would allow the subjects to develop internal models for the control of the prosthesis and establish the mapping between the desired grasping force and the contraction required to achieve that force (Dosen et al., 2015c; Shehata et al., 2018). However, the internal models acquired during the training would not be valid for the disturbed trials. Since the force feedback only becomes available after the hand has grasped the object and produced force, the altered system dynamics would not be immediately obvious to the subjects and, consequently, the execution of the task would be compromised. Therefore, our assumption was that the subjects using force feedback would achieve lower performance in the disturbed trials, compared to those using EMG feedback. Specifically, the high gain disturbance was expected to lead to overshooting of the target force in the first trial and longer adaptation, while the low gain disturbance would prolong the completion time of the task in disturbed trials with force feedback.

Indeed, EMG feedback enabled the subjects to better react to the high-gain disturbance and achieve higher success in the first attempt. The ability to generate the correct force level despite the disturbance reduces the likelihood of accidents, such as slippage or breakage. However, the performance was significantly better only in the case of power grasping (Figure 6B). The slightly better baseline (non-disturbed) performance of EMG feedback in power grasping became, therefore, even more expressed in the presence of high-gain disturbances. Surprisingly, the subjects could not exploit the EMG feedback as effectively during delicate grasping, where we, in fact, expected the largest advantage. This is likely due to a combination of factors, including the narrower EMG range corresponding to level 2 (compared to level 4), high level of disturbance (doubled gain) and a limited amount of time available (until object contact) to correct the EMG based on the online feedback. And indeed, the subjects reported that they often became aware of the overshoot, but the hand had already closed around the block and applied a higher-than-desired force, at which point the subjects had to repeat the task.

In the case of low-gain disturbance, the two feedback types achieved similar SR for both grasp types. This can be attributed to the smoother myoelectric signal due to lower sensitivity and higher stability of the system resulting from the reduced gain. However, and following our initial assumption, the subjects indeed required a significantly longer time to complete a power grasp with force feedback than with EMG feedback (Figure 7B). Presumably, the subjects initially attempted to generate a contraction that they believed will be close to the target, based on their training. EMG feedback then allowed the subjects to immediately react to a lower myoelectric signal level and modulate upwards, even before the prosthesis contacted the object, thus increasing the prosthesis closing speed. On the other hand, when using force feedback, the subjects had to wait until the force was applied on the object to realize that their contraction was too low, at which point they used the feedback to gradually increase the force step by step, through the levels. Although slow, this strategy still allowed for good force control and disturbance compensation already in the first attempt (hence similar success rates as EMG feedback).

The similarity in the numbers of repeated attempts when using either feedback type in both grasp types was another surprising result. As mentioned before, force feedback was expected to underperform compared to EMG feedback, with the subjects adapting to the disturbances over a larger number of attempts per trial. There was, however, no significant difference in the performance of the two feedback types in disturbed trials. Given that the subjects needed only 1-2 additional attempts to adapt to the disturbance, the adaptation appeared not to have been difficult overall. This point, in combination with intrinsic feedback from the prosthesis, might be the reason for the lack of difference between the feedback types. Namely, even though the subjects did not have explicit information about the change in the control signal gain with force feedback (unlike with EMG feedback), they could estimate this indirectly, for instance, by observing the prosthesis motion (e.g., the prosthesis responding

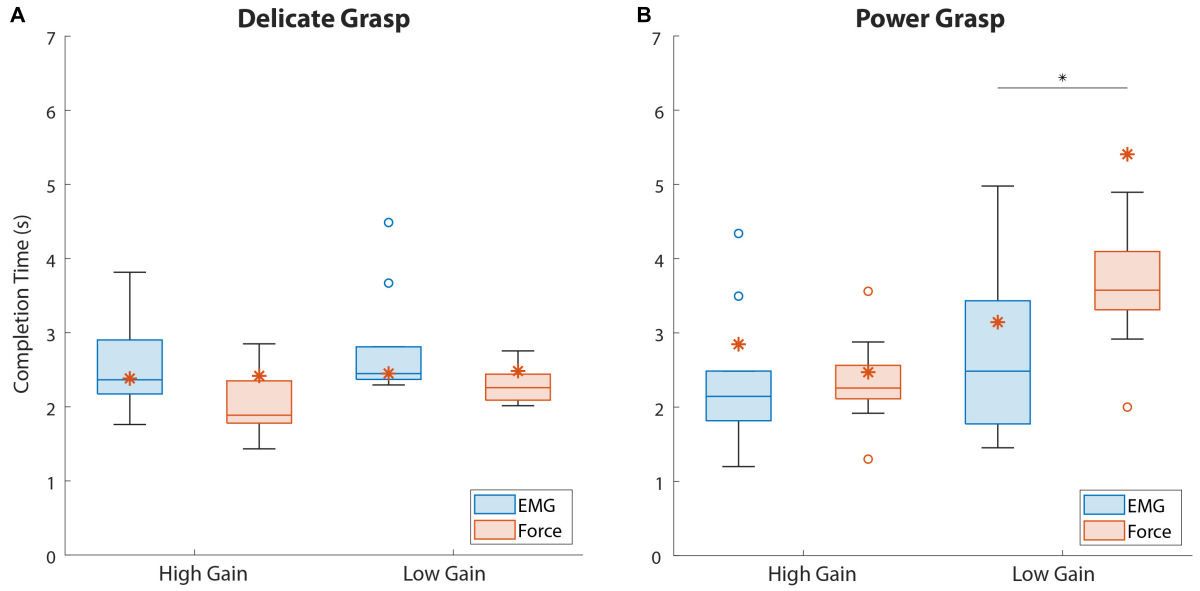

FIGURE 7
The last attempt completion time for both force targets. Boxplots **(A,B)** correspond to delicate and power grasps, respectively. The blue and red boxplots represent the summary performance with EMG and force feedback, respectively. The orange asterisks denote the performance of the amputee subject. The boxplots indicate the median (horizontal line), interquartile range (boxes), min/max values (whiskers), and outliers (circles). Statistically significant pairs are marked with horizontal bars (*$p < 0.05$). "High Gain" and "Low Gain" denote the disturbance conditions.

slower/faster than normal). Such incidental information might have been enough to drive the adaptation across repeated attempts. The use of incidental cues in prosthesis control has been reported in the past (Mann and Reimers, 1970; Prior et al., 1976) and investigated in more recent studies (Markovic et al., 2018b; Wilke et al., 2019; Gonzalez et al., 2021). These studies indeed showed that the subjects could accurately estimate the prosthesis closing velocity from visual observation of prosthesis motion (Wilke et al., 2019) and use this information together with natural muscle proprioception to control the grasping force (Markovic et al., 2018b).

Importantly, not only did the performance of the amputee subject follow the trends defined by the able-bodied subjects, but the EMG feedback seems to have been particularly beneficial in the case of the amputee. This is a promising result for the prospective clinical application of this approach. Moreover, the placement of the tactors on the upper arm did not have an impact on the quality of the feedback, since it remained intuitive and easily interpretable.

The gain disturbances used in the present study intend to simulate the changes in the amplitude of EMG signal that can arise during clinical applications (e.g., electrode shift or sweating) (Hahne et al., 2017; Yang et al., 2019). These factors can lead to either decreases or increases in the myoelectric signal amplitude (e.g., an electrode moving away from or closer to the signal source), and this corresponds to low and high gain disturbances of the present experiment, respectively. Nevertheless, the aim of this study was not to exhaustively investigate different types of signal changes but to demonstrate a fundamental insight, i.e., that different feedback types enable different disturbance compensation strategies. Other types of signal artifacts (e.g., transient changes), as well as disturbances during real-life uses, remain to be tested.

With EMG feedback, the subjects are likely to receive stimulation for a longer time (before and after contact) compared to force feedback (after contact only). However, the potential desensitization of the subjects due to prolonged constant stimulation was not assessed in the present study. Nevertheless, habituation is most pronounced when a prolonged stimulation is delivered to the same area on the skin (Buma et al., 2007). Considering that the EMG feedback is characterized by dynamic stimulation profiles (shift of active tactors) as well as the fact that the subjects can relax their muscles (no stimulation) after an object has been grasped (non-backdrivable prosthesis), we assume that desensitization will not be a serious limitation, even after prolonged use of a prosthesis equipped with EMG feedback. Indeed, none of the subjects reported difficulty in perceiving the feedback in the present experiment, despite the completion of many trials. Future studies could also be devoted to the systematic assessment of the subjective experience when using different feedback types.

Although the present study assessed the short-term adaptation to disturbance across successive trials, the potential learning over a longer time scale was not investigated. Nevertheless, it would be interesting to assess the evolution of disturbance compensation strategies as the user becomes

increasingly familiar with closed-loop myoelectric control. Such assessment could elucidate if and how the type of feedback affects the learning over extended use.

The present study explored how the performance in a functional task with a myoelectric hand prosthesis integrated with EMG and force feedback differed in terms of response to disturbances in the prosthesis control signal. Overall, the results of this study indicate that, when a disturbance gain is introduced, the two feedback types perform similarly during the execution of delicate grasping, but EMG feedback provides a significant advantage in power grasps. A control scheme that displays better performance in the presence of a disturbed control signal is an important step toward a more reliable prosthesis-user interface.

Data availability statement

The raw data supporting the conclusions of this article will be made available by the authors, without undue reservation.

Ethics statement

The studies involving human participants were reviewed and approved by the Research Ethics Committee of the Nordjylland Region (approval number: N-20190036). The patients/participants provided their written informed consent to participate in this study.

Author contributions

JT executed the data collection and analysis. All authors conceptualized the study, wrote the manuscript, and approved it for publication.

Funding

This work was supported by the projects 8022- 00243A (ROBIN) and 8022-00226B funded by the Independent Research Fund Denmark.

Conflict of interest

The authors declare that the research was conducted in the absence of any commercial or financial relationships that could be construed as a potential conflict of interest.

Publisher's note

All claims expressed in this article are solely those of the authors and do not necessarily represent those of their affiliated organizations, or those of the publisher, the editors and the reviewers. Any product that may be evaluated in this article, or claim that may be made by its manufacturer, is not guaranteed or endorsed by the publisher.

References

Abd, M. A., Ingicco, J., Hutchinson, D. T., Tognoli, E., and Engeberg, E. D. (2022). Multichannel haptic feedback unlocks prosthetic hand dexterity. *Sci. Rep.* 12:2323. doi: 10.1038/s41598-022-04953-1

Antfolk, C., D'Alonzo, M., Rosén, B., Lundborg, G., Sebelius, F., and Cipriani, C. (2013). Sensory feedback in upper limb prosthetics. *Expert Rev. Med. Devices* 10, 45–54. doi: 10.1586/erd.12.68

Bensmaia, S. J., Tyler, D. J., and Micera, S. (2020). Restoration of sensory information via bionic hands. *Nat. Biomed. Eng* [Preprint]. doi: 10.1038/s41551-020-00630-8

Brown, J. D., Paek, A., Syed, M., O'Malley, M. K., Shewokis, P. A., Contreras-Vidal, J. L., et al. (2015). An exploration of grip force regulation with a low-impedance myoelectric prosthesis featuring referred haptic feedback. *J. Neuroeng. Rehabil.* 12:104. doi: 10.1186/s12984-015-0098-1

Buma, D. G., Buitenweg, J. R., and Veltink, P. H. (2007). Intermittent Stimulation Delays Adaptation to Electrocutaneous Sensory Feedback. *IEEE Trans. Neural Syst. Rehabil. Eng.* 15, 435–441. doi: 10.1109/TNSRE.2007.903942

Cipriani, C., Segil, J. L., Clemente, F., Richard, R. F., and Edin, B. (2014). Humans can integrate feedback of discrete events in their sensorimotor control of a robotic hand. *Exp. Brain Res.* 232, 3421–3429. doi: 10.1007/s00221-014-4024-8

De Nunzio, A. M., Dosen, S., Lemling, S., Markovic, M., Schweisfurth, M. A., Ge, N., et al. (2017). Tactile feedback is an effective instrument for the training of grasping with a prosthesis at low- and medium-force levels. *Exp. Brain Res.* 235, 2547–2559. doi: 10.1007/s00221-017-4991-7

Dosen, S., Markovic, M., Somer, K., Graimann, B., and Farina, D. (2015b). EMG Biofeedback for online predictive control of grasping force in a myoelectric prosthesis. *J. Neuroeng. Rehabil.* 12:55. doi: 10.1186/s12984-015-0047-z

Dosen, S., Markovic, M., Hartmann, C., and Farina, D. (2015a). Sensory feedback in prosthetics: A standardized test bench for closed-loop control. *IEEE Trans. Neural Syst. Rehabil. Eng.* 23, 267–276. doi: 10.1109/TNSRE.2014.2371238

Dosen, S., Markovic, M., Wille, N., Henkel, M., Koppe, M., Ninu, A., et al. (2015c). Building an internal model of a myoelectric prosthesis via closed-loop control for consistent and routine grasping. *Exp. Brain Res.* 233, 1855–1865. doi: 10.1007/s00221-015-4257-1

Earley, E. J., Johnson, R. E., Sensinger, J. W., and Hargrove, L. J. (2021). Joint speed feedback improves myoelectric prosthesis adaptation after perturbed reaches in non amputees. *Sci. Rep.* 11:5158. doi: 10.1038/s41598-021-84795-5

Earley, E. J., Kaveny, K. J., Johnson, R. E., Hargrove, L. J., and Sensinger, J. W. (2017). Joint-based velocity feedback to virtual limb dynamic perturbations. *IEEE Int. Conf. Rehabil. Robot* 2017, 1313–1318. doi: 10.1109/ICORR.2017.8009430

Engels, L. F., Shehata, A. W., Scheme, E. J., Sensinger, J. W., and Cipriani, C. (2019). When less is more-discrete tactile feedback dominates continuous audio biofeedback in the integrated percept while controlling a myoelectric prosthetic hand. *Front. Neurosci.* 13:578. doi: 10.3389/fnins.2019.00578

Esquenazi, A. (2002). "Pain management post amputation," in *Pain Management in Rehabilitation*, eds T. N. Monga and M. Grabois (New York, NY: Demos Medical Publishing), 191–202.

Fu, Q., and Santello, M. (2018). Improving fine control of grasping force during hand-object interactions for a soft synergy-inspired myoelectric prosthetic hand. *Front. Neurorobot.* 11:17. doi: 10.3389/fnbot.2017.00071

Fu, Q., Shao, F., and Santello, M. (2019). Inter-limb transfer of grasp force perception with closed-loop hand prosthesis. *IEEE Trans. Neural Syst. Rehabil. Eng.* 27, 927–936. doi: 10.1109/TNSRE.2019.2911893

Gilman, S. (2002). Joint position sense and vibration sense: Anatomical organisation and assessment. *J. Neurol. Neurosurg. Psychiatry* 73, 473–477. doi: 10.1136/jnnp.73.5.473

Gonzalez, M. A., Lee, C., Kang, J., Gillespie, R. B., and Gates, D. H. (2021). Getting a Grip on the Impact of Incidental Feedback From Body-Powered and Myoelectric Prostheses. *IEEE Trans. Neural Syst. Rehabil. Eng.* 29, 1905–1912. doi: 10.1109/TNSRE.2021.3111741

Hahne, J. M., Markovic, M., and Farina, D. (2017). User adaptation in Myoelectric Man-Machine Interfaces. *Sci. Rep.* 7:4437. doi: 10.1038/s41598-017-04255-x

Hebert, J. S., and Lewicke, J. (2012). Case report of modified Box and Blocks test with motion capture to measure prosthetic function. *J. Rehabil. Res. Dev.* 49:1163. doi: 10.1682/JRRD.2011.10.0207

Isakovic, M., Malešević, J., Keller, T., Kostić, M., and Štrbac, M. (2019). Optimization of Semiautomated Calibration Algorithm of Multichannel Electrotactile Feedback for Myoelectric Hand Prosthesis. *Appl. Bionics Biomech.* 2019:9298758. doi: 10.1155/2019/9298758

Jabban, L., Dupan, S., Zhang, D., Ainsworth, B., Nazarpour, K., and Metcalfe, B. W. (2022). Sensory Feedback for Upper-Limb Prostheses: Opportunities and Barriers. *IEEE Trans. Neural Syst. Rehabil. Eng.* 30, 738–747. doi: 10.1109/TNSRE.2022.3159186

Johnson, R. E., Kording, K. P., Hargrove, L. J., and Sensinger, J. W. (2017). Adaptation to random and systematic errors: Comparison of amputee and non-amputee control interfaces with varying levels of process noise. *PLoS One* 12:e0170473. doi: 10.1371/journal.pone.0170473

Kristjansdottir, F., Dahlin, L. B., Rosberg, H.-E., and Carlsson, I. K. (2020). Social participation in persons with upper limb amputation receiving an esthetic prosthesis. *J. Hand Ther.* 33, 520–527. doi: 10.1016/j.jht.2019.03.010

Mann, R., and Reimers, S. (1970). Kinesthetic Sensing for the EMG Controlled "Boston Arm.". *IEEE Trans. Man Mach. Syst.* 11, 110–115. doi: 10.1109/TMMS.1970.299971

Marasco, P. D., Hebert, J. S., Sensinger, J. W., Beckler, D. T., Thumser, Z. C., Shehata, A. W., et al. (2021). Neurorobotic fusion of prosthetic touch, kinesthesia, and movement in bionic upper limbs promotes intrinsic brain behaviors. *Sci. Robot* 6:eabf3368. doi: 10.1126/scirobotics.abf3368

Markovic, M., Schweisfurth, M. A., Engels, L. F., Bentz, T., Wüstefeld, D., Farina, D., et al. (2018a). The clinical relevance of advanced artificial feedback in the control of a multi-functional myoelectric prosthesis. *J. Neuroeng. Rehabil.* 15:28. doi: 10.1186/s12984-018-0371-1

Markovic, M., Schweisfurth, M. A., Engels, L. F., Farina, D., and Dosen, S. (2018b). Myocontrol is closed-loop control: Incidental feedback is sufficient for scaling the prosthesis force in routine grasping. *J. Neuroeng. Rehabil.* 15:81. doi: 10.1186/s12984-018-0422-7

Ninu, A., Dosen, S., Muceli, S., Rattay, F., Dietl, H., and Farina, D. (2014). Closed-Loop Control of Grasping With a Myoelectric Hand Prosthesis: Which Are the Relevant Feedback Variables for Force Control? *IEEE Trans. Neural Syst. Rehabil. Eng.* 22, 1041–1052. doi: 10.1109/TNSRE.2014.2318431

Pasluosta, C., Kiele, P., and Stieglitz, T. (2018). Paradigms for restoration of somatosensory feedback via stimulation of the peripheral nervous system. *Clin. Neurophysiol.* 129, 851–862. doi: 10.1016/j.clinph.2017.12.027

Peerdeman, B., Boere, D., Witteveen, H., Huis in 'tVeld, R., Hermens, H., Stramigioli, S., et al. (2011). Myoelectric forearm prostheses: State of the art from a user-centered perspective. *J. Rehabil. Res. Dev* 48:719. doi: 10.1682/JRRD.2010.08.0161

Pomares, G., Coudane, H., Dap, F., and Dautel, G. (2020). Psychological effects of traumatic upper-limb amputations. *Orthop. Traumatol. Surg. Res.* 106, 297–300. doi: 10.1016/j.otsr.2019.12.013

Prahm, C., Schulz, A., Paaben, B., Schoisswohl, J., Kaniusas, E., Dorffner, G., et al. (2019). Counteracting Electrode Shifts in Upper-Limb Prosthesis Control via Transfer Learning. *IEEE Trans. Neural Syst. Rehabil. Eng.* 27, 956–962. doi: 10.1109/TNSRE.2019.2907200

Prior, R. E., Lyman, J., Case, P. A., and Scott, C. M. (1976). Supplemental sensory feedback for the VA/NU myoelectric hand. Background and preliminary designs. *Bull. Prosthet. Res.* 10, 170–191.

Raveh, E., Portnoy, S., and Friedman, J. (2018). Adding vibrotactile feedback to a myoelectric-controlled hand improves performance when online visual feedback is disturbed. *Hum. Mov. Sci.* 58, 32–40. doi: 10.1016/j.humov.2018.01.008

Roche, A. D., Rehbaum, H., Farina, D., and Aszmann, O. C. (2014). Prosthetic Myoelectric Control Strategies: A Clinical Perspective. *Curr. Surg. Rep.* 2:44. doi: 10.1007/s40137-013-0044-8

Salminger, S., Stino, H., Pichler, L. H., Gstoettner, C., Sturma, A., Mayer, J. A., et al. (2020). Current rates of prosthetic usage in upper-limb amputees – have innovations had an impact on device acceptance? *Disabil. Rehabil.* 44, 3708–3713. doi: 10.1080/09638288.2020.1866684

Schweisfurth, M. A., Markovic, M., Dosen, S., Teich, F., Graimann, B., and Farina, D. (2016). Electrotactile EMG feedback improves the control of prosthesis grasping force. *J. Neural Eng* 13:056010. doi: 10.1088/1741-2560/13/5/056010

Shahsavari, H., Matourypour, P., Ghiyasvandian, S., Ghorbani, A., Bakhshi, F., Mahmoudi, M., et al. (2020). Upper limb amputation; Care needs for reintegration to life: An integrative review. *Int. J. Orthop. Trauma Nurs.* 38:100773. doi: 10.1016/j.ijotn.2020.100773

Shehata, A. W., Engels, L. F., Controzzi, M., Cipriani, C., Scheme, E. J., and Sensinger, J. W. (2018). Improving internal model strength and performance of prosthetic hands using augmented feedback. *J. Neuroeng. Rehabil.* 15:70. doi: 10.1186/s12984-018-0417-4

Tchimino, J., Markovic, M., Dideriksen, J. L., and Dosen, S. (2021). The effect of calibration parameters on the control of a myoelectric hand prosthesis using EMG feedback. *J. Neural Eng* 18:046091. doi: 10.1088/1741-2552/ac07be

Thomas, N., Ung, G., McGarvey, C., and Brown, J. D. (2019). Comparison of vibrotactile and joint-torque feedback in a myoelectric upper-limb prosthesis. *J. Neuroeng. Rehabil.* 16:70. doi: 10.1186/s12984-019-0545-5

Vargas, L., Huang, H., Zhu, Y., and Hu, X. (2022). Evoked Tactile Feedback and Control Scheme on Functional Utility of Prosthetic Hand. *IEEE Robot. Autom. Lett.* 7, 1308–1315. doi: 10.1109/LRA.2021.3139147

Wilke, M. A., Niethammer, C., Meyer, B., Farina, D., and Dosen, S. (2019). Psychometric characterization of incidental feedback sources during grasping with a hand prosthesis. *J. Neuroeng. Rehabil.* 16:155. doi: 10.1186/s12984-019-0622-9

Witteveen, H. J. B., Droog, E. A., Rietman, J. S., and Veltink, P. H. (2012). Vibro- and electrotactile user feedback on hand opening for myoelectric forearm prostheses. *IEEE Trans. Biomed. Eng.* 59, 2219–2226. doi: 10.1109/TBME.2012.2200678

Yang, D., Gu, Y., Thakor, N. V., and Liu, H. (2019). Improving the functionality, robustness, and adaptability of myoelectric control for dexterous motion restoration. *Exp. Brain Res.* 237, 291–311. doi: 10.1007/s00221-018-5441-x

frontiers | Frontiers in Neuroscience

TYPE Clinical Trial
PUBLISHED 26 October 2022
DOI 10.3389/fnins.2022.1019880

OPEN ACCESS

EDITED BY
Yang Zheng,
Xi'an Jiaotong University, China

REVIEWED BY
Min Li,
Xi'an Jiaotong University, China
Luis Vargas,
ARCCA, Inc., United States

*CORRESPONDENCE
Rafael Morand
rafael.morand@bfh.ch

SPECIALTY SECTION
This article was submitted to Neuroprosthetics, a section of the journal Frontiers in Neuroscience

RECEIVED 15 August 2022
ACCEPTED 28 September 2022
PUBLISHED 26 October 2022

CITATION
Morand R, Brusa T, Schnüriger N, Catanzaro S, Berli M and Koch VM (2022) FeetBack–Redirecting touch sensation from a prosthetic hand to the human foot.
Front. Neurosci. 16:1019880.
doi: 10.3389/fnins.2022.1019880

FeetBack–Redirecting touch sensation from a prosthetic hand to the human foot

Rafael Morand [1]*, Tobia Brusa[1], Nina Schnüriger[2], Sabrina Catanzaro[2], Martin Berli[2] and Volker M. Koch[1]

[1]Biomedical Engineering Lab, Institute for Human Centered Engineering, Bern University of Applied Sciences, Bern, Switzerland, [2]Division of Prosthetics and Orthotics, Department of Orthopedics, Balgrist University Hospital, Zurich, Switzerland

Introduction: Adding sensory feedback to myoelectric prosthetic hands was shown to enhance the user experience in terms of controllability and device embodiment. Often this is realized non-invasively by adding devices, such as actuators or electrodes, within the prosthetic shaft to deliver the desired feedback. However, adding a feedback system in the socket adds more weight, steals valuable space, and may interfere with myoelectric signals. To circumvent said drawbacks we tested for the first time if force feedback from a prosthetic hand could be redirected to another similarly sensitive part of the body: the foot.

Methods: We developed a vibrotactile insole that vibrates depending on the sensed force on the prosthetic fingers. This self-controlled clinical pilot trial included four experienced users of myoelectric prostheses. The participants solved two types of tasks with the artificial hands: 1) sorting objects depending on their plasticity with the feedback insole but without audio-visual feedback, and 2) manipulating fragile, heavy, and delicate objects with and without the feedback insole. The sorting task was evaluated with Goodman-Kruskal's gamma for ranked correlation. The manipulation tasks were assessed by the success rate.

Results: The results from the sorting task with vibrotactile feedback showed a substantial positive effect. The success rates for manipulation tasks with fragile and heavy objects were high under both conditions (feedback on or off, respectively). The manipulation task with delicate objects revealed inferior success with feedback in three of four participants.

Conclusion: We introduced a novel approach to touch sensation in myoelectric prostheses. The results for the sorting task and the manipulation tasks diverged. This is likely linked to the availability of various feedback sources. Our results for redirected feedback to the feet fall in line with previous similar studies that applied feedback to the residual arm.

Clinical trial registration: Name: Sensor Glove and Non-Invasive Vibrotactile Feedback Insole to Improve Hand Prostheses Functions and Embodiment (FeetBack). Date of registration: 23 April 2019. Date the first participant was enrolled: 3 September 2021. ClinicalTrials.gov Identifier: NCT03924310.

KEYWORDS

upper limb prosthesis, sensory feedback, touch sensation, grip force, vibrotactile insole, discrete feedback

1. Introduction

The human hand allows us to explore the environment by touch sensation such that we feel the temperature, texture, and applied force. Myoelectric control for prosthetic hands advanced in terms of dexterity and allows for complex grip patterns. However, there is no commercially available system with sophisticated touch sensation[1]. There are only a few commercially available hands that provide information about initial contact and object release. Even less devices provide information about the grip force *via* vibrations within the socket of the prosthesis. Yet, adding touch sensation to prosthetic hands has been an ongoing topic in research in the past decades (Antfolk et al., 2013; Sensinger and Dosen, 2020). The motivation behind adding touch sensation lies in improving the system control and strengthening the user's feeling of agency and body ownership. Furthermore, the lack of sensory feedback in prostheses is a leading cause of device abandonment among other functional issues (difficult to control, slow response speed, poor dexterity) and comfort issues (temperature, weight, poor fit) (Smail et al., 2021; Jabban et al., 2022). The information from touch sensation that is commonly fed back are the grip force (or individual finger force), proprioception of the hand aperture, initial contact and object release, and grip selection (for hands with multiple degrees of freedom). Various approaches have been tried which can be divided into two categories: invasive and non-invasive methods. Invasive methods feed back the touch information through implanted electrodes that directly stimulate the nerves. Such methods achieve remarkable results with respect to user acceptance and improvement of control (Graczyk et al., 2018; Schiefer et al., 2018; D'Anna et al., 2019). However, improvements come with risks associated with surgery. Alternatively, information from touch sensation can be delivered with non-invasive methods. Commonly used channels are of mechanotactile, vibrotactile or electrotactile nature (Stephens-Fripp et al., 2018; Masteller et al., 2021). Vibrotactile systems employ vibrational motors and are perceived by receptors in the skin. They can be used to transmit information by varying the stimulation amplitude, frequency, duration, and shape. Vibration is used substitutionary when the source of the feedback is pressure, e.g., on the fingers of the prosthetic hand. Vibrotactile systems were shown to allow for simple to interpret signals (Stephens-Fripp et al., 2018). However, they introduce a short delay due to the ramp-up time and are limited in the bandwidth which in turn limits the capacity to transmit information. Electrotactile systems stimulate cutaneous fibers. This allows transmitting the sensations of vibration and pressure (Kaczmarek, 2000). Recent advances in electrotactile feedback showed promising results for intuitive non-invasive feedback. Gholinezhad et al. (2021) reported that the participants' central nervous system could adopt the feedback subconsciously within a training time of less than 5 min. However, the perception depends heavily on the user it is applied to and the minute conditions of the skin (e.g., sweat). Thus, frequent readjustment of the stimulation parameters is required (Stephens-Fripp et al., 2018). Mechanotactile systems employ tactors to deliver modality matched sensations of pressure. However, the used tactors are often too bulky and energy demanding for portable systems (Antfolk et al., 2013). Many sources state the obvious benefits of touch feedback (Sensinger and Dosen, 2020). Furthermore, users rank the addition of touch feedback to myoelectric hand prostheses as a top priority (Wijk and Carlsson, 2015). Nevertheless, there is no consensus on the actual benefit of non-invasive feedback in clinical applications outside the lab (Markovic and Schweisfurth, 2018; Wijk et al., 2020). The benefits were often shown under limitations such as obstruction of incidental feedback (vision, hearing, motor vibrations of the prostheses) or experimental tasks of routine grasping that could be executed by feedforward control alone (Sensinger and Dosen, 2020). Feedforward control is a crucial aspect of human motor control and it is governed by the individual's internal model and understanding of cause to effect (Engels et al., 2019; Sensinger and Dosen, 2020). The Feedforward control is subject to noise. Therefore, feedback sources are necessary to detect and correct mismatches between the outcome and the expectation. However, the internal model can be trained with feedback, e.g., learning how to use a prosthetic device under known circumstances as demonstrated with EMG biofeedback (Dosen et al., 2015; Schweisfurth et al., 2016). Another example was shown by Markovic and Schweisfurth (2018) where the participants learned the necessary feedforward control during routine tasks. Eventually, the participants performed equally well with and without feedback in the given tasks. However, inappropriate feedback strategies were found to degrade the internal model (Engels et al., 2019) and incidental feedback such as vision alone may also just outperform other strategies depending on the task (Wilke et al., 2019).

In our previous research, we tested various feedback strategies such as tactor based feedback, vibration with coin vibration motors, and combinations of both (Li et al., 2016; Huang et al., 2017). Furthermore, we tested different sites to redirect the feedback, i.e., the residual limb, the upper arm, or the contralateral hand. The focus lies in redirecting the feedback to the phantom map of amputees (Huang et al., 2018), where applicable. However, we found two main limitations to these approaches:

1. Only a few people have a phantom map which limits the application.
2. If present, phantom maps are often found on the residual limb. Redirecting the feedback to that region results in adding more devices to the already burdened limb, steals

1 https://bionicsforeveryone.com/current-options-for-bionic-hands

valuable space within the socket, and may interfere with surface electromyographic signals (sEMG) for myoelectric control.

Therefore, we searched for a different body part to which to apply the feedback. We settled for the sole of the feet because it is among the most sensitive parts of the human body (Kennedy and Inglis, 2002). Moreover, this answers the user need of reducing the weight and the complexity of the prosthetic socket (Jabban et al., 2022). To favor miniaturization, we chose to rely on vibrotactile information from coin vibration motors without additional tactors. These motors can be embedded within an insole which can be worn within a shoe. This adds a design benefit by hiding the device inside the shoe as opposed to wearing it openly, e.g., as a vibrational cuff around the upper arm or the shanks. The viability of such feedback was already shown in mobile robot control (Jones et al., 2020) and in supported navigation while walking (Velázquez et al., 2012; Meier et al., 2015). Importantly, neither research reported burdening of the participants by e.g., additional weight or induced gait disturbances. A similar approach (Sasaki et al., 2018) introduced body-worn robotic arms. These arms are piloted with the feet and the hands' touch sensation is fed back to the sole of the feet. However, the authors did not comment on the effect of the feedback and stated that they intended to improve it in a future step.

In a preliminary trial, we tested three feedback settings:

1. Continuous feedback for each finger applied to the toes.
2. Continuous feedback from the grasp force applied to the pinkie toe.
3. Discrete feedback from the grasp force applied as a spatially coded ramp along the foot.

We observed fair results with the discrete feedback which was likely the easiest to interpret (Aboseria et al., 2018). Therefore, we settled for a spatially coded discrete feedback device with a continuous sensing device for FeetBack. The sensed modality is the grip force. Users ranked it the top priority for sensory feedback in surveys with over hundred participants (Lewis et al., 2012; Smither et al., In Press).

The goal of this pilot study was to test the applicability of discrete tactile feedback applied to the feet to partially emulate touch sensation, i.e., grip force, of a prosthetic hand. We did not test to emulate proprioception, although the presented device should allow for it (similarly to Štrbac et al., 2016). Thus, we first describe the FeetBack system followed by the study participants and the experimental tasks. Eventually, the results are presented and discussed.

2. Methods

2.1. FeetBack system

2.1.1. System overview

The FeetBack system consists of a sensing glove and a feedback insole (Figure 1). The glove is equipped with one pressure sensor on the index finger and one on the thumb. The sensed force is sent wirelessly (Adafruit M0 RFM69 Packet Radio) to the insole, where the value is converted to a distinct force level. Depending on the force level, either none or one of five embedded vibration motors starts buzzing. The conversion from force to the motor is exponential to allow for a finer distinction at low forces. The force is updated at a frequency of 20 Hz. The transmission latency from the glove to the insole is 44 ± 3 ms which is sufficiently low for the intended application (Ismail and Shimada, 2016).

2.1.2. Subunits of the system

2.1.2.1. Glove

The glove was modeled especially for the iLimb quantum (Össur hf, Iceland) and can be donned on the index finger and thumb. It is made of silicone (Sili-Sil RTV-33 translucent, shore hardness A 33) and has embedded sensors (SingleTact 10 N, 8 mm) on the fingertips. The wires from the sensors to the microcontroller board are bent in waves to allow the silicone to stretch when the prosthesis is moving. Both sensor measure simultaneously. Only the higher value of the two sensors is taken as the grip force and sent from the glove to the insole.

2.1.2.2. Insole

The insole is made of medical grade silicone (Silbione RTV 4428, shore hardness A 28) and can be slipped into a common house shoe. It has five embedded eccentric rotating mass motors (JinLong Machinery, diameter 10 mm, thickness 2.7 mm) that vibrate at a buzz (250 ms at 100 Hz). The motors are positioned along the foot in regions of a high density of fast adapting mechanoreceptors. There are two types of fast adapting mechanoreceptors. They are predominant on the sole of the feet with a low detection threshold at vibrations from 50 to 100 Hz (Kennedy and Inglis, 2002).

Additionally, they have small receptive fields. The insole was produced in three sizes (small, medium, large) to provide the participants with adequate systems. We defined encoding small forces at the toes and increasing force toward the heel. The microcontroller board with motor driver is placed above the fastener of the house shoe (Figure 1).

FIGURE 1
FeetBack glove and insole. The glove senses the pressure on the fingertips of the index finger and the thumb. The higher force at either finger is defined to represent the grip force and is sent wirelessly to the insole. Depending on the force one of the five embedded coin vibration motors starts vibrating. The lower the force, the lower the number of the running motor (or no motor at all when the force is below a minimal threshold). The distribution of the motors was chosen accordingly to the distribution of fast adapting mechanoreceptors on the sole of the foot.

2.1.2.3. Monitoring

Additionally to the sensing and feedback device, the FeetBack system may include a monitoring unit. It connects to a computer *via* USB and wirelessly to the insole. It allows surveying the sensed force with the corresponding vibrating motor on the screen.

2.2. Participants

Four participants (Table 1) with unilateral congenital below elbow limb absence took part in the study. All were experienced users of myoeletric prosthesis with several years of experience. Especially, all participants were familiar with the same multi-articulating prosthesis and conducted the experiments with their personal device (iLimb quantum, Össur hf, Iceland). The prosthesis was merely modified by adding the sensor glove on top of the regular cover. This setup allowed the participants to experience the feedback with a virtually unaltered internal model of the feedforward control.

The participants were asked to answer a pre-study (Table 2) and a post-study (Table 3) questionnaire. The pre-study questionnaire focused on the participant's use of the prosthesis and the expectations of sensory feedback. The post-study questionnaire focused on their impressions of the used sensory feedback.

The first participant was enrolled in September 2021 and the last participant visit was in November 2021. The recruitment took place in August 2021 within the population of patients of the Balgrist University Hospital (Zürich, Switzerland). Inclusion criteria: healthy people, 18–55 years old, with basic knowledge of and trust in modern technology, and unilaterally experienced users of the iLimb quantum multi-articulating hand (independently of the cause, e.g., dysmelia or amputation). Exclusion criteria: skin incompatibilities with silicone or cognitive impairment.

2.3. Experiments

Four different tasks were conducted to test the applicability of force feedback from the hand to the feet. The tests varied in the availability of other feedback channels, i.e., audio-visual feedback, and in task complexity. All four tasks were conducted in two sessions of which the second followed 3–4 weeks after the first session. The participants remained seated throughout the experiments to maintain a stable sensation of the actuators (Figure 2). They were allowed to use only the thumb to index finger pinch grip for all tasks. The only exception was the object manipulation task with heavy objects. There, the participants were allowed to use the power grip due to the larger size of the object.

2.3.1. Calibration and training

Prior to the tasks, the FeetBack system was explained to the participants. They were told that the force at the fingers represented the grasp force. Small forces are felt at the toes,

TABLE 1 Demographic and clinical overview of the trial participants.

ID	Gender	Age	Reason for prosth.	Mostly used type of prosth.	Daily use of prosth.
1	M	43	Dysmelia	Myoelectric	Sometimes
2	F	41	Dysmelia	Myoelectric	Always
3	F	20	Dysmelia	Myoelectric	Sometimes
4	M	52	Dysmelia	Cosmetic	When working

TABLE 2 The participants' answers to the pre-study questionnaire.

ID	When do you use the prosth.?	When do you not use the prosth.?	When could feedback be beneficial?
1	Sports, presentations	When water is involved	Handshake
2	Almost everything	When water is involved	Unsure
3	Kitchen, chores, opening purses	Fine-motor tasks	When quick actions are required
4	Working, gardening, shopping	Sports, free time	Cooking, crafting

The questionnaire included open questions about the participants' personal use of the prosthetic hand and their expectations of sensory feedback.

TABLE 3 The participants' answers to the post-study questionnaire.

ID	Benefit	What did you like about FeetBack?	Comments and suggestions
1	Yes	N/A	N/A
2	No	To experience force feedback	Unsure about the benefit while other sensations, e.g., vision and audio, are available. The benefit was clear without other sensations.
3	Yes	To experience force feedback and to explore some of the fine-motoric capabilities and limits of the high-end prosthesis	N/A
4	No	Nothing in particular	Feedback at the feet seems unpractical - feedback in the socket may be a better idea. Suggestions for enhancements of the prosthesis: 1) add push buttons on the socket to quick select grasps, 2) reduce the weight of the prosthesis, 3) reduce the noise of the prosthesis, and 4) make thinner and more long living skin for the hand.

The questionnaire included open questions about their subjective impressions of the FeetBack system.

and increasing forces are felt toward the heel, respectively. Each participant was provided the insole that had the best fit in size. The participants were asked to adjust the position of their foot on the insole such that they could perceive every actuator. Thereafter, the system was calibrated to the prosthesis of the participants. The participants were asked to squeeze the softest and hardest cube halfway three times. The force was recorded at every squeeze and the minimum and maximum force were set by the respective average.

Then, the participants were given time to learn the force feedback provided by the FeetBack system. The participants were first given 2 min to freely handle a variety of soft cubic sponges and were allowed to compare the sensation with both hands. Then, they cracked two 3D printed egg shells with the prosthetic hand to feel the allowed threshold in a later task (fragile objects). Finally, they were given two more minutes to freely handle a heavy cylinder to determine the minimum grasp force needed to lift it (although all participants noticed that they might as well just apply the full force without losing much time). After the training was completed, the tasks were conducted directly. The participants were allowed to take breaks between tasks but none made use of the offer.

2.3.2. Object sorting

In one task, the participants had to sort five equal sized cubes of individual plasticity from softest to hardest without audio-visual feedback (Figure 2A). The final arrangement of the cubes was recorded as measurement. The side length of each cube was 50 mm. Four cubes were made of miscellaneous foamed plastic

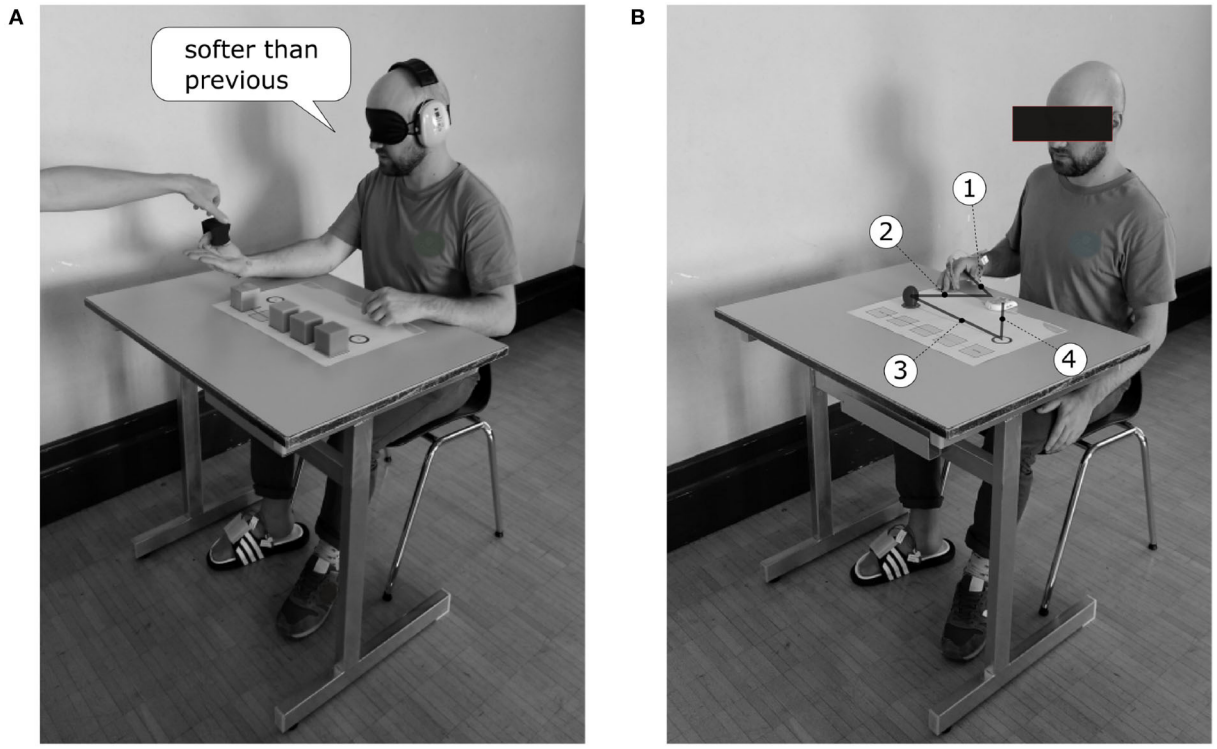

FIGURE 2
Setup of the experiments. The FeetBack glove was donned on the cover of the prosthetic hand and the FeetBack insole was worn on the right foot. The participants remained seated throughout the tests. **(A)** In the object sorting task, the participants were blindfolded and were wearing ear muffs. They rested the arm with the prosthesis on the table with the open hand upward. The investigator put the objects between the index finger and thumb. The participants had to answer if the current object was harder or softer than the previous object. **(B)** In the pick and place tasks, the participants started in a resting position as shown. After an oral start signal by the investigator, the participants moved the hand from the starting position to the clock and started said clock with the prosthesis in step 1. In step 2, the participants moved the prosthesis from the clock to the object and pinched it. In step 3, they lifted the pinched object from the side of the prosthesis to the contra-lateral target and released the object. In step 4, they stopped the clock with the prosthesis.

(weight: $<$ 6 g) with compression load deflections of 3.0 kPa, 4.1 kPa, 5.5 kPa, 11.0 kPa, respectively. The fifth cube was made of wood (weight: 45 g).

The participants were blindfolded and wore earmuffs to eliminate audio-visual feedback. They rested their arm on a table with the open hand upside. They were given one cube at a time by the investigator. The participants were allowed to close and open the artificial hand at their chosen pace. After each cube, they had to answer if the current cube was harder or softer than the previous cube. This procedure was repeated for five runs, where one run means that all cubes were handed to the participants once. The initial order in the first round was predefined random (same order for all participants). From the second to the last round, the first given cube was always the presumably softest.

To accomplish this task, the participants had to rely on the rate of change of the force feedback and their intended sEMG signal to close the hand. This task was only performed with the feedback switched on. A comparative measurement without feedback was omitted since previous comparative tests showed that the answers were close to random guesses (Huang, 2018).

2.3.3. Object manipulations

In three tasks, the participants had to manipulate fragile, heavy, and delicate objects. The success rate and time needed to accomplish a task were recorded as measurements. The success criterion depended on the specific task and will be addressed in the following paragraphs. The time was measured with a stop watch that the participants had to start before and stop after every manipulation (Figure 2B).

All object manipulation tasks were repeated 10 times with feedback and 10 times without feedback. In the first session, all tasks were conducted with feedback followed by repetitions without feedback. In the second session, the order of conduction was reversed to reduce the bias due to the learning of specific tasks through repetitions.

2.3.3.1. Fragile objects

The participants had to pick and relocate an egg shell (made of 3D printed PLA, break point: 9.2 N ± 0.8 N, height: 48 mm, width: 40 mm, wall thickness 0.4 mm). The distance was 30 cm with a precision of ±1 cm. The relocation was measured as successful when the egg was placed within the fixed boundary without being cracked or dropped on the way. This task is judged to be of moderate difficulty compared to the other two manipulation tasks. The reason, therefore, is that only one hand is needed, allowing the skilled participants to rely heavily on feedforward control.

2.3.3.2. Heavy objects

The participants had to pick and relocate a heavy cylinder (made of aluminum, weight: 462 g, diameter: 60 mm, height: 105 mm). The distance was 30 cm with a precision of ±1 cm. The relocation was measured as successful when the cylinder was placed within the fixed boundary without being dropped along the way. This task is judged to be the easiest of the three manipulation tasks since only one hand is needed and full force can be applied.

2.3.3.3. Delicate objects

The participants had to pick a cherry and remove the stem from the body (made of modeling clay and toothpick, diameter: 16 mm, height: 24 mm, depth of toothpick: 18 mm, weight: 7.5 g). The manipulation was measured as successful when the stem was removed from the body and if the body of the cherry was not squashed [similar to Tan et al. (2014)]. This task is judged to be the most complex of the three manipulation tasks since both hands are needed. Furthermore, the right amount of grasp force must be applied to securely hold the cherry without squashing it.

2.4. Data analysis

The primary and secondary outcomes are defined as follows:

Primary outcome: Success rate to detect the contact force levels to differentiate between different objects and to manipulate various objects, using a hand prosthesis with/without tactile feedback.

Secondary outcome: Time needed to finish a set of manipulation tasks, using a hand prosthesis with/without tactile feedback.

2.4.1. Primary outcomes

The primary outcome of the object sorting task was assessed with a measure of the ranked correlation between the participants' order and the true order from softest to hardest. We used Goodmann-Kruskal's gamma

$$G = \frac{N_s - N_d}{N_s + N_d}, \tag{1}$$

where N_s is the number of concordant pairs and N_d is the number of reversed pairs. A value of $G = 1$ represents perfect order, whereas $G = -1$ represents perfect inverse order (Goodman and Kruskal, 1954).

For the object manipulation tasks, the primary outcomes were compared qualitatively within individual participants. The reason for that is that the sample size in this pilot study is too small to use quantitative methods.

2.4.2. Secondary outcomes

The time needed for the manipulation tasks was modeled with linear mixed effects models. They are an extension of ordinary linear models that allow modeling fixed and random effects. The intervention (feedback turned on or off) is the fixed effect and the individual participants are random effects. This allows us to model the baseline time needed to manipulate an object depending on the participant. We used the *fitlme* method from the Statistics and Machine Learning Toolbox in MATLAB (version R2021a). The manipulation tasks with fragile and delicate objects were modeled as "time∼feedback+(1|ID)". This formulation corresponds to an individual offset per participant and a fixed slope for the fixed effect over all participants. The manipulation task with heavy objects was modeled as "time∼feedback+(feedback|ID)". This corresponds to an individual slope for the fixed effect per participant, since the residuals were not normally distributed with the former formulation.

3. Results

All participants conducted all tasks and all data was considered for the evaluation.

3.1. Pre-study and post-study questionnaires

The questionnaires (pre-study: Table 2; post-study: Table 3) give subjective impressions about the individual participant's expectations and impressions of force feedback. The expectations before the trials show that three out of four participants see potential situational benefits of adding force feedback to prosthetic hands. However, ID 2 who reportedly uses her prosthesis the most ("always," "[for] almost everything"), was unsure about the benefits. The impressions after the trials changed the point of view for ID 4 and remained the same for the other participants. Participants ID 1 and ID 3

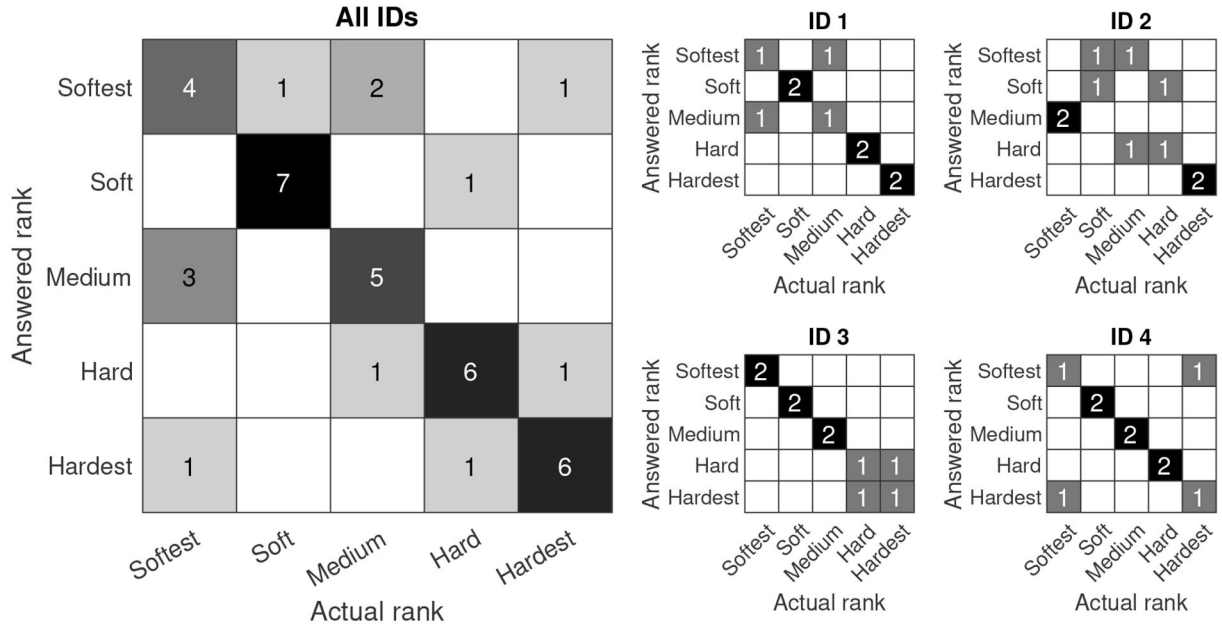

FIGURE 3
Confusion matrix of the object sorting task with feedback. In the ideal case, all answers would lie in the diagonal of the confusion matrix. Since the grading is ordinal, errors become more severe the farther they are from the diagonal. (left) Cumulative matrix with observations from all participants; (right) Individual observations per participant.

were believed to experience a benefit from FeetBack, although with limited excitement. Participant ID 2 repeated her prior opinion and observed a few advantages of force feedback under the presence of visual-audio feedback. Participant ID 4 saw no benefit in force feedback specifically at the feet. Furthermore, ID 4 suggested several improvements on the multi-articulating prosthetic hand as it is before adding force feedback.

3.2. Experiments

3.2.1. Object sorting task

Goodmann-Kruskal's gamma was $G = 0.639$, suggesting that feedback has a substantial positive effect. Three out of four participants merely confused two objects (Figure 3), meaning they all had one perfect sorting session out of two. Participant ID 2 confused two objects in one session ('*softest*' and '*medium*') and multiple objects in the other session.

3.2.2. Object manipulation tasks

3.2.2.1. Success rates

In the single-handed tasks with fragile and heavy objects, the success rates were high (SR $\geq$ 80%, Figure 4) for all participants regardless of the intervention (feedback switched on or off, respectively). In the two-handed task with delicate objects, however, the success rates were generally lower and varied between participants. Three participants performed worse when force feedback was provided.

3.2.2.2. Time needed to perform task

There is a positive effect (Table 4) in the tasks with fragile objects (4.209 s + 0.326 s, baseline intercept + feedback) and the delicate objects (3.900 s + 0.406 s, baseline intercept + feedback). The 95 % CI does not encompass 0.0 s in both cases. This suggests that there was a significant increase in time needed to complete these two manipulation tasks with feedback. There is no significant effect of the feedback in the task with heavy objects as the 95 % CI clearly encompasses 0.0 s (Table 4). Residuals of the models were normally distributed.

4. Discussion

Initially, the limitations of the study are discussed to put the results into context. The results are discussed according to the small number of research participants in this pilot study. Furthermore, the study design only allowed us to explore the *immediate* effect of vibrotactile feedback at the feet since the participants merely used the system twice for a couple of hours. Finally, we deliberately chose to simulate the user case scenarios that incorporate the internal model of the user in the interaction with their prosthesis. Although our approach allows for a holistic scenario with human-machine interaction, it is more challenging to isolate confounding factors; namely the accuracy

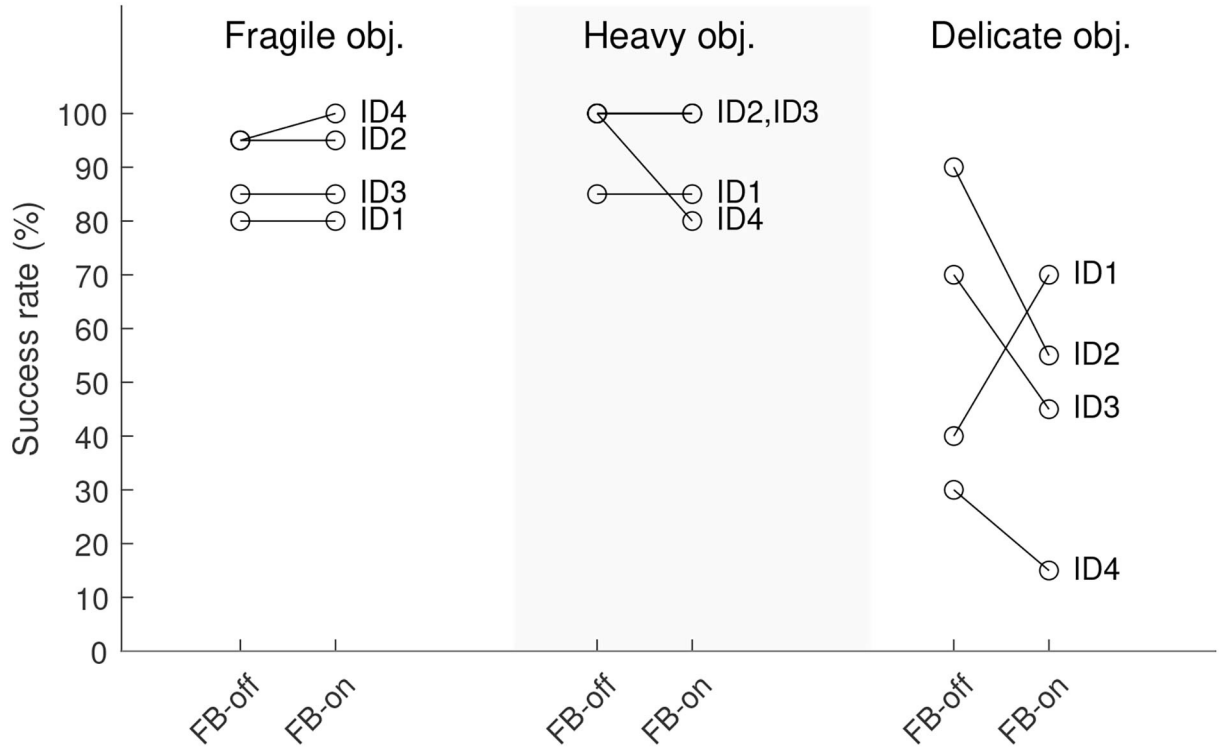

FIGURE 4
Success rates of the object manipulation tasks. All participants performed n=20 manipulations per task under each condition FB-on (feedback switched on) and FB-off (feedback switched off).

TABLE 4 Linear mixed effect model of the time needed for manipulation tasks.

Manipulation	Fixed effect	β	95 % CI	Participant (SD)	Corr
Fragile obj.	Intercept	4.209	[3.514, 4.904]	0.677	N/A
	Feedback	0.326	[0.058, 0.593]	N/A	
Heavy obj.	Intercept	4.242	[3.310, 5.173]	0.932	0.031
	Feedback	–0.019	[–0.551, 0.513]	0.499	
Delicate obj.	Intercept	3.900	[3.017, 4.783]	0.860	N/A
	Feedback	0.406	[0.087, 0.725]	N/A	

The estimated fixed effects (intercept, feedback) and random effect (participant ID) with the corresponding 95% confidence interval (CI) and standard deviation (SD) of the random effect are presented for every experiment individually. Since the experiment with heavy objects was modeled with an individual slope per participant, the correlation between the fixed effects is given, too.

of the feedforward control of the prosthesis and the incidental feedback. In fact, recent research (Gholinezhad et al., 2021) proposed a method to first assess the effects of the feedback on the natural hand against natural feedback. The benefit of the feedback may then be tested with active users of prosthetic devices once the effects are estimated. Nevertheless, we believe that this pilot trial toward a novel feedback approach resulted in valuable insights for future investigations.

The information of the vibrating insole was interpreted successfully when audio-visual feedback was prevented, as demonstrated in the sorting task. This shows that discrete vibrotactile feedback at the feet can indeed be used to translate information about the grasp force. However, participants ID 2 and ID 3 reported feeling rather unsure about their answers. At this stage, it is not possible to pin the exact causes. Although, the likely reasons can be the short time the participants had to learn to interpret the feedback and inadequate implementation of the feedback device in terms of resolution and perceptibility.

The success rates during manipulation tasks were overall equivalent or even lower when vibrotactile feedback at the feet was provided. The outcomes from the pick and place

tasks (fragile and heavy objects) were not altered noticeably by the intervention. In the task with heavy objects, this was anticipated, since the participants could merely use full force. However, the equivalent success rate for the task with fragile objects was unexpected. An exhaustive review on feedback strategies for prosthetic hands by Sensinger and Dosen (2020) provides possible reasons when feedback would not improve the success rate; namely, an already efficient internal model, sufficient incidental feedback, a task that is too simple, or a weak feedback method. We believe that the most dominant causes are the efficient internal models coupled with a rather simple task in which the experienced users did not rely on additional feedback (other than audio-visual and incidental feedback). The review by Jabban et al. (2022) supports the notion that object manipulation tasks with fragile objects may underestimate the benefit of sensory feedback. The reason for this is that such tasks can be solved by feedforward control alone.

In the most complex manipulation task with delicate objects, the success rate was considerably lower when feedback was provided. Unlike Tan et al. (2014), our approach to *the cherry stem removal task* resulted in overall inferior success. The tests are not directly comparable since one uses actual cherries and the other uses replica made of modeling clay and toothpicks. Nevertheless, we assume that our approach reached inferior success rates due to an insufficient resolution of the discrete spatial coding. In the case of participant ID 4 who reportedly tried to incorporate the feedback for fine-tuning, the interaction of human, prosthesis, and FeetBack resulted in fluttering pinches that squashed most of the fake cherries. Thus, the presented system does not allow for fine-tuning the grip for sophisticated closed-loop control. However, it serves to notify the user about initial contact and may help engage the user. This was likely the case for participant ID 1 who reportedly perceived a subjective benefit.

The increase of time needed for manipulation tasks with fragile and delicate objects could be explained by the new sensation of vibrotactile feedback, cognitive burdening, or a poorly chosen location to apply the feedback. According to participant ID 4, the feet may be a bad site which potentially distracts the user. Although, the remaining three participants did not comment on that notion. Wells et al. (2022) reported similar findings, where the mechanotactile feedback resulted in an increased time to finish a task. The respective authors believe this effect to be due to the added focus on the task with feedback. Such an increase in time was not observed in comparable studies that applied discrete feedback to the residual limb (Aboseria et al., 2018; Raveh et al., 2018). However, Clemente et al. (2016) who investigated the effect of feedback for object contact and release did not observe a speed boost with feedback in a long at home trial, either. Nevertheless, their success rate to manipulate fragile objects increased. Therefore, they reason that feedback may be costlier from a cognitive perspective but allows for more confidence. In our case, participant ID 1 appears to have had this experience, too.

No participant reported an adverse effect due to the feedback method. Nevertheless, a potential adverse effect of feedback applied to the feet could be *sensory steering* (Zehr et al., 2014). In that case, electrotactile stimulation at the sole of the feet provoked potentially unwanted muscle activities. Velázquez et al. (2012) also applied vibrotactile feedback in a walking navigation task and they did not encounter any such undesired effect. We did not investigate the effect of FeetBack in standing or walking tasks. However, we expect that our system would behave similarly to the system presented by Meier et al. (2015) where an increasing walking speed affects the perceptibility negatively. The reason therefore is that the foot may momentarily loose contact to the insole or exert too much pressure on the motors. However, such mechanical issues would need to be addressed in the next iteration of FeetBack. Also, according to a survey with 142 unique responses (Smither et al., In Press) the most anticipated benefits were reported in stationary tasks such as zipping jackets, tying shoes, buttoning shirts, and using a cup.

In summary, we observed that the proposed feedback method causes various effects depending on the tasks. Without audio-visual feedback, the gain was evident as the participants were generally able to distinguish between objects of distinct plasticity. However, in the more realistic setting with vision and hearing the anticipated benefit was not achieved. Similar observations were made by Markovic and Schweisfurth (2018) where an advanced feedback method was only helpful in complex tasks for regular users of hand prostheses. The easier tasks could be learned accurately by feedforward control after repeated executions. Thus, we further support the notion that the study design for experienced users of upper limb prostheses must be more complex in order to assess the feedback method's capacity and impact on the users (Sensinger and Dosen, 2020; Jabban et al., 2022).

5. Conclusion

The viability of vibrotactile feedback in (mobile) robot control and navigation tasks had already been shown. We anticipated investigating its potential within the field of hand prostheses. We showed for the first time that information from the prosthetic hand can be interpreted at the feet with beneficial effects when sight and vision are prevented. The results suggest that the immediate effect of discrete spatially coded vibrotactile feedback at the feet allows distinguishing between plastic objects without the help of vision and hearing. However, the interaction of human, myoelectric hand, and FeetBack does not allow the grasp force to be qualitatively fine-tuned under pressure of time. Moreover, there appears to be little benefit from FeetBack under the presence of audio-visual feedback for experienced users of myoelectric hands. These findings are in line with findings of similar studies with tactile feedback provided on the arm or within the prosthetic socket. Hence, we provide a rationale to further investigate the clinical benefit of feedback redirected

to the feet in a large-scale clinical trial. Ultimately, we suggest testing the clinical benefit of such feedback not only under laboratory conditions alone but also in an at-home trial over a longer period of time.

Data availability statement

The datasets generated for this study are available on request to the corresponding author.

Ethics statement

The studies involving human participants were reviewed and approved by Cantonal Ethics Committee in Zürich, Switzerland (Ref. No.: 2019-01639). All experiments were conducted in accordance with the declaration of Helsinki, and all participants provided written informed consent prior to participation in the experiments.

Author contributions

RM, NS, TB, and VK participated in the design of the study. MB screened the participants. RM, NS, and SC conducted the tests. RM, NS, and TB analyzed the data. RM wrote the manuscript. TB, NS, MB, SC, and VK revised and approved the manuscript. All authors contributed to the article and approved the submitted version.

Funding

This study was supported by the foundation Inventus Bern, Switzerland (Grant No. 39/2019).

Acknowledgments

The authors would like to thank all participants that took part in this study for their time and effort. Furthermore, they thank David Egger for recruiting the participants. Many thanks to Pierre-André Friederich and Ian Pastor for their support in developing the FeetBack system.

Conflict of interest

The authors declare that the research was conducted in the absence of any commercial or financial relationships that could be construed as a potential conflict of interest.

Publisher's note

References

Aboseria, M., Clemente, F., Engels, L. F., and Cipriani, C. (2018). Discrete vibro-tactile feedback prevents object slippage in hand prostheses more intuitively than other modalities. *IEEE Trans. Neural Syst. Rehabil. Eng.* 26, 1577–1584. doi: 10.1109/TNSRE.2018.2851617

Antfolk, C., Alonzo, M. D., Rosén, B., Lundborg, G., Sebelius, F., Cipriani, C., et al. (2013). Sensory feedback in upper limb prosthetics. *Expert. Rev. Med. Devices* 10, 45–54. doi: 10.1586/erd.12.68

Clemente, F., D'Alonzo, M., Controzzi, M., Edin, B. B., and Cipriani, C. (2016). Non-invasive, temporally discrete feedback of object contact and release improves grasp control of closed-loop myoelectric transradial prostheses. *IEEE Trans. Neural Syst. Rehabil. Eng.* 24, 1314–1322. doi: 10.1109/TNSRE.2015.2500586

D'Anna, E., Valle, G., Mazzoni, A., Strauss, I., Iberite, F., Patton, J., et al. (2019). A closed-loop hand prosthesis with simultaneous intraneural tactile and position feedback. *Sci. Robot*. 4, 1–21. doi: 10.1126/scirobotics.aau8892

Dosen, S., Markovic, M., Somer, K., Graimann, B., and Farina, D. (2015). EMG Biofeedback for online predictive control of grasping force in a myoelectric prosthesis. *J. Neuroeng. Rehabil*. 12, 55. doi: 10.1186/s12984-015-0047-z

Engels, L. F., Shehata, A. W., Scheme, E. J., Sensinger, J. W., and Cipriani, C. (2019). When less is more-discrete tactile feedback dominates continuous audio biofeedback in the integrated percept while controlling a myoelectric prosthetic hand. *Front. Neurosci.* 13, 578. doi: 10.3389/fnins.2019.00578

Gholinezhad, S., Dosen, S., and Jakob, D. (2021). Electrotactile feedback outweighs natural feedback in sensory integration during control of grasp force. *J. Neural Eng*. 18, 5. doi: 10.1088/1741-2552/ac1fce

Goodman, L. A., and Kruskal, W. H. (1954). Measures of association for cross classifications. *J. Am. Stat. Assoc*. 49, 732–764. doi: 10.1080/01621459.1954.10501231

Graczyk, E. L., Resnik, L., Schiefer, M. A., Schmitt, M. S., and Tyler, D. J. (2018). Home use of a neural-connected sensory prosthesis provides the functional and psychosocial experience of having a hand again. *Sci. Rep*. 8, 1–17. doi: 10.1038/s41598-018-26952-x

Huang, H. (2018). Phantom Map Modeling Detection, and Actuation for Upper Limb Sensory Feedback. [dissertation]. Lausanne: École polytechnique fédérale de Lausanne.

Huang, H., Bruschini, C., Antfolk, C., Enz, C., Li, T., Justiz, J., et al. (2018). Automatic hand phantom map generation and detection using decomposition support vector machines. *Biomed. Eng. Online* 17, 1–30. doi: 10.1186/s12938-018-0502-8

Huang, H., Li, T., Bruschini, C., Enz, C., Justiz, J., Antfolk, C., et al. (2017). "Multi-modal sensory feedback system for upper limb amputees," *Proceedings-2017 1st New Generation of CAS, NGCAS 2017* (Genova), 193–196.

Ismail, M. A. F., and Shimada, S. (2016). 'Robot' hand illusion under delayed visual feedback: relationship between the senses of ownership and agency. *PLoS ONE* 11, e0159619. doi: 10.1371/journal.pone.0159619

Jabban, L., Dupan, S., Zhang, D., Ainsworth, B., Nazarpour, K., and Metcalfe, B. W. (2022). Sensory feedback for upper-limb prostheses: opportunities and barriers. *IEEE Trans. Neural Syst. Rehabil. Eng.* 30, 738–747. doi: 10.1109/TNSRE.2022.3159186

Jones, B., Maiero, J., Mogharrab, A., Aguliar, I. A., Adhikari, A., Riecke, B. E., et al. (2020). "FeetBack: augmenting robotic telepresence with haptic feedback on the feet," in *ICMI 2020-Proceedings of the 2020 International Conference on Multimodal Interaction* (Virtual event), 194–203.

Kaczmarek, K. A. (2000). Electrotactile adaptation on the abdomen: preliminary results. *IEEE Trans. Rehabil. Eng.* 8, 499–505. doi: 10.1109/86.895953

Kennedy, P. M., and Inglis, J. T. (2002). Distribution and behaviour of glabrous cutaneous receptors in the human foot sole. *J. Physiol.* 538, 995–1002. doi: 10.1113/jphysiol.2001.013087

Lewis, S., Russold, M. F., Dietl, H., and Kaniusas, E. (2012). "User demands for sensory feedback in upper extremity prostheses," in *MeMeA 2012-2012 IEEE Symposium on Medical Measurements and Applications, Proceedings* (Budapest: IEEE), 188–191.

Li, T., Huang, H., Antfolk, C., Justiz, J., and Koch, V. M. (2016). Tactile display on the remaining hand for unilateral hand amputees. *Curr. Direct. Biomed. Eng.* 2, 399–403. doi: 10.1515/cdbme-2016-0089

Markovic, M., and Schweisfurth, M. A. (2018). The clinical relevance of advanced artificial feedback in the control of multifunctional myoelectric prosthesis. *J. Neuro Eng. Rehabil.* 15, 28. doi: 10.1186/s12984-018-0371-1

Masteller, A., Sankar, S., Kim, H. B., Ding, K., Liu, X., and All, A. H. (2021). Recent developments in prosthesis sensors, texture recognition, and sensory stimulation for upper limb prostheses. *Ann. Biomed. Eng.* 49, 57–74. doi: 10.1007/s10439-020-02678-8

Meier, A., Matthies, D. J., Urban, B., and Wettach, R. (2015). "Exploring vibrotactile feedback on the body and foot for the purpose of pedestrian navigation," in *ACM International Conference Proceeding Series* (Rostock), 25–26.

Raveh, E., Portnoy, S., and Friedman, J. (2018). Adding vibrotactile feedback to a myoelectric-controlled hand improves performance when online visual feedback is disturbed. *Hum. Mov. Sci.* 58, 32–40. doi: 10.1016/j.humov.2018.01.008

Sasaki, T., Saraiji, Y., Minamizawa, K., and Inami, M. (2018). "MetaArmS: Body remapping using feet-controlled artificial arms," in *UIST 2018 Adjunct - Adjunct Publication of the 31st Annual ACM Symposium on User Interface Software and Technology* (Berlin), 140–142.

Schiefer, M. A., Graczyk, E. L., Sidik, S. M., Tan, D. W., and Tyler, D. J. (2018). Artificial tactile and proprioceptive feedback improves performance and confidence on object identification tasks. *PLoS ONE* 13, e0207659. doi: 10.1371/journal.pone.0207659

Schweisfurth, M. A., Markovic, M., Dosen, S., Teich, F., Graimann, B., and Farina, D. (2016). Electrotactile EMG feedback improves the control of prosthesis grasping force. *J. Neural Eng.* 13, 1–15. doi: 10.1088/1741-2560/13/5/056010

Sensinger, J. W., and Dosen, S. (2020). A review of sensory feedback in upper-limb prostheses from the perspective of human motor control. *Front. Neurosci.* 14, 345. doi: 10.3389/fnins.2020.00345

Smail, L. C., Neal, C., Wilkins, C., and Packham, T. L. (2021). Comfort and function remain key factors in upper limb prosthetic abandonment: findings of a scoping review. *Disabil. Rehabil.* 16, 821–830. doi: 10.1080/17483107.2020.1738567

Smither, F., Andrews, K., Scrabeck, T., Lennon, R., and Zhao, K. (In Press). *Opinions on Noninvasive Sensory Feedback of Upper Limb Prosthetic Users*. Prosthetics and Orthotics International Publishing. Available online at: https://journals.lww.com/poijournal/Abstract/9900/Opinions_on_noninvasive_sensory_feedback_of_upper.53.aspx

Stephens-Fripp, B., Alici, G., and Mutlu, R. (2018). A review of non-invasive sensory feedback methods for transradial prosthetic hands. *IEEE Access* 6, 6878–6899. doi: 10.1109/ACCESS.2018.2791583

Štrbac, M., Belić, M., Isaković, M., Kojić, V., Bijelić, G., Popović, I., et al. (2016). Integrated and flexible multichannel interface for electrotactile stimulation. *J. Neural Eng.* 13, 046014. doi: 10.1088/1741-2560/13/4/046014

Tan, D. W., Schiefer, M. A., Keith, M. W., Anderson, J. R., Tyler, J., and Tyler, D. J. (2014). A neural interface provides long-term stable natural touch perception. *Sci. Transl. Med.* 6, 257ra138. doi: 10.1126/scitranslmed.3008669

Velázquez, R., Bazán, O., Varona, J., Delgado-Mata, C., and Gutiérrez, C. A. (2012). Insights into the capabilities of tactile-foot perception. *Int. J. Adv. Robot. Syst.* 9, 1–11. doi: 10.5772/52653

Wells, E. D., Shehata, A. W., Dawson, M. R., Carey, J. P., and Hebert, J. S. (2022). Preliminary evaluation of the effect of mechanotactile feedback location on myoelectric prosthesis performance using a sensorized prosthetic hand. *Sensors* 22, 3892. doi: 10.3390/s22103892

Wijk, U., and Carlsson, I. (2015). Forearm amputees' views of prosthesis use and sensory feedback. *J. Hand Therapy* 28, 269–278. doi: 10.1016/j.jht.2015.01.013

Wijk, U., Carlsson, I. K., Antfolk, C., Björkman, A., and Rosén, B. (2020). Sensory feedback in hand prostheses: a prospective study of everyday use. *Front. Neurosci.* 14, 663. doi: 10.3389/fnins.2020.00663

Wilke, M. A., Niethammer, C., Meyer, B., Farina, D., and Dosen, S. (2019). Psychometric characterization of incidental feedback sources during grasping with a hand prosthesis. *J. Neuroeng. Rehabil.* 16, 1–13. doi: 10.1186/s12984-019-0622-9

Zehr, E. P., Nakajima, T., Barss, T., Klarner, T., Miklosovic, S., Mezzarane, R. A., et al. (2014). Cutaneous stimulation of discrete regions of the sole during locomotion produces "sensory steering" of the foot. *BMC Sports Sci. Med. Rehabil.* 6, 1–21. doi: 10.1186/2052-1847-6-33

frontiers | Frontiers in Neuroscience

TYPE Original Research
PUBLISHED 28 October 2022
DOI 10.3389/fnins.2022.958415

OPEN ACCESS

EDITED BY
Min Li,
Xi'an Jiaotong University, China

REVIEWED BY
Francesco Negro,
University of Brescia, Italy
Sonya Bahar,
University of Missouri–St. Louis,
United States

*CORRESPONDENCE
Luis A. Pardo Jr.
luis.pardo@med.uni-goettingen.de

SPECIALTY SECTION
This article was submitted to Neuroprosthetics, a section of the journal Frontiers in Neuroscience

RECEIVED 31 May 2022
ACCEPTED 07 October 2022
PUBLISHED 28 October 2022

CITATION
Pardo LA Jr, Markovic M, Schilling AF, Wilke MA and Ernst J (2022) Vibrotactile mapping of the upper extremity: Absolute perceived intensity is location-dependent; perception of relative changes is not. *Front. Neurosci.* 16:958415. doi: 10.3389/fnins.2022.958415

Vibrotactile mapping of the upper extremity: Absolute perceived intensity is location-dependent; perception of relative changes is not

Luis A. Pardo Jr.[1]*, Marko Markovic[1], Arndt F. Schilling[1], Meike Annika Wilke[2] and Jennifer Ernst[1,3]

[1]Department of Trauma Surgery, Orthopaedics and Plastic Surgery, University Medical Center Göttingen, Göttingen, Germany, [2]Faculty of Life Sciences, Hamburg University of Applied Sciences (HAW), Hamburg, Germany, [3]Department of Trauma Surgery, Medical School Hannover, Hanover, Germany

Vibrotactile sensation is an essential part of the sense of touch. In this study, the localized vibrotactile sensation of the arm-shoulder region was quantified in 10 able-bodied subjects. For this analysis, the six relevant dermatomes (C3-T2) and three segments—the lower arm, the upper arm, and the shoulder region were studied. For psychometric evaluation, tasks resulting in the quantification of sensation threshold, just noticeable difference, Weber fraction, and perception of dynamically changing vibrotactile stimuli were performed. We found that healthy subjects could reliably detect vibration in all tested regions at low amplitude (2–6% of the maximal amplitude of commonly used vibrotactors). The detection threshold was significantly lower in the lower arm than that in the shoulder, as well as ventral in comparison with the dorsal. There were no significant differences in Weber fraction (20%) detectable between the studied locations. A compensatory tracking task resulted in a significantly higher average rectified error in the shoulder than that in the upper arm, while delay and correlation coefficient showed no difference between the regions. Here, we presented a conclusive map of the vibrotactile sense of the healthy upper limb. These data give an overview of the sensory bandwidth that can be achieved with vibrotactile stimulation at the arm and may help in the design of vibrotactile feedback interfaces (displays) for the hand/arm/shoulder-region.

KEYWORDS

vibrotactile sensation, dermatomes, able-bodies, feedback, psychometric

Introduction

The sense of touch allows us to continuously monitor the boundaries of the whole body. This not only enables safe interaction with our environment even in the absence of the other four main senses but also has a social function when the boundaries of two bodies meet. Consequently, the study of how we perceive the world through somatic

sensation has fascinated us for hundreds of years and a lot of data have been generated on this topic (Weber, 1834a, 1851; Weinstein, 1968).

Perception of tactile sensations originates from the receptors located in the skin. These can be divided into four distinct categories: two fast adapting types (FA I and FA II) and two slowly adapting types (SA I and SA II). Type I afferents have small, sharp-bordered receptive fields; type II afferents are larger and have more diffuse borders (Darian-Smith, 2011). The adaption type (slow or fast) indicates the ability to adapt to sustained indentation (Vallbo and Johansson, 1984). The fast-adapting units mainly fulfill vibration sensations. These have two types of end organs: the Meissner corpuscles (FA I), which possess an optimal sensitivity to frequencies of around 50 Hz, and the Pacini corpuscles (FA II), with a peak sensitivity at about 200–300 Hz (Saddik et al., 2011). The Meissner corpuscles are the primary receptors of hands and feet. In contrast, the Pacini corpuscles are mostly found on hairy skin present on the appendages, the trunk, and the head. Various neural roots give rise to the cutaneous nerves that innervate these receptors depending on their site (Johnson, 2001). In the case of the upper limbs and shoulder/ neck region, these roots, located in longitudinal bands around the arm and neck, give rise to seven different dermatomes: Cervical 3 (C3) to Cervical 8 (C8), Thoracic 1 (T1), and Thoracic 2 (T2).

Throughout the upper limbs, the receptor density varies depending on the skin type and the distance from the trunk. Mancini et al. (2014) measured two-point discrimination on the limbs of able-bodied subjects. Their results showed that the minimal distance between the two tips that can be perceived increased from ca. 0.25 cm at the fingertips, to 0.75 cm (the palm), 1.5 cm (the hand dorsum), 2.5 cm (the ventral forearm), and 3 cm (the dorsal shoulder). These results correlate with the findings of Corniani and her group, who estimated an innervation density (in $\frac{units}{cm^2}$) of 241 in the fingertips, 58 in the palm, and 13 in the arm (Corniani and Saal, 2020). Koo et al. (2016) studied two-point discrimination on the arm of young Koreans, differentiating between the anterior and posterior parts of the arm. The anterior part of the upper arm is defined as the biceps region and the posterior part as the triceps region. A limitation of this study is that the biceps region is divided between the dermatomes T2 and C5, and the fact that the size of the cortical representation of the dermatomes on the sensory cortex and the number of neurons responsible for interpreting the stimulus differs between dermatomes (Penfield and Boldrey, 1937). Fewer studies address the problem of detecting continuous variation of vibrotactile stimulation. Dideriksen et al. (2021) performed a psychometric evaluation by comparing electro stimulation versus vibrotactile stimulation on the lower arm by varying amplitude and frequency. He showed similar performance of both interfaces at frequencies of 200 Hz, though users are faster at responding to changes in the stimulation parameters during the vibrotactile conditions.

Pathological conditions, such as stroke, brachial plexus injury, cerebral palsy, Parkinson's disease, and amputation, lead to distinct somatosensory dysfunctions. Schneider et al. observed that patients suffering from Parkinson's disease show a significantly higher minimal distances of two-point discrimination than a healthy counterpart on the index finger, but not on the lower arm (Schneider et al., 1987). Tyson described that tactile impairment is more common than proprioceptive impairment after a stroke (Tyson et al., 2008). Similar to amputations in brachial plexus injuries, tactile impairment depends on the level of the injury (Tung and Mackinnon, 2003). Sensory dysfunctions can lead to additional difficulties. For example, Auld et al. showed that spatial tactile deficits account for ∼30% of the variance in upper-limb motor function in children with unilateral cerebral palsy (Auld et al., 2012). Furthermore, tactile sensibility plays an essential role in body image and is necessary for experiencing body ownership and pain (Botvinick and Cohen, 1998; Ehrsson et al., 2008; Dietrich et al., 2012).

So far, the analysis of touch mainly focused on its most rudimentary form: short mechanical stimulation. State-of-the-art prosthetics and orthotics, however, often use vibration feedback to communicate several functions, such as switching modalities and velocity among others (Stephens-Fripp et al., 2018a), and the studies including these concentrate on single regions of the arm (Dideriksen et al., 2021). Additionally, little is known about the functionality of named modalities or the requirements for feedback devices at different levels of injury. The necessary size and strength of a vibration device might highly depend on how well the patient perceives vibration on the intended stimulation site. Furthermore, vibrotactile displays are commonly used in a wide array of applications, not only for the upper-limb rehabilitation but also in everyday appliances such as smartwatches and VR headsets (Da-Silva et al., 2018; Orand et al., 2019; Tanaka et al., 2021). Therefore, a proper understanding of how humans perceive vibration is a key to improving these technologies. Most studies investigating vibration so far either focused on the lower arm and hand (Marasco et al., 2018; Stephens-Fripp et al., 2018b; Wilke et al., 2019), on localized spots on some of the main dermatomes (Shah et al., 2019) or predefined arrays on one of the arm regions (Guemann et al., 2019).

A comprehensive mapping of the vibratory tactile sensations in the upper limbs is lacking. To close this knowledge gap, we systematically evaluated the vibrotactile sensations in the lower arm, upper arm, and shoulder region of 10 able-bodied subjects. These included the sensation threshold, the just noticeable difference, and the sensation of dynamically changing stimulation on 12 locations on the arm.

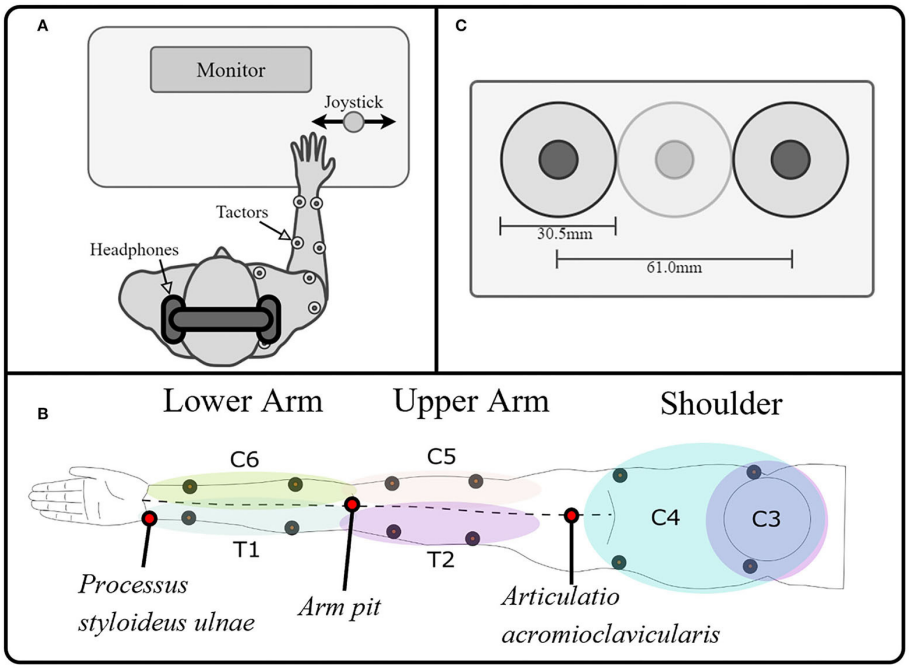

FIGURE 1
Experimental setup. **(A)** The experimental setup consisted of a PC for data recording, visual instructions, and tactile stimulation; a stimulator to control the tactors; and a joystick as the user interface. The subject was wearing noise-canceling headphones on which white noise was played whenever the tactors were on, to drown the noise generated by the vibration. **(B)**. A total of 12 tactors were placed on the arm and shoulder/neck, stimulating the dermatomes innervated by the cervical spinal nerves C6, C5 proximally and distally, the thoracic spinal nerves T1 and T2 proximally and distally, and the cervical spinal nerves C3 and C4 ventrally and dorsally, making it possible to map the tactile sensation to vibration over the whole arm. We divided the limb into three segments and evaluated each of them separately. These segments were defined as the lower arm (mainly innervated by T1 and C6), the upper arm (mainly innervated by T2 and C5), and the shoulder (mainly innervated by C3 and C4). **(C)** Additionally, we ensured that two tactors were always separated by at least a tactor-diameter, such that the minimum distance between the vibration centers was at least 61 mm.

Methods

Experimental setup

Ten healthy able-bodied subjects (three females and seven males, all right-handed) participated in the study. All subjects signed an informed consent form approved by the Ethics Committee of the University Medical Center Göttingen (Ethics Number: 26/6/20).

We investigated the vibrotactile sensation capacity for each of the six dermatomes of the arm-shoulder region, namely C3, C4, C5, C6, T1, and T2. The tactile sensations were elicited using vibro-tactors placed in pairs of two on each of the dermatomes (Figure 1B). Three types of psychometric evaluations (see sections Experimental tasks and protocol 1–3) were used to quantify the subject's response to the vibrotactile stimulation.

The subjects were seated comfortably in front of a desk with a computer screen during all experimental tasks. They wore active noise-canceling headphones on which white noise was played whenever the tactors were on to prevent the subjects from hearing the vibration of the tactor and ensure that the subject's decision was based solely on tactile sensation (Figure 1A). As a control interface, a modified joystick was connected to a PC *via* a USB port. Its spring was removed to achieve an optimal motion translation with only slight finger movement (HT Series, CH Products, USA). The PC controlled the output of the stimulation channels, which were attached to high-end vibration motors based on voice-coil technology that generate vibrations perpendicular to the skin (C2-tactor, Engineering Acoustics, Inc., USA; diameter: 30.5 mm). These tactors allow, to some extent, separated modulation of frequency and intensity, although the two parameters are coupled through a resonance effect (modulation of the amplitude did not affect the frequency, however, modulation of the frequency will, at some point, affect the amplitude). We controlled the amplitude with a precision of of 0.38% (arbitrary values between 0 and 255, from now on expressed in percentage of the maximal amplitude for easier reference) at their optimal operating frequency of 230 Hz (Engineering Acoustics Inc). We divided the limb into three segments and evaluated each of them separately. These segments were defined as the lower arm (mainly innervated

by T1 and C6), the upper arm (mainly innervated by T2 and C5), and the shoulder (mainly innervated by C3 and C4). On each dermatome of these segments, the tactors were positioned using the relevant anatomical features. We measured the length between the *Processus styloideus ulnae* and the armpit (PSU-AP), between the armpit and the *Articulatio acromioclavicularis (APAAC),* and between *the shoulders (SH).* We then placed the tactors as follows (Figure 1B):

1. Distal and Proximal T1, C6: $\frac{1}{3}$ $(PSU - AP)$ and $\frac{2}{3}$ $(PSU - AP)$ from the *Processus styloideus ulnae, respectively.*
2. Distal and proximal T2, C5: $\frac{1}{3}$ $(AP - ACC)$ and $\frac{2}{3}$ $(AP - ACC)$ from the *armpit, respectively.*
3. Dorsal C4 and C3: $\frac{1}{3}$ $(\frac{1}{2}$ $(SH))$ and $\frac{2}{3}$ $(\frac{1}{2}$ $(SH))$ from the *Articulatio acromioclavicularis, respectively.*

    - In the ventral part of C4 and C3, the placement had to be slightly adapted, avoiding the clavicle.

Additionally, we ensured that two tactors were always separated by at least a tactor-diameter, such that the minimum distance between the vibration centers was at least 61 mm (Figure 1C). On the lower arm, the tactors were proximal on C6 and T1 because the anatomical distance between distal points (for some subjects) could be lower than the minimally required distance for the simultaneous application of stimuli (i.e., lower than 61 mm). On the upper arm, the distal positions on C5 and T2 were selected to avoid unpleasant sensations induced by a constant vibration near the axilla, where the nervus ulnaris passes superficially. On the shoulder, the ventral locations on C3 and C4 were used because the sensation threshold there was significantly lower than on the dorsal part.

Experimental tasks and protocol

We performed three experimental tasks to evaluate the vibrotactile sensation capabilities of the lower arm, upper arm, and shoulder. The experimental tasks were carried out in three sessions, one per limb-shoulder region, lasting 1–2 h each with a break of at least 1 hour between the sessions (or the sessions were performed on three separate days). The order of the tested region was pseudo-randomized using all possible combinations ($3! = 6$). This means, that given the three regions (l – u – s), the list of possible combinations is l – u – s, l – s – u, u – l – s, u – s – l, s – l – u, and s – u – l. In our case, having more than six participants, we simply started the list all over again.

The tasks are summarized here and described below in more detail:

1. We measured the *tactile sensation threshold* by gradually increasing the amplitude of each of the 12 vibro-tactors individually, i.e., quantifying the sensation threshold in four points of each of the arm-regions mentioned above.
2. We calculated the *Weber fraction*, which describes the needed percentual change of the amplitude to be noticeably different for the participant, and the number of distinct intervals that the subject could perceive. This was performed by measuring the *just noticeable difference* in amplitude between two different vibrotactile stimulations delivered on the same spot, one after the other (again in four points per arm region).
3. Finally, we used a *compensatory tracking task* to study the subject's ability to distinguish continuous stimulation on the two main dermatomes of each arm segment. Here, we used an approach called frequency identification of human operators based on the control theory by McRuer and Weir (1969) already used by Dosen et al. (2014) for similar purposes. The human transfer functions obtained in this block allowed us to estimate the human operator's magnitude and phase delay for dynamically changing stimulation signals. This was performed only once per arm region, thus yielding a total of three data points per subject.

Sensation threshold

The sensation threshold (ST) was determined using the method of limits on each stimulation side (Botvinick and Cohen, 1998). The experimental task started by selecting one out of four tactors in the selected region from a randomly permutated list that was previously generated with MATLAB's *randperm()* function. This tactor was turned on while the others were kept off. Starting from 0% amplitude, the stimulation intensity of this tactor was increased in steps of 0.78% with a break of 0.5 s between consecutive stimuli. The duration of the stimuli was set to last for 1.25 s. The subject was asked to verbally report the first time (s)he was sure that (s)he perceived the stimulation. After the subject reported that (s)he perceived the stimuli, the stimulation was stopped, and one additional stimulus of 1.25 s duration at the maximum amplitude was applied. The subject was then asked to identify the location on her arm where she perceived the stimulation.

Hereafter, the next tactor in the same region was randomly selected as the active one, and the process was repeated until each of the four tactors was tested three times in each of the three arm-shoulder regions. The overall procedure lasted for about 1 h, and it was performed in one session. Herewith, we obtained the ST for each of the 12 measuring points.

Since the vibro-tactors did not produce painful sensations at the maximum intensity, the upper limit of the intensity range was defined as the maximal stimulation amplitude (100%). Therefore, for each stimulation site i, the testable intensity range was defined as $[ST_i, 100\%], i=1, \ldots, 12$.

Just noticeable difference

During the second task, we measured the just noticeable difference (JND), which described the minimal difference in

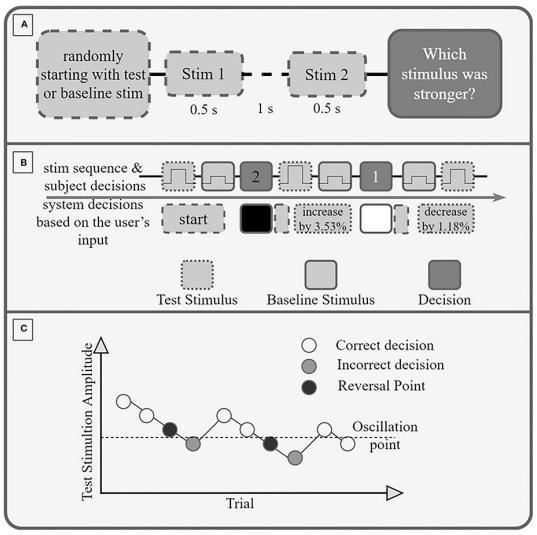

FIGURE 2
(A) Experimental Protocol. If the first stimulus is the test stimulus or the baseline stimulus is decided randomly. Each stimulus is 0.5 s long, and between the stimuli is a break of 1 s. After the second stimulus, the participant must decide (and select *via* the joystick) if the first or second stimulus had a higher amplitude (was stronger). **(B)** Exemplary sequence of trials. A wrong decision increases the amplitude of the test stimulus by 3.53%, a correct decision decreases it by 1.18%. **(C)** Exemplary Staircase sequence. The amplitude of the stimulation is reduced after each correct decision and increased after an incorrect decision. A reversal point is the last correctly recognized amplitude before an incorrect decision. The oscillation point is the average amplitude of 10 reversal points.

amplitude between two subsequent stimulations that the subject can perceive. The order of the evaluation of arm-shoulder regions was determined randomly. Once the region was selected, four tactors were placed on the proximal and distal (or ventral and dorsal, in case of the shoulder) sides of the corresponding dermatomes. Like in the previous experimental task, one tactor (i.e., one dermatome) was randomly selected as active. The task continued by stimulating the selected dermatome with two consecutive stimuli of different intensities— a base (lower and constant) and a test (higher and variable) stimulation. The duration of the stimuli was 0.5 s, followed by a break of 1 s before the second stimulus (Figure 2A). The order of the two stimuli was randomized. After each pair of stimuli, the subject was asked to select the stimuli with the higher intensity by turning the joystick left (indicating the first stimulus had higher intensity) or right (meaning the second stimulus had higher intensity). Put differently, the subject was asked to identify which of the two stimuli was the test stimulus. Afterward, the subject was stimulated again, and this process was repeated until a total of 10 reversal points were reached (see below). Within the selected stimulation site, the baseline stimulus always had the same intensity, whereas the intensity of the test stimulus was varied according to the staircase method. Namely, the baseline intensity was fixed to $ST_i + 0.15*(100\% - ST_i)$, while the test stimulus was initially set to $ST_i + 0.9*(100\% - ST_i)$. Increasing the baseline stimuli by 15% of the perceivable range was performed because we expected that applying stimulation continuously on the same spot would slightly shift the ST upward (due to the adaptation effect), thus rendering the baseline stimuli unperceivable. Likewise, decreasing the first test stimulus to 90% of the testable range was done to prevent overstimulation and thus slow down the overall adaptation to the stimuli. If the subject correctly identified the stimulus with the higher intensity (i.e., the test stimulus), the intensity of the following test stimulus was decreased by 1.18% of the maximum amplitude; if, on the other hand, the subject made a mistake, the intensity of the following test stimulus was increased by 3.53% (Figure 2B).

The oscillation point was identified as the average intensity preceding all stimuli with incorrect identifications across all trials, i.e., as the average of 10 reversal points (Figure 2C).

Finally, the JND of the selected stimulation site was obtained as the difference between the oscillation point (OP) and the baseline intensity expressed as a percentage of the maximum amplitude $JND_i = OP - (ST_i + 0.15*(100\% - ST_i)$. The overall process was repeated for each stimulation site (i) in each arm-shoulder region, thus yielding 12 distinct measurements of the JND_i, $i=1, \ldots, 12$.

Closed loop compensatory tracking

In order to investigate the subject's ability to differentiate between dynamically changing stimulations, we used a compensatory tracking task, in which the subject received two-dimensional information about her performance. More specifically, the subject performed compensatory tracking of a 90 s long reference signal in a real-time control loop by using a joystick as an input interface (Figure 3). The reference signal consisted of a pseudorandom multi-sine wave with nine components between 0.1 and 2 Hz, where the five sine waves with the higher frequencies (>0.4 Hz) had half the power as all other components combined. The signal was in the range of $[-1, 1]$. The tracking error was defined as the difference between the user input (i.e., the joystick position) and the reference signal. This error was conveyed either *via* two tactile units placed on two different dermatomes on one of the previously selected arm-shoulder regions or *via* the computer screen. To train the task, the subject first performed it using only visual feedback. In this condition, the error was indicated as a red circle on the computer screen, moving along a horizontal axis. In the middle, a green vertical line marked zero error. Therefore, the subject was instructed to move the joystick to keep the red circle on the green vertical line. In the vibrotactile feedback condition, the sign of the error was spatially encoded by the two stimulation units. The stimulation amplitude was

proportional to the error magnitude in the range from ST plus 15% of the intensity range (indicating a minimal error of just above zero) to ST plus 90% of the intensity range (indicating the maximum error of one unit; errors higher than one were capped to this value). The sign of error was thereby mapped to a spatial sensation while the intensity of the stimulation was proportional to the magnitude of the error. In the vibrotactile feedback condition, the task for the subject was to minimize the stimulation intensity (zero tracking error = no stimulation). To achieve this, the subject had to move the joystick proportionally to the perceived stimulation intensity and in a direction that is opposite from the active stimulation site. Importantly, although the task was repeated for each arm-shoulder region only one tactor per dermatome was used in the vibrotactile condition.

The subjects performed as many trials as needed in the visual condition to become familiarized with the task (usually one or two attempts). When the subjects reported that they were confident with the task, they were instructed to perform 10 additional trials using visual feedback only. After these 10 trials had been completed, vibrotactile feedback was added to the visual one, and the subject was asked to perform the task three additional times. While performing the task in this visual-tactile condition, the subject was asked to focus on the correlation between the movement of the red circle on the computer screen and the stimulation sensation. Therefore, while performing the task in this condition, the subject could associate the tactile sensation with the visual representation of the tracking error. Finally, the subject proceeded with training to use the tactile feedback only for at least three trials (or more, until (s)he was able to reach a tracking correlation coefficient of 0.6 or above–see data analysis). Afterwards, the actual evaluation started and consisted of 10 additional trials. A break of 1–2 min was introduced after each trial to avoid mental and physical fatigue. As in previous tasks, the order of the evaluated arm-shoulder regions was randomly selected. The overall process resulted in a total of 30 data points for the vibrotactile condition (10 per arm-shoulder region) and the additional 10 data points for the visual condition.

Data analysis

The following outcomes were used to interpret the acquired data: (1) the sensation threshold at which the participant was able to feel the stimulation, (2) the success rate of identifying the stimulation location (3) the number of distinct intervals (NDI), which refers to the number of intervals separated by the magnitude of the JND within the dynamic range, (4) the Weber fraction, as the needed percentual difference between two stimuli to be successfully identified as different, and (5) the tracking performance interpreted from the delay, the average rectified error, and the correlation coefficient during the tracking task.

For every individual subject, the ST of any of the 12 locations in the arm-shoulder region was estimated by averaging the data obtained from the three ST measurements (trials) that were performed for that location. Then, these values were additionally averaged and compared (1) the three different segments (the lower arm, upper arm, and shoulder) and (2) the two different sides of the arm-shoulder region (the ventral and dorsal).

Similarly, the subject's JND was calculated across individual locations, arm-shoulder segments, and ventral and dorsal sides. In addition, the JND was used to compute the number of distinct intervals (NDI) that a subject could perceive. Since the JND is expressed as a percentage of the maximal stimulation intensity, the NDI was calculated iteratively according to the equation: $I_{k+1} = I_{k'} + JND{*}I_k$, where I indicates the stimulation intensity and k counts the intervals. Initially, k was assigned the value of one and was increased in steps of one until I_{k+1} passed the upper limit of the dynamic range (maximum intensity). Once this happened, the NDI was set to the value of k. For instance, in a range from 1 to 100 arbitrary units with a JND of 5, there are 20 NDIs. Finally, the Weber fraction (WF) was also calculated from the JND by applying the following formula: $WF_i = \frac{JND_i}{b_i} {*} 100$ (Weber, 1834b), where b indicates the baseline intensity defined in Just noticeable difference.

The outcome measurement of the third experimental task was the trial tracking performance assessed by comparing the shape similarity, average deviation, and time delay between the generated and reference trajectories for each of the three arm-shoulder segments. The correlation between the reference and the generated trajectory was identified as the peak of the cross-correlation function. Furthermore, the time delay between the target and the generated trajectory was estimated from the temporal location of the peak in the cross-correlation. After compensating for this delay, the average rectified error was calculated. Finally, the mean values of these three parameters (shape similarity, average deviation, and delay) were calculated for each subject (and the arm-shoulder segment) by averaging the outcomes of the 10 compensatory tracking trials.

For all outcome measures separately, we performed one-sample Kolmogorov-Smirnov tests and found that none of the outcome parameters was normally distributed. Therefore, we utilized Friedman tests in combination with *post-hoc* Wilcoxon signed-rank tests to detect statistical differences between different locations, segments, and sides of the arm-shoulder region. More precisely, when all 12 locations in the arm-shoulder region were compared, a Friedman test with 12 levels was used. When comparing the three different segments (the lower arm, upper arm, and shoulder), a Friedman test with three levels and hence three *post-hoc* Wilcoxon signed-rank tests were conducted. For the two different sides of the arm-shoulder region (the ventral and dorsal), a single Wilcoxon signed-rank test was sufficient. As none of the outcome measures was normally distributed, only non-parametric statistics and hence one-factor tests could be used.

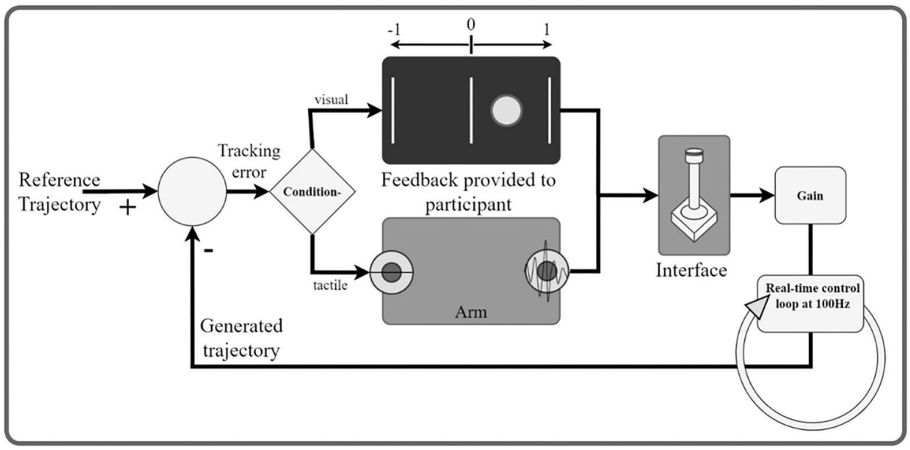

FIGURE 3
Schematic illustration of the real-time control loop. The participant (human operator) is a part of a dynamic system. The goal is to generate a signal with the joystick that minimizes the tracking error with respect to a predefined reference trajectory. The tracking error is communicated to the participant through tactile/visual feedback. In the visual feedback, the onscreen circle communicates the sign and the magnitude of the error. In the tactile conditions, the active stimulator codes for the sign and the amplitude for the magnitude of the error.

All statistical tests were corrected for multiple comparisons using the Bonferroni-Holm correction. The statistical difference threshold was set to 0.05. All results are presented as "median (interquartile range (IQR))".

Results

To achieve a comprehensive mapping of the tactile sensations in response to vibrotactile stimulation across the whole arm-shoulder region of 10 able-bodied participants, we performed three psychometric evaluations.

Sensation threshold

All participants were able to correctly identify the active tactor in all 36 trials (100% success rate; results not depicted). No statistical differences were detected between sensation thresholds (STs) of any of the 12 individual locations in the arm-shoulder region (Figure 4A). However, when the mean ST of the respective four locations on the lower arm, the upper arm, and the shoulder were compared, the shoulder segment exhibited a significantly higher ST than the lower arm (Figure 4B; 3.1 vs. 2.3% ($p = 0.0039$) of the maximal stimulation amplitude). Furthermore, the average ST of the six locations on the dorsal side of the arm was significantly larger than the mean of ST of the locations on its ventral side (Figure 4C; 2.88% in comparison with 2.27% ($p = 0.0078$) of the maximal amplitude).

Taking a closer look at the single segments, we found no significant differences between the distal and proximal parts of any segment (Figure 5A). Applying the same analysis to the ventral and dorsal area of each segment we identified significant differences in the lower arm and the shoulder (Figure 5B). In both locations, the threshold amplitude on the dorsal side needed to be significantly higher than on the ventral side to detect vibrotactile stimulation ($p = 0.0391$ on the lower arm; $p = 0.0313$ on the shoulder).

Just noticeable difference

During the second task, the participant had to differentiate between two sequential stimuli and select the one she perceived as having a higher amplitude. Differences between baseline and test stimuli above 20 [7%] were reliably detected across all arm-shoulder regions, without any significant differences between them [neither between single locations (Figure 6A) nor between the defined regions (Figure 6B) or sides (Figure 6C)]. Likewise, the number of discrete steps that could be provided using the obtained tactile sensation range 11 [3%] did not show any significant difference between the arm-shoulder segments (again, neither between single locations (Figure 7A) nor between the defined regions (Figure 7B) or sides (Figure 7C)). Again, a closer look at the single segments exposed neither significant differences between distal and proximal sides nor ventral and dorsal sides of any segment regarding the Weber fraction, and the number of distinct intervals (Figures 8, 9).

Closed loop compensatory tracking

In the compensatory tracking task, the participant acted as the controller in a closed-loop system, compensating for the error between a generated and a reference signal. (S)he

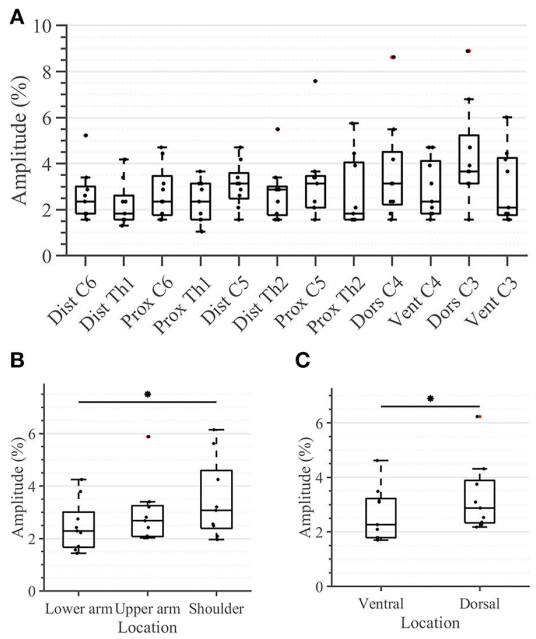

FIGURE 4
Task 1–Sensation thresholds (in percent of the maximum stimulation amplitude) for **(A)** all 12 locations in the arm-shoulder region, **(B)** the three arm-shoulder segments, and **(C)** the ventral and dorsal side of the arm-shoulder region. The box plots depict the median value (horizontal line) and the IQR (rectangle) of mean ST data collected from 10 subjects. Red crosses indicate statistical outliers within a single box plot ($n = 10$). An asterisk indicates that there is a statistical difference ($p < 0.05$, corrected).

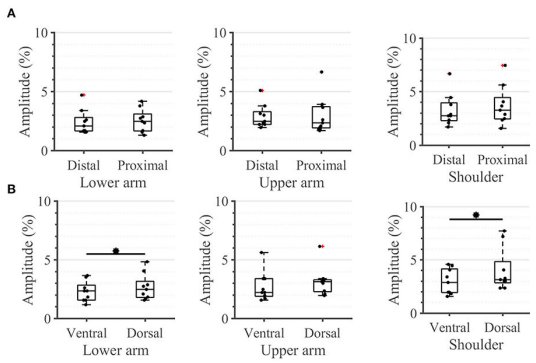

FIGURE 5
Task 1-Sensation thresholds. A closer look (in percent of the maximum stimulation amplitude) for **(A)** the distal and proximal parts of the three segments of the arm, **(B)** the ventral and dorsal parts of the three segments of the arm. The box plots depict the median value (horizontal line) and the IQR (rectangle) of mean ST data collected from 10 subjects. Red crosses indicate statistical outliers within a single box plot ($n = 10$). An asterisk indicates a significant statistical difference ($p < 0.05$).

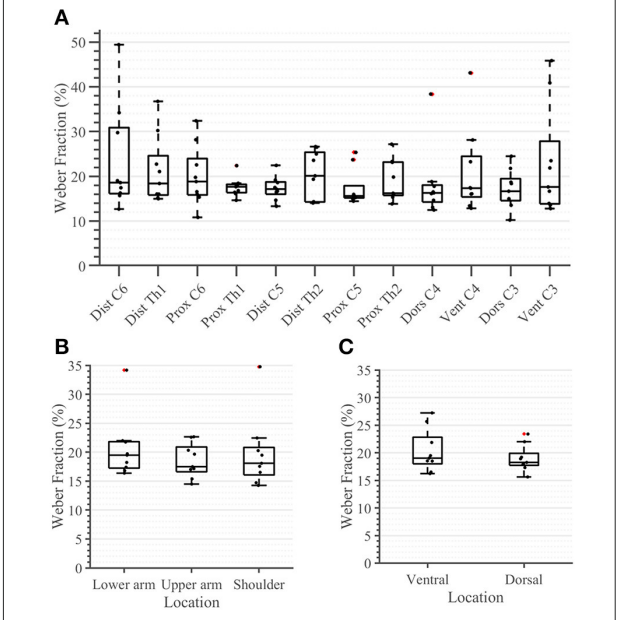

FIGURE 6
Task 2 -Weber Fraction (in percent) for all 12 locations in the arm-shoulder region **(A)** on the tested parts of the arm, as a combination of the results of the dermatomes in each region (the lower arm, the upper arm, and the shoulder), **(B)** and in each side (the ventral and dorsal), **(C)** ($n = 10$). The red points show outliers.

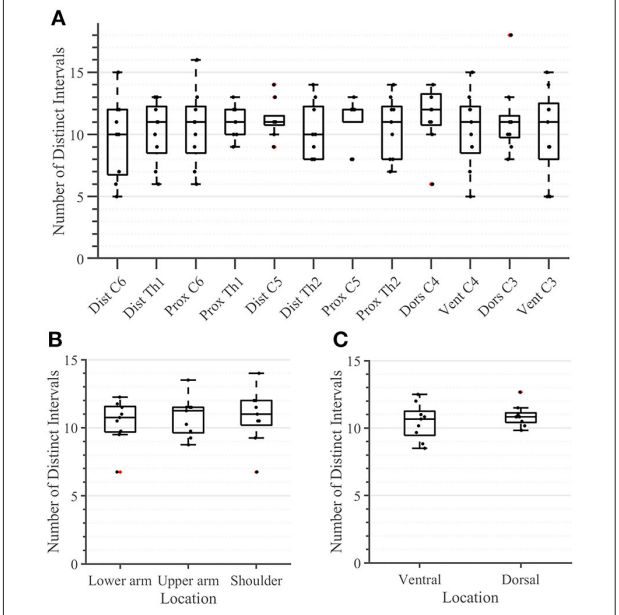

FIGURE 7
Task 2 -Number of Distinct Intervals for all 12 locations in the arm-shoulder region **(A)** on the tested parts of the arm, as a combination of the results of the dermatomes in each region (the lower arm, the upper arm, and the shoulder), **(B)** and in each side (the ventral and dorsal) **(C)**, ($n = 10$). The red points show outliers.

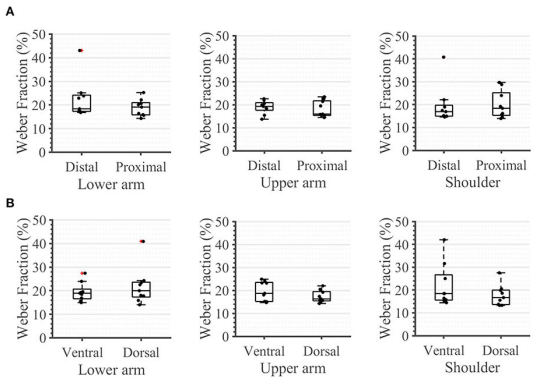

FIGURE 8
Task 2 -Weber Fraction. A closer look. in percent, for **(A)** the distal and proximal parts of the three segments of the arm, **(B)** the ventral and dorsal parts of the three segments of the arm. The box plots depict the median value (horizontal line) and the IQR (rectangle) of mean ST data collected from 10 subjects. Red crosses indicate statistical outliers within a single box plot (n = 10).

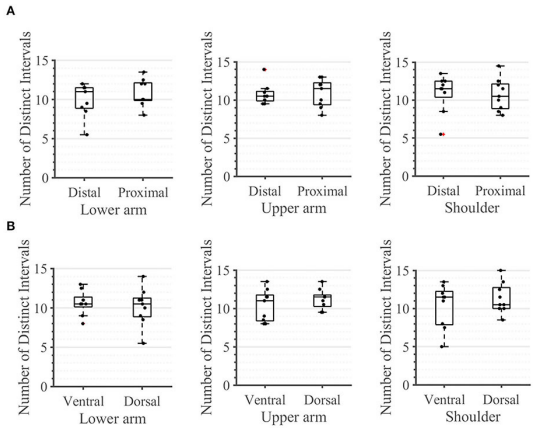

FIGURE 9
Task 2 -Number of Distinct Intervals. A closer look for **(A)** the distal and proximal parts of the three segments of the arm, **(B)** the ventral and dorsal parts of the three segments of the arm. The box plots depict the median value (horizontal line) and the IQR (rectangle) of mean ST data collected from ten subjects. Red crosses indicate statistical outliers within a single box plot (n = 10).

used a joystick as an input interface and received either visual or tactile feedback about her performance. To ensure the subjects understood and adequately performed the task, we used the session in which the subject performed the task receiving visual feedback on the monitor, as a baseline with optimal feedback. The subjects in this condition showed a significantly better performance in all aspects (results not shown).

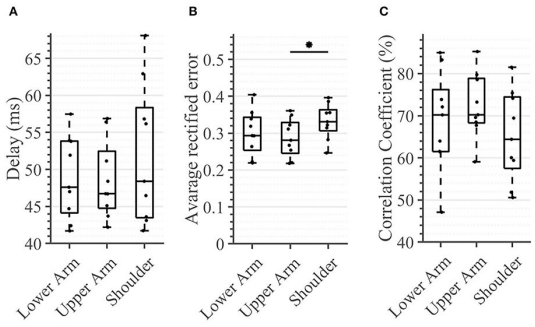

FIGURE 10
Task 3 -Average performance in the compensatory tracking task for all subjects and conditions. Here, time delay **(A)**, average rectified error **(B)**, and correlation coefficient **(C)** between the target and cursor is shown (n = 10). An asterisk indicates that there is a statistical difference ($p < 0.05$).

In the tactile feedback condition, neither the delay nor the correlation coefficient was significantly different between any segments (Figure 10). The delay was consistently below 48.5 ms [11.65 ms] and the correlation coefficient was in the range of 64.4–72.2% [13.6%], for the three evaluated segments. The only detected significant difference was between the shoulder and the upper arm where the average rectified error was significantly higher in the latter case (0.33 [0.06] vs. 0.28 [0.08] ($p = 0.0039$)).

Discussion

In this study, a map of the vibrotactile sense of the healthy upper limb was generated, seven males and three females. Neely and Burström (2006) reported, that no gender-specific differences are found during vibrotactile threshold measurements to the arm region, thus, we will not make any distinction between the gender of participants in the further discussion. The arm-shoulder region was divided into six dermatomes and three segments–the lower arm, the upper arm, and the shoulder region, each stimulated proximally and distally. For psychometric evaluation, tasks resulting in the quantification of sensation threshold, just noticeable difference, and perception of dynamically changing vibrotactile stimuli were used.

In our study, we decided to vary the amplitude of the stimulation, keeping the frequency fixed at 230 Hz. Due to the coupling effect between frequency and amplitude, while the frequency remains unaffected when the amplitude is modulated, the amplitude will change when the tactor operates outside the optimal frequency range, which is between 200–250 Hz for the C2 tactors (Engineering Acoustics Inc). Indeed, Dideriksen et al. (2021) shows that electrotactile stimulation performs better than C2 tactors at frequencies lower than 200 Hz. However, once the

frequency of the vibrotactile approaches the optimal range, both stimulation modalities perform similarly.

The sensation threshold

To be perceived, the stimulation applied to the shoulder segment needed to have a significantly higher vibration amplitude than the stimulation applied to the lower arm. The selected vibrotactile stimulation frequency (230 Hz) mainly targets the Pacini corpuscles in the skin (Saddik et al., 2011). The fact that the Pacini receptor density in the upper limb increases in the direction from the shoulder to the hand (Montagna, 1965; Johansson and Vallbo, 1979; Vallbo and Johansson, 1984), might explain our findings. As previously mentioned, we are not able to find any literature regarding differences in receptor density between the ventral and dorsal sides of the arm-shoulder region, as most of the studies investigate this only in the hand in which the dorsal side is covered in hairy skin and the ventral side in glabrous skin with their respective differences in innervation (Liu et al., 2007; Li et al., 2011). Since the arm is completely covered in hairy skin (Zimmerman et al., 2014) one would not expect such differences here. Interestingly, we find differences between the ST on the ventral and dorsal sides of the arm segments. These are significant only for the lower arm and the shoulder. In both segments, the ST is significantly lower ventrally. This might possibly be explained by the differential innervation of these locations. Another possible reason could be the thicker muscular tissue covering the bone on the dorsal parts of the lower arm and the shoulder, compared with their ventral counterparts. This proximity of the vibrotactile stimulation to the bone and the missing dampening of the soft tissue might lead to a better perception of the vibration. Indeed, Jacobs et al. (2000) performed an experiment in which they vibrotactilely stimulated the thumb/foot sole of the prosthetic and normal limb of amputees. They reported that upon vibratory stimulation of the residual limb, bone-anchored prostheses yielded better perception than socket prostheses, which are based on soft tissue support. Comparing the sensation threshold between the healthy hand and the socket prosthesis exposed an average increment of 20% for the affected side. When comparing the sensation threshold between healthy hands and bone-anchored prostheses, the affected side is similar to the control limb. This would also be consistent with the lack of significant differences in the upper arm in our study, where the ventral and dorsal muscle cover is similar.

Finally, all participants are able to correctly spatially identify the active vibrotactile unit. Given the spatial layout of tactile stimulation that is used in our experimental setup (see Figure 1B), it follows that vibrotactors can be successfully distinguished at a distance of 61 mm. This result is comparable with the reported ability of discrimination between two points (two-point discrimination) ranging from 30.7 to 42.4 mm (mid-posterior lower arm and lateral upper arm, respectively) (Nolan, 1982), suggesting that the perception of vibrotactile localization is in the same order of magnitude as two-point discrimination. Obviously, the lack of measurements at smaller distances leaves the possibility open that the subjects could correctly perceive distances between tactors below 61 mm.

The Weber fraction and NDI

In contrast to the ST, we found no significant difference in any segment regarding either the Weber fraction (WF) or the number of discrete intervals (NDI). The same applies when comparing these outcomes ventrally vs. dorsally or observing the single segments (Figures 8, 9). These results are somewhat expected since the WF defines a *relative* change of amplitude between two stimuli, not an *absolute* one. In this case, it is the activation threshold of a single receptor (and to some extent, its signal to noise ratio) and not the density of receptors that determines the result. Therefore, assuming that we are activating the same family of receptors over the whole arm-shoulder region, the WF, and consequently, the NDI too, are expected to be similar in every location. In this light, our results suggest that we activated the same types of receptors at different sites of the investigated regions. Overall, previous studies on the perception of vibration on the lower arm show that the Weber fraction is in the range of 17% (at 200 Hz) to 30% (at 300 Hz) (Rothenberg et al., 1977; Mahns et al., 2006), which is consistent with our findings of a WF value of 20% across all locations in the arm-shoulder region at a 230 Hz stimulation frequency. Interestingly, the WF obtained on the fingertips using a similar setup and a frequency of 200 Hz was only ca. 18% lower than that of the lower arm, although the ST of the fingertip was ca. 63% below the value obtained on the lower arm (Mahns et al., 2006). This further supports the claim that the sensation threshold indeed decreases substantially more from the proximal to distal on the whole limb and that this is not the case for the Weber fraction.

Whereas, the sensation threshold represents a minimum *absolute* value of stimulation intensity that one can perceive, the Weber fraction measures, in contrast, a minimal *relative* change of stimulation intensity that an individual can detect. Therefore, while the ST can give some information about the receptor density this is not true for the WF, which reflects the receptors' overall physiological functioning and their interaction with the surrounding tissue. In the applied case of feedback reproduction in the healthy arm, it is possible to calculate the required difference between two stimuli at all points based on the measurement of the sensation threshold at the desired points, as well as the measurement of the Weber fraction at one of these points. This is possible if all regions have the same skin and similar structures. In fact, we tested this assumption by taking

the ST at all measuring points and computing WF using the measured WF at one of these points. We repeated the procedure for all WFs and calculated a standard deviation of 0.31% with an absolute mean error of 0.44%. This error is about 2.2% of the mean measured Weber fraction and is therefore acceptable. This might help in the implementation of feedback, as the calibration would need to be performed once if the used frequency and amplitude are targeting one kind of receptor. The stimulation could then be provided over the whole arm with the same relative signal.

The compensatory tracking task

There were no significant differences between the arm regions in the time delay that the subject exhibited in following the reference trajectory. This outcome could be potentially explained by the fact that the delay of the sensory pathway was relatively small in comparison with the other delays that were present in the control loop (e.g., the motor delay and cognitive processing delay), thus failing to account for a substantial difference across different arm-regions. Indeed, the mean distance from the stimulation site on the lower arm to the spinal cord was 63 cm, from the upper arm 43 cm, and from the shoulder 13 cm for our participants. The Pacinian corpuscles are innervated by Aβ (large, myelinated) fibers with conduction velocities up to 70 m/s (Montaño et al., 2010); this implies a travel time of 8.96 ms from the stimulation site of the lower arm, 6.15 ms from the upper arm, and 1.8 ms from the shoulder. These times lie in the interquartile range of the delay observed for each site and therefore do not account for differences in the time delay, thus correlating with our results. Therefore, the travel time of the stimuli, which is a consequence of nerve conduction velocity, do not significantly contribute to the measured time delay. This likewise suggests that the cognitive processing of the stimuli and the motor command execution delay are invariant to the alterations between the stimulation regions. Stepp et al. came to a similar conclusion investigating the importance of training compared with the importance of the vibration site. They found out that participants experienced a strong learning effect within a single session. The effects of the vibration site, however, are less dramatic (Stepp and Matsuoka, 2011).

Looking at the average rectified error, we found a difference between stimulated regions. In contrast to the the time delay, the rectified error is not dependent on the physiological reaction time but on the user's ability to correctly classify the provided feedback and properly react to it (see Figure 10B). Similar to the experimental task in which we calculated the WF, the subject could have been just differentiating between two consecutive stimuli and deciding which one was stronger. Consequently, a rectified error of zero would imply that the user would have been able to distinguish between infinite NDIs. As all regions possess the same NDIs, one might expect that no significant differences will be seen between the regions. However, the shoulder showed a significantly higher tracking error when compared with the upper arm. An explanation for this might be that the subject was using the aforementioned mechanism of comparing subsequent stimulations to determine the sign of the trend of the error (i.e., to determine if the error is increasing/decreasing), but here, (s)he also needed to know if the error is large or small (in absolute terms) in order to react accordingly. Therefore, the compensatory tracking task requires a combination of skills, that is, the ability of differentiating between *relative* changes and appropriately identifying the overall magnitude of the stimulation (i.e., its *absolute* value). This second aspect might contribute, just as it happens in the sensation threshold, to a deterioration of performance as one moves proximally. Indeed, the correlation coefficient indicates at least a statistical trend (corrected $p < 0.1$) of worsening performance between the lower arm and the shoulder.

Practical implications for design of vibrotactile displays

Some of the results obtained during our experiment might have a significant impact on the design and evaluation of devices for vibrotactile stimulation of the upper limbs. For instance, we obtained significant differences between the sensation threshold of proximal and distal segments (Figures 4, 5). However, the perception of the relative changes in the stimulation intensity is invariant to the arm region (Figure 6). Moreover, the STs, although significantly different, are still very small with respect to the overall amplitude range–none of the measured locations exhibited an ST >6% of the maximal amplitude. One practical implication of these results is that the vibrotactors applied to the arm could be of similar size and power, independent of their location, facilitating their optimized mechanical design. This observation is further supported by the delays measured during the compensatory tracking task. Here, we discussed that the cognitive processing of the stimuli and the execution delay of motor commands are not significantly affected by the distance of the stimulation site to the spinal cord or its origin on the arm. Therefore, individuals are capable to use the feedback devices efficiently and with similar cognitive effort across all arm-shoulder dermatomes.

A specific application scenario could be vibrotactile feedback for upper-limb prostheses that communicates the prosthesis' grip force (or a similar variable) by modulating the vibration intensity (e.g., the higher the intensity the higher the grip force (Stephens-Fripp et al., 2018a)). In this context, our results are promising for amputees since the arm location on which feedback is delivered can significantly vary. This allows supplying individuals with different amputation levels with feedback (for transradial amputees on the lower arm, for

transhumeral amputates on the upper arm or the shoulder). Given that the overall implementations of the feedback and prosthetic systems are similar, our results suggest that both transhumeral and transradial prosthetic users may have a similar level of proficiency in perceiving and interpreting the feedback (i.e., the prosthesis grip force). More specifically, since the WF was largely invariant between the upper and lower arm, both groups of individuals should be able to perceive and quantify the (relative) changes in grip force with similar performance (i.e., its relative increase or decrease from arbitrary nominal value). However, the lower ST of the lower arm also suggests that individuals suffering from transradial amputation could have advantages over their transhumeral counterparts in quantifying the actual amplitude of the prosthesis' grip force, i.e., in classifying the vibration intensity in absolute terms (e.g., as high, medium, or low). Nonetheless, the difference in the overall performance of the two subject groups is still unlikely to be functionally relevant: The tracking task has demonstrated remarkable similarity in the real-time interpretation of feedback across different arm-regions and every feedback interface is a part of an overarching sensory-motor integration framework. This framework consists of several intertwined layers, namely, the feedforward motor control, the control system, and the end-effector that, in combination with feedback, ultimately determine the outcome of the user's actions (Sensinger and Dosen, 2020).

Our data suggest that the receptors show a similar response to relative changes of the vibration stimuli, i.e., to those changes that are normalized to the perceivable range of stimulation—Weber fraction and number of distinct intervals are the same across all segments of the arm-shoulder region. However, different arm segments have different perceivable ranges of stimulation—the sensation threshold is significantly increasing from the distal to proximal regions. The higher tracking error in the tracking task in the shoulder compared with the arm region might have resulted from the smaller perceivable stimulation range in the shoulder region (i.e., the higher sensation threshold), leading to a decreased ability to properly assess the magnitude of the error in the tracking task. Nonetheless, even if some variations exist, the healthy arm and shoulder region can perceive vibrations at 230 Hz at relatively low amplitudes (in the range of 2–6%) and differentiate between two sequential stimulations if their amplitudes differ by 20%. As two of three outcome measures in the compensatory tracking task are invariant to a change in arm location, the ability of the subject to perceive dynamically changing stimuli is only marginally dependent on where it is applied.

Our discussion assumes that we are targeting the Pacini corpuscles. Even if the design of our study does not allow us to establish if there are differences between receptors since we do not correlate our results with histological studies, our data suggest that the receptors activated by the vibration stimuli show the same behavior across all locations, independent of their structural entity.

In summary, our experiments provide elementary insights regarding the vibrotactile sensation capacity of the healthy upper extremity. Since vibrotactile displays are the state-of-art in a wide array of applications, these results might contribute to an increased effectiveness of their use.

Data availability statement

The raw data supporting the conclusions of this article will be made available by the authors, without undue reservation.

Ethics statement

The studies involving human participants were reviewed and approved by the Clinical Ethics Committee of the University Medical Center Göttingen (Ethics Number: 26/6/20). The patients/participants provided their written informed consent to participate in this study.

Author contributions

LP, MM, AS, and JE contributed to the conception and design of the study. LP and MM collected the data and wrote the first draft of the manuscript. LP and MAW performed the statistical analysis. All authors contributed to manuscript revision, read, and approved the submitted version.

Funding

This study was partly supported by unrestricted grants of the German Federal Ministry of Education and Research BMBF to JE and AS (13GW0340B/16SV7657).

Conflict of interest

The authors declare that the research was conducted in the absence of any commercial or financial relationships that could be construed as a potential conflict of interest.

Publisher's note

References

Auld, M. L., Boyd, R. N., Moseley, G. L., Ware, R. S., and Johnston, L. M. (2012). Impact of tactile dysfunction on upper-limb motor performance in children with unilateral cerebral palsy. *Arch. Phys. Med. Rehabil.* 93, 696–702. doi: 10.1016/j.apmr.2011.10.025

Botvinick, M., and Cohen, J. (1998). Rubber hands 'feel'touch that eyes see. *Nature* 391, 756–756. doi: 10.1038/35784

Corniani, G., and Saal, H. P. (2020). Tactile innervation densities across the whole body. *J. Neurophysiol.* 124, 1229–1240. doi: 10.1152/jn.00313.2020

Darian-Smith, I. (2011). "The sense of touch: performance and peripheral neural processes," in *Comprehensive Physiology*, ed R. Terjung. doi: 10.1002/cphy.cp010317

Da-Silva, R. H., van Wijck, F., Shaw, L., Rodgers, H., Balaam, M., Brkic, L., et al. (2018). Prompting arm activity after stroke: a clinical proof of concept study of wrist-worn accelerometers with a vibrating alert function. *J. Rehabil. Assist. Technol. Eng.* doi: 10.1177/2055668318761524

Dideriksen, J., Markovic, M., Lemling, S., Farina, D., and Dosen, S. (2021). Electrotactile and vibrotactile feedback enable similar performance in psychometric tests and closed-loop control. *IEEE Trans. Haptics* 15, 222–231. doi: 10.1109/TOH.2021.3117628

Dietrich, C., Walter-Walsh, K., Preißler, S., Hofmann, G. O., Witte, O. W., Miltner, W. H. R., et al. (2012). Sensory feedback prosthesis reduces phantom limb pain: proof of a principle. *Neurosci. Lett.* 507, 97–100. doi: 10.1016/j.neulet.2011.10.068

Dosen, S., Markovic, M., Hartmann, C., and Farina, D. (2014). Sensory feedback in prosthetics: a standardized test bench for closed-loop control. *IEEE Trans. Neural Syst. Rehabilitation Eng.* 23, 267–276. doi: 10.1109/TNSRE.2014.2371238

Ehrsson, H. H., Rosén, B., Stockselius, A., Ragnö C., Köhler, P., and Lundborg, G. (2008). Upper limb amputees can be induced to experience a rubber hand as their own. *Brain* 131, 3443–3452. doi: 10.1093/brain/awn297

Engineering Acoustics Inc. Available online at: https://www.eaiinfo.com/product/c2 (accessed August 20, 2021).

Guemann, M., Bouvier, S., Halgand, C., Paclet, F., Borrini, L., Ricard, D., et al. (2019). Effect of vibration characteristics and vibror arrangement on the tactile perception of the upper arm in healthy subjects and upper limb amputees. *J. Neuroeng. Rehabil.* 16, 1–16. doi: 10.1186/s12984-019-0597-6

Jacobs, R., Brånemark, R., Olmarker, K., Rydevik, B., Van Steenberghe, D., and Brånemark, P. I. (2000). Evaluation of the psychophysical detection threshold level for vibrotactile and pressure stimulation of prosthetic limbs using bone anchorage or soft tissue support. *Prosthet. Orthot. Int.* 24, 133–142. doi: 10.1080/03093640008726536

Johansson, R. S., and Vallbo, A. B. (1979). Tactile sensibility in the human hand: relative and absolute densities of four types of mechanoreceptive units in glabrous skin. *J. Physiol.* 286, 283–300. doi: 10.1113/jphysiol.1979.sp012619

Johnson, K. O. (2001). The roles and functions of cutaneous mechanoreceptors. *Curr. Opin. Neurobiol.* 11, 455–461. doi: 10.1016/S0959-4388(00)00234-8

Koo, J. P., Kim, S.-H., An, H.-J., Moon, O.-G., Choi, J.-H., Yun, Y.-D., et al. (2016). Two-point discrimination of the upper extremities of healthy Koreans in their 20's. *J. Phys. Ther. Sci.* 28, 870–874. doi: 10.1589/jpts.28.870

Li, L., Rutlin, M., Abraira, V. E., Cassidy, C., Kus, L., Gong, S., et al. (2011). The functional organization of cutaneous low-threshold mechanosensory neurons. *Cell* 147, 1615–1627. doi: 10.1016/j.cell.2011.11.027

Liu, Q., Vrontou, S., Rice, F. L., Zylka, M. J., Dong, X., and Anderson, D. J. (2007). Molecular genetic visualization of a rare subset of unmyelinated sensory neurons that may detect gentle touch. *Nat. Neurosci.* 10, 946–948. doi: 10.1038/nn1937

Mahns, D. A., Perkins, N. M., Sahai, V., Robinson, L., and Rowe, M. J. (2006). Vibrotactile frequency discrimination in human hairy skin. *J. Neurophysiol.* 95, 1442–1450. doi: 10.1152/jn.00483.2005

Mancini, F., Bauleo, A., Cole, J., Lui, F., Porro, C. A., Haggard, P., et al. (2014). Whole-body mapping of spatial acuity for pain and touch. *Ann. Neurol.* 75, 917–924. doi: 10.1002/ana.24179

Marasco, P. D., Hebert, J. S., Sensinger, J. W., Shell, C. E., Schofield, J. S., Thumser, Z. C., et al. (2018). Illusory movement perception improves motor control for prosthetic hands. *Sci. Transl. Med.* 10, eaao6990. doi: 10.1126/scitranslmed.aao6990

McRuer, D., and Weir, D. H. (1969). Theory of manual vehicular control. *Ergonomics* 12, 599–633. doi: 10.1080/00140136908931082

Montagna, W. (1965). The skin. *Sci. Am.* 212, 56–69. doi: 10.1038/scientificamerican0265-56

Montaño, J. A., Pérez-Piñera, P., Garcia-Suárez, O., Cobo, J., and Vega, J. A. (2010). Development and neuronal dependence of cutaneous sensory nerve formations: lessons from neurotrophins. *Microsc. Res. Tech.* 73, 513–529. doi: 10.1002/jemt.20790

Neely, G., and Burström, L. (2006). Gender differences in subjective responses to hand–arm vibration. *Int. J. Ind. Ergon.* 36, 135–140. doi: 10.1016/j.ergon.2005.09.003

Nolan, M. F. (1982). Two-point discrimination assessment in the upper limb in young adult men and women. *Phys. Ther.* 62, 965–969. doi: 10.1093/ptj/62.7.965

Orand, A., Erdal Aksoy, E., Miyasaka, H., Weeks Levy, C., Zhang, X., and Menon, C. (2019). Bilateral tactile feedback-enabled training for stroke survivors using microsoft kinecttm. *Sensors* 19, 3474. doi: 10.3390/s19163474

Penfield, W., and Boldrey, E. (1937). Somatic motor and sensory representation in the cerebral cortex of man as studied by electrical stimulation. *Brain* 60, 389–443. doi: 10.1093/brain/60.4.389

Rothenberg, M., Verrillo, R. T., Zahorian, S. A., Brachman, M. L., and Bolanowski, J. S Jr. (1977). Vibrotactile frequency for encoding a speech parameter. *J. Acoust. Soc. Am.* 62, 1003–1012. doi: 10.1121/1.381610

Saddik, A. E., Orozco, M., Eid, M., and Cha, J. (2011). Human haptic perception. *Haptics Technologies*. 45–66. doi: 10.1007/978-3-642-22658-8_3

Schneider, J. S., Diamond, S. G., and Markham, C. H. (1987). Parkinson's disease: sensory and motor problems in arms and hands. *Neurology* 37, 951–951. doi: 10.1212/WNL.37.6.951

Sensinger, J. W., Dosen, S. (2020). A review of sensory feedback in upper-limb prostheses from the perspective of human motor control. *Front. Neurosci.* 14, 345. doi: 10.3389/fnins.2020.00345

Shah, V. A., Casadio, M., Scheidt, R. A., and Mrotek, L. A. (2019). Spatial and temporal influences on discrimination of vibrotactile stimuli on the arm. *Exp. Brain Res.* 237, 2075–2086. doi: 10.1007/s00221-019-05564-5

Stephens-Fripp, B., Alici, G., and Mutlu, R. (2018a). A review of non-invasive sensory feedback methods for transradial prosthetic hands. *IEEE Access* 6, 6878–6899. doi: 10.1109/ACCESS.2018.2791583

Stephens-Fripp, B., Mutlu, R., and Alici, G. (2018b). "Using vibration motors to create tactile apparent movement for transradial prosthetic sensory feedback," in *2018 7th IEEE International Conference on Biomedical Robotics and Biomechatronics (Biorob)*. (IEEE), 213–218.

Stepp, C. E., and Matsuoka, Y. (2011). Object manipulation improvements due to single session training outweigh the differences among stimulation sites during vibrotactile feedback. *IEEE Trans. Neural. Syst. Rehabi. Eng.* 19, 677–685. doi: 10.1109/TNSRE.2011.2168981

Tanaka, E., Lian, W.-L., Liao, Y.-T., Yang, H., Li, L.-N., Lee, H.-H., et al. (2021). Development of a tele-rehabilitation system using an upper limb assistive device. *J. Robot. Mechatron.* 33, 877–886. doi: 10.20965/jrm.2021.p0877

Tung, T. H. H., and Mackinnon, S. E. (2003). Brachial plexus injuries. *Clin. Plast. Surg.* 30, 269–287. doi: 10.1016/S0094-1298(02)00094-9

Tyson, S. F., Hanley, M., Chillala, J., Selley, A. B., and Tallis, R. C. (2008). Sensory loss in hospital-admitted people with stroke: characteristics, associated factors, and relationship with function. *Neurorehabil. Neural Repair.* 22, 166–172. doi: 10.1177/1545968307305523

Vallbo, A. B., and Johansson, R. S. (1984). Properties of cutaneous mechanoreceptors in the human hand related to touch sensation. *Hum Neurobiol* 3, 3–14.

Weber, E. H. (1834a). De Tactu ("Concerning Touch") in *De Pulsu, Resorptione, Auditu, et Tactu. Annotationes Anatomicae et Physiologicae [Concerning Pulse, Respiration, Hearing, and Touch: Anatomical and Physiological Notes]* (C.F. Koehler), 44–174.

Weber, E. H. (1834b). *Weber's Law of Just Noticeable Differences povzetek iz USD Internet Sensation and Perception Laboratory, dostopno*. Available online at: http://apps.usd.edu/coglab/WebersLaw.html (accessed October 10, 2021).

Weber, E. H. (1851). "Der Tastsinn und das Gemeingefühl (1846)," *in Published as Off-Print from R. Wagner's Handwörterbuch der Physiologie* (Vieweg).

Weinstein, S. (1968). "Intensive and extensive aspects of tactile sensitivity as a function of body part, sex and laterality," in *The skin senses*, ed D. Kenshalo (Springfield, IL: C. C. Thomas), 195–222.

Wilke, M. A., Niethammer, C., Meyer, B., Farina, D., and Dosen, S. (2019). Psychometric characterization of incidental feedback sources during grasping with a hand prosthesis. *J. Neuroeng. Rehabil.* 16, 1–13. doi: 10.1186/s12984-019-0622-9

Zimmerman, A., Bai, L., and Ginty, D. D. (2014). The gentle touch receptors of mammalian skin. *Science.* 346, 950–954. doi: 10.1126/science.1254229

frontiers | Frontiers in Neuroscience

TYPE Original Research
PUBLISHED 03 November 2022
DOI 10.3389/fnins.2022.1047070

OPEN ACCESS

EDITED BY
Chenyun Dai,
Fudan University, China

REVIEWED BY
Xinyu Jiang,
University of Edinburgh,
United Kingdom
Haoran Ren,
University of Shanghai for Science
and Technology, China

*CORRESPONDENCE
Xiang Chen
xch@ustc.edu.cn

SPECIALTY SECTION
This article was submitted to
Neuroprosthetics,
a section of the journal
Frontiers in Neuroscience

RECEIVED 17 September 2022
ACCEPTED 17 October 2022
PUBLISHED 03 November 2022

CITATION
Ruan Y, Chen X, Zhang X and Chen X
(2022) Principal component analysis
of photoplethysmography signals
for improved gesture recognition.
Front. Neurosci. 16:1047070.
doi: 10.3389/fnins.2022.1047070

Principal component analysis of photoplethysmography signals for improved gesture recognition

Yuwen Ruan, Xiang Chen*, Xu Zhang and Xun Chen

School of Information Science and Technology, University of Science and Technology of China, Hefei, Anhui, China

In recent years, researchers have begun to introduce photoplethysmography (PPG) signal into the field of gesture recognition to achieve human-computer interaction on wearable device. Unlike the signals used for traditional neural interface such as electromyography (EMG) and electroencephalograph (EEG), PPG signals are readily available in current commercial wearable devices, which makes it possible to realize practical gesture-based human-computer interaction applications. In the process of gesture execution, the signal collected by PPG sensor usually contains a lot of noise irrelevant to gesture pattern and not conducive to gesture recognition. Toward improving gesture recognition performance based on PPG signals, the main contribution of this study is that it explores the feasibility of using principal component analysis (PCA) decomposition algorithm to separate gesture pattern-related signals from noise, and then proposes a PPG signal processing scheme based on normalization and reconstruction of principal components. For 14 wrist and finger-related gestures, PPG data of three wavelengths of light (green, red, and infrared) are collected from 14 subjects in four motion states (sitting, walking, jogging, and running). The gesture recognition is carried out with Support Vector Machine (SVM) classifier and K-Nearest Neighbor (KNN) classifier. The experimental results verify that PCA decomposition can effectively separate gesture-pattern-related signals from irrelevant noise, and the proposed PCA-based PPG processing scheme can improve the average accuracies of gesture recognition by 2.35∼9.19%. In particular, the improvement is found to be more evident for finger-related (improved by 6.25∼12.13%) than wrist-related gestures (improved by 1.93∼5.25%). This study provides a novel idea for implementing high-precision PPG gesture recognition technology.

KEYWORDS

gesture recognition, KNN, PCA, PPG, SVM

Introduction

Photoplethysmography (PPG) sensors embedded in wearable devices currently on the market are often used for health detection (Raj et al., 2021; Dhar et al., 2022; Loh et al., 2022), identity verification (Alotaiby et al., 2021; Dae et al., 2021), and emotion recognition (Lee et al., 2019; Goshvarpour and Goshvarpour, 2020). In recent years, researchers have begun to explore the feasibility of using PPG signal for gesture recognition to achieve human-computer interaction. Taking advantage of PPG signals, Zhao et al. (2021) recognized 9 gestures with the average accuracy of 88%, and Yu et al. (2018) recognized 10 gestures with the average accuracy of 90.55%. Based on these studies, there is a growing consensus that PPG has the potential to replace EMG, accelerometer and other inertial sensors in the field of gesture recognition. Subramanian et al. (2020) conducted a comparative gesture recognition study on PPG and surface electromyography (EMG), and verified that the performance of these two types of signals was at the same level. Ling et al. (2021) proved that PPG signal is more suitable than acceleration signal for gesture interactions in wearable devices from three perspectives: (1) PPG is less affected by background motion noise; (2) PPG has better recognition performance of finger-related gestures; (3) PPG is more robust in reducing training burden. However, although PPG gesture recognition technology has made some progress, it is still in early research stage. The recognition accuracy and robustness have not met the needs of commercial use yet.

The main principle of using PPG signals for gesture recognition is that hand movement can cause deformation of blood vessels or tissues, resulting in PPG signal change with different movement patterns. In occasions such as heart rate estimation or blood oxygen detection, it is necessary to reduce motion artifacts to prevent their influence on measurement performance. However, for human-computer interaction, the motion information contained in the PPG signal is the key to realize gesture recognition, on the contrary, the vital sign-related information is regarded as noise. Consequently, the traditional PPG signal motion artifacts elimination methods are no longer applicable in this case.

When gesture actions are used for human-computer interaction, the signals collected by PPG sensors contain components related to multiple factors such as heart rate, gesture relevant motion and gesture irrelevant motion. In terms of signal sources, the components can be regarded as independent of each other, and the component irrelevant to gesture motion is not conducive to gesture recognition. Meanwhile, the energy levels of PPG signals caused by different factors may vary greatly. When there exist high-energy noise components, gesture recognition accuracy is bound to suffer significantly. Based on above analysis, we believe that if the PPG signals can be decomposed into components corresponding to different factors, it is expected to improve the accuracy of PPG-based gesture recognition through effective noise reduction.

In aspect of signal decomposition algorithms, principal component analysis (PCA), independent component analysis (ICA), and empirical mode decomposition (EMD), etc., can realize the effective decomposition of multi-channel or single-channel signals, and have been widely used in processing of biomedical signals such as electroencephalograph (EEG) (Turnip and Junaidi, 2014; Agarwal and Zubair, 2021; Farsi et al., 2021) and EMG (Masri et al., 2021; Xiong et al., 2021) etc. In PPG-based measurement of heart rate and other vital sign parameters, PCA, ICA, and EMD also have been adopted to remove motion artifacts, and the ability of these signal decomposition algorithms in separating the components related to vital signs and motion artifacts have been confirmed. For instance, Lee et al. (2020) proposed an ICA-based motion artifact reduction algorithm for PPG heart rate measurement. Liu et al. (2021) presented a PCA-based scheme to remove motion artifacts in PPG signals for blood pressure measurement. Adopting a method based on ensemble EMD and PCA, Motin et al. (2018) realized the estimation of heart rate, respiratory rate, and respiratory activity from PPG signals. For pulse rate detection, Wang et al. (2010) proposed an approach based on EMD and Hilbert transform to reduce the artifacts in PPG signals.

Inspired by the research progress of motion artifacts elimination based on signal decomposition algorithms, this study tried to explore the feasibility of using signal decomposition technology for separating gesture-related signals from physiological noise and gesture irrelevant motion noise, and subsequently developed effective PPG processing scheme for improving the accuracy of PPG gesture recognition. Its main innovation and contribution lie in that: (1) PCA algorithm was applied to decompose multi-channel PPG signals associated with 14 kinds of gestures, and the characteristic analysis of different principal components was carried out to explore the feasibility of separating gesture pattern related signal from irrelevant noise; (2) An effective gesture PPG signal processing method based on normalization and reconstruction of principal components was accordingly developed and carried out.

Materials and methods

Gesture set and data acquisition

In this study, the target PPG gesture dataset is the same as that in our previous work (Ling et al., 2021). As shown in **Figure 1**, the target gesture set consists of 14 kinds of wrist and finger joint related actions. Gestures G1–G6 mainly focus on wrist movements, gestures G7–G13 focus on finger movements, and gesture G14 is a baseline gesture, which requires the hand

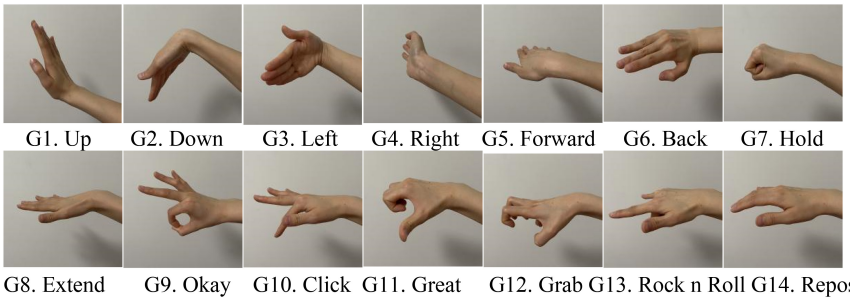

FIGURE 1
Fourteen gestures in the target gesture set.

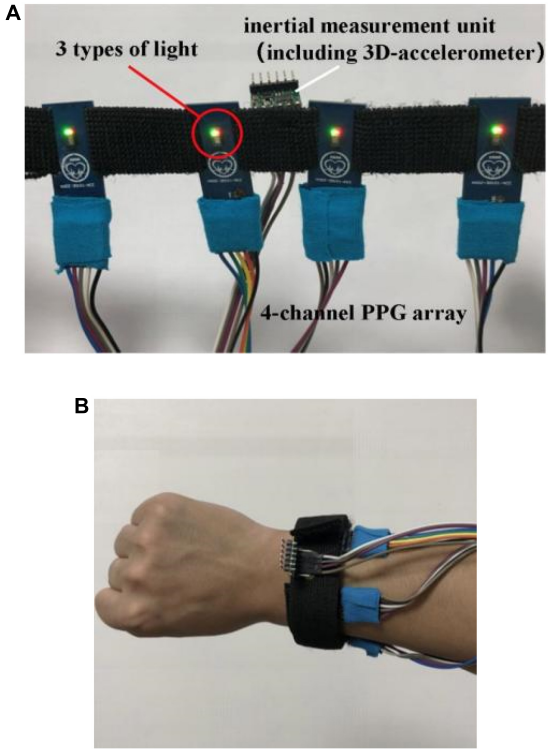

FIGURE 2
Schematic diagram of **(A)** the acquisition device and **(B)** the wearing example.

in a natural relaxed state. The execution process of each gesture starts from the resting state that the arm is naturally drooping and relaxed. When performing the gestures, subject raises the arm in front of the chest, completes the action, and finally returns to the relaxed state.

Fourteen healthy subjects (8 males and 6 females) participated in the data acquisition. The subjects were between 22 and 24 years old. All of them are right-handed and have no known history of any neural or musculoskeletal disease. All of the subjects were informed about the experiments and signed an informed consent form (No. PJ 2014-08-04) approved by the Ethics Review Committee of First Affiliated Hospital of Anhui Medical University. Each subject was asked to finish a set of experiments in four exercise states, namely: Sitting, Walking (speed of 3 km/h), Jogging (speed of 5 km/h), and Running (speed of 8 km/h). Except Sitting, the experiments in the other three exercise states were carried out on a treadmill (Sole F63) to make sure that the subjects exercise at a constant speed. In the states of Sitting and Walking, the subjects were asked to repeat each gesture about 50 times, while in the states of Jogging and Running, each gesture was repeated about 25 times. There was a 2-s interval between repetitions, and subjects were asked to rest about 5 min between gestures to avoid muscle fatigue.

A wristband-type multi-channel PPG acquisition device (Figure 2A) developed and manufactured by the research team was used for data collection. The device was equipped with four PPG sensors (MAX30105, Maxim Integrated Inc., San Jose, CA, USA). As shown in Figure 2B, the device was worn on the right forearm at distance of about one finger from the wrist and were placed near radial artery, ulnar artery, cephalic vein and guillotine vein, respectively, to obtain PPG signals from the four major blood vessels. Each PPG sensor alternately emitted the red light, infrared light and green light, and the 4-channel signals of the same light from the four PPG sensors were collected synchronously. The sampling frequency of each channel was set to 100 Hz.

Principal component characteristic analysis of gesture photoplethysmography signals

The PCA algorithm is adopted to decompose multi-dimensional data into a series of linearly uncorrelated elements called principal components using orthogonal transformation (Bro and Smilde, 2014; Lever et al., 2017). As depicted in Equation 1, the gesture PPG signal matrix X (4-channel, N data

points) is transformed into principal component matrix PC and the corresponding weight vector matrix W using PCA algorithm according to the specific steps as follows:

$$PC^{4\times N} = W^{4\times 4}X^{4\times N}$$

$$X = [X_1, X_2, X_3, X_4]^T, W = [W_1, W_2, W_3, W_4]^T \quad (1)$$

$$PC = [PC1, PC2, PC3, PC4]^T$$

(1). Perform de-averaging operation on each row of X, which is also called zero-averaging;
(2). Calculate the 4×4 covariance matrix according to Equation 2;

$$\sigma = \frac{1}{N-1}XX^T \quad (2)$$

(3). Perform eigenvalue decomposition on the covariance matrix to find the eigenvalues and corresponding eigenvectors, and arrange the eigenvectors in descending order of eigenvalues to get the eigenvector matrix W;
(4). Calculate the principal components according to Equation 3.

$$PCi = \omega_i{}^T X \quad (3)$$

Then the characteristic analysis of different principal components is carried out to explore the feasibility of separating gesture pattern related signal from irrelevant noise. Principal component characteristic analysis is carried out in time domain and frequency domain, respectively. In the time domain, the envelope, energy, and variance levels of each channel of the raw PPG signals and each principal component are analyzed. In the frequency domain, Fast Fourier Transform (FFT) is performed on the raw PPG signals and principal components, respectively, to obtain the corresponding frequency domain signals. The frequency distributions of each channel of the raw PPG signals and each principal component are analyzed through mean frequency (*MNF*) and median frequency (*MDF*) calculated by Equations 4, 5, respectively, where M is the number of the frequency points, f_j is the frequency of point$j$ and P_j is its power spectrum.

$$MNF = \frac{\sum_{j=1}^{M} f_j P_j}{\sum_{j=1}^{M} P_j} \quad (4)$$

$$\sum_{j=1}^{MDF} P_j = \sum_{j=MDF}^{M} P_j = \frac{1}{2}\sum_{j=1}^{M} P_j \quad (5)$$

In order to depict the relationship between the principal components and the raw PPG signals, Pearson correlation coefficient (Ly et al., 2018) is used to measure the correlation between the signal sequences.

The photoplethysmography gesture recognition scheme based on principal component analysis processing

Figure 3 shows the PPG gesture recognition scheme based on the proposed PCA processing method, including: collecting 4-channel gesture PPG signals, PCA processing of the 4-channel PPG gesture signals, segmentation of gesture action activity; and gesture recognition with SVM classifier and KNN classifier. Gesture PPG signal collection is the same as described above, and details of the other steps are described below.

The purpose of PCA processing is to reduce the negative impact of high-energy noise components on gesture recognition by normalizing different principal components to the same level, so as to achieve the effect of denoising. For the 4-channel gesture PPG signals, the detailed procedure of the PCA processing is as follows:

(1). Decompose the 4-channel PPG signals into four principal components by means of PCA algorithm as described above.
(2). Normalize the four principal components with unequal energy to the same level. In particular, for each *PC*, to find the maximum and minimum values firstly, then normalize the data points greater than zero to [0 1] by the maximum value, and normalize the data points less than zero to [−1 0] by the absolute value of the minimum;
(3). Obtain the processed PPG signals by reconstructing the normalized principal components according to Equation 6.

$$X_{processed} = W \cdot PC_{normalized} \quad (6)$$

The goal of gesture segmentation is to extract gesture repetition samples from continuous signals. A motion background noise-based segmentation strategy proposed in our previous work (Ling et al., 2021) is adopted in this study. In this strategy, considering that the waveform and amplitude of gesture signals are far greater than the motion background signal, the starting and ending positions of a gesture repetition is determined by setting suitable thresholds. The details of the motion noise-based strategy can be found in Ling et al. (2021). In addition, the lengths of the gesture repetitions are not always consistent in different exercise states in this study. In the states of Sitting and Walking, the completion time of a gesture is about 1 s. As the movement speed increasing, the time to complete a gesture will get shorter, and the gesture completion time in the Running state is about 0.5 s. According to the sampling rate of 100 Hz, the signal length of a gesture repetition is about 40–120 data points. To normalize the length of gesture samples, the down-sampling method is used to extract a 32-point envelope of each gesture repetition as gesture feature sample in further classification. Thus, each PPG gesture sample

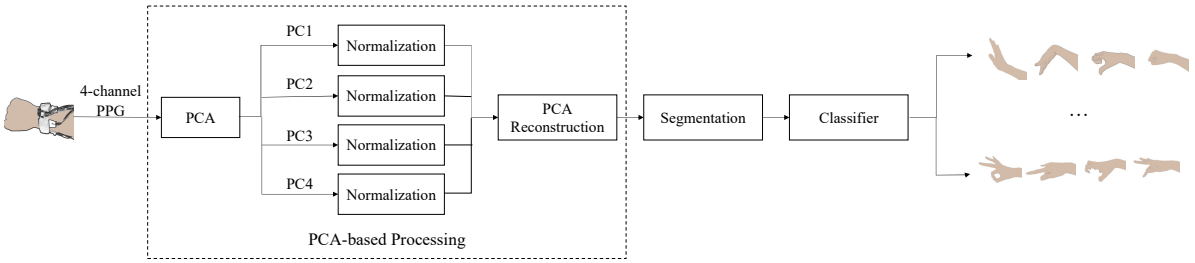

FIGURE 3
The PPG gesture recognition scheme based on PCA processing.

is in the form of a matrix of size 4 (channels) ×32 (data points).

Considering the limited number of samples in the target database, two classical and traditional machine learning classifiers, namely Support Vector Machine (SVM) classifier and K-Nearest Neighbor (KNN) classifier are adopted for gesture classification in this study. SVM is considered as one of the most successful machine learning algorithms in recent years (Cortes and Vapnik, 1995). The basic idea is to solve a separation hyperplane that can correctly classify the training data set, and the hyperplane needs to satisfy the maximum geometric interval between dissimilar data. SVM can solve the nonlinear case by choosing a suitable kernel function, using nonlinear processing to map the samples to a high-dimensional space, and then finding the best classification hyperplane in the high-dimensional space. In our previous work (Ling et al., 2021), the SVM classifier achieve the best performance in PPG gesture recognition compared to Convolutional Neural Network (CNN) and Long Short-Term Memory (LSTM). KNN algorithm originally proposed by Cover and Hart (1967). Since it is easy to realize and needs less training time, KNN classifier is commonly used in the field of pattern recognition. After the analysis of the distribution characteristics of gesture PPG samples and the experimental verification, for SVM classifier, a linear kernel function is used, and the penalty factor is set to 1. And for KNN classifier, the Euclidean distance is selected, and K is set to 1.

In view of the large individual differences in PPG signals, as a primary study, PPG gesture recognition in this study is carried out in a subject-specific way. In the meanwhile, considering that it is difficult to obtain large-scale gesture training data in practical human-computer interaction applications, this study focuses on gesture recognition with small training size. In particular, for each gesture, all samples of each subject are randomly divided into 10 parts, one part of samples is used for training data, and the remaining nine parts testing data. That is, 10% data is used for training the classifier and 90% for testing. The result of the recognition task is obtained by cross-validation method.

Two denoising schemes for comparison

In order to evaluate the effectiveness and superiority of the proposed PCA processing method, gesture recognition adopting two common signal denoising methods, namely Butterworth low-pass filter (Li, 2007; Liao et al., 2014) and wavelet threshold denoising (Pan et al., 2007; Cheng and Zhang, 2014; Wang et al., 2019), have also been conducted in this study. Because the main spectrum of PPG gesture signals is concentrated in 0∼5 Hz, a 5-order Butterworth low-pass filter with a cut-off frequency of 5 Hz is adopted.

The wavelet threshold denoising is carried out as follows: (1) Calculate the orthogonal wavelet transform of the noisy PPG signal, decompose the signal into 4 layers and get the corresponding wavelet decomposition coefficient. The wavelet used is "sym6"; (2) Threshold the wavelet coefficients to obtain the estimate of the wavelet coefficients of the real signal. In specific, the soft threshold function shown in Equation 7 is adopted, where th is the threshold and γ is the wavelet coefficient. The minimax thresholding, which is defined as Equations 8, 9, is used to determine the threshold, where N is the sum of the total number of wavelet coefficients of the noisy signal on scales 1 4, J is the binary scale, and $W_{1,k}$ is the wavelet coefficients of scale 1; (3) Do the inverse wavelet transform, and regard the reconstructed signal as the de-noised signal.

$$T(\gamma, th) = \begin{cases} sgn(\gamma)(|\gamma| - th), & |\gamma| \geq th \\ 0, & |\gamma| < th \end{cases} \quad (7)$$

$$th = \begin{cases} \sigma\left(0.3936 + 0.1892 log_2 N\right), & N > 32 \\ 0, & N < 32 \end{cases} \quad (8)$$

$$\sigma = middle\left(\left|W_{1,k}\right|, 0 \leq k \leq 2^{J-1} - 1\right) / 0.6745 \quad (9)$$

Statistical analysis

Considering the data in this study do not strictly satisfy the conditions of normal distribution and homogeneity of

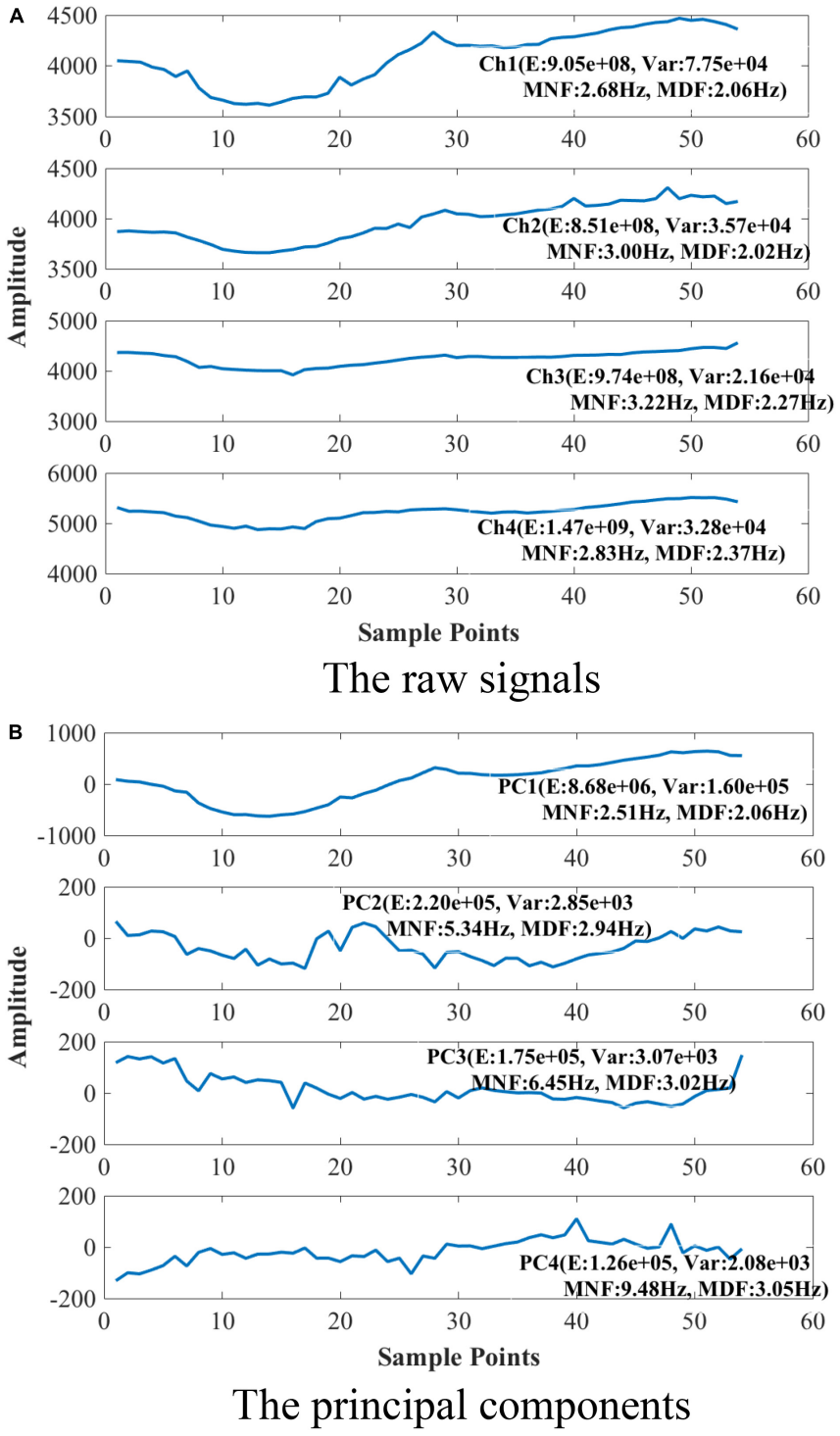

FIGURE 4
Raw signals and PCA decomposition results of a green light PPG sample (PC, principal component; E, energy; Var, variance; MNF, mean frequency; MDF, median frequency). **(A)** The raw signals. **(B)** The principal components.

variance, non-parametric tests (Kruskal–Wallis test) were performed to explore the impacts of the independent variables (wavelength, motion state, denoising method, and classifier) on the dependent variable (recognition accuracy). The statistical analysis was carried out on IBM SPSS Statistics (Version 25), and the significance level is 5%.

Results and analyses

Principal component characteristics analysis of multi-channel gestural photoplethysmography signals

Figure 4 shows the raw signals and PCA decomposition results of one PPG sample of gesture G5 from a representative subject (Sub11) in the Running state. From Figure 4A, it can be seen that the raw signals of different channels have similar changing trend (average similarity coefficient of pairwise channels ρ 0.92). The four channels are at almost the same level in terms of energy. The *MNF* and *MDF* of the four channels only vary slightly. In contrast, as shown in Figure 4B, the envelopes of the 4 principal components obtained by PCA decomposition are more distinct (average similarity coefficient of pairwise components ρ 0.35). For example, *PC*1 has the highest energy (8.68e + 06), which is more than 39 times higher than the other three components (1.26e + 05∼2.20e + 05). At the same time, the four components have significant frequency differences. *PC*1 has the lowest *MNF* (2.51 Hz) and *MDF* (2.06 Hz), while *PC*4 has the largest *MNF* (9.48 Hz) and *MDF* (3.05 Hz). Above results demonstrate that PCA can effectively decompose multi-channel gesture PPG signals into multiple components with different energy levels and frequency bands.

To explore which principal components are beneficial to gesture recognition, all gesture samples of the subject in the four motion states were analyzed. Figure 5 shows a similarity comparison between the four channels of raw PPG signals and the four principal components for all gesture samples, by calculating the correlation coefficients of pairwise channels or pairwise *PC* components (mean ± standard deviation). In all the 4 motion states, the average correlation coefficients of raw PPG are up to 0.7, while those of the principal components are only in the range of 0.29 and 0.35. These results verify that the four channels of raw signals have a large common component, however, the four principal components are much independent of each other.

Figure 6 shows the similarities between the four principal components and the raw PPG signals for all gesture samples. The values (mean ± standard deviation) in the figure were obtained by calculating the correlation coefficients between one *PC* component and the four channels of raw signals and averaging them. From Figure 6 we can find that *PC*1 is similar to the raw PPG (ρ 0.83∼0.92) while *PC*2, *PC*3, and *PC*4 are less similar to the raw PPG (ρ 0.30∼0.54). According to the above analysis, we believe that component *PC*1, which has the largest energy level and the lowest frequency, maybe represents the common trend of the four channels of raw PPG signal.

Figure 7 compares the correlation coefficients between the same principal components of the samples belonging to different gesture types. For samples belonging to different gestures, the mean correlation coefficients of *PC*1 are all up to 0.68, while those of *PC*2, *PC*3, and *PC*4 are mostly lower than 0.4. These results demonstrate further that *PC*1 mainly represents a common part in all kinds of gesture samples. This kind of trend item at a high energy level will mask the information related to gesture pattern, which may reduce the recognition accuracy. On the contrary, the other three principal

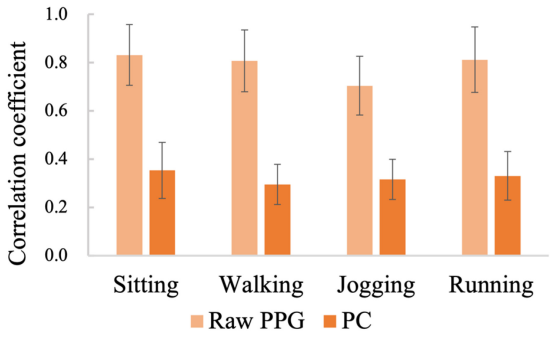

FIGURE 5
The similarities between the four channels of raw PPG signals and between the four principal components (Subject 11).

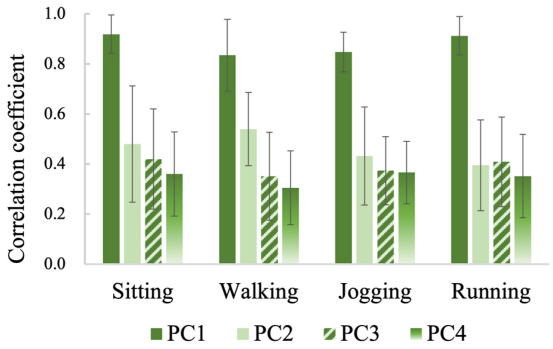

FIGURE 6
The similarities between principal components and raw PPG signals.

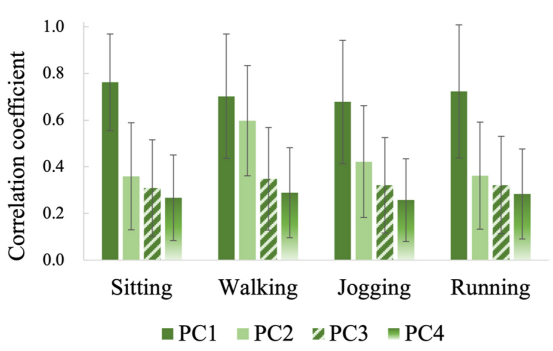

FIGURE 7
The similarities between the same principal components of the samples belonging to different gestures.

components may contain more valuable gesture pattern related details.

In summary, PCA decomposition and principal component characteristics analysis of multi-channel gestural PPG signals verify the feasibility of using PCA to separate gesture pattern related signals from irrelevant motion noise.

The photoplethysmography gesture recognition based on principal component analysis processing

Feature distribution of gesture samples obtained by different denoising schemes

Taking the green light PPG samples of the 14 gestures of the 2nd subject (Sub 2) in the Sitting state as example, we perform t-SNE (van der Maaten and Hinton, 2008; Pezzotti et al., 2017) dimensionality reduction on PPG envelopes obtained by PCA processing, Butterworth low-pass filter and Wavelet threshold denoising, respectively. The obtained scatter plots of feature distribution are shown in **Figure 8**. In the cases of Butterworth low-pass filter and Wavelet threshold denoising, as shown in **Figures 8B,C**, respectively, there are six gestures that can be easily distinguished from other gestures. For the remaining eight gestures, the features are too close to meet the recognition condition. However, when PCA processing is applied, as shown in **Figure 8A**, the features of all 14 gestures can be separated effectively from each other. Above results demonstrate, to some extent, the possibility of improving gesture recognition accuracy by the proposed PCA processing scheme.

Recognition results for 14 gestures

Photoplethysmography gesture recognitions of 14 gestures are carried out in the cases of three lights and four motion states, using SVM and KNN classifiers, respectively. For each case, the average gesture recognition accuracies among 14 gestures and 14 subjects are shown in **Table 1**. In order to compare the effect of different denoising schemes and classifiers on PPG gesture recognition in the cases of different lights and different motion states, nonparametric tests are performed further and the results are shown in **Table 2**. Combined the **Tables 1**, **2**, the following phenomena can be observed (The values presented in following parts, if not otherwise specified, are the average recognition accuracies and standard deviations for all recognition tasks involving the discussing factors):

(1). The wavelength of PPG signal has a significant impact on the recognition accuracy (p = 0.000**). Specifically, the recognition accuracy of green light (86.71 ± 7.53%) is significantly (p = 0.000**) lower than those of red light (93.25 ± 5.44%) and infrared light (93.48 ± 4.49%), and there is no significant difference between red light and infrared light (p = 0.975). From this result, it can be seen that although the green PPG suitable for heart rate detection is generally embedded in wearables, it is not the best choice for gesture recognition.

(2). The intensity of the motion has a significant impact on the recognition accuracy (p = 0.000**). In general, the recognition accuracy decreases with the increase of background motion speed: 92.70 ± 5.93% for Sitting, 92.94 ± 6.05% for Walking, 90.35 ± 7.01% for Jogging and 88.60 ± 6.92% for Running. However, there is no significant difference between Sitting and Walking (p = 0.501). This result shows that the low-intensity background motion has little influence on the recognition effect. Only movement that reaches a certain intensity makes the recognition accuracy decrease.

(3). The performance of the PCA processing is significantly (p = 0.000**) better than the other two denoising schemes. For the four motion states, three lights of PPG and two classifiers, the average recognition accuracies obtained by the three different denoising schemes are respectively: 94.61 ± 5.24% for PCA, 89.22 ± 6.87% for Butterworth and 89.61 ± 6.58% for Wavelet. Furthermore, the performances of Butterworth denoising and Wavelet denoising have no significant difference (p = 0.536). This result verifies the superiority of the proposed PCA denoising scheme.

(4). According to the results shown in **Table 1**, the recognition accuracy of SVM classifier (91.87 ± 6.20%) is slightly higher than that of KNN (90.11 ± 8.91%), and the statistical analysis result also shows that the classifier truly has some impact on the accuracy (p = 0.002*). However, in terms of the accuracy requirement of human-computer interaction, a difference of only one percent is not enough to conclude that SVM is superior to KNN. Considering the advantage of KNN in computing speed, it can still be considered that both SVM and KNN classifiers are well-suited for the PPG gesture recognition.

Recognition results for wrist-related gestures and finger-related gestures

As mentioned above, the target gesture set contains 6 wrist-related gestures (G1–G6) and 7 finger-related gestures (G7–G13). In order to compare the performance of the three denoising schemes on these two types of gesture, we further conduct recognition experiments on wrist-related gestures and finger-related gestures, respectively. The gesture recognitions are carried out using the red-light PPG data under the four motion states. **Figures 9A,B** give the recognition results of wrist-related gestures and finger-related gestures using SVM and KNN classifiers, respectively. Nonparametric tests are performed to explore the effects of denoising methods on recognition.

The recognition of finger-related gestures has always been a difficulty in the field of gesture recognition. As shown in **Figure 9**, when PPG gesture signals are denoised by general

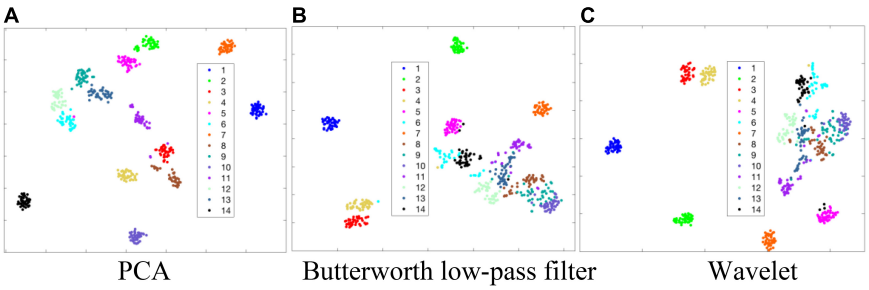

FIGURE 8
t-SNE dimensionality reduction feature distributions of gesture signal envelope in the cases of three denoising schemes. **(A)** PCA. **(B)** Butterworth low-pass filter. **(C)** Wavelet.

TABLE 1 Hand gesture recognition accuracies (%) of 14 gestures.

Classifier		SVM			KNN		
Motion states	**Lights**	**PCA**	**Butterworth**	**Wavelet**	**PCA**	**Butterworth**	**Wavelet**
Sitting	Red	99.44 ± 0.41	93.57 ± 3.18	93.86 ± 3.17	99.25 ± 0.56	91.89 ± 4.43	92.16 ± 4.30
	Infrared	98.24 ± 1.65	94.02 ± 2.92	94.02 ± 3.16	97.70 ± 1.93	92.57 ± 3.79	92.41 ± 4.07
	Green	93.21 ± 5.20	88.38 ± 4.34	88.51 ± 4.50	91.22 ± 6.75	84.01 ± 6.62	84.14 ± 6.62
Walking	Red	98.81 ± 1.20	93.76 ± 4.12	93.96 ± 4.08	98.62 ± 1.47	92.04 ± 5.24	92.23 ± 5.11
	Infrared	97.87 ± 1.60	95.14 ± 2.37	95.28 ± 2.39	97.55 ± 1.51	93.97 ± 2.49	93.99 ± 2.82
	Green	92.86 ± 4.08	88.39 ± 6.35	88.55 ± 6.07	90.42 ± 5.35	84.70 ± 8.29	84.83 ± 7.97
Jogging	Red	95.43 ± 4.20	90.69 ± 5.97	91.59 ± 5.36	94.80 ± 4.38	89.51 ± 6.50	90.28 ± 5.97
	Infrared	95.31 ± 2.55	91.96 ± 5.60	92.96 ± 4.98	94.68 ± 2.97	91.35 ± 6.19	92.18 ± 5.66
	Green	89.57 ± 5.51	85.08 ± 8.60	85.47 ± 8.11	88.28 ± 5.59	83.48 ± 9.05	83.75 ± 8.60
Running	Red	97.00 ± 2.31	88.15 ± 4.22	88.74 ± 4.66	96.72 ± 2.35	87.53 ± 4.64	88.08 ± 5.14
	Infrared	94.19 ± 3.18	88.88 ± 3.89	89.22 ± 3.65	93.61 ± 3.33	88.15 ± 4.15	88.31 ± 4.06
	Green	88.48 ± 5.89	82.82 ± 8.51	83.82 ± 7.54	87.47 ± 6.94	81.30 ± 9.62	82.40 ± 8.25
Total		95.03 ± 4.86	90.07 ± 6.35	90.50 ± 6.05	94.19 ± 5.58	88.38 ± 7.28	88.73 ± 6.97

TABLE 2 The results of non-parametric tests for gesture recognition.

Factors		**Sig. for accuracy**	**Multiple comparisons (Motion state)**		**Sig. for accuracy**
Main	Light	0.000**	Running	Jogging	0.001*
	Motion state	0.000**		Walking	0.000**
	Processing method	0.000**		Sitting	0.000**
	Classifier	0.002*	Jogging	Walking	0.000**
				Sitting	0.000**
			Walking	Sitting	0.501
Multiple comparisons (Light)		**Sig. for accuracy**	**Multiple comparisons (Processing method)**		**Sig. for accuracy**
Green	Red	0.000**	PCA	Butterworth	0.000**
	Infrared	0.000**		Wavelet	0.000**
Red	Infrared	0.975	Butterworth	Wavelet	0.536

*$p < 0.05$, **$p < 0.001$.

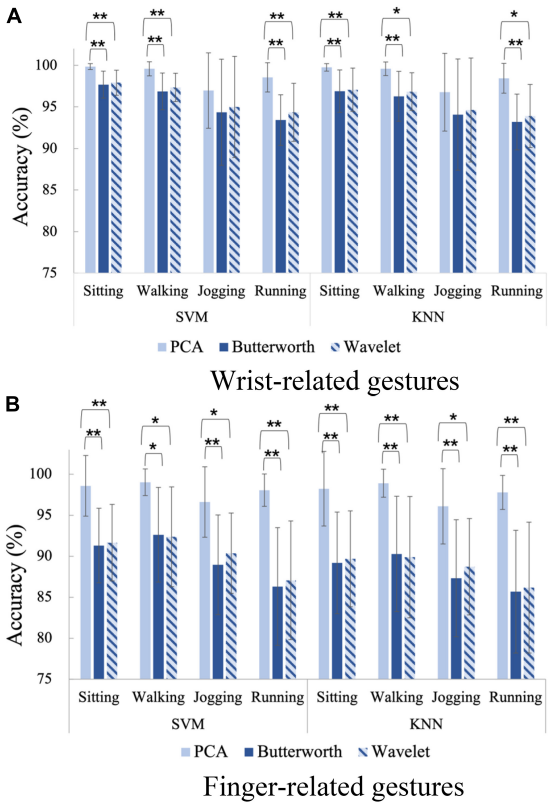

FIGURE 9
The gesture recognition results for wrist-related gestures and finger-related gestures under the four motion states, $^{*}p < 0.05$, $^{**}p < 0.001$. **(A)** Wrist-related gestures. **(B)** Finger-related gestures.

denoising means, the recognition accuracies of finger-related gestures are obviously lower than those of wrist-related gestures: 95.34 ± 4.23% for wrist-related and 88.95 ± 6.69% for finger-related when performing Butterworth low-pass filter denoising; 95.88 ± 4.02% for wrist-related and 89.49 ± 6.46% for finger-related when performing wavelet threshold denoising. In comparison, the proposed PCA denoising scheme can effectively improve the recognition performance of finger-related gestures. Applying the PCA processing scheme, the recognition accuracy of the finger-related gestures (97.91 ± 3.36%) is close to that of the wrist-related gestures (98.68 ± 2.70%). In the meanwhile, PCA processing improves finger-related gestured recognition accuracy better than wrist-related gestures. Taking the state of Running as example, for finger-related gestures, the average accuracy of PCA denoising scheme is 11.77% higher than Butterworth and 11.00% higher than Wavelet when using SVM classifier, and 12.13% higher than Butterworth and 11.63% higher than Wavelet when using KNN classifier. However, for wrist-related gestures, the average accuracy of PCA denoising scheme is only 5.14% higher than Butterworth and 4.21% higher than Wavelet when using SVM classifier, and 5.25% higher than Butterworth and 4.52% higher than Wavelet when using KNN classifier.

Discussion

To the best of our knowledge, this is the first research paper that specifically focuses on gestural PPG signal denoising. Combined with the state of the art relevant to PPG gesture recognition technology, the research results obtained in this study can be discussed from the following aspects.

The feasibility of separating gesture pattern related signals from irrelevant noises using principal component analysis algorithm

For PPG gesture recognition, how to extract gesture motion information from irrelevant motion and physiological signals is the key to determine the recognition performance. Inspired by the research progress of motion artifact elimination of PPG signal based on signal decomposition algorithm, this study carries out multi-channel PPG signal decomposition and principal component feature analysis using PCA algorithm to explore the feasibility of separating gesture pattern related signals from irrelevant noises. The experimental results demonstrate that PCA algorithm can effectively decompose the four-channel gesture PPG signals into four components with different energy levels and frequency bands. The component *PC*1, which has the largest energy level and the lowest frequency, maybe represent the common trend item of the four channels of raw PPG signal. We speculate that this kind of trend item at a high energy level will mask the information related to gesture pattern, thus reduce the recognition accuracy. On the contrary, the other three principal components may contain more valuable gesture pattern related details. The results of PCA decomposition and principal component analysis of gesture PPG signal provide a new way to propose effective signal processing method.

In fact, PCA algorithm has been widely used to decompose PPG signals to extract the needed physiological information. Liu et al. (2021) used PCA to separate the arterial pulse, capillary pulse and motion artifacts. Their acquisition device contains four colors of light, namely: blue, green, yellow, and infrared light, and one channel for each light. Because lights of different wavelengths reach the skin at different depths, the PPG signals of different lights can reflect different physiological information. In their study, based on PCA decomposition of the 4-channel PPG, *PC*1 was considered as arterial pulse which should have the largest energy. However, when PCA was applied to blue PPG and green PPG, *PC*1 was considered to be capillary pulse and *PC*2 was motion artifact. In the study

of Motin et al. (2018) which used PCA with ensemble empirical mode decomposition (EEMD) to decompose PPG signals, the *PC*1 and *PC*2 were considered to represent heart and respiratory activity, respectively.

In summary, in related studies of physiological signal extraction, the first and second principal components which always have the largest energy, are often considered as the approximation of the required signals. However, in this study, we find that the first *PC* with the largest energy is likely the noise that interferes gesture recognition, and the last three principal components with low energy are more likely to be the gesture-pattern-related signal.

The superiority of the proposed principal component analysis processing scheme in photoplethysmography gesture recognition

Although a number of studies have verified the feasibility of using PPG signals for gesture recognition in recent years, the problem of signal denoising has not attracted enough attention. In this study, a PPG processing method based on principal component normalization and reconstruction is proposed and implemented. The results of gesture recognition experiments on the data of 14 gestures, three kinds of light (red, infrared, and green) and four motion states (sitting, walking, jogging, and running) demonstrate the superiority of the PCA processing scheme from the following aspects.

First, the PCA processing method can improve the accuracy of gesture recognition to a certain extent (as shown in **Tables 1**, **2**). As shown in **Table 3**, which summarizes representative studies in the field of PPG gesture recognition in recent years, most studies adopted common denoising methods such as Discrete Wavelet Transform (DWT) (Yu et al., 2018), Butterworth filter (Ling et al., 2021; Zhao et al., 2021), de-averaging (Subramanian et al., 2020), etc., for PPG signal processing. As we know, the objective of the common denoising methods usually is to remove motion noise that is not in the frequency band of gesture-related signals. In this study, compared with Butterworth denoising and Wavelet denoising, PCA denoising shows obvious superiority in improving the accuracy of PPG gesture recognition. This result verifies that, the simple denoising methods of removing signal in certain frequency band cannot sufficiently remove noise and thus improve the accuracy of gesture recognition. On the contrary, PCA is a better choice for PPG gesture recognition. Therefore, we should deeply explore PPG signal denoising scheme based on PCA and other signal decomposition algorithms in the future.

TABLE 3 The representative researches of PPG gesture recognition.

Author	Task	Light	Motion state	Denoising method	Classifier	The proportion of training data	Recognition accuracy
Zhao et al.	Nine finger-level gestures	Green	Stationary body-motion scenarios	Butterworth high-pass filter (cut-off frequency: 2 Hz)	GBT, ResNet	50%	88%
Yu et al.	Ten wrist/finger-level gestures	Green	Stationary (Sitting, leaning, standing), walking, taking transportation, jogging	Discrete Wavelet Transform (DWT), gradient-based denoising scheme	SVM, random forest classifiers	90%	73.6~90.55%
Subramanian K. et al.	Four wrist/finger-level gestures	Green	Stationary	De-averaging, low-pass filter	SVM, XG-boosted trees	66%	88%
Ling et al.	Fourteen wrist/finger-level gestures	Red, infrared, green	Sitting, walking, jogging, running	Butterworth low-pass filter (cut-off frequency: 5 Hz)	SVM, CNN, LSTM	80%	83.3~95.4 (95.28% for 6 wrist-related, 89.30% for 7 finger-related)
This study	Fourteen wrist/finger-level gestures	Red, infrared, green	Sitting, walking, jogging, running	PCA processing scheme	SVM, KNN	10%	87.47~99.44% (98.68% for 6 wrist-related, 97.91% for 7 finger-related)

Second, the PCA processing scheme is of great significance for the realization of human-computer interaction based on finger-related gestures. From the perspective of actual application, the finger-related gestures are more suitable for interactive scenarios because they usually have more clear and easy-to-understand meaning. However, limited by factors such as small motion range and low degree of muscle contraction, when using electromyography or acceleration signals for gesture recognition, the distinguishability of finger joint motion is usually lower than that of wrist joint motion. In this study, the experimental results indicate that, for PPG gesture recognition technology, the distinguishability of finger-related gestures is also lower than that of wrist-related gestures. However, the proposed PCA processing scheme can improve the finger-related gestures recognition performance significantly. The PCA processing scheme is able to increase the recognition accuracy of finger-related gestures to a level similar to that of wrist-related gestures. With only 10% of the samples for training, the average recognition accuracy of seven finger-related gestures can achieve 97.91%, which can basically meet the commercial needs.

The advantage of the photoplethysmography gesture recognition framework implemented in this study

Compared with the first three studies (Yu et al., 2018; Subramanian et al., 2020; Zhao et al., 2021) in **Table 3**, a relatively large target gesture set consisting of six wrist-related gestures, seven finger gestures, and a baseline gesture is targeted in this study, and the advancement of the research results is reflected in the following aspects:

1) Gesture recognition performance of PPG signals with different wavelengths is explored. Most current commercial wearable products are embedded with green PPG sensors because green light has a greater absorption rate for oxyhemoglobin and deoxyhemoglobin, which makes it more suitable for detection of physiological information. However, the experimental results in this study show that green PPG is not the best choice for gesture recognition. Regardless of motion state and denoising method used, the recognition performance of green PPG is obviously lower than that of red and infrared lights;
2) The recognition performance of PPG signals in more motion scenarios is investigated. In the works of Subramanian et al. (2020) and Zhao et al. (2021), PPG gesture recognition were carried out only in stationary state and simple body-motion scenarios. The work of Yu et al. (2018) added some motion scenarios such as walking and jogging. In this study, the background motion is designed more purposefully. We designed a series of tasks with sequentially increasing background motion velocities from 0 to 8 km/h, and strictly controlled the motion velocity to be constant using a treadmill. The experimental results demonstrate the low-intensity motion backgrounds such as walking at a speed of 3 km/h have little impact on the recognition, while the high-intensity movements have certain influences;
3) The gesture recognition framework proposed in this study has low training burden, which makes it valuable in the application of human-computer interaction. As shown in **Table 3**, the data for training accounts for 50∼90% of the target dataset in the relevant works. Considering the needs of practical application, we only use 10% of the samples to train the classifier in this study, which means that for each gesture, no more than 5 samples are included in the training dataset. Although the training test ratio is as low as 1:9, it still achieves satisfactory gesture recognition accuracy. In sitting state, using SVM classifier, the recognition accuracy of red PPG achieves 99.44%, and even the green PPG, which is not good at gesture recognition, achieves 93.21%.

Compared with our previous work published in 2021 (Ling et al., 2021), this study follows the same design of the gesture set and recognition tasks, but changes the gesture recognition framework. The recognition accuracies obtained in this study are significantly higher than those of our previous study. Taking Sitting state and SVM classifier as example, when the train test ratio is 1:9, the recognition accuracies are improved by 16.84% for red PPG, 14.84% for infrared PPG and 24.51% for green PPG. We believe the main reason why this study achieves better gesture recognition performance lies in that it adopts the proposed PCA processing scheme, which aims to weaken the noise component and highlight the gesture pattern related signal that is beneficial for gesture recognition. In our previous work, the signal preprocessing employed Butterworth low-pass filtering with a cutoff frequency of 5 Hz and amplitude normalization for each channel. According to the experimental result of this study, the denoising effect of Butterworth low-pass filtering is lower than the PCA processing method. At the same time, amplitude normalization also does not necessarily have a positive effect on gesture recognition. Since the four-channel PPG signals are collected at different locations on the wrist, each channel mainly responds to blood flow changes in different vessels. When performing different gestures, there should exist differences in the blood flow at the corresponding locations of these four channels, which helps to increase the distinguishability of the gestures. However, the normalization process puts the amplitude of the four channels at the same level, which means that the

important difference information between gestures is erased. Therefore, the normalization is not conducive to gesture recognition.

Furthermore, SVM achieves the best performance for PPG gesture recognition in the previous work. Therefore, this study still uses the SVM classifier to complete the gesture recognition task. Meanwhile, considering that it is easier to implement and requires less training time, the KNN classifier is also adopted in this study. The experimental results show that, although the accuracy is slightly lower than that of SVM, the KNN classifier also has good recognition performance when using the proposed PCA processing scheme.

Limitations and future work

Although this study provides a thought to improve the performance of PPG gesture recognition, it still has some limitations. First of all, the performance of the PCA processing method proposed in this study is only verified offline, but not tested online. Therefore, when the proposed method is applied to short signal sequences in online situations, the performance may degrade; Second, this study only takes the PCA algorithm as an example to preliminarily prove that the signal decomposition algorithm can effectively separate gesture pattern related signal from irrelevant noise. Of course, signal decomposition algorithms such as ICA, EMD, etc., may have the same function, and may even achieve better performance than the proposed PCA processing scheme. Third, the PPG gesture recognition in this study only uses a single batch of data and does not consider the effects of sensor displacement and other factors on the recognition performance. To promote the practicality of PPG gesture recognition technology, issues such as sensor displacement caused by repeated wearing of the device will be the focus of our future work.

Conclusion

In this study, PCA decomposition technique is introduced into the noise processing of gesture PPG signals. After verifying the feasibility of using the PCA algorithm to separate the gesture pattern-related signals and irrelevant noises, a PCA processing method based on normalization and reconstruction is proposed and implemented. The superiority of the PCA processing scheme for improving the gesture recognition accuracy is verified in the recognition tasks of 14 gestures from 14 subjects, three kinds of light and four motion states, using two classifiers. In addition, the proposed PCA processing scheme is found to be more effective in improving the recognition accuracy of finger-related gestures. The research of this paper contributes to the development of PPG gesture recognition technology.

Data availability statement

The raw data supporting the conclusions of this article will be made available by the authors, without undue reservation.

Ethics statement

The studies involving human participants were reviewed and approved by the Ethics Review Committee of First Affiliated Hospital of Anhui Medical University. The patients/participants provided their written informed consent to participate in this study.

Author contributions

YR designed the research scheme, did the data acquisition, data analysis, and gesture recognition experiments, and wrote the manuscript. XiC directed the research and substantially revised the manuscript. XZ and XuC participated in the interpretation of the research results and manuscript revision. All authors approved the final version of the manuscript.

Funding

This work was supported by the National Nature Science Foundation of China under grants 61871360 and 61671417.

Acknowledgments

The authors appreciate the cooperation of all the participants during the data collection procedure.

Conflict of interest

The authors declare that the research was conducted in the absence of any commercial or financial relationships that could be construed as a potential conflict of interest.

Publisher's note

References

Agarwal, S., and Zubair, M. (2021). Classification of alcoholic and non-alcoholic EEG signals based on sliding-SSA and independent component analysis. *IEEE Sens. J.* 21, 26198–26206. doi: 10.1109/JSEN.2021.3081714

Alotaiby, T. N., Alshebeili, S. A., and Alotaibi, G. (2021). "Multimodal signals subject authentication system," in *Proceedings of the 2021 18th international conference on electrical engineering/electronics, computer, telecommunications and information technology(ECTI-CON)*, Chiang Mai, TH, 846–848. doi: 10.1109/ECTI-CON51831.2021.9454711

Bro, R., and Smilde, A. K. (2014). Principal component analysis. *Anal. Methods* 6, 2812–2831. doi: 10.1038/nmeth.4346

Cheng, X., and Zhang, Z. (2014). Denoising method of heart sound signals based on self-construct heart sound wavelet. *AIP Adv.* 4:087108. doi: 10.1063/1.4891822

Cortes, C., and Vapnik, V. J. M. I. (1995). Support-vector networks. *Mach. Learn.* 20, 273–297. doi: 10.1111/stan.12111

Cover, T., and Hart, P. (1967). Nearest neighbor pattern classification. *IEEE Trans. Inf. Theory* 13, 21–27. doi: 10.1109/TIT.1967.1053964

Dae, Y., Taha, B., and Hatzinakos, D. (2021). PBGAN: Learning PPG representations from GAN for time-stable and unique verification system. *IEEE Trans. Inf. Forensics Secur.* 16, 5124–5137. doi: 10.1109/TIFS.2021.3122817

Dhar, S., Chakraborty, A., Sadhukhan, D., Pal, S., and Mitra, M. (2022). Effortless detection of premature ventricular contraction using computerized analysis of photoplethysmography signal. *Sadhana Acad. Proc. Eng. Sci.* 47:28. doi: 10.1007/s12046-021-01781-3

Farsi, L., Siuly, S., Kabir, E., and Wang, H. (2021). Classification of alcoholic EEG signals using a deep learning method. *IEEE Sens. J.* 21, 3552–3560. doi: 10.1109/JSEN.2020.3026830

Goshvarpour, A., and Goshvarpour, A. (2020). Evaluation of novel entropy-based complex wavelet sub-bands measures of PPG in an emotion recognition system. *J. Med. Biol. Eng.* 40, 451–461. doi: 10.1007/s40846-020-00526-7

Lee, J., Kim, M., Park, H. K., and Kim, I. (2020). Motion artifact reduction in wearable photoplethysmography based on multi-channel sensors with multiple wavelengths. *Sensors* 20:1493. doi: 10.3390/s20051493

Lee, M., Lee, Y., Pae, D., Lim, M., Kim, D., and Kang, T. (2019). Fast emotion recognition based on single pulse PPG signal with convolutional neural network. *Appl. Sci.* 9:3355. doi: 10.3390/app9163355

Lever, J., Krzywinski, M., and Atman, N. (2017). Points of significance principal component analysis. *Nat. Methods* 14, 641–642.

Li, Z. (2007). "Design and analysis of improved Butterworth low pass filter," in *Proceedings of the 8th international conference on electronic measurement and instruments*, Xi An, CN, 729–732.

Liao, Y., Zhao, H., Liu, Y., and Yu, Q. (2014). "The design of active low pass filter," in *Proceedings of the 5th international conference on mechanical, industrial, and manufacturing technologies (MIMT)*, Singapore, 419–423. doi: 10.4028/www.scientific.net/AMM.541-542.419

Ling, Y., Chen, X., Ruan, Y., Zhang, X., and Chen, X. (2021). Comparative study of gesture recognition based on accelerometer and photoplethysmography sensor for gesture interactions in wearable devices. *IEEE Sens. J.* 21, 17107–17117.

Liu, J., Qiu, S., Luo, N., Lau, S., Yu, H., Kwok, T., et al. (2021). PCA-based multi-wavelength photoplethysmography algorithm for cuffless blood pressure measurement on elderly subjects. *IEEE J. Biomed. Health Inform.* 25, 663–673. doi: 10.1109/JBHI.2020.3004032

Loh, H., Xu, S., Faust, O., Ooi, C., Barua, P., Chakraborty, S., et al. (2022). Application of photoplethysmography signals for healthcare systems: An in-depth review. *Comput. Methods Programs Biomed.* 216:106677. doi: 10.1016/j.cmpb.2022.106677

Ly, A., Marsman, M., and Wagenmakers, E. (2018). Analytic posteriors for Pearson's correlation coefficient. *Stat. Neerl.* 72, 4–13.

Masri, G., Harb, H., Diab, N., and Halabi, R. (2021). "Design and control of a myoelectric prosthetic hand using multi-channel blind source separation techniques," in *Proceedings of the 2021 sixth international conference on advances in biomedical engineering (ICABME)*, Werdanyeh, MH, 54–58. doi: 10.1109/ICABME53305.2021.9604876

Motin, M. A., Karmakar, C. K., and Palaniswami, M. (2018). Ensemble empirical mode decomposition with principal component analysis: A novel approach for extracting respiratory rate and heart rate from photoplethysmographic signal. *IEEE J. Biomed. Health Inform.* 22, 766–774. doi: 10.1109/JBHI.2017.2679108

Pan, Q., Meng, J., Zhang, L., Cheng, Y., and Zhang, H. (2007). Wavelet filtering method and its application. *J. Electron. Inf. Technol.* 29, 236–242.

Pezzotti, N., Lelieveldt, B. P. F., van der Maaten, L., Hollt, T., Eisemann, E., and Vilanova, A. (2017). Approximated and user steerable tSNE for progressive visual analytics. *IEEE Trans. Vis. Comput. Graph.* 23, 1739–1752. doi: 10.1109/TVCG.2016.2570755

Raj, R., Selvakumar, J., and Maik, V. (2021). Smart automated heart health monitoring using photoplethysmography signal classification. *Biomed. Eng. Biomed. Tech.* 66, 247–256. doi: 10.1515/bmt-2020-0113

Subramanian, K., Savur, C., and Sahin, F. (2020). "Using photoplethysmography for simple hand gesture recognition," in *Proceedinds of the 2020 IEEE 15th international conference of system of systems engineering (SoSE 2020)*, Budapest, 307–312.

Turnip, A., and Junaidi, E. (2014). "Removal artifacts from EEG signal using independent component analysis and principal component analysis," in *Proceedinds of the 2014 2nd international conference on technology, informatics, management, engineering and environment (TIME-E 2014)*, Bandung, ID, 296–302.

van der Maaten, L., and Hinton, G. (2008). Visualizing data using t-SNE. *J. Mach. Learn. Res.* 9, 2579–2605.

Wang, Q., Yang, P., and Zhang, Y. (2010). Artifact reduction based on empirical mode decomposition (EMD) in photoplethysmography for pulse rate detection. *Annu. Int. Conf. IEEE Eng. Med. Biol. Soc.* 2010, 959–962. doi: 10.1109/IEMBS.2010.5627581

Wang, Z., Zhu, J., Yan, T., and Yang, L. (2019). A new modified wavelet-based ECG denoising. *Comput. Assist. Surg.* 24, 174–183. doi: 10.1080/24699322.2018.1560088

Xiong, D., Zhang, D., Zhao, X., Chu, Y., and Zhao, Y. (2021). Synergy-based neural interface for human gait tracking with deep learning. *IEEE Trans. Neural Syst. Rehabil. Eng.* 29, 2271–2280. doi: 10.1109/TNSRE.2021.3123630

Yu, Z., Tao, G., Chu, L., Kostakos, V., and Seneviratne, A. (2018). FinDroidHR: Smartwatch gesture input with optical heartrate monitor. *Proc. ACM Interact. Mob. Wearable Ubiquitous Technol.* 2, 1–42. doi: 10.1145/3191788

Zhao, T., Liu, J., Wang, Y., Liu, H., and Chen, Y. (2021). Towards low-cost sign language gesture recognition leveraging wearables. *IEEE Trans. Mob. Comput.* 20, 1685–1701. doi: 10.1109/TMC.2019.2962760

frontiers | Frontiers in Neuroscience

TYPE Original Research
PUBLISHED 16 February 2023
DOI 10.3389/fnins.2023.1078846

OPEN ACCESS

EDITED BY
Emanuele Lindo Secco,
Liverpool Hope University, United Kingdom

REVIEWED BY
Angelo Davalli,
National Institute for Insurance against Accidents at Work (INAIL), Italy
Fernando Vidal-Verdú,
University of Malaga, Spain

*CORRESPONDENCE
Andrea Marinelli
✉ andrea.marinelli@iit.it

†These authors have contributed equally to this work and share first authorship

SPECIALTY SECTION
This article was submitted to Neuroprosthetics, a section of the journal Frontiers in Neuroscience

RECEIVED 24 October 2022
ACCEPTED 24 January 2023
PUBLISHED 16 February 2023

CITATION
Bruni G, Marinelli A, Bucchieri A, Boccardo N, Caserta G, Di Domenico D, Barresi G, Florio A, Canepa M, Tessari F, Laffranchi M and De Michieli L (2023) Object stiffness recognition and vibratory feedback without *ad-hoc* sensing on the Hannes prosthesis: A machine learning approach. *Front. Neurosci.* 17:1078846. doi: 10.3389/fnins.2023.1078846

Object stiffness recognition and vibratory feedback without *ad-hoc* sensing on the Hannes prosthesis: A machine learning approach

Giulia Bruni[1†], Andrea Marinelli[1,2*†], Anna Bucchieri[1,3], Nicolò Boccardo[1,4], Giulia Caserta[1], Dario Di Domenico[1,5], Giacinto Barresi[1], Astrid Florio[1], Michele Canepa[1,4], Federico Tessari[6], Matteo Laffranchi[1] and Lorenzo De Michieli[1]

[1]Rehab Technologies, Istituto Italiano di Tecnologia, Genoa, Italy, [2]Department of Informatics, Bioengineering, Robotics System Engineering (DIBRIS), University of Genova, Genoa, Italy, [3]Department of Electronics, Information and Bioengineering (NearLab), Politecnico of Milan, Milan, Italy, [4]The Open University Affiliated Research Centre at Istituto Italiano di Tecnologia (ARC@IIT), Genoa, Italy, [5]Department of Electronics and Telecommunications, Politecnico of Torino, Turin, Italy, [6]Newman Laboratory, Massachusetts Institute of Technology, Boston, MA, United States

Introduction: In recent years, hand prostheses achieved relevant improvements in term of both motor and functional recovery. However, the rate of devices abandonment, also due to their poor embodiment, is still high. The embodiment defines the integration of an external object – in this case a prosthetic device – into the body scheme of an individual. One of the limiting factors causing lack of embodiment is the absence of a direct interaction between user and environment. Many studies focused on the extraction of tactile information *via* custom electronic skin technologies coupled with dedicated haptic feedback, though increasing the complexity of the prosthetic system. Contrary wise, this paper stems from the authors' preliminary works on multi-body prosthetic hand modeling and the identification of possible intrinsic information to assess object stiffness during interaction.

Methods: Based on these initial findings, this work presents the design, implementation and clinical validation of a novel real-time stiffness detection strategy, without *ad-hoc* sensing, based on a Non-linear Logistic Regression (NLR) classifier. This exploits the minimum grasp information available from an under-sensorized and under-actuated myoelectric prosthetic hand, Hannes. The NLR algorithm takes as input motor-side current, encoder position, and reference position of the hand and provides as output a classification of the grasped object (no-object, rigid object, and soft object). This information is then transmitted to the user *via* vibratory feedback to close the loop between user control and prosthesis interaction. This implementation was validated through a user study conducted both on able bodied subjects and amputees.

Results: The classifier achieved excellent performance in terms of F1Score (94.93%). Further, the able-bodied subjects and amputees were able to successfully detect the objects' stiffness with a F1Score of 94.08% and 86.41%, respectively, by using our proposed feedback strategy. This strategy

allowed amputees to quickly recognize the objects' stiffness (response time of 2.82 s), indicating high intuitiveness, and it was overall appreciated as demonstrated by the questionnaire. Furthermore, an embodiment improvement was also obtained as highlighted by the proprioceptive drift toward the prosthesis (0.7 cm).

KEYWORDS

closed-loop control, stiffness recognition, vibrotactile feedback, vibromotor, Hannes prosthetic hand, non-linear logistic regression

1. Introduction

Upper limb loss is a serious impairment due to its explicit and direct interaction with the external world. To compensate for this loss, prostheses have been introduced to restore the functionality of human limbs during activities of daily living (ADLs). This necessity led to the development of high-tech devices with multiple degrees of freedom (Medynski and Rattray, 2011; Van Der Niet and Van Der Sluis, 2013), capable of performing a variety of gestures and grasps. However, the embodiment of these devices into the human body scheme and their acceptance are also essential elements for reconnection with the outside world (Cuberovic et al., 2019; Castellini, 2020). The term "Embodiment" means the integration of an external object in the internal corporal scheme as if it was part of the body itself. In this specific context, the external object is, precisely, the prosthesis (Longo et al., 2008). Embodiment comprises three correlated factors, namely, ownership, localization, and agency (Stiegelmar et al., 2020), and it has been suggested to promote intuitive control, learning, and comfort when using new tools, thus providing the opportunity to improve the user interface for devices such as artificial limbs. The introduction of direct feedback modalities can prevent amputees to rely exclusively on sight (Biddiss et al., 2007; Pylatiuk et al., 2007), reducing the mental effort and, therefore, facilitating the communication between user intention and prosthesis action (Markovic et al., 2018; Valle et al., 2018; Clemente et al., 2019). In fact, it has been demonstrated that the introduction of haptic feedback improves the control of the prosthesis (Mayer et al., 2020; Sensinger and Dosen, 2020; Yildiz et al., 2020; Chai et al., 2022) due to its fundamental role during human–objects interactions (Hsiao et al., 2011; Valle et al., 2018; Pena et al., 2019; Di Pino et al., 2020; Shehata et al., 2020; Raspopovic et al., 2021), allowing subjects to embody the device (Antfolk et al., 2013; Svensson et al., 2017; Raspopovic et al., 2021), hence, improving the compliance among the user, the prosthesis, and the grasped objects (Osborn et al., 2016). In the literature, this interaction is mainly assessed by providing grasp force or proprioceptive information (Stephens-Fripp et al., 2018). Contrarily, the aim of this study is to deliver information about the grasped object's stiffness that in normal conditions, occurs due to the combination of visual sensory information, proprioceptive sensations related to shape and size, and tactile sensations related to stiffness (Garland and Miles, 1997). Therefore, the current research activity offers an intuitive, non-invasive, and easy-to-use prosthetic system capable of identifying simple grasped object proprieties when visual sensory information of the user is not available or limited (Sensinger and Dosen, 2020). For instance, when the user is taking an object from a bag without looking at it or when the light in the environment is off. This situation was also treated by the Cybathlon 2020 competition, which introduced the Haptic Box task, considering it as a common ADL (Caserta et al., 2022).

Focusing on tactile sensations, several studies tried to reproduce the properties of human skin endowing the device with tactile sensing technologies that typically requires cumbersome add-on like sensing skin with different kinds of sensors such as piezoresistive (Osborn et al., 2018), capacitive (Cannata et al., 2008), piezoelectric (Yi and Zhang, 2016), and also optical (Zhao et al., 2016). The measurements acquired by these tactile sensors are often given as input to machine learning algorithms, which extract useful information that may be conveyed to the prosthesis users, as described by Jamali and Sammut (2011), Liarokapis et al. (2015), Konstantinova et al. (2017), Devaraja et al. (2020), Huang and Rosendo (2022).

Once the tactile information has been extracted, it is necessary to effectively provide it to the subject. The sensory substitution process can be exploited non-invasively, involving the connection of a certain event with specific feedback that is not the natural one, such as tactile sensory feedback (Clemente et al., 2015; Dosen et al., 2016; Patel et al., 2016; Štrbac et al., 2016; Sensinger and Dosen, 2020). For example, the subject can be taught to associate a certain vibratory stimulus with the contact of the prosthesis with an object (Antfolk et al., 2012b; Clemente et al., 2015, 2019; Dosen et al., 2016; Štrbac et al., 2016; De Nunzio et al., 2017; Nemah et al., 2020; Mamidanna et al., 2021). In contrast, superficial stimulation could target portions of the missing limb's skin that are innervated by afferent neurons after the amputation, the so-called referred touch, to stimulate the phantom limb and improve the embodiment (Antfolk et al., 2013; Masteller et al., 2021), such as kinesthetic sensory feedback.

The most common feedback restoration method is through vibration (Masteller et al., 2021), given its compatibility with electromyography (EMG) control and better acceptance by the subjects with respect to electrostimulation, capable of stimulating phantom limb sensation with electric surface charge (Shannon, 1976; Kaczmarek et al., 1991; Vargas et al., 2019). It is possible to provide different types of information acting on the amplitude and frequency of the vibration, as exploited in the study of Witteveen et al. (2013), in which the magnitude of the grasp force was transmitted using different levels of amplitude. An alternative to this feedback is the mechanotactile, as proposed using tactors by Meek et al. (1989), producing a one-to-one correspondence of

touch sensation to user stimulation, or with a cuff, as proposed by Casini et al. (2015).

However, despite the high potentiality offered by these solutions, they are mainly bulky and heavy, and difficult to integrate, along with high-power consumption due to high computational burden. An example is proposed by Antfolk et al. (2012a) who designed a touch sensory feedback *via* air-mediated pressure from the hand to the forearm skin. This is a no-power solution that has neither impact on power consumption nor on computational burden. However, the final integration within the prosthesis does not guarantee the anthropomorphism of the hand device. It is also important to point out that the quick disconnection between the socket and the hand prosthesis is lost due to the mechanical connections running from the fingers' hand to the on-socket actuators. Standard devices use an electronic slip ring combined with a quick disconnect mechanism integrated into the prono-supinator wrist to guarantee the overall disconnection of the hand prosthesis from the socket in case of emergency. However, in the proposed design, this feature is compromised. Other examples are Oddo et al. (2016) and Shehata et al. (2018) who proposed an artificial fingertip to improve the performance of prosthetic hands by using intraneural stimulation. That solution can be nicely integrated into a fingertip by maintaining the anthropomorphic characteristics. However, the on-board electronics that record, process the tactile information, and encode the stimulation are cumbersome. Moreover, the high-power consumption of the FPGA-based solution does not permit the entire system to last for an entire day and to fit into a standard socket. Similarly, Clemente et al. (2019) developed a solution whose electronic skin offers high sensitivity ranging from light touch to heavy touch. However, a similar integration problem of the dedicated board occurs. In contrast, Vargas et al. (2021) finally proposed force and position sensors on the fingers to provide object stiffness recognition on amputees through vibrotactile feedback. That solution can be easily integrated; however, the performances of such a solution are limited in comparison with our results. Due to these issues, the lack of a suitable feedback restitution method in the prosthetic field is still far from being solved. Two other solutions for object stiffness recognition, without dedicated sensors, were implemented by Balasubramanian et al. (2021) and Wang et al. (2021). Their studies demonstrated the feasibility of these approaches in a robotic scenario using an actuated mechanical gripper.

Considering the advantages of providing feedback to amputees to improve the comfort between the user and the device, in this study, we first investigated the possibility of detecting void grasp and object grasp. Then, we identify the softness and hardness of the objects, therefore, permitting the user to discriminate among "void grasp," "rigid object," and "soft object" without visual sensory information. In the first preliminary study (Bruni and Bucchieri, 2021), a virtual multi-body model of Hannes was developed to offline demonstrate, with a virtual simulation, how the motor-side current absorption and the position measurement could be correlated with the hand grasp force and the grasped object's stiffness. Subsequently, in the following study (Bruni et al., 2022), an Ensemble Bagged Trees classifier was implemented and offline tested with simulated data to validate an approach to distinguish two different objects' stiffness.

Consequently, in the present article, we exploited the previously preliminary validated approach to develop an online (real-time) solution to perform object stiffness recognition and sensory feedback. The performance of this solution was assessed on end-users, both able-bodied and amputees. A non-linear logistic regression (NLR) classifier was used to recognize rigid or soft objects and void grasps. We excluded embedded force sensors, whose introduction would require facing many challenges, starting from the choice of the right sensor with basic requirements like high resolution, high sensitivity, and robustness, to the difficulties of managing the wiring (Kappassov et al., 2015). Instead, we proposed a methodology that uses *intrinsic sensors* (sensors and parameters already available on the prosthesis) for the normal functionality of the prosthesis that does not increase the cost and complexity of the device. In particular, we exploited the following intrinsic sensors: the motor-side current, whose relationship with the contact stiffness has been analytically demonstrated by Deng et al. (2020); the reference position, given as input to control the device closure; and the position effectively measured by the encoder (encoder position). We implemented a closed-loop vibratory feedback, using a single vibromotor embedded in the Hannes system, closely related to the predictions made by the classifier. In detail, we applied the strategy of strong vibration for rigid objects and small vibration for soft objects, which was identified in this study as "Two Feedback (2FB) condition" (Cipriani et al., 2011; Tejeiro et al., 2012). In the first phase, the classifier performance and the 2FB effectiveness were evaluated with 18 able-bodied subjects by measuring the classification accuracy through F1Score. In the second phase, a comparison between our proposed feedback method (2FB) and three other control feedback conditions was carried out on five amputees. This comparison was performed both objectively by measuring F1Score, users' response time, and proprioceptive drift, and subjectively through the questionnaire to investigate the users' appreciation of the feedback strategies and identify the most intuitive and effective one.

2. Materials and methods

2.1. Subjects

A total of 18 able-bodied subjects aged between 24 and 50 years (28.8 ± 6.2) and 5 mono-lateral amputees (right transradial amputees and users of active prostheses) were recruited for this study, with the definition described in Table 1. Written informed consent was obtained from all the subjects. The experimental protocol was approved by the Area Vasta Emilia Centro (AVEC) Ethics Committee (Protocol Code: CP-PPRAS1/1-03) and performed in accordance with the guidelines of the Declaration of Helsinki.

2.2. Experimental setup

The experimental setup that used for performing the entire experiment (Figure 1) was composed of (A) the myoelectric prosthesis Hannes, fixed on a rigid cone; (B) a custom master-board to control the hand, decode the stiffness of the grasped object, and

TABLE 1 Population of amputees.

Amputees	Age	Time from amputation	Dominant limb (before amputation)	Amputated limb	Etiology	Level of amputation	Type of prosthesis
A1	53	32 years	Right	Right	Work accident	Unilateral medial	Michelangelo hand
A2	42	18 years	Right	Right	Car accident	Unilateral proximal	Variplus hand
A3	58	37 years	Right	Right	Work accident	Unilateral distal	Michelangelo hand
A4	35	12 years	Right	Right	Work accident	Unilateral distal	Variplus hand
A5	68	53 years	Right	Right	Work accident	Unilateral distal	Michelangelo hand

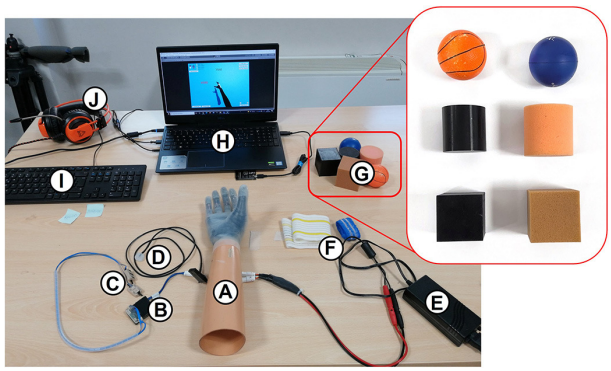

FIGURE 1
Experimental setup used to perform the task on healthy subjects and amputees. It consists of: **(A)** socket with the Hannes prosthesis; **(B)** the EMGM to control the Hannes hand, recognize the grasped object, and provide feedback; **(C)** EMG sensors; **(D)** vibromotors; **(E)** power supply; **(F)** elastic band to attach the EMGs and vibromotors to the forearm; **(G)** the objects used to perform the task; **(H)** laptop with the virtual reality; **(I)** keyboard to choose between rigid, soft, or void; **(J)** headphones to isolate the participants during the experiment.

communicate with the PC *via* Bluetooth; (C) two EMG sensors (standard Ottobock, 13E200 = 50 AC) to close or open the hand; (D) an eccentric rotating mass (ERM) vibromotor to convey the feedback; (E) a power supply for the prosthetic system; (F) two wristbands to attach the EMG sensors and the vibromotor to the subject's forearm; (G) three rigid objects and three soft objects with spherical, cubic, and cylindrical shape used during the Cybathlon 2020 edition (Medynski and Rattray, 2011; Caserta et al., 2022); (H) a laptop to choose the feedback condition and to collect the data; (I) a keyboard, placed in front of the subject, to press the left (rigid object) and right (soft object) arrows to indicate the guessed stiffness of the grasped object; and (J) headphones reproducing white noise to prevent the users from hearing the prosthesis motor.

The vibromotor was inserted into a custom silicone holder to localize and absorb the radiating stimulation and to avoid the possible heating of the skin due to prolonged vibration. The vibromotor was placed vertically with respect to the skin to produce a stronger and more focused sensation. The vibration frequency was set to 200 Hz, using a supply voltage of 2.5 V (Vybronics, 2021)[1], and the amplitude was varied through pulse width modulation (PWM).

2.2.1. The Hannes hand

Hannes is an under-actuated poly-articulated prosthetic hand characterized by a leader-follower wire configuration used to control the movements of fingers (Laffranchi et al., 2020). The hand powertrain consists of a single DC motor coupled with a custom planetary gearhead, which drives the grasping movement (refer to Supplementary material). The actuation system is controlled by a position reference (ϑ_{ref}) synthesized from the user's EMG signals. A magnetic encoder measures the slow shaft position (ϑ_{out}) of the hand drive train, therefore, controlling the desired grasp configuration. The low-level control system is based on a series of proportional–integrative–derivative (PID) controllers. The outer loop is position based (where only proportional and derivative (PD) terms are deployed), while the inner loop is current based and concerns proportional and integrative (PI) terms only. In particular, the error (ε_{pos}) between ϑ_{ref} (hand control command) and ϑ_{out} (outer feedback) is fed to the outer PD loop. The related output is then multiplied by a proportional gain, resulting in a current reference (i_{ref}) which is subtracted with the measured one (i_{out}, inner secondary feedback which is the current absorbed by the DC motor during hand movement and grasp). As consequence, the related error (ε_i) is then fed to the inner PI controller, hence, generating the control command (V) to be delivered to the motor driver. As with many under-actuated prostheses, Hannes is under-sensorized. Indeed, the only available measurements are motor-side current and position.

2.2.2. Feedback conditions

The following four different feedback conditions were assessed in this study: (i) no FB condition (NoFB); (ii) audio FB condition (AFB); (iii) one FB condition (1FB); and (iv) two FB conditions (2FB). The NoFB condition was characterized by the absence of any possible feedback. The subjects were visibly (with closed eyes) and

1 Vybronics is a datasheet of a product available in the following link: https://www.vybronics.com/wp-content/uploads/datasheet-files/Vybronics-VC0625B001L-Jinlong-C0625B001L-datasheet.pdf.

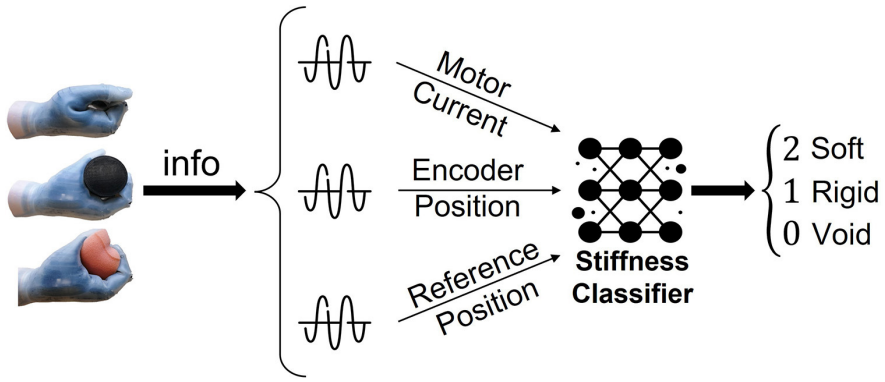

	NoFB	AudioFB	1FB	2FB
Soft	-	-	30% PWM	30% PWM
Rigid	-	-	30% PWM	100% PWM
Void	-	-	0% PWM	0% PWM

FIGURE 2
Scheme representing the object stiffness classification process. The motor-side current, the reference, and the encoder positions are acquired from Hannes and sent as input to the classifier, which gives as output the resulting stiffness.

auditorily (headphones with white noise) blind and without any vibratory feedback. In the AFB condition, no vibratory feedback was supplied to the user, but the absence of the headphones permitted accidental auditory feedback of the moving prosthesis. In the 1FB condition, the vibratory feedback was provided, but the same vibration intensity (30% of PWM) was associated with both rigid and soft objects, while no vibration was given during void closures (refer to the table in Figure 2). The 2FB condition provided a strong vibration for rigid objects (100% of PWM) and a light vibration for soft objects (30% of PWM, a value found during some previous pilot tests to be perceived sufficiently different from the 100% used for rigid objects; refer to the table in Figure 2). As in the 1FB condition, void closures did not provide any kind of vibration. The no FB condition was implemented as a baseline for validation and comparison of subjects' performance. In fact, in the total absence of feedback, subjects' performance should be close to a random guess. The audio FB condition was introduced, since it represents a reasonable scenario of the use of the prosthetic hand by amputees, namely with no direct vision of the prosthesis but accidental auditory information from the prosthesis motion. Therefore, this second condition works as a real-case scenario ground truth for the user. The other two conditions, i.e., 1FB and 2FB, were implemented to observe, respectively, if additional vibratory feedback could improve the stiffness estimation performance, and if a different degree of vibration could further help amputees in discerning between harder and softer objects.

2.3. Non-linear logistic regression

2.3.1. Algorithm model

The algorithm chosen for the object stiffness discrimination task is the NLR classifier. This machine learning algorithm was selected given the good performance shown for multiclass classification problems, and for simplicity reasons, since the NLR is already employed for the Hannes pattern recognition control strategy (Marinelli et al., 2020; Di Domenico et al., 2021). It is based on the calculation of the class membership probability through the following formulation:

$$P(1|x,\vartheta) = \begin{cases} g\left(\vartheta^T \cdot x\right) = \frac{1}{1+e^{-(\vartheta^T \cdot x+\vartheta_0)}} \\ 1 - P(y=0|x,\vartheta) \end{cases}$$

Where ϑ and ϑ_0 are the internal parameters vector of the classifier and the bias term, respectively; x is the input feature vector, while g(·) is the sigmoid logistic function. The class prediction is obtained from the comparison between the distribution $P(y|x)$ with a decision threshold (TH) as:

$$h_\vartheta(x) = \begin{cases} P(1|x,\vartheta) \geq TH \rightarrow 1 \\ P(1|x,\vartheta) \leq TH \rightarrow 0 \end{cases}$$

The TH value was obtained after an optimization phase on the validation set. Since the NLR is a binary classifier, a One-vs-All approach was implemented to address the multiclass classification problem for the discrimination between rigid, soft, and void closures. This involves the use of as many binary classifiers as the classes for prediction, and each of them is trained to recognize the specific class. The model parameters (ϑ) are the result of an optimization process that involves the minimization of a cost function called cross-entropy error J:

$$J(\vartheta,\vartheta_0) = -\frac{1}{m} \cdot \left[\sum_{i=1}^{m} y(i) \cdot \ln(g(\vartheta^T \cdot x + \vartheta_0))\right] - \frac{1}{m} \cdot \left[\sum_{i=1}^{m} (1-y^{(i)}) \cdot \ln(1-g(\vartheta^T \cdot x + \vartheta_0))\right]$$

	Spring 1	Spring 2	Spring 3	Spring 4
K [N/mm]	1.55	4.09	4.09	2.9
L_0 [mm]	40	40	40	35
Deflection max [mm]	26	25	24	12.5

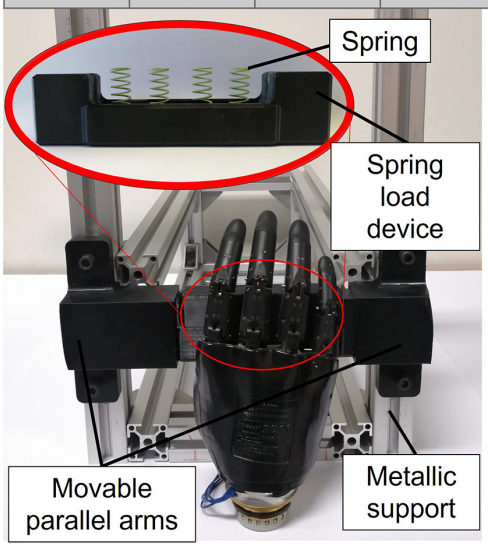

FIGURE 3
Custom-made hand dynamometer mounted on test bench used for the classifier training. The device is composed of a base where at maximum four strings can be inserted, and a cover which can slide along the base when compressed by the prosthesis fingers. The test bench consists of a custom-made system composed by movable parallel arms and a two-cuff system acting as holder. The table represents the different spring force and levels to characterize the stiffness of the dynamometer.

Where m is the number of samples used to train the algorithm and $y(i)$ is the known class membership of the i_{th} sample (Dellacasa Bellingegni et al., 2017; Marinelli et al., 2020).

2.3.2. Algorithm training

To adapt the model to distinguish multiple rigidities, the classifier required a training phase involving the repetitive closure of the prosthesis on objects of different stiffness. To simplify this work and to create a reproducible acquisition setup, a custom-made object was 3D printed. This device, as shown in Figure 3, was designed to reproduce the same shape and dimension of the Go Direct® Hand Dynamometer (Vernier, 2021), used in the previous study (Bruni and Bucchieri, 2021), which offers the possibility to insert springs of different stiffness, simulating the grasping of soft and rigid objects, as shown in the table of Figure 3.

The device was mounted in an *ad-hoc* designed test bench. It was composed of movable parallel arms and a two-cuff system acting as a holder. The prosthesis was fixed at the base of this test bench, as shown in Figure 3, in such a way that only the distal phalanges of the four fingers had an impact on the upper plate of the device when performing a closure.

Hannes was controlled through a USB GUI, which allowed the data acquisition (motor-side current and encoder position) as well.

The NLR model generation was performed offline through MATLAB and it required training and test datasets, both characterized by the following four-column structure: (i) the motor-side current, (ii) the reference position sent as input, (iii) the encoder position measured, and (iv) the labels of the objects (rigid, soft, and void), as it is a supervised learning algorithm. All these measurements are fed to the classifier as analog signals; thus, they are directly used as the input dataset. Moreover, the label zero was associated with void closures (for motor-side currents, below 300 mA), one to the rigid objects and two to the soft objects. The dataset was created using the test bench described in Figure 3.

The choice of relying on only the motor current and the reference and measured motor encoder position was based on the immediate and relevant available sensor information on the prosthesis. Specifically, the motor current is proportional to the motor torque and, thus, to the grasp force, while the encoder position is related to the grasping motion of the fingers. In addition, the difference between reference and measured encoder position provides good information regarding the distinction between a void closure and the actual grasping of an object (this is due to the variation between the reference encoder positions that continues to grow due to EMG residuals, while the actual measured encoder position stops when encountering an object during grasp). These three quantities (current, reference, and measured positions) represent, according to the authors, the minimum set of variables to properly classify the different types of grasping (refer to the "Results" section for details on the performances). Nonetheless, it is worth mentioning that additional sensors or derived quantities could be beneficial for a more complex classifier structure. For example, motor speed, if not particularly noisy or delayed, could help in more advanced classification algorithms.

To generate the variability of the data, multiple grasps with various stiffness were performed by the prosthesis, which was controlled by both EMG and sinusoidal references. The hand dynamometer was used to simulate rigid objects, while four types of springs with distinct stiffness were used to reproduce a range of softness/soft objects, as shown in the table of Figure 3. The springs are placed under a bar to distribute the stiffness of their combination to the entire grasp. The chosen combination of springs is different for each case because the total stiffness of parallel springs varies according to their sum, thus affecting the total grasp behavior. In particular, several closures were performed for each case, as described in Table 2, to collect data for the training and validation of the NLR model. The training dataset was split into a training set (80%), used for the model generation (selection of the best model parameters (ϑ) by minimizing the cost function J), and a validation set (20%) to find the best threshold (TH). Lastly, the classifier was evaluated on the test dataset.

2.4. Experimental protocol

The subjects were seated comfortably in front of a table (refer to Figure 4) with EMG sensors positioned on the forearm or stump

TABLE 2 Dataset realization for training the NLR for object stiffness recognition algorithm.

Number closures	Grasped object	Stiffness	Control signal
10	Void	Void	Sinusoidal
10	Hand dynam	Rigid	Sinusoidal
10	Hand dynam	Rigid	EMG
5	4xS1	Soft	Sinusoidal
5	4xS1	Soft	EMG
5	2xS1	Soft	Sinusoidal
5	2xS1	Soft	EMG
5	4xS2	Rigid	Sinusoidal
5	4xS2	Rigid	EMG
5	4xS3	Rigid	Sinusoidal
5	4xS3	Rigid	EMG
5	2xS1–2xS4	Soft	Sinusoidal
5	2xS1–2xS4	Soft	EMG

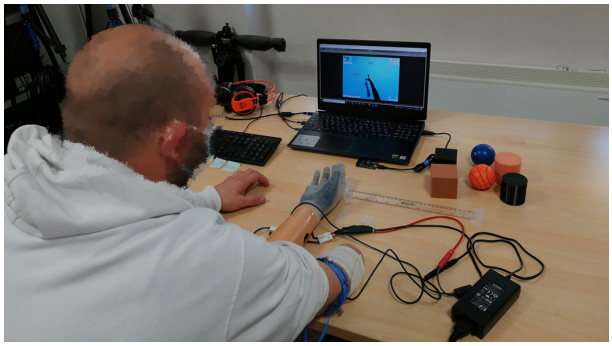

FIGURE 4
Example of trial involving an amputee. Two EMGs are attached to the stump for the dual-side control of the prosthesis with an elastic band. The vibromotor is fixed to the upper side of the stump with a second elastic band for the feedback restitution. The objects are placed within Hannes hand by the experimenter while the participant has closed eyes. The keyboard, placed in front of the participant, is used to indicate the grasped object stiffness by the user using the left hand.

using an elastic band. The electrodes measured the activity of the forearm muscles involved in the opening and closing of the hand (Flexor Carpi Ulnaris and Extensor Carpi Ulnaris, respectively), which were selected by manual inspection. The Hannes system was detached from the users' bodies (except for the two EMGs) and fixed on the table, lying between the subjects' arms with the palm up, to allow the experimenter place the objects to be grasped within the prosthetic hand. Hence, subjects were only asked to close and open their hand, not to approach or grasp the objects. The prosthesis was commanded in proportional-speed-control mode through the EMG signals. To convey the vibratory feedback, the vibromotor was positioned on the pisiform bone for able-bodied subjects and on the lateral epicondyle for the amputees by means of a second elastic band.

First, the minimum and maximum amplitude for the vibromotor was determined using the method of limits (Prins, 2016), to find the minimum level of perception and avoid discomfort. To this aim, the vibration intensity was increased in small steps (4–5% in the normalized scale of PWM). When the subject warned, as soon as it was perceptible, the sensing of a small and then of a strong sensation, the respective PWM was saved. Subsequently, 30% of the PWM range was adopted for soft objects and 100% was adopted for rigid objects. The vibration intensity was then modulated between these two values to generate clearly perceivable and localized vibrations that were not intrusive to the subject but intuitive for the encoding of the object stiffness.

Six objects (Figure 1) were randomly presented three times to the user by the experimenter and three void closures were also inserted along the test, to have a total number of 21 trials. Before the test phase, a training phase was performed to let the user become familiar with the feedback. A total of six closures were performed, alternating between rigid and soft objects without headphones and with open eyes, so the user could learn to associate the proper feedback with the right stiffness. Furthermore, the involved upper limb side was covered with a black blanket to strengthen a possible embodiment effect.

In the first phase to evaluate the classifier performance and the feedback effectiveness, the able-bodied subjects underwent a single test with a single condition. They performed the test with the 2FB condition. The participant was asked to wear headphones with white noise and to close the eyes (avoiding the sight of the prosthesis and the grasped object). The subject was not required to reach out to the object. Instead, the experimenter proceeded to insert it directly into the prosthesis, asking the subject to perform a full closure, and then to identify the stiffness of the squeezed object. The answer was provided by the subject's left hand pressing the keyboard arrows, left for rigid objects and right for soft objects. No button needed to be pressed when the prosthesis performed a void closure. Finally, the subject could reopen the eyes to check if the answer was correct.

In the second phase, a comparison between the four different feedback conditions, discussed in the "Feedback conditions" section, was carried out by five transradial amputees. The order of these four sessions was randomly presented to the amputees. Each condition had the same test protocol already described in the first phase with able-bodied subjects, in which the experimenter places the object inside the prosthetic hand and the amputee performs a grasp with closed eyes and gives the answer using the keyboard. At the end of each session, the proprioceptive drift was detected with respect to the initial arm position (refer to the "Amputees" section) and an *ad-hoc* questionnaire was administered (refer to Supplementary material).

2.5. Data analysis

All the outcomes and the evaluation methods used in this study were tested for normality using the Shapiro–Wilk test.

A repeated measure one-way ANOVA or Friedman test was conducted depending on the outcome of the normality test (for the analysis of dataset with missing data, Skilling's Mack was applied in substitution of the Friedman test), while the multiple comparison test with Bonferroni correction was used for a *post-hoc* analysis. Mathworks MATLAB 2020b was used for the statistical analysis. The average of the measures used (error and efficiency) was computed for each subject and condition and compared across conditions. The threshold for statistical significance was set at $p < 0.05$. The results in the text are reported as mean and standard deviation.

2.5.1. Able-bodied subjects

The primary outcome measure was the F1Score of the classifier on detecting the grasped object's stiffness expressed as a percentage, which takes into account the rate of false and true positives and false negatives (Powers, 2020). This result demonstrates that our approach to intrinsic sensor stiffness detection works properly. In addition, the F1Score was calculated on users' performance in recognizing objects' stiffness using the 2FB approach described in the "Feedback conditions" section. This latter was used to verify the usability and clarity of our feedback method.

2.5.2. Amputees

The second phase involving five amputees was carried out to compare the four feedback conditions. To validate and demonstrate that the 2FB condition was effective and the best feedback restoration for the recognition of objects' stiffness, our hypothesis involving the following four evaluation methods was used: (i) F1Score of performance; (ii) reaction time to recognize the stiffness of the objects; (iii) proprioceptive drift; and (iv) *ad-hoc* questionnaire.

The F1Score of amputees' performance was calculated in all feedback conditions. Furthermore, the response time of each trial was also recorded for the four conditions. Low response times were considered positive results. For each amputee, the mean response time of each feedback condition was calculated to allow comparison.

As a quantitative measure of the embodiment, the proprioceptive drift toward the artificial limb was detected (Tsakiris and Haggard, 2005). Before covering the involved upper limb side with a black blanket, the initial position of the hand was marked with white tape. Immediately, after the experiment, the blanket was removed and the amputees were asked to close their eyes, raise their stump, and replace it in the perceived initial position. The lateral distance between the initial position and the one estimated after the trials was measured by the experimenter with a ruler in centimeters, together with the direction of the deviation (Barresi et al., 2021). Deviations toward the prosthesis were considered an effect of the embodiment process.

At the end of each session, amputees also had to complete a Likert-type 5-point questionnaire, providing a subjective evaluation. The questionnaire (refer to Supplementary material) aimed to assess subjectively the intuitiveness and comfortability of the feedback (seven questions), its utility for ADLs (three questions), and the embodiment (four questions). The possible answers ranged between 1 (strongly disagree) and 5 (strongly agree). Since all amputees performed the test in all conditions, the experimental design is within-subject.

3. Results

3.1. Able-bodied subjects

The classifier's average accuracy in identifying the object stiffness was tested on a total of 378 grasps (21 grasps $\times$ 18 subjects). Its average F1Score resulted to be 94.93% $\pm$ 3.94. The able-bodied subjects instead, due to the 2FB condition, reached an average F1Score of 94.08% $\pm$ 4.0 for the object's stiffness discrimination task.

Figure 5A shows the F1Score obtained by able-bodied subjects during the 2FB condition compared to the F1Score of the classifier performance. Since these data did not present a normal distribution, the Friedman test was applied to demonstrate that no statistical difference was detected between the two populations ($p = 0.1$).

3.2. Amputees

Figure 5B shows the boxplot of F1Score obtained by amputees for each of the four feedback conditions. It is possible to observe an ascending trend in the scores from the NoFB condition to the 2FB condition. In the NoFB condition, Amputee A3 data are missing because he found it impossible to accomplish the task without any feedback, stating that it was not possible to understand if the prosthesis was opened or closed. In the 1FB condition, Amputee A5 data are missing due to a recording problem.

For the NoFB condition, the F1Score among amputees is 31.41% $\pm$ 8.57, as indicated in Figure 5B with points, which is below the random chance probability of 33%. The statistically significant difference is indicated by "*" ($p < 0.05$). Only Amputee A1 achieved a higher F1Score with respect to random chance (F1Score = 44.03%). The distributions resulted to be normal, so the statistical analysis applied was the ANOVA. As shown in Figure 5B, the 2FB condition presents a statistically significant difference with respect to the NoFB ($p < 0.001$) and AFB ($p < 0.001$) conditions. Furthermore, the 1FB condition is statistically different from the NoFB condition ($p = 0.0031$). The average F1Score calculated from the five amputees' responses during the 2FB experimental session is 86.41% $\pm$ 11.6.

Figure 5C shows the average response time for amputees in each feedback condition, in which the statistically significant difference is indicated by "*" ($p < 0.05$). All amputees, except A1, achieved the lowest response time during the 2FB condition (2.82 s $\pm$ 1.2), which also produced the best results in terms of F1Scores. A statistical analysis was performed between the different conditions. The distribution resulted to be not normal and, given the presence of some missing data, the Skillings–Mack test was applied. As shown in Figure 5C, there is a statistically significant

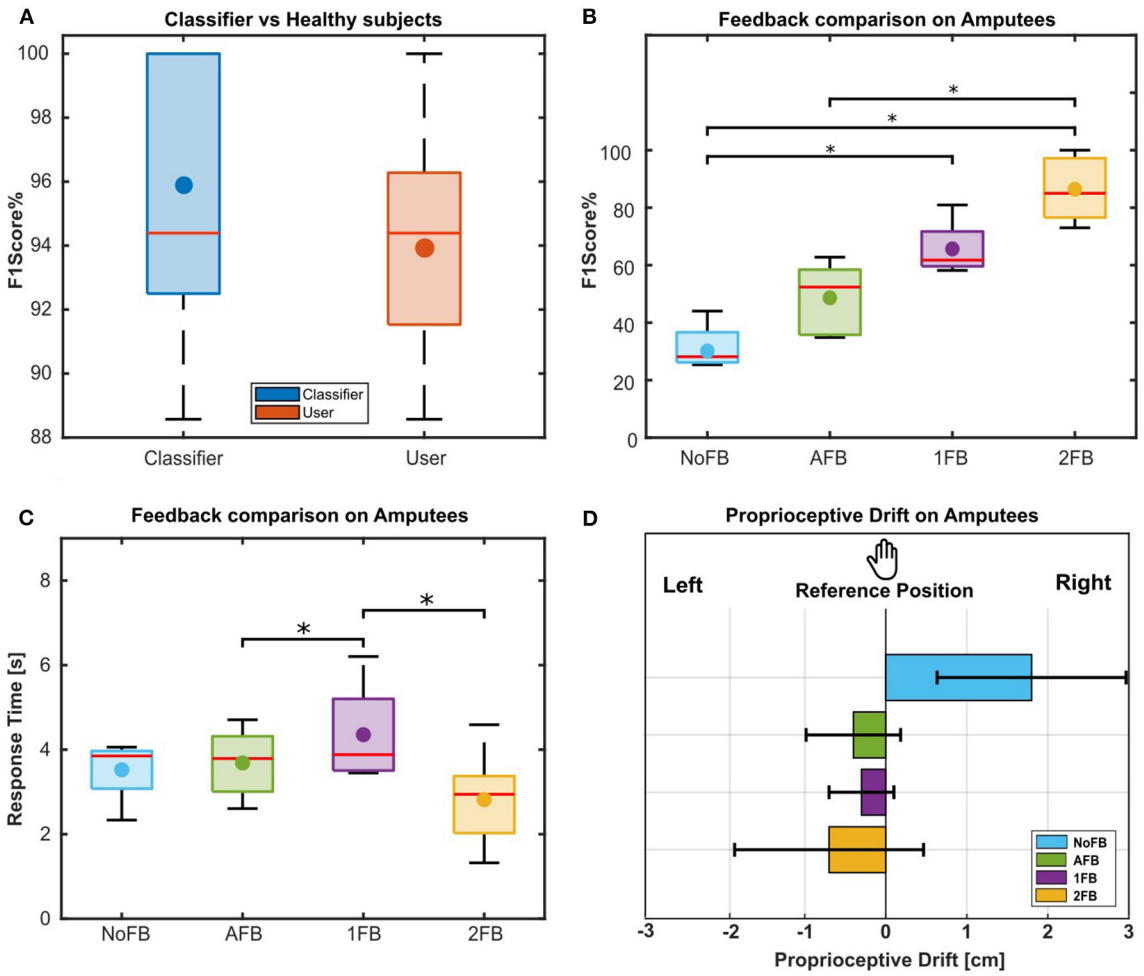

FIGURE 5
(A) F1Scores results of classifier with respect to able-bodied subjects. First, the F1Score of the classifier is calculated (blue box). Then, the F1Score of 18 able-bodied subjects is evaluated, based on the answer of classifier, in recognizing the objects' stiffness while receiving the 2FB condition (red box). A comparison between classifier's and subjects' F1Score was assessed and no significant difference was found between the two populations. **(B)** F1Scores results for amputees. F1Score obtained by amputees for each feedback condition. The Box chart shows the comparison between the distributions of the F1Scores obtained in each condition. The statistically significant difference is indicated by "*" ($p < 0.05$). **(C)** Response time results for amputees. Response time obtained by amputees for each experimental condition. The Box chart shows the comparison between the distributions of the response time obtained in each condition. The statistically significant difference is indicated by "*" ($p < 0.05$). **(D)** Proprioceptive drift of amputees for the different feedback conditions as a quantitative embodiment measure. The barplot shows the mean and standard deviation of the drift over amputees for each condition, the left direction is toward Hannes hand, and the right direction indicates a movement on the opposite side of Hannes hand. Deviations toward the prosthesis were considered an effect of the embodiment process.

difference between AFB and 1FB conditions ($p = 0.02$) and between 1FB and 2FB conditions ($p = 0.04$).

The mean proprioceptive drift for each feedback condition was calculated, and it is reported in Figure 5D as bar plots with standard deviations. On average, the five amputees estimated the position of their right arm after the experiment as 1.8 cm ± 1.17 right (in the opposite side of the prosthesis) during the NoFB condition while 0.4 cm ± 0.58, 0.3 cm ± 0.4, and 0.7 cm ± 1.17 toward left and hence Hannes during AFB, 1FB, and 2FB conditions, respectively. The only significant difference was found between NoFB and 2FB conditions ($p = 0.017$) with the Nemenyi test for a *post-hoc* comparison.

According to comparisons performed through the Friedman test (because the scales are discrete and the actual data do not match the assumptions for other inferential techniques), three scales of the questionnaire showed significant effects of the feedback conditions. The subjective evaluations collected about the sessions show that in the 2FB condition:

- Scale 1 made it significantly easier to perceive the difference between soft and hard objects ($p = 0.027$);
- Scale 2 was significantly more intuitive for soft objects ($p = 0.015$);
- Scale 3 was significantly intuitive for rigid objects ($p = 0.005$).

According to Scale 3 scores, the *post-hoc* comparisons performed through the Nemenyi test show how the proposed feedback condition was significantly more intuitive for rigid objects than the NoFB condition ($p = 0.025$) and 1FB condition ($p = 0.017$). Furthermore, the Friedman test showed a significant effect

of the 2FB condition ($p = 0.019$), especially considering the results of the Nemenyi test for the *post-hoc* comparison between 2FB and NoFB conditions ($p = 0.017$).

4. Discussion

The present study explored the possibility to recognize objects' stiffness with an under-sensorized prosthesis. The reference position, the encoder position, and the motor-side current available on Hannes were used to feed a pattern recognition algorithm, capable of generating different vibratory feedback to allow the subject to decode the relative objects' stiffness.

The F1Score of the classifier during the 2FB condition tested with able-bodied subjects (Figure 5A) was very high (94.93% ± 3.94), demonstrating that the only sensors available on Hannes (motor-side current and encoder position) provide sufficient information for an object stiffness discrimination task using an NLR algorithm. However, it is necessary to consider that the classifier, during this experiment, was only tested on six objects of different shapes but with almost the same dimensions (chosen to replicate the objects used during the Cybathlon race, Caserta et al., 2022). Furthermore, the F1Score obtained by able-bodied subjects (Figure 5A) on discriminating the object stiffness was also very good, proving the usability and efficacy of this feedback approach on a user case.

The positive results of the first phase allowed us to evaluate the object stiffness recognition approach on five transradial amputees. In this second phase, we tested four approaches of the feedback scheme (Figure 5B). In the NoFB condition, we expected a correct identification of the right stiffness around the random chance probability (33%). Actually, the F1Score for the NoFB condition was even lower than this percentage (F1Score = 31.41% ± 8.57), as amputees stated they were forced to guess since being deprived of any possible clue. The AFB condition presents a higher average F1Score (48.62% ± 12.56) with respect to the NoFB one, indicating that the motor noise provides less help in this kind of task. This is true for expert users like Amputee A1, who reached the highest score (62.78%), while it is less evident from others like Amputees A3 (34.85%) and A5 (36.11%), who scored almost as random chance. Differently, in the 1FB condition, almost everyone improved their performance (F1Score = 65.67% ± 10.34) with respect to NoFB and AFB conditions. In this condition, the users were clearly helped in recognizing the void closures, since those were the only ones without vibratory feedback. Moreover, most of the amputees declared that even if the intensity of the vibration was the same for rigid and soft objects, they were able to perceive a difference based on the vibration onset. Since soft objects are more compliant, the motor-side current takes more time to rise with respect to a rigid object. Hence, the vibration is slightly late. For this reason, the 1FB condition resulted to be statistically better than the NoFB one, unlike the AFB condition which has no significant difference with respect to the NoFB condition. Overall, the 2FB condition provided the best results (F1Score 86.41% ± 11.6), demonstrating to be significantly more helpful with respect to the other conditions and indicating that the difference in vibration, correspondent to the rigid and soft objects, was sufficiently distinguishable by the users, as we expected. This proves the advantages that this type of feedback can provide to prosthesis users as additional information to the incidental feedback (i.e., auditory feedback).

The reduction in the response time (Figure 5C) in the 2FB condition (2.82 s ± 1.2) is another proof of the efficiency of the implemented distinct vibratory feedback, meaning the amputees needed a short time to understand object's stiffness and enhancing the intuitiveness of the method. This parameter is significantly lower in 2FB (2.82 s ± 1.2) condition with respect to the NoFB (3.52 s ± 0.8), AFB (3.7 s ± 0.83), and 1FB (4.35 s ± 1.28) ones, suggesting that in these latter, the amputees needed to put quite an effort in discriminating between the objects instead.

The proprioceptive drift (Figure 5D) shows an effect of the feedback on the embodiment, especially according to the comparison between 2FB (0.7 cm ± 1.17 toward Hannes hand) and NoFB (1.8 cm ± 1.17 opposite to Hannes hand) conditions. Interestingly, the results could indicate that the presence of a source of feedback is important for summoning the embodiment process. Precisely, the highest impact on the proprioceptive drift was found with the 2FB condition, suggesting that this specific vibratory feedback was the most effective one during the embodiment process. However, a larger sample size is necessary to check potentially higher effects caused by the 2FB condition.

Three scales in the subjective questionnaire significantly highlight the benefits offered by the stimulations provided in the 2FB condition as intuitive feedback, especially for rigid objects. This indicates a possible effect of the feedback on the embodiment (refer to Figure 5D). However, a larger sample is necessary to deepen our understanding of the potential effects of the 2FB condition on embodiment measures in dedicated experiments. Overall, and regardless of the statistical significance, the results seem to point out the superiority of the 2FB condition over all aspects of user experience considered in this study. The qualitative observations provided by the amputees need a larger sample to extract potential user requirements.

5. Conclusion

This study presents the implementation of an online, i.e., real-time, dedicated stiffness detection strategy to provide grasp-oriented vibratory feedback using the Hannes prosthetic hand in a closed-loop scenario. As a further progression of our previous studies, in which we exploited a virtual simulation to find the intrinsic variables correlated to the grasped object's stiffness, this study builds upon those preliminary findings and presents a refined and improved methodology, its implementation, and its clinical validation. The main aim was to implement an online strategy exploiting such measurements (motor-side current, encoder position, and reference position) to detect the stiffness of real objects (without increasing the system complexity with *ad-hoc* force sensing) and to validate such strategy with a first preliminary study with end-users.

The classifier was tested by 18 able-bodied subjects on six objects and resulted to be sufficiently accurate in discriminating between void, soft, and rigid grasps. The stiffness information was conveyed to the users through a single vibromotor, whose intensity changed based on the grasp type, i.e., high intensity for

rigid objects and low intensity for soft objects in our proposed feedback condition (2FB condition). This feedback modality was compared to three other control conditions (NoFB, AFB, and 1FB) in a user study involving five mono-lateral amputees. Results showed a statistically significant improvement in users' performances both in terms of F1Score and response time for the 2FB condition. Moreover, this condition was appreciated by the users, as demonstrated by the subjective questionnaires, which highlighted its intuitiveness, comfortability, and usefulness. This result was also confirmed by the analysis of the proprioceptive drift, which showed an improvement in the prosthesis embodiment. Hence, we can state that our proposed feedback modality was the best among those tested.

In the future, the classifier should be tested on a higher variety of objects with different dimensions and stiffness, especially to investigate the influence of the dimension on the algorithm's performance. Reach and grasp tasks, with active usage of prosthesis, will be implemented to provide a more realistic validation of the usability and effectiveness of our solution within ADL and real scenarios. A higher number of prosthesis users will be involved to better assess the effect of the feedback on the embodiment and its appreciation.

The present study can have a relevant impact on the application of intrinsic sensor detection of object stiffness, as it points out that this object recognition strategy and vibrotactile feedback restitution on upper limb prosthesis could be effectively used as an intuitive and effective closed-loop daily living solution. Such a solution could facilitate the identification of a precise and delicate grasp rather than a strong and powerful one during different object manipulations.

Data availability statement

The raw data supporting the conclusions of this article will be made available by the authors, without undue reservation.

Ethics statement

The studies involving human participants were reviewed and approved by AVEC Area Vasta Emilia Centro Protocol Code: CP-PPRAS1/1-03. The patients/participants provided their written informed consent to participate in this study.

Author contributions

GiuB, AM, NB, GiaB, and GC conceived the study. GiuB and GC administered the experiments. GiuB, AM, NB, and GC designed the figures. AM prepared the figures. All the authors contributed to the writing and reading and approved the final version of the manuscript.

Funding

This study was partially supported by the INAIL-IIT project PR19-PAS-P1-iHannes.

Acknowledgments

The authors thank Paolo Rossi for his help in assembling the prosthetic devices. The Open University Affiliated Research Centre at Istituto Italiano di Tecnologia (ARC@IIT) is part of the Open University, Milton Keynes MK7 6AA, United Kingdom.

Conflict of interest

The authors declare that the research was conducted in the absence of any commercial or financial relationships that could be construed as a potential conflict of interest.

Publisher's note

Supplementary material

The Supplementary Material for this article can be found online at: https://www.frontiersin.org/articles/10.3389/fnins.2023.1078846/full#supplementary-material

References

Antfolk, C., Björkman, A., Frank, S.-O., Sebelius, F., Lundborg, G., and Rosen, B. (2012a). Sensory feedback from a prosthetic hand based on air-mediated pressure from the hand to the forearm skin. *J. Rehabil. Med.* 44, 702–707. doi: 10.2340/16501977-1001

Antfolk, C., D'alonzo, M., Controzzi, M., Lundborg, G., Rosen, B., Sebelius, F., et al. (2012b). Artificial redirection of sensation from prosthetic fingers to the phantom hand map on transradial amputees: vibrotactile versus mechanotactile sensory feedback. *IEEE Trans. Neural Syst. Rehabil. Eng.* 21, 112–120. doi: 10.1109/TNSRE.2012.2217989

Antfolk, C., D'alonzo, M., Rosén, B., Lundborg, G., Sebelius, F., and Cipriani, C. (2013). Sensory feedback in upper limb prosthetics. *Expert Rev. Med. Dev.* 10, 45–54. doi: 10.1586/erd.12.68

Balasubramanian, A. B., Magee, D. P., and Taylor, D. G. (2021). "Stiffness estimation in single degree of freedom mechanisms using regression," in *IECON 2021-47th Annual Conference of the IEEE Industrial Electronics Society* (IEEE), 1–6.

Barresi, G., Marinelli, A., Caserta, G., De Zambotti, M., Tessadori, J., Angioletti, L., et al. (2021). Exploring the embodiment of a virtual hand in a spatially augmented respiratory biofeedback setting. *Front. Neurorobot.* 15, 683653. doi: 10.3389/fnbot.2021.683653

Biddiss, E., Beaton, D., and Chau, T. (2007). Consumer design priorities for upper limb prosthetics. *Disab. Rehabil. Assistive Technol.* 2, 346–357. doi: 10.1080/17483100701714733

Bruni, G., and Bucchieri, A. (2021). *Analysis and Optimization of Hannes Prosthetic Hand: A Multi-Body Approach*. Available online at: politesi.polimi.it

Bruni, G., Bucchieri, A., Tessari, F., Boccardo, N., Marinelli, A., De Momi, E., et al. (2022). "A multi-body model of an upper-limb prosthesis for grip force estimation and related object interaction application," in *2022 9th IEEE RAS/EMBS International Conference for Biomedical Robotics and Biomechatronics* (IEEE), 1–7. doi: 10.1109/BioRob52689.2022.9925478

Cannata, G., Maggiali, M., Metta, G., and Sandini, G. (2008). "An embedded artificial skin for humanoid robots," in *2008 IEEE International Conference on Multisensor Fusion and Integration for Intelligent Systems* (IEEE), 434–438. doi: 10.1109/MFI.2008.4648033

Caserta, G., Boccardo, N., Freddolini, M., Barresi, G., Marinelli, A., Canepa, M., et al. (2022). Benefits of the Cybathlon 2020 experience for a prosthetic hand user: a case study on the Hannes system. *J. Neuroeng. Rehabil.* 19, 1–15. doi: 10.1186/s12984-022-01046-y

Casini, S., Morvidoni, M., Bianchi, M., Catalano, M., Grioli, G., and Bicchi, A. (2015). "Design and realization of the cuff-clenching upper-limb force feedback wearable device for distributed mechano-tactile stimulation of normal and tangential skin forces," in *2015 IEEE/RSJ International Conference on Intelligent Robots and Systems* (IEEE), 1186–1193. doi: 10.1109/IROS.2015.7353520

Castellini, C. (2020). Upper limb active prosthetic systems—overview. *Wear. Robot.* 365–376. Available online at: https://www.sciencedirect.com/science/article/pii/B9780128146590000199. doi: 10.1016/B978-0-12-814659-0.00019-9

Chai, G., Wang, H., Li, G., Sheng, X., and Zhu, X. (2022). Electrotactile feedback improves grip force control and enables object stiffness recognition while using a myoelectric hand. *IEEE Trans. Neural Syst. Rehabil. Eng.* 30, 1310–1320. doi: 10.1109/TNSRE.2022.3173329

Cipriani, C., D'alonzo, M., and Carrozza, M. C. (2011). A miniature vibrotactile sensory substitution device for multifingered hand prosthetics. *IEEE Trans. Biomed. Eng.* 59, 400–408. doi: 10.1109/TBME.2011.2173342

Clemente, F., D'alonzo, M., Controzzi, M., Edin, B. B., and Cipriani, C. (2015). Non-invasive, temporally discrete feedback of object contact and release improves grasp control of closed-loop myoelectric transradial prostheses. *IEEE Trans. Neural Syst. Rehabil. Eng.* 24, 1314–1322. doi: 10.1109/TNSRE.2015.2500586

Clemente, F., Valle, G., Controzzi, M., Strauss, I., IBERITE, F., Stieglitz, T., et al. (2019). Intraneural sensory feedback restores grip force control and motor coordination while using a prosthetic hand. *J. Neural Eng.* 16, 026034. doi: 10.1088/1741-2552/ab059b

Cuberovic, I., Gill, A., Resnik, L. J., Tyler, D. J., and Graczyk, E. L. (2019). Learning of artificial sensation through long-term home use of a sensory-enabled prosthesis. *Front. Neurosci.* 13, 853. doi: 10.3389/fnins.2019.00853

De Nunzio, A. M., Dosen, S., Lemling, S., Markovic, M., Schweisfurth, M. A., GE, N., et al. (2017). Tactile feedback is an effective instrument for the training of grasping with a prosthesis at low-and medium-force levels. *Exp. Brain Res.* 235, 2547–2559. doi: 10.1007/s00221-017-4991-7

Dellacasa Bellingegni, A., Gruppioni, E., Colazzo, G., Davalli, A., Sacchetti, R., Guglielmelli, E., et al. (2017). NLR, MLP, SVM, and LDA: a comparative analysis on EMG data from people with trans-radial amputation. *J. Neuroeng. Rehabil.* 14, 1–16. doi: 10.1186/s12984-017-0290-6

Deng, H., Xu, X., Zhuo, W., and Zhang, Y. (2020). Current-sensor-based contact stiffness detection for prosthetic hands. *IEEE Access* 8, 29456–29466. doi: 10.1109/ACCESS.2020.2972588

Devaraja, R. R., Maskeliunas, R., and Damaševičius, R. (2020). Design and evaluation of anthropomorphic robotic hand for object grasping and shape recognition. *Computers* 10, 1. doi: 10.3390/computers10010001

Di Domenico, D., Marinelli, A., Boccardo, N., Semprini, M., Lombardi, L., Canepa, M., et al. (2021). "Hannes prosthesis control based on regression machine learning algorithms," in 2021 *IEEE/RSJ International Conference on Intelligent Robots and Systems (IROS 2021)*. doi: 10.1109/IROS51168.2021.9636391

Di Pino, G., Romano, D., Spaccasassi, C., Mioli, A., D'alonzo, M., Sacchetti, R., et al. (2020). Sensory-and action-oriented embodiment of neurally-interfaced robotic hand prostheses. *Front. Neurosci.* 14, 389. doi: 10.3389/fnins.2020.00389

Dosen, S., Markovic, M., Strbac, M., Belić, M., Kojić, V., Bijelić, G., et al. (2016). Multichannel electrotactile feedback with spatial and mixed coding for closed-loop control of grasping force in hand prostheses. *IEEE Trans. Neural Syst. Rehabil. Eng.* 25, 183–195. doi: 10.1109/TNSRE.2016.2550864

Garland, S. J., and Miles, T. S. (1997). Control of motor units in human flexor digitorum profundus under different proprioceptive conditions. *J. Physiol.* 502, 693–701. doi: 10.1111/j.1469-7793.1997.693bj.x

Hsiao, S. S., Fettiplace, M., and Darbandi, B. (2011). Sensory feedback for upper limb prostheses. *Prog. Brain Res.* 192, 69–81. doi: 10.1016/B978-0-444-53355-5.00005-1

Huang, J., and Rosendo, A. (2022). Variable stiffness object recognition with a CNN-bayes classifier on a soft gripper. *Soft Robot.* 9, 1220–1231. doi: 10.1089/soro.2021.0105

Jamali, N., and Sammut, C. (2011). Majority voting: material classification by tactile sensing using surface texture. *IEEE Trans. Robot.* 27, 508–521. doi: 10.1109/TRO.2011.2127110

Kaczmarek, K. A., Webster, J. G., Bach-Y-Rita, P., and Tompkins, W. J. (1991). Electrotactile and vibrotactile displays for sensory substitution systems. *IEEE Trans. Biomed. Eng.* 38, 1–16. doi: 10.1109/10.68204

Kappassov, Z., Corrales, J.-A., and Perdereau, V. (2015). Tactile sensing in dexterous robot hands. *Rob. Auton. Syst.* 74, 195–220. doi: 10.1016/j.robot.2015.07.015

Konstantinova, J., Cotugno, G., Stilli, A., Noh, Y., and Althoefer, K. (2017). "Object classification using hybrid fiber optical force/proximity sensor," in *2017 IEEE SENSORS* (IEEE), 1–3. doi: 10.1109/ICSENS.2017.8234057

Laffranchi, M., Boccardo, N., Traverso, S., Lombardi, L., Canepa, M., Lince, A., et al. (2020). The Hannes hand prosthesis replicates the key biological properties of the human hand. *Sci. Robot.* 5, eabb0467. doi: 10.1126/scirobotics.abb0467

Liarokapis, M. V., Calli, B., Spiers, A. J., and Dollar, A. M. (2015). "Unplanned, model-free, single grasp object classification with underactuated hands and force sensors," in *2015 IEEE/RSJ International Conference on Intelligent Robots and Systems* (IEEE), 5073–5080. doi: 10.1109/IROS.2015.7354091

Longo, M. R., Schüür, F., Kammers, M. P., Tsakiris, M., and Haggard, P. (2008). What is embodiment? A psychometric approach. *Cognition.* 107, 978–998.

Mamidanna, P., Dideriksen, J. L., and Dosen, S. (2021). The impact of objective functions on control policies in closed-loop control of grasping force with a myoelectric prosthesis. *J. Neural Eng.* 18, 056036. doi: 10.1088/1741-2552/ac23c1

Marinelli, A., Semprini, M., Canepa, M., Lombardi, L., Stedman, S., Bellingegni, A. D., et al. (2020). "Performance evaluation of pattern recognition algorithms for upper limb prosthetic applications," in *2020 8th IEEE RAS/EMBS International Conference for Biomedical Robotics and Biomechatronics* (IEEE), 471–476. doi: 10.1109/BioRob49111.2020.9224466

Markovic, M., Schweisfurth, M. A., Engels, L. F., Bentz, T., Wüstefeld, D., Farina, D., et al. (2018). The clinical relevance of advanced artificial feedback in the control of a multi-functional myoelectric prosthesis. *J. Neuroeng. Rehabil.* 15, 1–15. doi: 10.1186/s12984-018-0371-1

Masteller, A., Sankar, S., Kim, H. B., Ding, K., liu, X., and All, A. H. (2021). Recent developments in prosthesis sensors, texture recognition, and sensory stimulation for upper limb prostheses. *Ann. Biomed. Eng.* 49, 57–74. doi: 10.1007/s10439-020-02678-8

Mayer, R. M., Garcia-Rosas, R., Mohammadi, A., Tan, Y., Alici, G., Choong, P., et al. (2020). Tactile feedback in closed-loop control of myoelectric hand grasping: conveying information of multiple sensors simultaneously via a single feedback channel. *Front. Neurosci.* 14, 348. doi: 10.3389/fnins.2020.00348

Medynski, C., and Rattray, B. (2011). *Bebionic Prosthetic Design*. Myoelectric Symposium. Available online at: dukespace.lib.duke.edu

Meek, S. G., Jacobsen, S. C., and Goulding, P. P. (1989). Extended physiologic taction: design and evaluation of a proportional force feedback system. *J. Rehabil. Res. Dev.* 26, 53–62.

Nemah, M. N., Aldulaymi, O. H., Low, C. Y., Zakaria, N. A. C., and Mohamaddan, S. (2020). "A hybrid haptic feedback stimulation device to recover the missing sensation of the upper limb amputees," in *IOP Conference Series: Materials Science and Engineering, Vol. 834* (IOP Publishing), 012013. doi: 10.1088/1757-899X/834/1/012013

Oddo, C. M., Raspopovic, S., Artoni, F., Mazzoni, A., Spigler, G., Petrini, F., et al. (2016). Intraneural stimulation elicits discrimination of textural features by artificial fingertip in intact and amputee humans. *Elife* 5, e09148. doi: 10.7554/eLife.09148

Osborn, L., Kaliki, R. R., Soares, A. B., and Thakor, N. V. (2016). Neuromimetic event-based detection for closed-loop tactile feedback control of upper limb prostheses. *IEEE Trans. Haptics* 9, 196–206. doi: 10.1109/TOH.2016.2564965

Osborn, L. E., Dragomir, A., Betthauser, J. L., Hunt, C. L., Nguyen, H. H., Kaliki, R. R., et al. (2018). Prosthesis with neuromorphic multilayered e-dermis perceives touch and pain. *Sci. Robot.* 3, eaat3818. doi: 10.1126/scirobotics.aat3818

Patel, G. K., Dosen, S., Castellini, C., and Farina, D. (2016). Multichannel electrotactile feedback for simultaneous and proportional myoelectric control. *J. Neural Eng.* 13, 056015. doi: 10.1088/1741-2560/13/5/056015

Pena, A. E., Rincon-Gonzalez, L., Abbas, J. J., and Jung, R. (2019). Effects of vibrotactile feedback and grasp interface compliance on perception and control of a sensorized myoelectric hand. *PLoS ONE* 14, e0210956. doi: 10.1371/journal.pone.0210956

Powers, D. M. (2020). Evaluation: from precision, recall and F-measure to ROC, informedness, markedness and correlation. *arXiv [Preprint]*. arXiv: 2010.16061.

Prins, N. (2016). *Psychophysics: A* Practical *Introduction*. Academic Press. Available online at: https://books.google.it/books?hl=it&lr=&id=3sHQBAAAQBAJ&oi=fnd&pg=PP1&dq=Psychophysics:+A+Practical+Introduction.+Academic+Press&ots=-M1GjWipBb&sig=KX6c5IzJkTnrBQYu9GdsA6KEDe0#v=onepage&q=Psychophysics%3A%20A%20Practical%20Introduction.%20Academic%20Press&f=false

Pylatiuk, C., Schulz, S., and Döderlein, L. (2007). Results of an Internet survey of myoelectric prosthetic hand users. *Prosthet. Orthot. Int.* 31, 362–370. doi: 10.1080/03093640601061265

Raspopovic, S., Valle, G., and Petrini, F. M. (2021). Sensory feedback for limb prostheses in amputees. *Nat. Mater.* 20, 925–939. doi: 10.1038/s41563-021-00966-9

Sensinger, J. W., and Dosen, S. (2020). A review of sensory feedback in upper-limb prostheses from the perspective of human motor control. *Front. Neurosci.* 14, 345. doi: 10.3389/fnins.2020.00345

Shannon, G. (1976). A comparison of alternative means of providing sensory feedback on upper limb prostheses. *Med. Biol. Eng.* 14, 289–294. doi: 10.1007/BF02478123

Shehata, A. W., Engels, L. F., Controzzi, M., Cipriani, C., Scheme, E. J., and Sensinger, J. W. (2018). Improving internal model strength and performance of prosthetic hands using augmented feedback. *J. Neuroeng. Rehabil.* 15, 1–12. doi: 10.1186/s12984-018-0417-4

Shehata, A. W., Rehani, M., Jassat, Z. E., and Hebert, J. S. (2020). Mechanotactile sensory feedback improves embodiment of a prosthetic hand during active use. *Front. Neurosci.* 14, 263. doi: 10.3389/fnins.2020.00263

Stephens-Fripp, B., and alici, G., and, M. U. T. L.U., R. (2018). A review of non-invasive sensory feedback methods for transradial prosthetic hands. *IEEE Access* 6, 6878–6899. doi: 10.1109/ACCESS.2018.2791583

Stiegelmar, C., Blustein, D., Sensinger, J., Hebert, J., and Shehata, A. (2020). "Towards quantifying the sense of agency and its contribution to embodiment of myoelectric prostheses," in *MEC20 Symposium*.

Štrbac, M., Belić, M., Isaković, M., Kojić, V., Bijelić, G., Popović, I., et al. (2016). Integrated and flexible multichannel interface for electrotactile stimulation. *J. Neural Eng.* 13, 046014. doi: 10.1088/1741-2560/13/4/046014

Svensson, P., Wijk, U., Björkman, A., and Antfolk, C. (2017). A review of invasive and non-invasive sensory feedback in upper limb prostheses. *Expert Rev. Med. Dev.* 14, 439–447. doi: 10.1080/17434440.2017.1332989

Tejeiro, C., Stepp, C. E., Malhotra, M., Rombokas, E., and Matsuoka, Y. (2012). "Comparison of remote pressure and vibrotactile feedback for prosthetic hand control," in *2012 4th IEEE RAS & EMBS International Conference on Biomedical Robotics and Biomechatronics* (IEEE), 521–525. doi: 10.1109/BioRob.2012.6290268

Tsakiris, M., and Haggard, P. (2005). The rubber hand illusion revisited: visuotactile integration and self-attribution. *J. Exp. Psychol. Hum. Percept. Perform.* 31, 80. doi: 10.1037/0096-1523.31.1.80

Valle, G., Mazzoni, A., Iberite, F., D'anna, E., Strauss, I., Granata, G., et al. (2018). Biomimetic intraneural sensory feedback enhances sensation naturalness, tactile sensitivity, and manual dexterity in a bidirectional prosthesis. *Neuron* 100, 37–45. e7. doi: 10.1016/j.neuron.2018.08.033

Van Der Niet, O., and Van Der Sluis, C. K. (2013). Functionality of i-LIMB and i-LIMB Pulse hands: case report. *J. Rehabil. Res. Dev.* 50, 1123. doi: 10.1682/JRRD.2012.08.0140

Vargas, L., Huang, H., Zhu, Y., and Hu, X. (2021). object recognition via evoked sensory feedback during control of a prosthetic hand. *IEEE Robot. Autom. Lett.* 7, 207–214. doi: 10.1109/LRA.2021.3122897

Vargas, L., Shin, H., Huang, H. H., Zhu, Y., and Hu, X. (2019). Object stiffness recognition using haptic feedback delivered through transcutaneous proximal nerve stimulation. *J. Neural Eng.* 17, 016002. doi: 10.1088/1741-2552/ab4d99

Vernier (2021). *Go Direct® Hand Dynamometer*. Available online at: https://www.vernier.com/product/go-direct-hand-dynamometer/

Wang, L., Li, Q., Lam, J., and Wang, Z. (2021). Tactual recognition of soft objects from deformation cues. *IEEE Robot. Automat. Lett.* 7, 96–103.

Witteveen, H. J., Luft, F., Rietman, J. S., and Veltink, P. H. (2013). Stiffness feedback for myoelectric forearm prostheses using vibrotactile stimulation. *IEEE Trans. Neural Syst. Rehabil. Eng.* 22, 53–61. doi: 10.1109/TNSRE.2013.2267394

Yi, Z., and Zhang, Y. (2016). Bio-inspired tactile FA-I spiking generation under sinusoidal stimuli. *J. Bionic Eng.* 13, 612–621. doi: 10.1016/S1672-6529(16)60332-3

Yildiz, K. A., Shin, A. Y., and Kaufman, K. R. (2020). Interfaces with the peripheral nervous system for the control of a neuroprosthetic limb: a review. *J. Neuroeng. Rehabil.* 17, 1–19. doi: 10.1186/s12984-020-00667-5

Zhao, H., O'brien, K., Li, S., and Shepherd, R. F. (2016). Optoelectronically innervated soft prosthetic hand via stretchable optical waveguides. *Sci. Robot.* 1, eaai7529. doi: 10.1126/scirobotics.aai7529

frontiers | Frontiers in Neuroscience

TYPE Original Research
PUBLISHED 21 February 2023
DOI 10.3389/fnins.2023.1135687

OPEN ACCESS

EDITED BY
Min Li,
Xi'an Jiaotong University, China

REVIEWED BY
Wenyuan Liang,
National Research Center for Rehabilitation Technical Aids, China
Weihua Pei,
Institute of Semiconductors (CAS), China
Hangue Park,
Sungkyunkwan University, Republic of Korea

*CORRESPONDENCE
Xing Wang
✉ wangxing@cqu.edu.cn

SPECIALTY SECTION
This article was submitted to Neuroprosthetics, a section of the journal Frontiers in Neuroscience

RECEIVED 01 January 2023
ACCEPTED 01 February 2023
PUBLISHED 21 February 2023

CITATION
Han Y, Lu Y, Zuo Y, Song H, Chou C-H, Wang X, Li X, Li L, Niu CM and Hou W (2023) Substitutive proprioception feedback of a prosthetic wrist by electrotactile stimulation. *Front. Neurosci.* 17:1135687. doi: 10.3389/fnins.2023.1135687

Substitutive proprioception feedback of a prosthetic wrist by electrotactile stimulation

Yichen Han[1], Yinping Lu[1], Yufeng Zuo[1], Hongliang Song[1], Chih-Hong Chou[2], Xing Wang[1]*, Xiangxin Li[3], Lei Li[4], Chuanxin M. Niu[5] and Wensheng Hou[1]

[1]Biomedical Engineering Department, Bioengineering College, Chongqing University, Chongqing, China, [2]Laboratory of Neurorehabilitation Engineering, School of Biomedical Engineering, Shanghai Jiao Tong University, Shanghai, China, [3]Shenzhen Institutes of Advanced Technology, Chinese Academy of Sciences (CAS), Shenzhen, Guangdong, China, [4]Department of Rehabilitation, Southwest Hospital, Army Medical University, Chongqing, China, [5]Department of Rehabilitation Medicine, Ruijin Hospital, School of Medicine, Shanghai Jiao Tong University, Shanghai, China

Objective: Sensory feedback of upper-limb prostheses is widely desired and studied. As important components of proprioception, position, and movement feedback help users to control prostheses better. Among various feedback methods, electrotactile stimulation is a potential method for coding proprioceptive information of a prosthesis. This study was motivated by the need for proprioception information for a prosthetic wrist. The flexion-extension (FE) position and movement information of the prosthetic wrist are transmitted back to the human body through multichannel electrotactile stimulation.

Approach: We developed an electrotactile scheme to encode the FE position and movement of the prosthetic wrist and designed an integrated experimental platform. A preliminary experiment on the sensory threshold and discomfort threshold was performed. Then, two proprioceptive feedback experiments were performed: a position sense experiment (Exp 1) and a movement sense experiment (Exp 2). Each experiment included a learning session and a test session. The success rate (SR) and discrimination reaction time (DRT) were analyzed to evaluate the recognition effect. The acceptance of the electrotactile scheme was evaluated by a questionnaire.

Main results: Our results showed that the average position SRs of five able-bodied subjects, amputee 1, and amputee 2 were 83.78, 97.78, and 84.44%, respectively. The average movement SR, and the direction and range SR of wrist movement in five able-bodied subjects were 76.25, 96.67%, respectively. Amputee 1 and amputee 2 had movement SRs of 87.78 and 90.00% and direction and range SRs of 64.58 and 77.08%, respectively. The average DRT of five able-bodied subjects was less than 1.5 s and that of amputees was less than 3.5 s.

Conclusion: The results indicate that after a short period of learning, the subjects can sense the position and movement of wrist FE. The proposed substitutive scheme has the potential for amputees to sense a prosthetic wrist, thus enhancing the human-machine interaction.

KEYWORDS

proprioceptive feedback, prosthetic wrist, transradial amputee, sensory substitution, electrotactile stimulation

1. Introduction

Prostheses help amputees improve their quality of life (Burçak et al., 2021). The increasing degrees of freedom (DoF) and more exquisite structure of current prostheses importantly contribute to the dexterity of movement (Bo et al., 2019; George et al., 2019). Several studies have found that in addition to comfort, function, appearance, and durability, prosthesis users also desire sensory feedback in the upper-limb prosthesis (Farina and Amsüss, 2016; Markovic et al., 2018; Wijk et al., 2020). Therefore, transmitting information about grasping force (Dosen et al., 2017), hand aperture (Witteveen et al., 2014), fingertip pressure (Wu et al., 2020), temperature (Ueda and Ishii, 2017), etc., of the prosthesis has been widely studied.

Proprioception of the limbs and trunk is arisen by several proprioceptors (Proske and Gandevia, 2012), such as the muscle spindle and Golgi tendon organ. Proprioceptive and tactile feedback are indispensable for sensorimotor integration in daily activities of human, especially for control of dexterous movement. For amputees, the muscle spindle, tendon, tactile receptor, and afferent fibers in the muscle of the residual limb are damaged and cannot work normally (Kaya et al., 2018). So proprioceptive substitution helps amputee sense the prosthesis, improves the confidence (Schiefer et al., 2018), and controls the prosthesis better (Grushko et al., 2020; Guémann et al., 2022). The senses of limb position and movement are significant because they provide us with one aspect of our self-awareness (Chen et al., 2021). Position feedback ranked second in a recent survey on requirements for feedback of prostheses (Stephens-Fripp et al., 2018). Position and movement sense (also called kinesthetic sense) are the subtypes of proprioception (Gilman, 2002; Proske and Gandevia, 2012). Earlier research found better performance in a myoelectric prosthetic arm when introducing vibration feedback to provide the user with the position information of the prosthetic elbow (Mann and Reimers, 1970). In recent decades, D'Anna et al. (2019) transmitted the position and tactile sense of a prosthetic finger by means of an invasive method, which enabled participants to identify the size of the object better when grasping. To reduce mental effort and improve the grasping performance of prostheses, Gonzalez et al. (2012) implemented position feedback of the prosthetic thumb, pointer, and middle finger through auditory stimulation. Vargas et al. (2021a) chose vibration stimulation to convey the static position and movement of the prosthetic fingers; as a result, the control accuracy of the joint angle was improved. Marasco et al. (2018) endowed amputees with a kinesthetic perception of dexterous prosthetic hands. The recent studies above have demonstrated the effectiveness of position and movement feedback.

The prosthetic wrist is crucially important for upper-limb prostheses (Fan et al., 2022) since it greatly contributes to the mobility of the hand and reduces additional compensation movements of the upper limb (Kyberd et al., 2011). The prosthetic wrist has three DoFs: flexion-extension (FE), ulnar-radial deviations (UR), and supination-pronation (SP) (Omarkulov et al., 2016); of these, SP and FE are the most requested (Demofonti et al., 2022). Therefore, there have been several approaches to sensory feedback of the prosthetic wrist. After Erwin employed a three-node tactor array to provide feedback information about the FE angle of a virtual wrist, the movement control of the wrist *via* electromyography was improved (Erwin and Sup, 2015). Kayhan et al. (2018) also developed a retractable skin stretching tractor, which provided feedback on the position of the prosthetic wrist during three DoF movements. Zheng et al. (2022) analyzed the effectiveness of wrist position feedback by comparing three kinds of feedback methods and demonstrated the importance of position feedback to the control of arm prostheses. In the above studies, it is undoubted that an appropriate and concise feedback method helps to promote the control and embodiment of the prosthesis (Page et al., 2018; Tchimino et al., 2022).

Homology and somatotopy are the priority factors affecting the acceptability of prosthetic sensory feedback methods because they affect the training periods that patients require (Raspopovic et al., 2021) and acceptance of the feedback device (Makin et al., 2017; Lan et al., 2019). In the literature, there are a variety of feedback methods, including invasive electrical stimulation (Schiefer et al., 2016; Vu et al., 2022), skin stretching (Battaglia et al., 2019), vibration (Vargas et al., 2021b), mechanical pressure (Godfrey et al., 2016), audio (Gonzalez et al., 2012), and electrotactile stimulation (Franceschi et al., 2017; Chai et al., 2022). Although the sensations induced by electrotactile stimulation are not somatotopic, users can learn to interpret the feedback with a few days of training (Bensmaia et al., 2020). Moreover, the electrotactile substitution system is easier to embed into upper-limb prostheses (Svensson et al., 2017) due to its benefits, such as non-invasiveness, portability, and low power consumption (Cornman et al., 2017). Therefore, electrotactile sensory substitution is one of the most promising bridges for connecting intelligent prosthetic fingertips and upper-limb amputees' brains (Chai et al., 2014).

The effect of electrotactile feedback depends on the parameters of electrical stimulation, including intensity (Alotaibi et al., 2022), frequency (Farina et al., 2021; Graczyk et al., 2022), pulse width (Yang et al., 2012), spatial distribution (Rafiei et al., 2014), and temporal distribution (Nataletti et al., 2020). For multi-DoF intelligent prosthetics, the stimulation of multiple channels is more suitable for spatiotemporal encoding than that of a single channel because continuous stimulation causes skin adaptation (Buma et al., 2007) and limits the interpretation of changes in stimulation (Nataletti et al., 2022). Four channels electrotactile feedback method was proved to be feasible in lower-limb prostheses. Yang et al. (2012) provided feedback on the angles of a prosthetic knee and pressures at three sites on the prosthetic foot for transfemoral amputees through four electrodes, and the results showed increased temporal gait symmetry and augmented confidence when walking with sensory feedback compared to the no-feedback condition. More channels were also proven feasible, such as a 16-channel feedback scheme for transmitting four kinds of information about the hand and wrist to amputees (Štrbac et al., 2016), and different multichannel schemes were compared by the target-reaching task results of thirteen able-bodied subjects (Garenfeld et al., 2020). However, amputation results in cutaneous sensitivity changes (Koc et al., 2008; Templeton et al., 2018), which affects the comfort and dynamic range of electrotactile stimulation (Kaczmarek et al., 1991). It is reasonable to expect that amputee's ability to use electrotactile stimulation for sensing wrist FE position and movement of prostheses may be substantially different from able-bodied subject. Besides, the wrist FE sensation includes not only movement direction but also movement range.

Therefore, this study aims to explore whether amputees can receive proprioceptive feedback on the prosthetic wrist through electrotactile method combined with spatial encoding and multiple electrodes. We proposed a multiple channels electrotactile stimulation scheme to provide wrist FE proprioception. In addition to recruiting amputees, we also recruited able-bodied subjects for comparison and validation. We hypothesized that the amputee's performance of position sense and movement sense of the prosthetic wrist was different from that of able-bodied subjects and the success rate of position sense was higher than that of movement sense. To answer this question, the present study designed three experiment and a stimulation platform to verify the feasibility of the scheme by amputees' recognition results, DRT, and questionnaire responses.

2. Materials and methods

2.1. Subject recruitment

Two transradial amputees (amputee 1: a 55-year-old male with electric shock amputation in 1989, amputee 2: a 60-year-old male with explosion amputation in 1980) were recruited for this research. Five able-bodied subjects (1 male, 4 females, 20∼25 years old) were recruited. All subjects met the following requirements: (a) not taking drugs that affect hormones or neurotransmitters in the last 30 days, (b) no electromagnetic hypersensitivity, (c) no psychiatric or cognitive disorder, and (d) experience using a myoelectric prosthesis. The experimental procedure was approved by the Chongqing University Three Gorges Hospital Ethics Committee (2021-KY-24). All subjects signed informed consent forms before the experiments, which includes the stimulation and prompts they would receive and what operations they needed to perform in the experiment.

2.2. Experimental setup

The experimental platform mainly includes a PC, a control module, an upper-limb prosthesis and other devices, as shown in Figure 1. We independently designed, drew, and welded the control module and integrated the parts above to perform the following experiment.

(a) A host PC [Intel® Core (TM) i7-7700HQ CPU at 2.80 GHz, 8 GB RAM] was used for running a Python program. A 22″ screen was used to provide guidance to the subjects, and the graphical user interface (GUI) created in the tkinter library was used for user input. The input content and discrimination reaction time (DRT) were saved in .csv format. The program called the pyserial library gives the prosthesis control signal and communicates with the microcontroller.

(b) The control module is used for outputting multiple channels electrotactile stimulation and driving the prosthesis, including main control board and daughter board. Main control board: (I) microcontroller minimum system (STM32F103RCT6) for generating PWM waveforms, selecting stimulation channels (CH1-CH8) and providing motor control signal, etc., (II) a chip for communicating with the PC, (III) interfaces that connect to the other device. Daughter board: (I) an H-bridge circuit, a constant current source, 70 V DC power supply, a quadruple high-current motor driver for executing prosthesis control signals, (II) solid-state relays as actuators for generating stimulation waveforms (square biphasic current waveforms). (III) Interfaces that connect to the motor of the prosthesis and other devices. The main control board and daughter board are connected by male and female headers (board to board). The shape of the boards is a rounded rectangle (60 mm*37 mm). The control module is connected to the inner shell of the prosthetic limb by screws.

(c) Upper limb prosthesis (SJQ21 SJS32 left hand, Danyang Prosthetic Factory, China) includes two DC micromotors (FAULHABER 2224006SR with magnetoelectric encoder IEH2-4096). The encoder feeds back the angle of the prosthetic wrist. This prosthesis supports two DoFs: hand aperture opening-closing and wrist FE. This strengthens the connection between the electrotactile scheme and the prosthesis. The inner shell of the prosthetic limb has screw holes for fixing the control module.

(d) Other devices: (I) Round hydrogel electrodes were used as the 1st to 8th stimulation channel (CH1∼CH8) and reference channel (Ref) (diameter = 2 cm and 5 cm, Shenzhen Baijianda Technology Development Co., Ltd., Shenzhen, China), (II) a 3.5″ TFT LCD was used to adjust the parameters of the stimulation waveform, and (III) a chargeable 9 V lithium battery was used as a power supply embedded in the prosthetic limb shell.

The parameters of the biphasic current waveform are adjustable (orange dashed rectangle in Figure 1): frequency (reciprocal of period) = 100∼500 Hz (100 Hz increments), pulse width = 100∼500 μs (100 μs increments), delay = 100∼500 μs (100 μs increments), current amplitude = 0∼8 mA (0.25 mA increments, 5 mA max for position and movement sense experiment), and burst duration = 0.5∼1 second (100 ms increments).

All subjects were required to sit on a chair in a comfortable posture; the able-bodied subjects' dominant arms were placed on a sponge pad, and the plane of the palms was perpendicular to the ground. Amputees placed the residual limb on a sponge pad as well and were asked to keep the phantom palm in a straight (ST) position. For consistency, the circumference of 10–12 cm above the styloid process of the ulna and 2–4 cm above the amputation end were the places where able-bodied and amputees attached stimulation electrodes, respectively. A reference electrode was attached to the olecranon for each subject. CH1 is on the volar side, and eight channels were equally attached and arranged along the pronation direction. The connecting line of the centers of eight circular electrodes formed a plane perpendicular to the connecting line of the wrist and elbow (Figure 1).

2.3. Preliminary experiment of stimulation range selection

First, we conducted a preliminary experiment to explore the forearm skin sensory threshold and discomfort threshold of

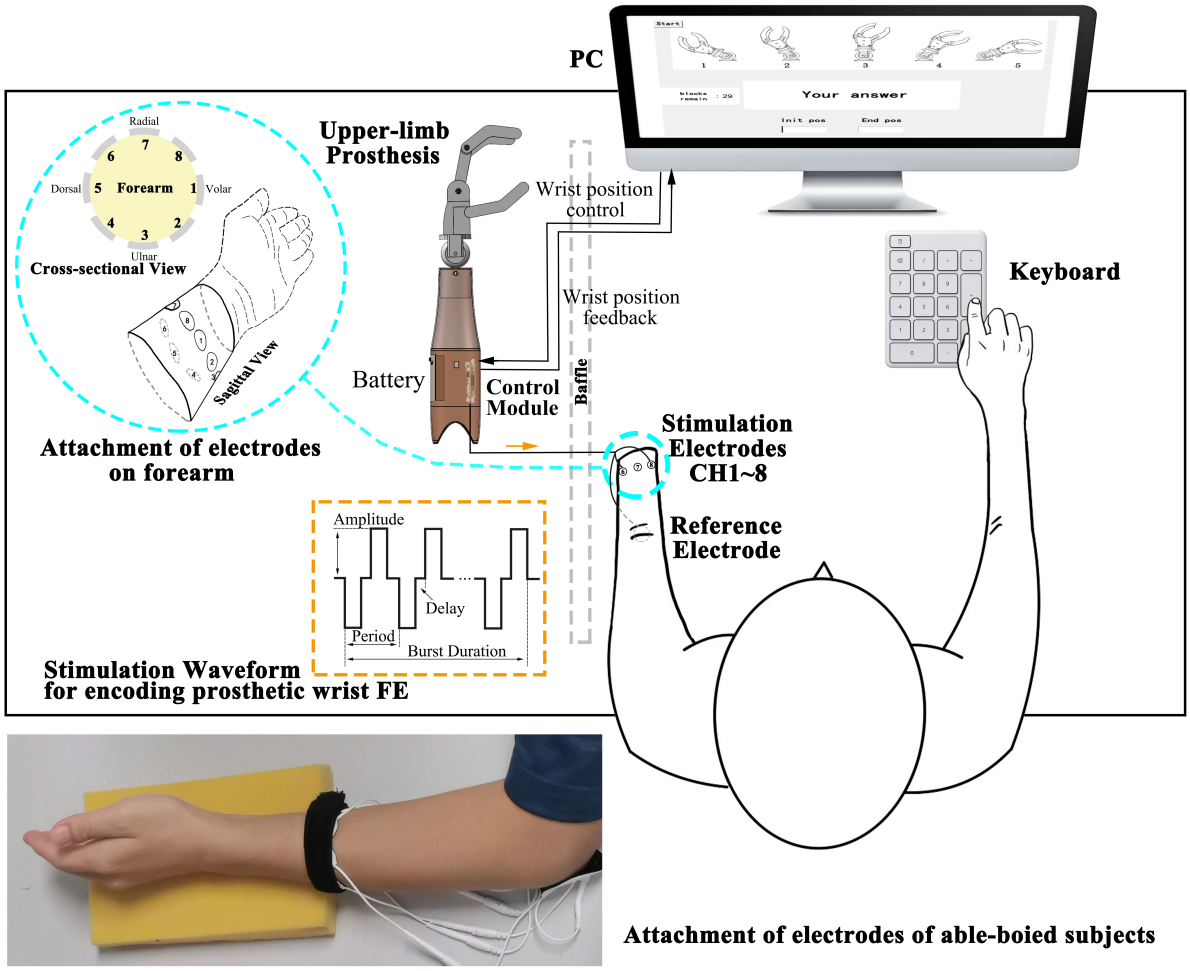

FIGURE 1
Illustration of the modules comprising the experimental platform. The control module and battery are embedded in the shell of the upper-limb prosthesis. The control module receives the wrist position control signal from the PC to drive the prosthesis and provided feedback on the wrist position to the PC. The square biphasic current stimulation waveforms in orange dashed line rectangle (amplitude, period, delay, and burst duration as adjustable parameters) are generated and conveyed to the subjects through electrodes. A cross-sectional and sagittal view of eight stimulation electrodes distribution around the forearm are shown in the enlarged blue circle. CH1 (Channel 1) is on the volar side, and eight channels are equally attached and arranged along the pronation direction. Subjects perceive the stimulation and input the answer by a keyboard. The photograph at the bottom shows the attachment of electrodes of an able-bodied subject.

each subject. Referring to the general experimental paradigm of electrotactile evoked sensation (Chai et al., 2015; Zheng and Hu, 2018), we fixed the frequency of all electrical stimulation at 200 Hz, the pulse width at 500 μs, and the delay at 100 μs. Taking the ith channel as an example, the current amplitude was incremented from 0 μA in steps of 500 μA. Each stimulation lasted for 1 s and was then followed by a 10 s rest period. Once the stimulation was perceived, it was repeated 3 times to ensure that subjects perceived the stimulation clearly. The stimulation amplitude was recorded as the sensory threshold A_{i1-up} if perceived and then increased until the subjects felt discomfort, and the current amplitude was recorded as the discomfort threshold A_{i2}. The current value was set to 40% of the maximal current, then it decreased in steps of 250 μA until the subjects could not perceive the stimulation. The last current value was recorded as $A_{i1-down}$. The maximum value between A_{i1-up} and $A_{i1-down}$ was considered the sensory threshold A_{i1}. In addition, subjects were asked to describe the perceived sensations of stimulation, such as pressure, vibration, numbness, and pain, during this experiment. The current amplitude of each channel was fine-tuned by comparing the sensory threshold in neighboring channels to achieve similar tactile sensation across channels (Garenfeld et al., 2020).

2.4. Wrist FE static position sense experiment (Exp 1)

The study chose spatial coding to feedback the positions of wrist flexion and extension (FE), because spatial coding is easier for recognition than intensity coding or temporal coding. As shown in Figure 2, we primarily chose five angular positions of wrist FE with 30° of resolution, which were named extension 60° (E60), extension 30° (E30), ST, flexion 30° (F30), and flexion 60° (F60). As shown as attachment of electrodes in Figure 1, active electrodes among eight electrodes around the forearm correspond to the five positions of wrist FE. The position of active channel corresponds

to the direction of wrist FE movement. As the limit positions of wrist FE movement, E60 and F60 are configured with single channel of active electrode. For example, the CH5 on the dorsal forearm corresponds to the limit extension direction of the prosthetic wrist, so it is coded as E60 position. The CH1 on the volar forearm corresponds to the limit flexion direction of the prosthetic wrist, so it is coded as F60 position. As the initial position of wrist FE movement, ST is configured with dual channels of active electrodes. The dual channels are related to CH7 and CH3. As the non-limited positions of wrist FE movement, E30 and F30 are configured with dual channels of active electrodes. For example, the CH 6 and CH4 close to the dorsal forearm corresponds to the extension position of the prosthetic wrist, so it is coded as E30 position. The CH 8 and CH2 close to the volar forearm corresponds to the flexion of the prosthetic wrist, so it is coded as F30 position. The recognition of a single channel is easier than that of dual channel (Geng et al., 2016), so we related the single channel to the limit position of wrist FE, informing the subject that the prosthetic wrist has moved to the limit position. The burst duration for each stimulation mode is fixed at 0.5 s. Before the electrical stimulation was executed, the prosthetic wrist moved to the corresponding position.

This experiment was composed of two sessions: a learning session and a test session. A learning session was arranged before the test session to familiarize the subjects with the electrotactile scheme. The stimulation modes occurred randomly. At the same time, the stimulating channel map and the corresponding prosthetic wrist state were displayed on the screen (**Figure 3A**). After 0.5 s of stimulation, there was a 10-s rest period. The learning session lasted approximately 10 min. After subjects passed an evaluation of learning, the test session would be executed.

The paradigm of the experiment in the test session is shown in **Figure 3B**. Each session contains 30 blocks (5 kinds of wrist FE positions *6 blocks), and each wrist FE position accounts for 6 blocks. Each block consisted of three identical trials. Each trial consisted of 2 s of preparation time during which a beep sound was played to prompt the subjects, a 0.5 s stimulation period, time for the participant to answer, and 5 s of rest time. Then, 30 s of rest was used to relieve mental fatigue. There was no reminder (including audition) in the test session. When waiting for the answer of subjects, a dialog box popped up on the screen. The subject needed to give the index of the prosthetic wrist FE position corresponding to the stimulation in the dialog box as fast as possible by pressing a single number and the enter key on the keyboard. The DRT was counted from the end of the stimulation to the time when the enter key was pressed. If there was no answer within 20 s, the trial was considered to be a failed recognition.

2.5. Wrist FE movement sense experiment (Exp 2)

Based on the static position sense experiment, the study selected initial and end position from five wrist positions to form a movement mode. Our study chose eight movement modes from 20 combinations (5*4). Eight movement modes are: extension small 1 (ES1), extension small 2 (ES2), extension small 3 (ES3), extension large (EL), flexion small 1 (FS1), flexion small 2 (FS2), flexion small 3 (FS3), and flexion large (FL) (**Figure 4**). The variables include direction (F or E) and range (S:60° or L:120°). When the prosthetic wrist moved within the perception range of the five positions, the corresponding stimulation channels were active. After the prosthetic wrist moved in the next range of the preestablished positions, the previous channels were inactive. For consistency with the static position sense experiment, the burst duration on each electrode also lasted for 0.5 s. Therefore, the total duration of stimulation of ES1, 2, and 3 and FS1, 2, and 3 was 1.5 s, while that of EL and FL was 2.5 s.

The movement experiment also includes learning and test sessions. During the learning session, the subjects were provided with three kinds of guidance: 1. the movement of the prosthetic wrist, 2. the stimulating channel map, and 3. the dynamic illustrations of wrist FE movements on a 22″ screen. The above guidance helped subjects establish the connection between electrotactile stimulation and wrist movement to achieve a better learning effect. The learning session lasted approximately 15 min. The paradigm of the test session is similar to that of the static position sense experiment. The test session consisted of 32 blocks of random movement modes. To simplify user input, we numbered E60∼F60 as indexes 1∼5. Similarly, the subjects were asked to respond to the perceived movement by a keyboard. They needed to press the first index on the keyboard to represent the initial position, then the cursor was automatically switched to the next dialog box in which the second index represents the end position, and they finally pressed the enter key to submit the answer (**Figure 3C**). Similarly, we recorded the input and DRTs of the subjects. For consistency of the stimulation electrode position on the forearm in the two experiments, we used multiple reference positions such as the styloid process of ulna, olecranon, etc. In addition, we took photos of each subject's forearm and marked the position of each electrodes with a color pen that is harmless to the skin.

Subjects' subjective feelings need to be considered. To evaluate the acceptance of the electrotactile scheme in this study, after each subject completed the movement experiment, we distributed a questionnaire and invited the subjects to use a score from 1 to 5, where 5 represents the highest outcome, to rate the following aspects: 1. degree of pain and numbness, 2. the resolution of each channel, 3. the comfort of electrotactile stimulation, 4. intuitiveness, and 5. ease of learning.

2.6. Data and statistical analysis

We analyzed the sensory and discomfort thresholds and SR of each stimulation mode in two experiments. Specifically, in the movement experiment, we analyzed the SR from the following two aspects. (a) FE direction and range. Eight movements were divided into four categories (ES, FS, EL, and FL) by FE direction and range. For example, the given stimulation is ES2, while the answer is ES1, ES2, or ES3. This counts as a successful recognition in this aspect. (b) Each mode: only when both the initial position and end position were correctly identified can it be counted as a successful recognition. The DRT of success and wrong recognition of each stimulation were analyzed. The non-parametric Kolmogorov-Smirnov test (K-S test) and Bonferroni test were performed to detect the difference in each channel of sensory threshold and

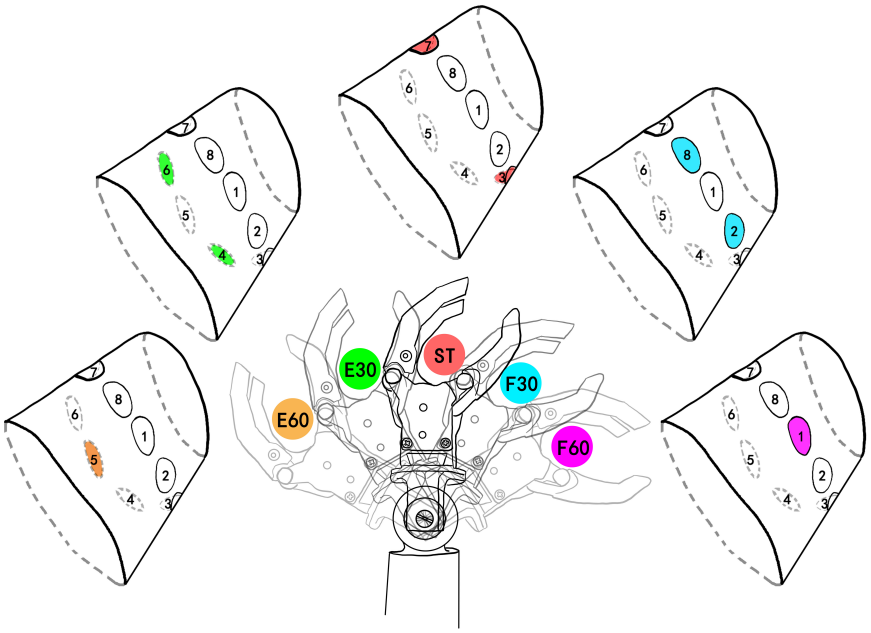

FIGURE 2
Five wrist FE (flexion and extension) positions and corresponding stimulating channels. The colored channel represents the active (under stimulating) channel. E60, extension 60°; E30, extension 30°; ST, straight 0°; F30, flexion 30°; F60, flexion 60°. E60 and F60 are limit positions of prosthetic wrist and they are coded by single channel. ST was defined as the initial position. The number after F and E was defined as the angle deviating from the ST position. The colors of active channels are consistent with the stimulation mode.

discomfort threshold and DRT, since previous tests have shown that all statistics failed to pass homogeneity of variance. The threshold for statistical significance was set at $p < 0.05$. Statistical analysis and graphing were performed in Prism 8.0.2 (GraphPad Software Inc, CA, USA).

3. Results

3.1. Preliminary experiment of stimulation range selection

3.1.1. Individual electrotactile sensitivity

The preliminary experiment examined the participants' sensitivity to electrotactile stimulation. We analyzed the sensory and discomfort thresholds of able-bodied subjects and amputees, as shown in Figure 5A. Statistical analysis showed that the sensory thresholds of the 2 amputees (3.22 ± 0.57 mA, 3.25 ± 0.61 mA) were higher than those of the able-bodied subjects (1.64 ± 0.56 mA), but no such phenomenon was found in the discomfort thresholds. In addition, there was no significant difference between the sensory thresholds of the two amputees.

3.1.2. Sensory sensitivity of different locations

The sensory thresholds at eight channels on the forearm of five able-bodied subjects are shown in Figure 5B. The sensory thresholds of the dorsal forearm and volar forearm sides are significantly different, which can be found in CH4 and CH8 (2.25 ± 0.79 mA and 1.35 ± 0.22 mA, $p < 0.05$, see the black stars in Figure 5B). Among all channels, CH1 and CH8 (both 1.35 mA) had the lowest mean values of sensory thresholds, and CH4 and CH5 (2.25 mA and 1.80 mA) had the highest sensory thresholds. The overall variability in the sensory threshold (1.64 ± 0.56 mA) was less than that in the discomfort threshold (6.61 ± 1.64 mA).

Figure 5C shows the distribution of thresholds around the forearm of all subjects. The sensory thresholds of each position of able-bodied subjects were lower than those of two amputees. The discomfort threshold of the CH1 channel of the amputee 1 showed an abnormal value of 5.75 mA, which was lower than that of able-bodied subjects (5.90 mA).

3.2. Proprioceptive feedback experiment

3.2.1. Evaluation of wrist FE position sense

This experiment examined the subjects' mastery of the position sense after a short period of study. Figure 6A represents the position recognition of five able-bodied subjects. The overall SR was 83.78 ± 3.69%. Able-bodied subjects had the highest SR for E60, which reached 97.78%. The SR for F30 was the lowest, only reaching 58.89%. Among the errors, 32.22% of F30 were identified as F60, and 8.82% of F60 were identified as F30. A total of 16.67% of those in the ST position were identified as F30. Figures 6B, C represent the SRs of amputee 1 and amputee 2, respectively. The total SR of amputee 1 was 97.78%. The SRs of the ST position, F30 and F60 reached 100%. The total SR of subject 2 was 82.22%. The SRs of E30 and E60 reached 100%, but the SR of F30 was only 50%. The subjects' DRT was also an important index to evaluate the mastery of the electrotactile scheme.

The DRTs for successful recognition by able-bodied subjects, amputee 1 and amputee 2 were 1.891 ± 1.369 s, 2.974 ± 1.715 s,

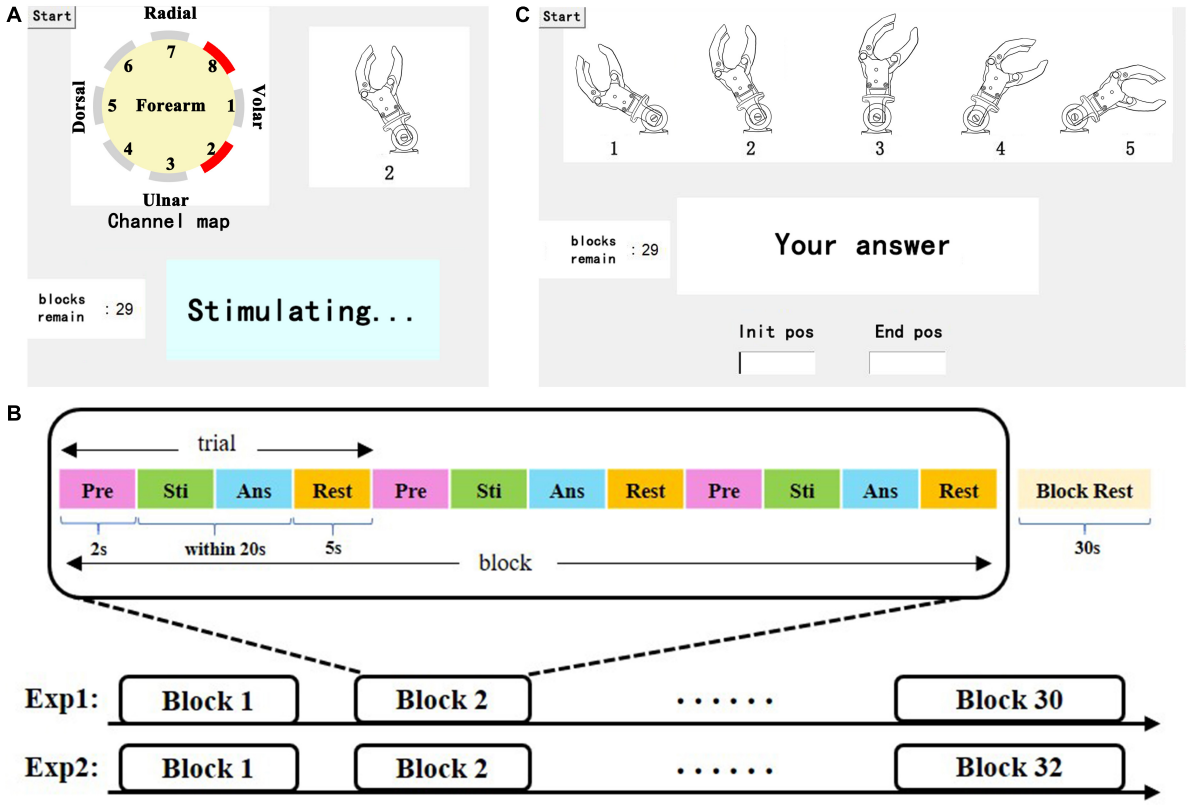

FIGURE 3
(A) Representation of the learning session, including a dynamic stimulating channel map, in which the red channel represents the active (under stimulating) channel, the illustrations of wrist FE, real-time status display, and the tip of the remaining blocks. **(B)** Depiction of the test session, including an illustration of the wrist position index (a static picture), a dialog box, and the tip of the remaining blocks. **(C)** Paradigm of the experiment, which consists of a certain number of blocks that consist of 3 of the same trials and 30 s of rest. Each trial consisted of four parts: preparation (Pre), stimulation (Sti), answer (Ans) and rest.

and 3.384 ± 2.342 s, respectively (Figure 7A). The DRTs for wrong recognition were 2.253 ± 1.287 s, 8.030 ± 0.568 s, and 4.861 ± 2.861 s, respectively. As shown in Figure 6, significant differences were observed between the DRT for successful and wrong recognition by five able-bodied subjects ($p < 0.001$) as well as that by amputee 1 ($p < 0.01$). The DRT for successful recognition by able-bodied subjects was significantly shorter than that of amputees ($p < 0.001$).

3.2.2. Evaluation of wrist FE movement sense

First, we calculated the SR of the direction and range of wrist FE movements. The total SR of able-bodied subjects was 96.67 ± 4.87%, in which the four categories were all over 90%, as shown in Figure 8A. The recognition effect of EL was slightly worse, and 10% of EL were recognized as ES. The total SR of amputee 1 was 90.00%. ES and FL were both 100%, and ES (83.3%) was the lowest, as shown in Figure 8B. The total SR of amputee 2 was 77.08%. ES (66.67%) had the worst SR, and 1/3 of that was recognized as FS. One-fourth of FS was recognized as ES, as shown in Figure 8C.

Figure 8D shows the recognition of stimulation modes for five able-bodied subjects, and the overall SR was 76.25 ± 18.97%. The SRs of EL, FS1, and FL were over 90%. The SR of FL was the highest, reaching 98%. Wrong recognitions mainly occurred around diagonal elements. ES2 had the lowest SR at 55%, with 37% wrongly answered as ES3. Figure 8E shows the SR of amputee 1. The total SR was 90.25%. EL, FS1, FS2, and FS3 all had SRs of 100%. The lowest SR was for ES2 (75%), and all wrong recognitions of ES2 were identified as E4. Figure 8F shows the SR of amputee 2. The total SR was 64.625%; the SRs for EL, FS3, and FL were higher than 95%, but those of ES2, ES3, and FS2 were 50%. None of the FS1 positions were identified, 75% of FS1 positions were wrongly identified as ES3, and the rest were identified as FS2.

The DRTs for successful recognition by able-bodied subjects, amputee 1 and amputee 2 were 2.666 ± 1.515 s, 4.238 ± 2.041 s, and 3.869 ± 1.528 s, respectively. The times for wrong recognitions were 4.207 ± 2.312 s, 4.459 ± 2.440 s, and 4.860 ± 2.771 s, respectively. As shown in Figure 7B, significant differences were observed between the DRT for successful and wrong recognition by five able-bodied subjects ($p < 0.001$). The DRT for successful recognition by able-bodied subjects was significantly shorter than that of amputees ($p < 0.001$). The results of the questionnaire are shown in Table 1 below.

4. Discussion

We attempted to convey the wrist FE sense of a prosthesis by using electrotactile feedback to the amputee. Accordingly, we built an integrated platform and designed a spatiotemporal electrotactile

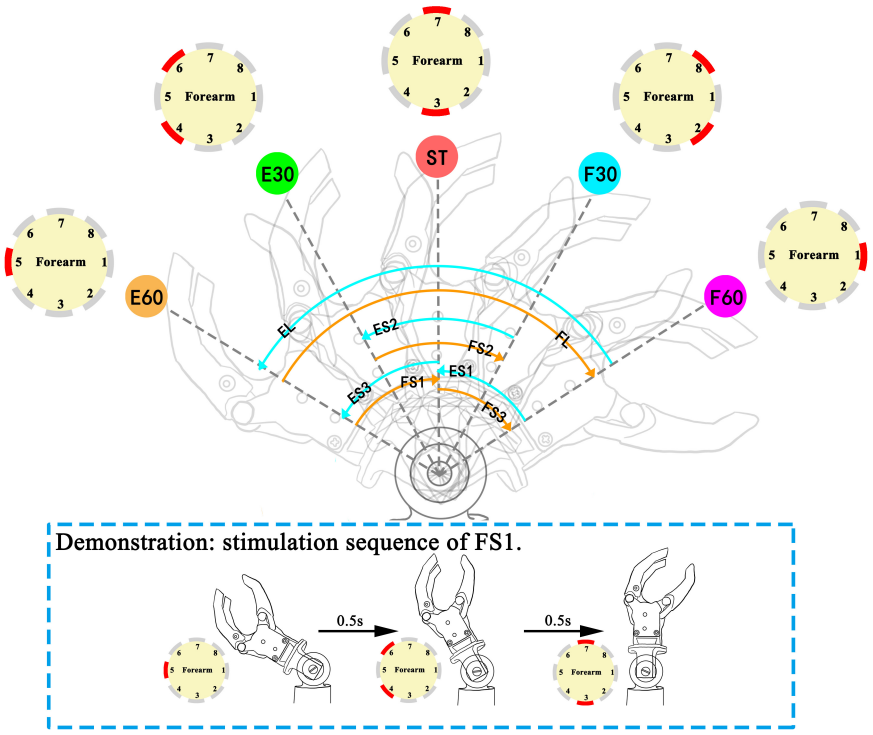

FIGURE 4
Movement modes in the movement experiment: ES (ES1, extension small 1; ES2, extension small 2; ES3, extension small 3), EL (extension large), FS (FS1, flexion small 1; FS2, flexion small 2; FS3, flexion small 3), and FL (flexion large). The sequence of active channels and the corresponding movement modes: ES1 (CH1→CH2, 8→CH3, 7), ES2 (CH2, 8→CH3, 7→CH4, 6), ES3 (CH3, 7→CH4, 6→CH5), EL (CH1→CH2, 8→CH3, 7→CH4, 6→CH5), FS1 (CH5→CH4, 6→CH3, 7), FS2 (CH4, 6→CH3, 7→CH2, 8), FS3 (CH3, 7→CH2, 8→CH1), FL (CH5→CH4, 6→CH3, 7→CH2, 8→CH1). The red channel in channel maps represents the active (under stimulating) channel. Demonstration for stimulation sequence of FS1 is illustrated in dashed line rectangle.

scheme for mapping a group of prosthetic wrist position states. The study tested the recognition of position sense and movement sense in five able-bodied subjects and two amputees. The results showed that the coding could be well-recognized (average SR > 80%). This kind of coding is a potential method for proprioceptive sense feedback of prosthetic wrist FE in transradial amputees.

4.1. Preliminary experiment of stimulation range selection

In the preliminary experiment, the sensitivity of eight electrode channels was measured in all subjects. Differences in sensory thresholds between volar forearms and dorsal forearms of able-bodied subjects (Figure 5) may be due to anatomical structures. The average sensory thresholds on the volar side (such as for CH1, CH2, and CH8) of able-bodied subjects were lower than those on the dorsal side (CH4 and CH5). Transcutaneous electrical stimulation can not only act on skin to induce superficial sensation but also activate afferent sensory nerves. If the nerve distribution in this area is more superficial, the threshold is lower. The muscle spindle in the middle of the muscle is in a relatively superficial position under the skin, which results in the lowest mean sensory threshold of its sensory nerve. The muscles at the CH4 position are relatively thick, and the muscle spindles in the middle of the muscles are deeply distributed under the skin, resulting in a higher sensory threshold. Stimulation close to the median nerves may induce uncomfortable numbness. Therefore, we tried to avoid this volar forearm area or reduce the amplitude in these channels.

The difference in electrotactile sensitivity between the amputees and the able-bodied subjects was the sensory threshold (Figures 5A, C). The sensory thresholds in the two amputees were higher than those of the able-bodied subjects. The higher sensory threshold indicates that the nervous system of amputees needs to be injected with more stimulation energy to produce a similar sensory type to that of healthy subjects. The results reflected that amputee's sensitivity is decreased than healthy subjects. This may be due to the sensory nerve impairment caused by transradial amputation. Kosasih and Silver-Thorn (1998) showed that unilateral tibial amputation caused superficial pain, vibration, and/or impaired touch sensation. In addition, electrotactile sensation is also relevant to mechanoreceptors distribution (He et al., 2016), reason and time of amputation, the age of subjects, etc. The discomfort threshold of CH1 was rather low in amputee 1. This might have been caused by the amputation operation performed on this subject. The skin sensitivity of the residual limb varies widely in space. Therefore, it is necessary to set the amplitude current independently on each channel.

The real current amplitude in each subject was fine-tuned around the sensory threshold to induce similar tactile sensation. Considering that long-term stimulation can induce sensory adaptation and numbness, we chose a relatively small

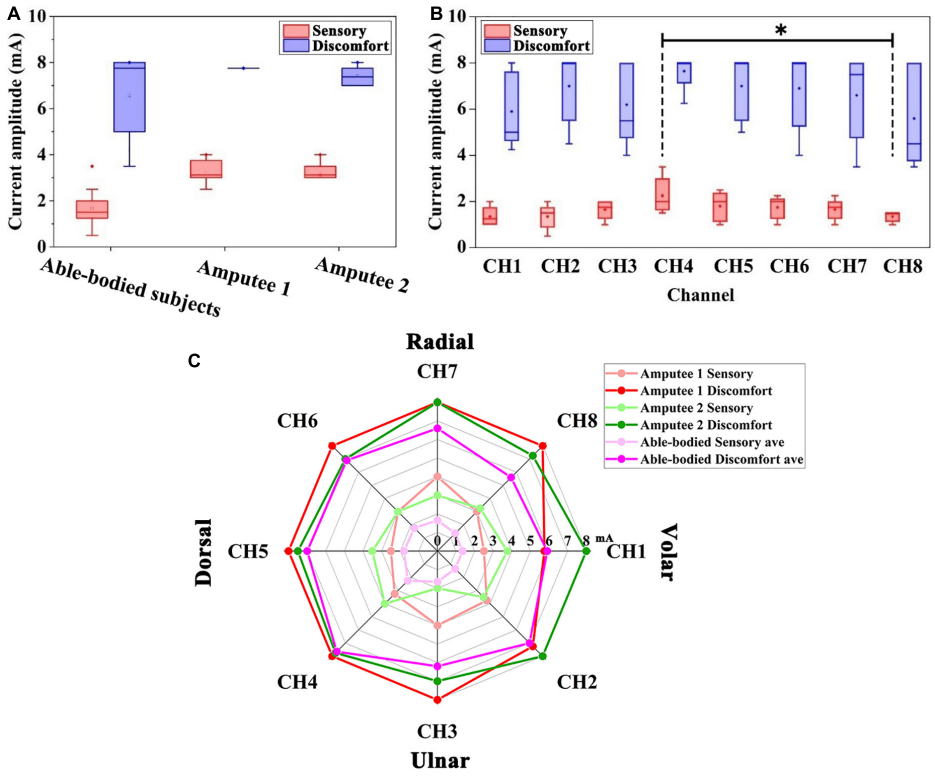

FIGURE 5
(A) Distribution of the sensory threshold and discomfort threshold of able-bodied subjects and two amputees. **(B)** Sensory threshold and discomfort threshold of able-bodied subjects among the eight positions. Black stars show the comparison of the sensory threshold for the eight positions. *$p < 0.05$. **(C)** Radar chart of the sensory threshold (light red, light green, and light purple) and discomfort threshold (red, green, and purple) around the forearm of five able-bodied subjects, amputee 1 and amputee 2. The dots in radar chart correspond to the threshold for eight electrodes around the forearm of the subjects.

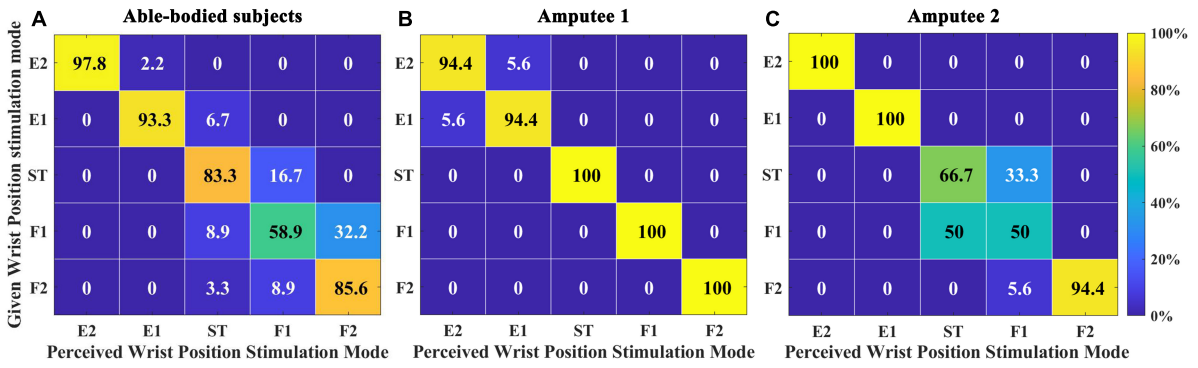

FIGURE 6
Confusion matrix quantifying the percentage of instances when comparing the perceived wrist position stimulation mode with a given stimulation mode in Exp 1. **(A)** Five able-bodied subjects, **(B)** amputee 1, and **(C)** amputee 2. The number in the each rectangle represents the SR (success rate), and the shade of the color represents the level of SR.

amplitude for each channel, but this may have decreased the channel discrimination.

4.2. Proprioceptive feedback experiment

The study employed five kinds of stimulation modes to code the FE position of the prosthetic wrist, and the study also employed eight kinds of stimulation modes to code the FE movement of the prosthetic wrist.

For position sense, the test results in all able-bodied subjects preliminarily demonstrated the effectiveness of the electrotactile scheme. Upon further analysis of the wrongly recognized positions, dual-channel stimulation mode (F30, ST, E30) often reduced the difference between two channels, such as in the F30, F60, and ST positions. In our limited results, the SR of amputees was not

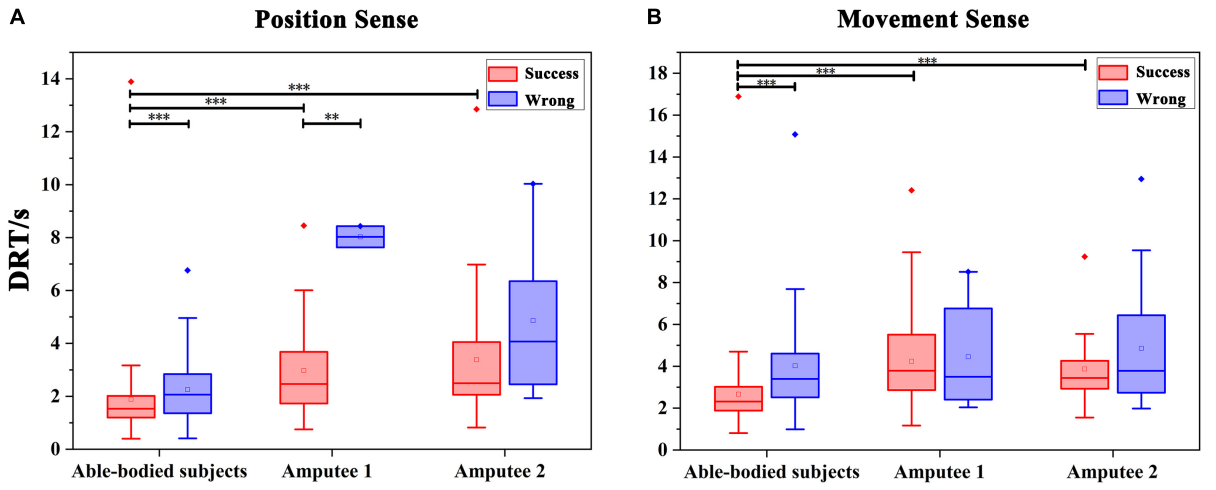

FIGURE 7
Statistics of the DRT (discrimination reaction time) in Exp 1 and Exp 2. **(A)** DRT for the evaluation of wrist FE position sense by all subjects. $^{**}p < 0.01$, $^{***}p < 0.001$. **(B)** DRT for all subjects spent in evaluating the wrist FE movement sense. $^{***}p < 0.001$.

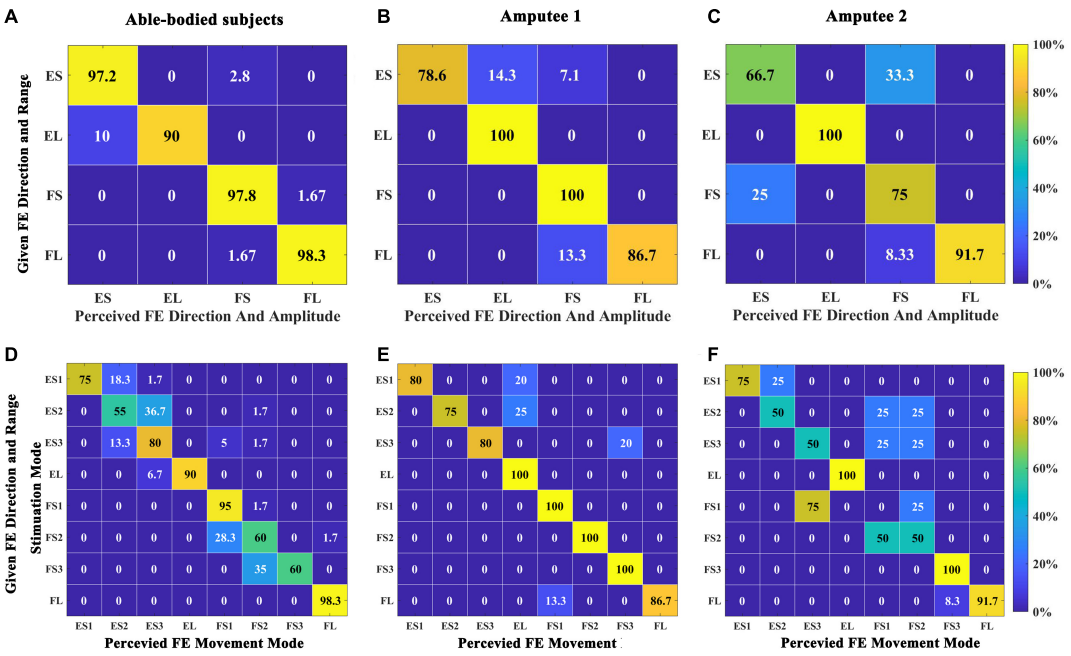

FIGURE 8
Confusion matrix quantifying the percentage of instances when comparing the perceived direction and range of wrist FE movements with the given stimulation in Exp 2. **(A)** Five able-bodied subjects. **(B)** Amputee 1. **(C)** Amputee 2. Confusion matrix quantifying the percentage of instances when comparing the perceived wrist movement stimulation mode with a given stimulation mode in Exp 2. **(D)** Five able-bodied subjects. **(E)** Amputee 1. **(F)** Amputee 2. The number in each rectangle represents the SR of the answer.

inferior to that of able-bodied subjects. The possible reason is that amputation leads to different neural plasticity outcomes between amputees and able-bodied subjects with intact proprioceptive circuits (Di Pino et al., 2009; Terlaak et al., 2015). The overall SR of amputee 1 was better than that of subject 2. The slightly higher learning ability of subject 1 is a possible reason for this result, and the influencing factors might include subject 1's younger age, higher education level, and higher economic level. Subject 2 did not clearly distinguish between ST and F30 positions. The possible reason for this result is that since the upper arm is not an ideal cylinder, CH3 and CH7 are close to CH2 and CH8. The induced sensations may also be quite similar, making them difficult to distinguish. This wrong recognition caused by spatial adjacency was also found for able-bodied subjects.

For movement sense, a temporal combination of multiple position sensations, hence the subject needs to perceive not only spatial change but also temporal change (F direction or E direction). Therefore, we predicted that the success rate of movement sense is

TABLE 1 Results of the questionnaire.

Question	Able-bodied average	Amputee 1	Amputee 2
Pain, numbness	1.6	1	1
Resolution	3.6	4	5
Comfort	4.2	4	5
Intuitiveness	4.2	5	5
Ease	4.2	5	5

lower than that of position sense. The results are consistent with the prediction. All subjects had a high SR for both the direction and the range of movement. Amputee 2 acquired a better SR in large-range FE movements than in small-range movements. For the same speed of movement in the prosthetic wrist, the burst duration of a large-range movement is longer than that of a small-range movement. Therefore, subjects can easily distinguish the large-angle range and the small-angle range at the time of stimulation. From the results of each stimulation mode, ES2, FS2, and FS3 were poorly recognized by able-bodied subjects. We speculate that the reason for this outcome is that the three modes all included position-F30, which was poorly recognized by able-bodied subjects in the position sense experiment (58.89%). The SR of amputee 1 was not lower than that of the able-bodied subjects, which may be due to the subject's better performance in position learning. Different sensory threshold and recognition results all indicated that there is difference between amputees and able-bodied subjects. Similar interesting phenomena have also been observed. Both the amplitude and latency of the maximum ERP peaks for the amputee were smaller than those for the able-bodied subjects (Wang et al., 2022). One possible explanation is that the peripheral nerves regenerated in the stump were different from the intact one in structure and characteristics. Perhaps the nerve fibers in the residual stump may be fewer, and less sensitive compared to those in the intact limb. Another possible reason may be that the sensory neural pathways in amputee are different. For the amputee, electrical stimulation directly actives nerve endings of stump, arouses sensations, and transfers to the brain. But for able-bodied subjects, the electrical signals are transmitted to the nerves in the hand and returned back to the brain. In addition, brain reorganization after amputation (Chai et al., 2015; Björkman et al., 2016) may lead to different process of the central nerve system. The SRs of ES1, ES2, and ES3 were slightly lower than those of the remaining movement modes, which can be explained by the slightly lower SR (94.44%) of position sense for F60 and F30 than that for the other positions (100%). Seventy-five percent of FS1 (E60→E30→ST) positions were wrongly recognized as ES3 (ST→E60→E30) by amputee 2; these positions consist of two completely opposite movement modes. Because the subject's recognition of the ST condition in the position sense experiment was low, the subject did not recognize the end position. Poor recognition of ST and F30 conditions was found in position sense experiments, resulting in poor recognition of ES2, ES3, and FS2 movements. We believe that for this subject, the confusion of a single position in this small-angle range movement misled the perception of the entire movement. When encoding wrist FE movements, F30, ST, and E30 using dual-channel stimulation may lead to confusion in the subjects' perception.

For movement recognition, the DRT of able-bodied subjects was shorter than that of the two amputees, likely for the same reason mentioned for the wrist FE position sense. The DRTs of the two amputees did not show obvious differences in either successful recognition or wrong recognition. Both subjects were possibly confident that they had mastered the coding after their learning session for position sense and movement sense. In the learning session, all subjects were asked to watch the moving prosthetic limb or the wrist diagram on the display when they perceived the electrotactile stimulation. Other studies have shown that visual and tactile sensory systems share common features in object recognition, which proved that these systems have the potential to promote each other in the process of learning and cognition (Gonzalez et al., 2012; Tabrik et al., 2021). For transradial amputees, proprioception interruption caused by a missing wrist and hand decreased activity in their sensorimotor cortex circuit. After amputees underwent the above multisensory substitution training, their perceptual learning activity was induced in their sensorimotor cortex (Proulx et al., 2014). In our experiment, intuition guided the subjects to integrate the designed code method and prosthetic wrist movement without causing too much of a learning burden. The subjective responses of the two amputees to intuitiveness and ease of learning were in line with our expectations. Sensory feedback is important in the rehabilitation process of amputees who lack limb sensation, and the application of this system to somatosensory and motor training is expected to lead to enhanced motor and sensory cortical activation. The subjective responses of the two amputees to intuitiveness and ease of learning were in line with our expectations. Sensory feedback is important in the rehabilitation process of amputees who lack limb sensation, and the application of this system to somatosensory and motor training is expected to lead to enhanced motor and sensory cortical activation.

The current research had some limitations. First, too few amputees lead to the lack of universality of results and we will increase the number of amputees in future. Second, more evaluations, such as the time stability of the coding in combination with the forgetting curve (D'Anna et al., 2019), control performance of a prosthetic hand (Luo et al., 2021), and the activation of sensory cortex and mental burden through electroencephalogram (EEG) and functional near-infrared spectroscopy (fNIRS) (Midha et al., 2021; Zhu et al., 2021), need to be performed and the results need to be verified. Third, we focused on more reasonable experimental paradigms by setting the stimulation time and rest time (Buma et al., 2007; Marion et al., 2013).

5. Conclusion

In conclusion, this study demonstrated that our multichannel electrotactile substitutive scheme can provide effective prosthetic wrist FE proprioception information. The experimental results of the position sense and movement sense of two transradial amputees and five able-bodied subjects showed that after a short period of learning, the subjects can quickly grasp the electrotactile scheme to clearly identify the position and movement of the prosthesis.

After simple improvement, the platform can be used in upper-limb prostheses to provide wrist proprioception feedback to transradial amputees, thereby improving subjects' acceptance of the prosthesis.

Data availability statement

The original contributions presented in this study are included in this article/supplementary material, further inquiries can be directed to the corresponding author.

Ethics statement

The studies involving human participants were reviewed and approved by Chongqing University Three Gorges Hospital Ethics Committee. The patients/participants provided their written informed consent to participate in this study.

Author contributions

XW, YH, WH, C-HC, CN, and YL designed the experiments. YH and YL conducted the experiments, analyzed the results, and created the figures. XW, YH, and YZ wrote the manuscript. HS participated in picture drawing. LL recruited the participants and was responsible for all the clinical activities. C-HC, WH, CN, and XL modified the manuscript. All authors reviewed the manuscript and approved the submitted version.

Funding

This research was supported by the National Key Research and Development Program of China (2020YFC2007900), the National Natural Science Foundation of China (NSFC31771069), and the Key-Area Research and Development Program of Guangdong Province (2020B0909020004).

Acknowledgments

We would like to acknowledge the support of Chongqing City Disabled Persons' Federation and Chongqing Disabled Persons' Rehabilitation Association.

Conflict of interest

The authors declare that the research was conducted in the absence of any commercial or financial relationships that could be construed as a potential conflict of interest.

Publisher's note

All claims expressed in this article are solely those of the authors and do not necessarily represent those of their affiliated organizations, or those of the publisher, the editors and the reviewers. Any product that may be evaluated in this article, or claim that may be made by its manufacturer, is not guaranteed or endorsed by the publisher.

References

Alotaibi, Y., Williamson, J. H., and Brewster, S. A. (2022). "First steps towards designing electrotactons: investigating intensity and pulse frequency as parameters for electrotactile cues," in *Proceedings of the 2022 CHI conference on human factors in computing systems (CHI '22)*, (New Orleans, LA). doi: 10.1145/3491102.3501863

Battaglia, E., Clark, J. P., Bianchi, M., Catalano, M. G., Bicchi, A., and O'Malley, M. K. (2019). Skin stretch haptic feedback to convey closure information in anthropomorphic, under-actuated upper limb soft prostheses. *IEEE Trans. Haptics* 12, 508–520. doi: 10.1109/toh.2019.2915075

Bensmaia, S. J., Tyler, D. J., and Micera, S. (2020). Restoration of sensory information *via* bionic hands. *Nat. Biomed. Eng.* doi: 10.1038/s41551-020-00630-8 [Epub ahead of print].

Björkman, A., Wijk, U., Antfolk, C., Björkman-Burtscher, I., and Rosén, B. (2016). Sensory qualities of the phantom hand map in the residual forearm of amputees. *J. Rehabil. Med.* 48, 365–370. doi: 10.2340/16501977-2074

Bo, Z., Yaqi, C., and Xingang, Z. (2019). Research progress on perception and feedback technology in artificial prosthesis. *J. Biomed. Eng.* 36, 1048–1054.

Buma, D. G., Buitenweg, J. R., and Veltink, P. H. (2007). Intermittent stimulation delays adaptation to electrocutaneous sensory feedback. *IEEE Trans. Neural Syst. Rehabil. Eng.* 15, 435–441. doi: 10.1109/TNSRE.2007.903942

Burçak, B., Kesikburun, B., Köseoğlu, B. F., Öken, Ö, and Doğan, A. (2021). Quality of life, body image, and mobility in lower-limb amputees using high-tech prostheses: a pragmatic trial. *Ann. Phys. Rehabil. Med.* 64:101405. doi: 10.1016/j.rehab.2020.03.016

Chai, G., Sui, X., Li, S., He, L., and Lan, N. (2015). Characterization of evoked tactile sensation in forearm amputees with transcutaneous electrical nerve stimulation. *J. Neural Eng.* 12, 066002. doi: 10.1088/1741-2560/12/6/066002

Chai, G., Wang, H., Li, G., Sheng, X., and Zhu, X. (2022). Electrotactile feedback improves grip force control and enables object stiffness recognition while using a myoelectric hand. *IEEE Trans. Neural Syst. Rehabil. Eng.* 30, 1310–1320. doi: 10.1109/tnsre.2022.3173329

Chai, G.-H., Sui, X.-H., Li, P., Liu, X.-X., and Lan, N. (2014). Review on tactile sensory feedback of prosthetic hands for the upper-limb amputees by sensory afferent stimulation. *J. Shanghai Jiaotong Univ.* 19, 587–591. doi: 10.1007/s12204-014-1546-y

Chen, B., Allen, T., and Proske, U. (2021). Position sense at the human forearm over a range of elbow angles. *Exp. Brain Res.* 239, 675–686. doi: 10.1007/s00221-020-05999-1

Cornman, J., Akhtar, A., and Bretl, T. (2017). A portable, arbitrary waveform, multichannel constant current electrotactile stimulator. *Int. IEEE EMBS Conf. Neural Eng.* 2017, 300–303. doi: 10.1109/ner.2017.8008350

D'Anna, E., Valle, G., Mazzoni, A., Strauss, I., Iberite, F., Patton, J., et al. (2019). A closed-loop hand prosthesis with simultaneous intraneural tactile and position feedback. *Sci. Robot* 4:eaau8892. doi: 10.1126/scirobotics.aau8892

Demofonti, A., Carpino, G., Tagliamonte, N. L., Baldini, G., Bramato, L., and Zollo, L. (2022). Design of a modular and compliant wrist module for upper limb prosthetics. *Anat. Rec.* 10, 1–13. doi: 10.1002/ar.24911

Di Pino, G., Guglielmelli, E., and Rossini, P. M. (2009). Neuroplasticity in amputees: main implications on bidirectional interfacing of cybernetic hand prostheses. *Prog. Neurobiol.* 88, 114–126. doi: 10.1016/j.pneurobio.2009.03.001

Dosen, S., Markovic, M., Strbac, M., Belic, M., Kojic, V., Bijelic, G., et al. (2017). Multichannel electrotactile feedback with spatial and mixed coding for closed-loop control of grasping force in hand prostheses. *IEEE Trans. Neural Syst. Rehabil. Eng.* 25, 183–195. doi: 10.1109/tnsre.2016.2550864

Erwin, A., and Sup, F. (2015). A haptic feedback scheme to accurately position a virtual wrist prosthesis using a three-node tactor array. *PLoS One* 10:e0134095. doi: 10.1371/journal.pone.0134095

Fan, H., Wei, G., and Ren, L. (2022). Prosthetic and robotic wrists comparing with the intelligently evolved human wrist: a review. *Robotica* 40, 4169–4191.

Farina, D., and Amsüss, S. (2016). Reflections on the present and future of upper limb prostheses. *Expert Rev. Med. Dev.* 13, 321–324. doi: 10.1586/17434440.2016.1159511

Farina, D., Vujaklija, I., Brånemark, R., Bull, A. M. J., Dietl, H., Graimann, B., et al. (2021). Toward higher-performance bionic limbs for wider clinical use. *Nat. Biomed. Eng*. doi: 10.1038/s41551-021-00732-x [Epub ahead of print].

Franceschi, M., Seminara, L., Dosen, S., Strbac, M., Valle, M., and Farina, D. (2017). A system for electrotactile feedback using electronic skin and flexible matrix electrodes: experimental evaluation. *IEEE Trans. Haptics* 10, 162–172. doi: 10.1109/toh.2016.2618377

Garenfeld, M. A., Mortensen, C. K., Strbac, M., Dideriksen, J. L., and Dosen, S. (2020). Amplitude versus spatially modulated electrotactile feedback for myoelectric control of two degrees of freedom. *J. Neural Eng.* 17:046034. doi: 10.1088/1741-2552/aba4fd

Geng, B., Paramanathan, S. A., Pedersen, K. F., Lauridsen, M. V., Gade, J., Lontis, E. R., et al. (2016). Discrimination of spatial and temporal parameters in electrocutaneous stimulation. *Int. J. Phys. Med. Rehabil.* 4:333.

George, J. A., Kluger, D. T., Davis, T. S., Wendelken, S. M., Okorokova, E. V., He, Q., et al. (2019). Biomimetic sensory feedback through peripheral nerve stimulation improves dexterous use of a bionic hand. *Sci. Robot.* 4:eaax2352. doi: 10.1126/scirobotics.aax2352

Gilman, S. (2002). Joint position sense and vibration sense: anatomical organisation and assessment. *J. Neurol. Neurosurg. Psychiatry* 73:473. doi: 10.1136/jnnp.73.5.473

Godfrey, S. B., Bianchi, M., Bicchi, A., and Santello, M. (2016). Influence of force feedback on grasp force modulation in prosthetic applications: a preliminary study. *Annu. Int. Conf. IEEE Eng. Med. Biol. Soc.* 2016, 5439–5442. doi: 10.1109/embc.2016.7591957

Gonzalez, J., Soma, H., Sekine, M., and Yu, W. (2012). Psycho-physiological assessment of a prosthetic hand sensory feedback system based on an auditory display: a preliminary study. *J. Neuroeng. Rehabil.* 9:33. doi: 10.1186/1743-0003-9-33

Graczyk, E. L., Christie, B. P., He, Q., Tyler, D. J., and Bensmaia, S. J. (2022). Frequency shapes the quality of tactile percepts evoked through electrical stimulation of the nerves. *J. Neurosci.* 42, 2052–2064. doi: 10.1523/jneurosci.1494-21.2021

Grushko, S., Spurn, T., and Ern, M. J. S. (2020). Control methods for transradial prostheses based on remnant muscle activity and its relationship with proprioceptive feedback. *Sensors* 20:4883. doi: 10.3390/s20174883

Guémann, M., Halgand, C., Bastier, A., Lansade, C., Borrini, L., Lapeyre, É, et al. (2022). Sensory substitution of elbow proprioception to improve myoelectric control of upper limb prosthesis: experiment on healthy subjects and amputees. *J. Neuroeng. Rehabil.* 19:59. doi: 10.1186/s12984-022-01038-y

He, K., Yu, P., Li, M., Yang, Y., and Liu, L. (2016). "The quantitative evaluation of electrotactile stimulation mode," in *2016 IEEE International conference on real-time computing and robotics (RCAR)*, 346–351.

Kaczmarek, K. A., Webster, J. G., Bach-y-Rita, P., and Tompkins, W. J. (1991). Electrotactile and vibrotactile displays for sensory substitution systems. *IEEE Trans. Biomed. Eng.* 38, 1–16. doi: 10.1109/10.68204

Kaya, D., Yosmaoglu, B., and Doral, M. N. (2018). "Neurophysiology and assessment of the proprioception," in *Proprioception in orthopaedics, sports medicine and rehabilitation*, eds D. Kaya, F. Kaya Yertutanol, and M. Calik (Cham: Springer), 3–11. doi: 10.1007/978-3-319-66640-2

Kayhan, O., Nennioglu, A. K., and Samur, E. (2018). "A skin stretch tactor for sensory substitution of wrist proprioception," in *IEEE Haptics symposium (HAPTICS)*, (San Francisco, CA), 26–31.

Koc, E., Tunca, M., Akar, A., Erbil, A. H., Demiralp, B., and Arca, E. (2008). Skin problems in amputees: a descriptive study. *Int. J. Dermatol.* 47, 463–466. doi: 10.1111/j.1365-4632.2008.03604.x

Kosasih, J. B., and Silver-Thorn, M. B. (1998). Sensory changes in adults with unilateral transtibial amputation. *J. Rehabil. Res. Dev.* 35, 85–90.

Kyberd, P. J., Lemaire, E. D., Scheme, E., MacPhail, C., Goudreau, L., Bush, G., et al. (2011). Two-degree-of-freedom powered prosthetic wrist. *J. Rehabil. Res. Dev.* 48, 609–617. doi: 10.1682/jrrd.2010.07.0137

Lan, N., Niu, C., Hao, M., Chou, C., and Dai, C. (2019). Achieving neural compatibility with human sensorimotor control in prosthetic and therapeutic devices. *IEEE Trans. Med. Robot. Bionics* 1, 122–134. doi: 10.1109/TMRB.2019.2930356

Luo, Q., Niu, C. M., Liu, J., Chou, C. H., Hao, M., and Lan, N. (2021). Evaluation of model-based biomimetic control of prosthetic finger force for grasp. *IEEE Trans. Neural Syst. Rehabil. Eng.* 29, 1723–1733. doi: 10.1109/TNSRE.2021.3106304

Makin, T. R., de Vignemont, F., and Faisal, A. A. (2017). Neurocognitive barriers to the embodiment of technology. *Nat. Biomed. Eng.* 1:0014. doi: 10.1038/s41551-016-0014

Mann, R. W., and Reimers, S. D. (1970). Kinesthetic sensing for the EMG controlled "Boston Arm". *IEEE Trans. Man-Machine Syst.* 11, 110–115. doi: 10.1109/TMMS.1970.299971

Marasco, P. D., Hebert, J. S., Sensinger, J. W., Shell, C. E., Schofield, J. S., Thumser, Z. C., et al. (2018). Illusory movement perception improves motor control for prosthetic hands. *Sci. Transl. Med.* 10:eaao6990. doi: 10.1126/scitranslmed.aao6990

Marion, M. S., Wexler, A. S., and Hull, M. L. (2013). Predicting non-isometric fatigue induced by electrical stimulation pulse trains as a function of pulse duration. *J. Neuroeng. Rehabil.* 10:13. doi: 10.1186/1743-0003-10-13

Markovic, M., Schweisfurth, M. A., Engels, L. F., Bentz, T., Wüstefeld, D., Farina, D., et al. (2018). The clinical relevance of advanced artificial feedback in the control of a multi-functional myoelectric prosthesis. *J. Neuroeng. Rehabil.* 15:28. doi: 10.1186/s12984-018-0371-1

Midha, S., Maior, H. A., Wilson, M. L., and Sharples, S. (2021). Measuring mental workload variations in office work tasks using fNIRS. *Int. J. Hum. Comput. Stud.* 147:102580. doi: 10.1016/j.ijhcs.2020.102580

Nataletti, S., Leo, F., Dideriksen, J., Brayda, L., and Dosen, S. (2022). Combined spatial and frequency encoding for electrotactile feedback of myoelectric signals. *Exp. Brain Res.* 240, 2285–2298. doi: 10.1007/s00221-022-06409-4

Nataletti, S., Leo, F., Seminara, L., Trompetto, C., Valle, M., Dosen, S., et al. (2020). Temporal asynchrony but not total energy nor duration improves the judgment of numerosity in electrotactile stimulation. *Front Bioeng. Biotechnol.* 8:555. doi: 10.3389/fbioe.2020.00555

Omarkulov, N., Telegenov, K., Zeinullin, M., Tursynbek, I., and Shintemirov, A. (2016). "Preliminary mechanical design of NU-Wrist: a 3-DOF self-aligning wrist rehabilitation robot," in *IEEE International conference on biomedical robotics & biomechatronics*), (Singapore).

Page, D. M., George, J. A., Kluger, D. T., Duncan, C., Wendelken, S., Davis, T., et al. (2018). Motor control and sensory feedback enhance prosthesis embodiment and reduce phantom pain after long-term hand amputation. *Front. Hum. Neurosci.* 12:352. doi: 10.3389/fnhum.2018.00352

Proske, U., and Gandevia, S. C. (2012). The proprioceptive senses: their roles in signaling body shape, body position and movement, and muscle force. *Physiol. Rev.* 92, 1651–1697. doi: 10.1152/physrev.00048.2011

Proulx, M. J., Brown, D. J., Pasqualotto, A., and Meijer, P. (2014). Multisensory perceptual learning and sensory substitution. *Neurosci. Biobehav. Rev.* 41, 16–25. doi: 10.1016/j.neubiorev.2012.11.017

Rafiei, S., Darestani Farahani, E., and Moradi, M. (2014). "A fully programmable multi-channel electrotactile stimulator," in *Proceedings of the 2014 22nd Iranian conference on electrical engineering (ICEE)* (Tehran, Iran).

Raspopovic, S., Valle, G., and Petrini, F. M. (2021). Sensory feedback for limb prostheses in amputees. *Nat. Mater.* 20, 925–939. doi: 10.1038/s41563-021-00966-9

Schiefer, M. A., Graczyk, E. L., Sidik, S. M., Tan, D. W., and Tyler, D. J. (2018). Artificial tactile and proprioceptive feedback improves performance and confidence on object identification tasks. *PLoS One* 13:e0207659. doi: 10.1371/journal.pone.0207659

Schiefer, M., Tan, D., Sidek, S. M., and Tyler, D. J. (2016). Sensory feedback by peripheral nerve stimulation improves task performance in individuals with upper limb loss using a myoelectric prosthesis. *J. Neural Eng.* 13:016001. doi: 10.1088/1741-2560/13/1/016001

Stephens-Fripp, B., Alici, G., and Mutlu, R. (2018). A review of non-invasive sensory feedback methods for transradial prosthetic hands. *IEEE Access* 6, 6878–6899.

Štrbac, M., Belić, M., Isaković, M., Kojić, V., Bijelić, G., Popović, I., et al. (2016). Integrated and flexible multichannel interface for electrotactile stimulation. *J. Neural Eng.* 13:046014. doi: 10.1088/1741-2560/13/4/046014

Svensson, P., Wijk, U., Björkman, A., and Antfolk, C. (2017). A review of invasive and non-invasive sensory feedback in upper limb prostheses. *Expert Rev. Med. Dev.* 14, 439–447. doi: 10.1080/17434440.2017.1332989

Tabrik, S., Behroozi, M., Schlaffke, L., Heba, S., Lenz, M., Lissek, S., et al. (2021). Visual and tactile sensory systems share common features in object recognition. *eNeuro* 8, ENEURO.101–ENEURO.121. doi: 10.1523/eneuro.0101-21.2021

Tchimino, J., Dideriksen, J. L., and Dosen, S. (2022). EMG feedback outperforms force feedback in the presence of prosthesis control disturbance. *Front. Neurosci.* 16:952288. doi: 10.3389/fnins.2022.952288

Templeton, C. A., Strzalkowski, N. D. J., Galvin, P., and Bent, L. R. (2018). Cutaneous sensitivity in unilateral trans-tibial amputees. *PLoS One* 13:e0197557. doi: 10.1371/journal.pone.0197557

Terlaak, B., Bouwsema, H., van der Sluis, C. K., and Bongers, R. M. (2015). Virtual training of the myosignal. *PLoS One* 10:e0137161. doi: 10.1371/journal.pone.0137161

Ueda, Y., and Ishii, C. (2017). Feedback device of temperature sensation for a myoelectric prosthetic hand. *Adv. Sci. Technol. Eng. Syst. J.* 2, 41–47. doi: 10.25046/aj020307

Vargas, L., Huang, H. H., Zhu, Y., and Hu, X. (2021a). Closed-loop control of a prosthetic finger via evoked proprioceptive information. *J Neural Eng* 18:066029. doi: 10.1088/1741-2552/ac3c9e

Vargas, L., Huang, H. H., Zhu, Y., and Hu, X. (2021b). Static and dynamic proprioceptive recognition through vibrotactile stimulation. *J. Neural Eng.* 18:046093.

Vu, P. P., Lu, C. W., Vaskov, A. K., Gates, D. H., Gillespie, R. B., Kemp, S. W. P., et al. (2022). Restoration of proprioceptive and cutaneous sensation using regenerative peripheral nerve interfaces in humans with upper limb amputations. *Plast Reconstr. Surg.* 149, 1149e–1154e. doi: 10.1097/PRS.0000000000009153

Wang, Y., Fang, P., Tang, X., Jiang, N., Tian, L., Li, X., et al. (2022). Effective evaluation of finger sensation evoking by non-invasive stimulation for sensory function recovery in transradial amputees. *IEEE Trans. Neural Syst. Rehabil. Eng.* 30, 519–528. doi: 10.1109/tnsre.2022.3155756

Wijk, U., Carlsson, I. K., Antfolk, C., Björkman, A., and Rosén, B. (2020). Sensory feedback in hand prostheses: a prospective study of everyday use. *Front. Neurosci.* 14:663. doi: 10.3389/fnins.2020.00663

Witteveen, H., Rietman, J., and Veltink, P. (2014). Vibrotactile grasping force and hand aperture feedback for myoelectric forearm prosthesis users. *Prosthet. Orthot. Int.* 39, 204–212. doi: 10.1177/0309364614522260

Wu, H., Fang, Y., and Sheng, X. (2020). "Design of fingertip pressure sensors for prosthetic hands," in *2020 IEEE International conference on real-time computing and robotics* (RCAR) Asahikawa, 32–37. doi: 10.1109/RCAR49640.2020.9303278

Yang, L., Dyer, P. S., Carson, R. J., Webster, J. B., Bo Foreman, K., and Bamberg, S. J. M. (2012). Utilization of a lower extremity ambulatory feedback system to reduce gait asymmetry in transtibial amputation gait. *Gait Post.* 36, 631–634. doi: 10.1016/j.gaitpost.2012.04.004

Zheng, Y., and Hu, X. (2018). Improved muscle activation using proximal nerve stimulation with subthreshold current pulses at kilohertz-frequency. *J. Neural Eng.* 15:046001. doi: 10.1088/1741-2552/aab90f

Zheng, Y., Tian, L., Li, X., Tan, Y., Yang, Z., and Li, G. (2022). Toward improving control performance of myoelectric arm prosthesis by adding wrist position feedback. *Front. Hum. Neurosci.* 16:905885. doi: 10.3389/fnhum.2022.905885

Zhu, Y., Wang, Q., and Zhang, L. (2021). Study of EEG characteristics while solving scientific problems with different mental effort. *Sci. Rep.* 11:23783. doi: 10.1038/s41598-021-03321-9

frontiers | Frontiers in Neuroscience

TYPE Original Research
PUBLISHED 28 March 2023
DOI 10.3389/fnins.2023.1113009

OPEN ACCESS

EDITED BY
Min Li,
Xi'an Jiaotong University, China

REVIEWED BY
Gemma Carolina Bettelani,
Technical University of Munich, Germany
Shan Luo,
King's College London, United Kingdom

*CORRESPONDENCE
Raphael M. Mayer
✉ raphaelmariamayer@gmail.com

SPECIALTY SECTION
This article was submitted to Neuroprosthetics, a section of the journal Frontiers in Neuroscience

RECEIVED 30 November 2022
ACCEPTED 24 February 2023
PUBLISHED 28 March 2023

CITATION
Mayer RM, Mohammadi A, Tan Y, Alici G, Choong P and Oetomo D (2023) Temporal and spatial characteristics of bone conduction as non-invasive haptic sensory feedback for upper-limb prosthesis.
Front. Neurosci. 17:1113009.
doi: 10.3389/fnins.2023.1113009

Temporal and spatial characteristics of bone conduction as non-invasive haptic sensory feedback for upper-limb prosthesis

Raphael M. Mayer[1]*, Alireza Mohammadi[1], Ying Tan[1], Gursel Alici[2,3], Peter Choong[3,4] and Denny Oetomo[1,3]

[1]Department of Mechanical Engineering, The University of Melbourne, Parkville, VIC, Australia, [2]School of Mechanical, Materials, Mechatronic and Biomedical Engineering, University of Wollongong, Wollongong, NSW, Australia, [3]ARC Centre of Excellence for Electromaterials Science, Wollongong, NSW, Australia, [4]Department of Surgery, St Vincent's Hospital, The University of Melbourne, Parkville, VIC, Australia

Bone conduction is a promising haptic feedback modality for upper-limb prosthesis users, however, its potential and characteristics as a non-invasive feedback modality have not been thoroughly investigated. This study aimed to establish the temporal and spatial characteristics of non-invasive bone conduction as a sensory feedback interface for upper-limb prostheses. Psychometric human-subject experiments were conducted on three bony landmarks of the elbow, with a vibrotactile transducer affixed to each to provide the stimulus. The study characterized the temporal domain by testing perception threshold and resolution in amplitude and frequency. The spatial domain was evaluated by assessing the ability of subjects to detect the number of simultaneous active stimulation sites. The experiment was conducted with ten able-bodied subjects and compared to two subjects with trans-radial amputation. The psychometric evaluation of the proposed non-invasive bone conduction feedback showed results comparable to invasive methods. The experimental results demonstrated similar amplitude and frequency resolution of the interface for all three stimulation sites for both able-bodied subjects and subjects with trans-radial amputation, highlighting its potential as a non-invasive feedback modality for upper-limb prostheses.

KEYWORDS

neuroprosthesis, sensory feedback restoration, human-robot interaction (HRI), tactile feedback, bone conduction (BC)

1. Introduction

Haptic sensory feedback plays an important role in effective closed-loop control of upper-limb prostheses (Saunders and Vijayakumar, 2011; Antfolk et al., 2013; Markovic et al., 2018; Stephens-Fripp et al., 2018; Farina et al., 2021), promoting the body ownership of prosthetic arm users (Canzoneri et al., 2013; Shehata et al., 2020; Richard et al., 2021) and the reduction of phantom limb pain management (Dietrich et al., 2012). This feedback is generated through a form of stimulation that is encoded with relevant feedback information and delivered to the user's residual limb. The sensory feedback information can be used in a variety of applications including upper-limb prosthesis, e.g., for grasp force control (Childress, 1980; Westling and Johansson, 1984; Augurelle et al., 2003; Antfolk et al., 2013), haptic applications e.g., robotic teleoperation (Dahiya et al., 2010) or virtual reality applications (Richard et al., 2021).

Invasive and non-invasive haptic sensory feedback approaches have been investigated in the past (Cordella et al., 2016; Stephens-Fripp et al., 2018). Invasive approaches, such as implanted nerve electrodes, show great potential but limited applicability or desirability to a subset of the people living with limb loss due to the inherent surgical risks and potential limited lifetime of the electrodes (Schofield et al., 2014; Cordella et al., 2016; Farina and Amsüss, 2016; Svensson et al., 2017). Non-invasive stimulation will therefore continue to play a strong role in prosthetic applications (Farina and Amsüss, 2016). It is also directly applicable in other areas such as in haptics and human robot interaction (Goodrich and Schultz, 2007) and more generally in human machine interfaces (HMI) (Tahir et al., 2018). The state of the arts of non-invasive tactile feedback are conventionally applied on the skin through electrotactile, vibrotactile and mechanotactile modalities to varying degrees of success (Antfolk et al., 2013; Schofield et al., 2014; Sensinger and Dosen, 2020; Farina et al., 2021). The shortcomings of these methods were comprehensively studied and summarized in two thorough review papers (Svensson et al., 2017; Stephens-Fripp et al., 2018). These shortcomings include: (1) The force dependency of perceived sensation in vibrotactile feedback, which can affect the accuracy and consistency of feedback information when the transducer is pressed against the skin; (2) Changes in the perception of both electrotactile and vibrotactile stimulation on the skin with varying locations, making it difficult to achieve precise and reliable feedback; (3) The bulky and high power consumption setup of the mechanotactile feedback, which can limit its practicality in real-world applications.

This paper focuses on the investigation of a non-invasive bone conduction modality as an interface to convey information to the human user. Bone conduction is a method of providing vibrotactile feedback through the bone. This approach relies on the transmission of vibrations/sound through the bone, which stimulates the Pacinian Corpuscles located around the bone (Clemente et al., 2017). Bone conduction is a relatively recent and emerging modality which can potentially address the aforementioned shortcomings.

The potential of bone conduction as a haptic feedback interface for upper-limb prosthesis has been studied in Clemente et al. (2017) through mechanical stimulation of a bone-anchored (osseointegrated) prosthesis. Superior bandwidth compared to vibrotactile feedback on the skin was found in Clemente et al. (2017) for invasive bone conduction. This allows for richer feedback of sensory information to the human user.

While the results of the osseoperception using bone conduction were promising, it is only applicable for users with osseointegrated upper-limb prostheses. There are cases that osseointegration is not suited for people with upper-limb loss due to the lack of length or strength in the residual limb or the inherent surgical risks of the invasive technique (Schofield et al., 2014; Cordella et al., 2016; Farina and Amsüss, 2016; Svensson et al., 2017). Therefore, non-invasive options such as stump sockets are expected to continue to play an important role in prosthesis.

In Mayer et al. (2019), the authors proposed the non-invasive bone conduction as haptic feedback system through vibrotactile stimulation of bony landmarks of the elbow. The preliminary results, with limited number of psychometric parameters and subjects, demonstrated comparable performance to the invasive bone conduction method (Mayer et al., 2019, 2020c). It provides a higher sensitivity of the perception of lower frequencies, allowing for the use of lower stimulation forces and therefore smaller and lower power consuming transducers. In addition, it has been observed that the non-invasive bone conduction is independent from the force pressing the transducers against the human subject (Mayer et al., 2018). This is an important characteristic as volume fluctuations, present in residual limbs (Sanders et al., 2012; Paterno et al., 2018), no longer affect the perception of the provided sensory feedback.

TABLE 1 Subjects were in the following results of able-bodied subjects are indicated as (SA) and for subjects with trans-radial Amputation as (ST).

Subject group	Number	Age (years)	Gender
Able bodied Subjects (SA)	10	26 ± 3.9	2 F, 8 M
Subjects with trans-radial Amputation (ST)	2	29 ± 8.5	0 F, 2 M

F, female; M, male.

The objective of this paper is to thoroughly investigate and determine the temporal and spatial characteristics of the non-invasive bone conduction with different user groups including subjects with amputation. The temporal parameters of the interface will be characterized by the lowest perceivable stimulation threshold and the smallest perceivable resolution in amplitude as well as frequency. The spatial parameters define the capabilities of the interface to perceive stimulation on multiple sites on the physiologically given bony landmarks on the elbow when stimulation was applied one-at-a-time. This is of interest in prosthetic grasping as combination of different types of feedback information are required (Westling and Johansson, 1984; Johansson and Westling, 1987; Augurelle et al., 2003; Mayer et al., 2020b). The temporal and spatial characteristics of the bone conduction has been conducted on both able-bodied subjects and subjects with trans-radial amputation and compared to each other and to the invasive bone conduction method.

2. Methodology

In this section, the measuring parameters, experimental setup, and protocol used to obtain temporal and spatial parameters as well as the statistical analysis are presented. The experiment was conducted with ten able-bodied subjects (SA) and two subjects with trans-radial amputation (ST), see Table 1. All subjects read the plain language statement and signed the consent form approved by the Ethics Committee of the University of Melbourne (Ethics Id 1852875.1).

2.1. Temporal and spatial parameters

The temporal domain is characterized by the perception threshold (PT) and the minimum noticeable difference for subjects, referred to as "just noticeable difference" (JND). The

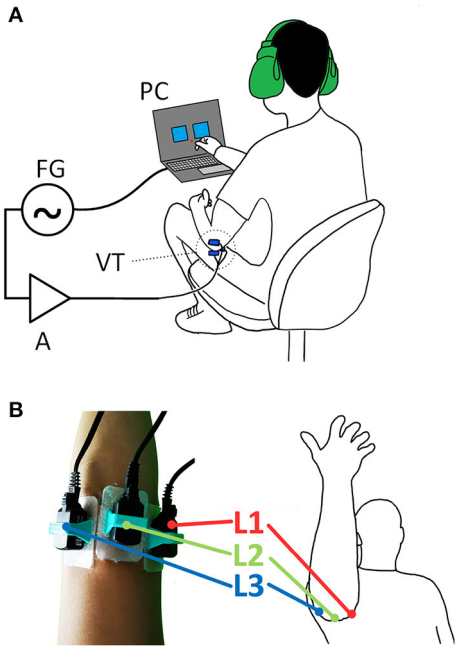

FIGURE 1
The experimental setup: **(A)** three vibrotactile transducers (VT) are controlled *via* a personal computer (PC) connected *via* USB to a frequency generator (FG) and an amplifier (A); **(B)** the transducers are fixed onto the bony landmarks (figure shows right arm) of the dominant hand: (L1) epicondylis medialis, (L2) ulnar olecranon and (L3) epicondylus lateralis in 3D printed holder and medical grade double sided sticker and mounted.

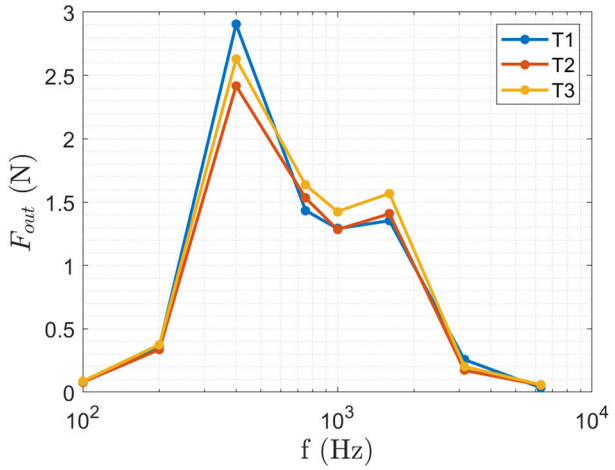

FIGURE 2
The calibration curve for the transducers T1-T3 is used to calculate the perception threshold in Newton from the recorded Voltage applied to the transducers. The produced force F_{out} was measured for $f \in [100, 200, 400, 750, 1{,}500, 3{,}000, \text{and } 6{,}000]$ Hz at an amplitude of $a \in [0.1, 0.3, 0.5]$ V where the figure shows the obtained results at $a = 0.5$ V.

JND is obtained to quantify the perceivable resolution of the bone conduction interface for frequency and amplitude. The spatial domain is characterized by the ability to identify different stimulation sites (SPLIR).

2.1.1. Perception threshold

PT is the minimum stimulation amplitude that subjects can perceive at a certain stimulation frequency at a certain stimulation site and can be represented as $PT(f, l)$. For any given frequency f and site l, the amplitude thresholds changes for each person, as shown in Clemente et al. (2017, 2016), and Mayer et al. (2019), thus it is necessary to be identified.

2.1.2. Just noticeable difference

The JND is determined for amplitude as well as frequency describing the resolution of the interface and therefore specifying the possible information rate of the interface. It is the minimum difference a subject can discriminate with a pre-determined probability. The $JND_f(f, a, l)$ varies with stimulation amplitude a for a given stimulation frequency f and site l. The $JND_a(f, a, l)$ varies with stimulation frequency f for a given stimulation amplitude a and site l. For a non-invasive bone conduction interface applied to the elbow (a natural location for the case of a transradial prosthetic arm), three accessible bony landmarks exist, namely the epicondylus (medialis and lateralis) and the ulnar olecranon. Therefore, multiple vibrotactile transducers can be deployed and potentially be used simultaneously. The spatial domain is therefore characterized by the spatial parameter single-point location identification rate (SPLIR).

2.1.3. Single-point location identification rate

SPLIR is the success rate that the subject correctly identifies the correct stimulation site. SPLIR is different for each site l:

$$SPLIR(l) = \frac{N_{corr}(l)}{N(l)}, \tag{1}$$

where $N_{corr}(l)$ is the number of correct identified stimulations for the number of presented stimulations $N(l)$ at site l.

2.2. Experimental setup

The experiment was conducted using the setup shown in Figure 1, where three *Vibrotactile Transducers (VT)* were driven by the *frequency generator (FG)* and *amplifier (A)* and controlled by the *personal computer (PC)*. The three transducers T1-T3 were placed onto the 3 bony landmarks of the elbow: epicondylis medialis (L1), ulnar olecranon (L2) and epicondylus lateralis (L3), see Figure 1.

2.2.1. Vibrotactile transducers

Three B81 transducers T1-T3 from RadioEar Corporation (USA) were utilized to provide the vibrotactile stimulus to the bony landmarks. All three transducers were calibrated using an Artificial Mastoid Type 4930 from Brüel & Kjære (Denmark) adjusted to produce the same force output of 121.5 dB at $f = 1$ kHz. The transducers were affixed to the bony landmarks, see Figure 1, of the

subjects using a 3D printed holder (PLA/TPU) and medical grade double sided sticker Type 1510 (3M™).

2.2.2. Frequency generator

A National Instruments NI USB-6343 is used.

2.2.3. Amplifier

A 15W Public Address amplifier type A4017 from Redback Inc. (Australia) with $4-16\Omega$ output to drive the 12.5Ω B81 transducers and achieve a harmonic distortion of $< 3\%$ at 1 kHz.

2.2.4. Personal computer

A Windows Surface Book 2 (Intel Core i7-8, 16GB RAM, Windows 10™) and a MATLAB® GUI, guiding the user through the experiment and controlling the stimulation parameters.

2.3. Experimental protocol

The experiment is divided into temporal and spatial parameters. In order to reduce time effort for the subjects with trans-radial amputation, the able-bodied subjects carried out the whole experiment first. The longest time effort in the experiment was in the identification of the just noticeable difference. Therefore, this was carried out in stages: it was first done on the able-bodied subjects. The site with the lowest perception threshold was identified as L1. For the subjects with transradial amputation, this experiment was done for L1 instead of for all three sites, thus reducing the time-effort required from the subjects with amputation. The following explains the protocol for determining each parameter.

The temporal parameters, PT and JND, are obtained utilizing a single interval adjustment matrix (SIAM) method in order to reduce long trial times, requiring half the amount of repetitions compared to a standard two-interval forced-choice (2IFC). SIAM methods has been previously been implemented by Dosen et al. (2016) and shown to achieve same precision as a 2IFC test in Kaernbach (1990). In the SIAM procedure the outcome (hit, miss, false alarm, correct rejection) is used to adjust the signal level in a staircase manner. The response criterion is set to 0.5 which means the obtained PTs / JNDs are recognized with a 50% probability which is the same performance as in 2IFC tests (Kaernbach, 1990). This was chosen according to Kaernbach (1990) where it was shown that it results in the best threshold estimate.

A SIAM matrix,

$$SIAM = \begin{bmatrix} -1 & 1 \\ 2 & 0 \end{bmatrix} \tag{2}$$

as shown in Kaernbach (1990), achieves the best threshold estimate *via* a 50% target performance, i.e., half of the presented stimuli are blank. Blank stimulus means that it carries no stimulation for perception threshold and no change for JND tests. The provided stimulus S_i is therefore adjusted based on the response of the subject

$$S_{i+1} = S_i + SIAM(a, b)\delta S \tag{3}$$

where δS is the step size. The index a determines if the stimulus was a blank ($a = 1$) or a true stimulation ($a = 0$). The index b is determined by the subject's yes/no response, where a yes means $b = 1$ and a no means $b = 0$. A correctly perceived stimulation changes the stimulus by $-1\delta S$ while an incorrectly perceived stimulation increases the stimulus by $+1\delta S$. An incorrect perception of a blank stimulation increases the stimulus by $+2\delta S$ while a correct perception of a blank keeps it at the current level (Kaernbach, 1990; Dosen et al., 2016).

2.3.1. Perception threshold

A complete psychophysical evaluation of the perception threshold would imply determining the PT at a step size determined by the Just Noticeable Difference Frequency difference (JND_f). As the JND_f is not known *a priori*, the preliminary results obtained in Mayer et al. (2018, 2019, 2020c) are used to define the frequency range, where the three sites L1-3 are each individually perceivable as well as dominant tactile perception is shown in a frequency range of $f \in [100, 400, 750]$ Hz. The perception threshold $PT(f, l)$ is obtained *via* SIAM (Kaernbach, 1990) method. The threshold for each frequency f at the site l is obtained by presenting 26 repetitions and the amplitude adjusted according to the subjects feedback *via* SIAM method. The frequencies f are presented in a randomized manner at each site l. To allow for a technical implementation and selection of suitable transducers the Perception Threshold is given in Newton utilizing the previously obtained calibration (Figure 2).

2.3.2. Just noticeable difference

Similar to PT, a complete psychophysical characterization of the JND would imply determining a full range in amplitude/frequency (AF). This would result in an impractically large number of measurements, resulting in an excessively long duration of experiments for subjects. Hence, the AF domain was divided into discrete steps, called AF reference points, where $f_{ref} \in [100, 400, 750]$ Hz and $a_{ref} \in [0.1, 0.3, 0.5]$ V resulting in a combination of 9 AF points where the reference amplitudes and frequencies where chosen according to the preliminary results obtained in Mayer et al. (2019). At each AF reference point, the JND_f and JND_a were obtained in increasing direction (toward the maximum value). The JND is given in Volt, which can be used to derive the smallest necessary step size for an implementation and selection of suitable driver circuitry.

2.3.3. Single-point location identification rate

Spatial parameters were obtained according to Mayer et al. (2020c). The subjects were asked to report on the site L1-L3 of the stimulation. Therefore, the subjects were presented with the stimuli on the three different sites without *a priori* knowledge of the stimulation site. The order of stimulation sites were applied randomly from $f \in [100, 200, 400, 750, 1{,}500, 3{,}000,$ and $6{,}000]$ Hz, $a = 0.5$ V and each repeated 10 times. Frequencies are choose according to the shown bandwidth in Clemente et al. (2017) and Mayer et al. (2019). Each stimulation was ON for 1 s. At the start of the experiment, the subjects were provided with the opportunity to familiarize themselves with the stimulation and therefore explore

the association of the three stimulation sites by voluntary inducing stimuli on each site.

2.4. Analysis

The statistical analysis in this study is utilized to investigate the difference between the physiological sites and the different subject groups.

2.4.1. Effect of physiological locations

A non-parametric statistical analysis, specifically a Friedman Test (Daniel, 1990) was applied to compare the three physiological sites for each temporal and spatial parameter. In case of statistical significant differences, this was followed up by a *post-hoc* analysis *via* Wilcoxon signed rank test (Wilcoxon, 1945) to determine which of the three physiological sites was different. The *p*-value results are presented for the Friedman as well as the applied *post-hoc* Wilcoxon signed rank test.

2.4.2. Perception threshold

The achieved results of perception threshold are visually presented by plotting the mean and the stand deviation as an error bar.

2.4.3. Just noticeable difference

A summary plot shows the JND_a and JND_f at each AF reference point by its mean value, with the origin at the AF reference point. More details are shown in individual plots for each AF reference point for each site showing the obtained mean value and the stand deviation as an error bar.

2.4.4. Single-point location identification rate

The achieved results of perception threshold is visually presented similar as in Mayer et al. (2020c) by plotting the mean and the stand deviation as an error bar.

2.4.5. Difference between subject groups

A qualitative comparison between able-bodied subjects and subjects with trans-radial amputation (ST) was carried out to compare the two subject groups for each temporal and spatial parameter. The obtained mean values for the parameters are use for such comparison.

3. Results

In this section, the temporal and spatial parameters are presented and compared statistically for the different sites/bony landmarks (L1-L3) at the elbow and qualitatively across different subject groups.

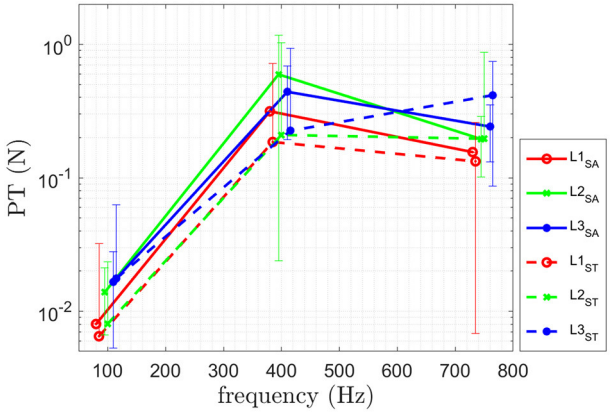

FIGURE 3
Results of the psychophysical evaluation for PT of ten able-bodied subjects (SA) and for two trans-radial amputees (ST). Means and standard deviations of the identified PT at frequencies [100 400 750] Hz are shown.

TABLE 2 The *p*-values of the Friedman for perception threshold comparing the three different physiological sites L1, L2, and L3 at all frequencies is shown.

		Frequency		
		100 Hz	400 Hz	750 Hz
Friedman	*L1* vs. *L2* vs. *L3*	≤ 0.001*	0.273	≤ 0.001*
Wilcoxon	*L1* vs. *L2*	0.002*	-	0.002*
	L1 vs. *L3*	0.002*	-	0.002*
	L2 vs. *L3*	0.059	-	0.059

Significance level is $p < 0.05$. The *p*-values of the *post-hoc* Wilcoxon signed rank test for Perception Threshold comparing the three different physiological sites L1, L2 and L3 to each other over $f \in [100, 400, 750]$ Hz of the ten able-bodied subjects is shown. Significance level is $p < 0.05$. *Indicates statistically significance.

3.1. Physiological sites

3.1.1. Perception threshold

The results for PT are shown in Figure 3 and Table 2. The results of the obtained perception threshold, for the three physiological sites of able-bodied subjects (SA) and trans-radial amputees (ST) are shown in Figure 3. The mean perception thresholds for *SA* is [0.015 0.45 0.2] N and for *ST* [0.015 0.21 0.25] N for [100 400 750] Hz.

The Friedman test results, comparing the three different sites, are shown in Table 2. The obtained results indicate a statistically significant difference in performance for [100 750] Hz for the perception threshold for the three different sites. No statistical difference is observed at 400 Hz. A *post-hoc* test (Wilcoxon signed rank test), is performed for [100 750] Hz and the corresponding *p*-values are shown in Table 2. In the following, the obtained results are summarized:

L1 vs. L2: A statistical significant difference for perception threshold at [100 750] Hz is shown in Table 2 with L1 having a lower PT.

L1 vs. L3: A statistical significant difference for perception threshold at [100 750] Hz is shown in Table 2 with L1 having a lower PT.

TABLE 3 The p-values of the Friedman for JND_a comparing the three different physiological sites L1, L2, and L3 at all frequencies and amplitudes of the ten able-bodied subjects (SA) is given.

		Amplitude	Frequency		
			100 Hz	400 Hz	750 Hz
Friedman	L1 vs. L2 vs. L3	*0.1 V*	0.318	0.063	0.255
		0.3 V	0.900	0.407	0.905
		0.5 V	0.509	0.527	0.318

Significance level is taken at $p < 0.05$.

L2 vs. L3: No statistical significant difference was obtained for perception threshold at [100 750] Hz shown in Table 2.

Note that the p-values are at 0.059 for both cases, therefore they are only slightly above significance level of $p < 0.05$.

3.1.2. Just noticeable difference

The results for the just noticable difference in amplitude JND_a are shown in Figure 5A and Table 3. The results for the just noticable difference in frequency JND_f are shown in Figure 5B and Table 4. A combined plot is shown in Figure 4, showing the mean at each site. The details of JND_a and JND_f are shown and discussed in the following.

3.1.2.1. JND_a

The obtained results of JND_a are shown in Figure 5A. The obtained results of the Friedman test comparing the three sites, as shown in Table 3, indicate no statistically significant difference between the three physiological sites, therefore no *post-hoc* test was performed.

3.1.2.2. JND_f

The obtained results of JND_f are shown in Figure 5B. The results of the Friedman test for the three sites of JND_f, as shown in Table 4, indicate a statistically significant difference for JND_f at [0.1 V, 400 Hz] as well as for [0.3 V, 750 Hz]. No statistically significant difference was found for all other discrete steps in the AF domain. The results of the *post-hoc* Wilcoxon signed rank test comparing the three different physiological sites L1, L2 and L3 to each other for 0.1 V at 400 Hz and 0.3 V at 750 Hz, shown in Table 4. In the following, the obtained results are summarized:

L1 vs. L2: A statistical significant difference for JND_f at 400 Hz for 0.1 V and 0.3 V is shown in Table 4.

No statistical significant difference was obtained for 0.1 V at 400 Hz and 0.3 V at 750 Hz is shown for

L1 vs. L3 as well as **L2 vs. L3** in Table 4.

3.1.3. Single-point location identification rate

The results of the obtained SPLIR are shown in Figure 6 for all three physiological sites. The Friedman results for the three different sites, as shown in Table 5, indicate no statistically significant difference in performance for the different sites for SPLIR, hence, no *post-hoc* test was performed.

TABLE 4 The p-values of the Friedman for JND_f comparing the three different physiological sites L1, L2, and L3 at all frequencies and amplitudes is given.

		Amplitude	Frequency		
			100 Hz	400 Hz	750 Hz
Friedman	L1 vs. L2 vs. L3	0.1 V	0.828	0.018*	0.174
		0.3 V	0.565	0.717	0.008*
		0.5 V	0.140	0.143	0.500
Wilcoxon	***L1vs.L2***	0.1 V	-	0.031*	-
		0.3 V	-	-	0.031*
	L1vs.L3	0.1 V	-	0.406	-
		0.3 V	-	-	0.063
	L2vs.L3	0.1 V	-	0.094	-
		0.3 V	-	-	1.0

Significance level is $p < 0.05$. Furthermore, the p-values of the *post-hoc* Wilcoxon signed rank test for JND_f comparing the three different physiological sites L1, L2 and L3 to each other over all frequencies and amplitudes of the ten able-bodied subjects is shown. Significance level is $p < 0.05$. *Indicates statistically significance.

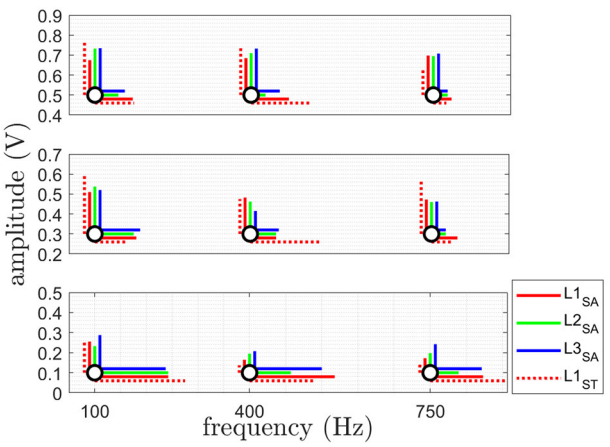

FIGURE 4
This plot shows the combination of JND_a (vertically) and JND_f (horizontally) at each AF point. The JND_a showing the amplitude resolution for 3 different frequencies at 3 different amplitudes and JND_f giving the frequency resolution for 3 different amplitudes at 3 different frequencies in a summary plot of the obtained mean value of JND_a (blue) and JND_f (red) at each reference stimulus (black) giving. See Figure 5 for the detailed trends of each JND_a and JND_f. The results are shown for all three sites L1-L3 for the able-bodied subjects (SA) and for site L1 subjects with trans-radial amputation (ST).

3.2. Subject groups

The obtained perception threshold of the two user groups, able-bodied subjects (SA) and subjects with trans-radial amputation (ST), are shown in Figure 3. The results show a lower to similar

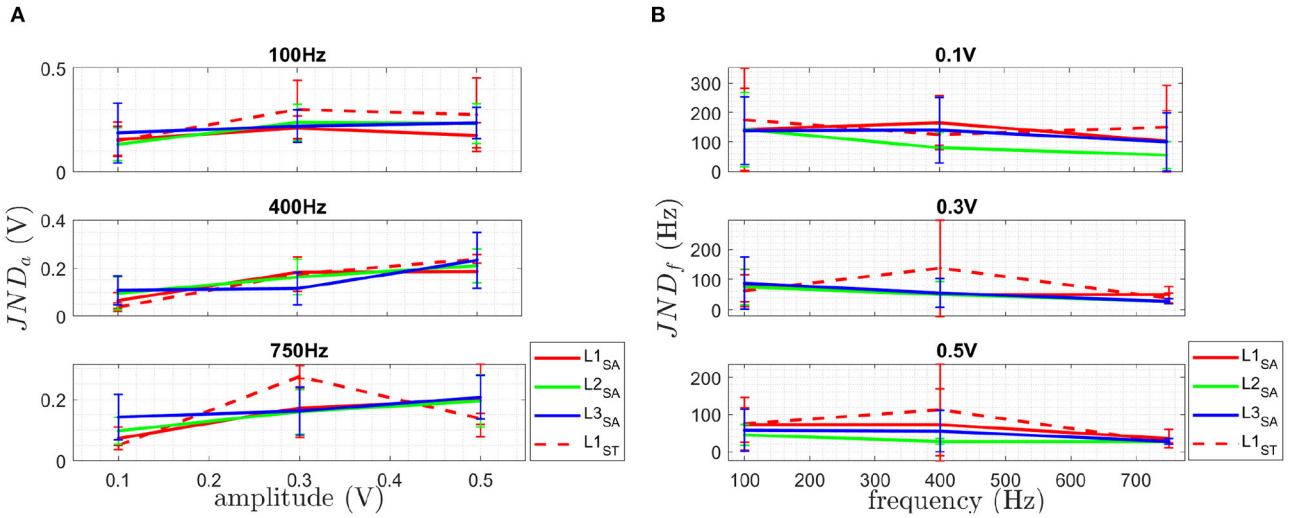

FIGURE 5
The plot in **(A)** shows the detailed JND_a at the three different chosen AF reference frequencies for the three different AF reference amplitudes and **(B)** shows the detailed JND_f for at the three different chosen AF reference amplitudes for the three different AF reference frequencies. Both are given for the three sites L1-L3 for *SA* and *ST*. The mean is plotted as solid line and the standard deviation given as error bar.

perception threshold for *ST* compared to *SA*. A higher value is obtained for L3 at 750 Hz.

The obtained JND_a of the two user groups is shown in Figure 5A. The obtained JND_f of the two user groups is shown in Figure 5B. The obtained SPLIR of the two user groups is shown in Figure 6.

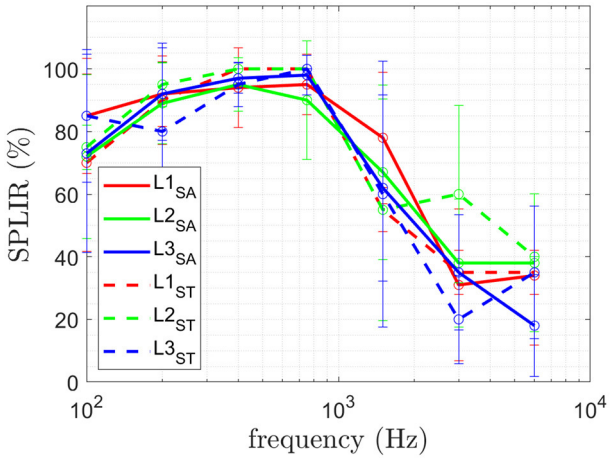

FIGURE 6
The mean and standard deviation of the SPLIR for each site L1, L2, and L3 is shown. The results of the ten able-bodied subjects (SA) is plotted in solid lines and for subjects with trans-radial amputation (ST).

4. Discussion

In this section, the obtained results are discussed for: (a) the three physiological sites; (b) the different subject groups and compared to results obtained for invasive bone conduction in Clemente et al. (2017).

4.1. Physiological sites

For perception threshold site L1 performed better (in statistically significance manner) than L2 and L3 at 100 and 750 Hz, while no difference was obtained at 400 Hz. Better performance of L1 can be explained by on the one hand allowing better contact to the bones in a non-invasive manner due to little skin and soft tissue in between transducer and bone. On the other hand the ulnar nerve runs behind the medial epicondyle on the inside of the elbow and might increase the perception by being mechanically stimulated. The results of the study did not reveal any statistically significant differences in PT between the three stimulation sites at 400 Hz. While the L1 site demonstrated the lowest value, the high variance of the results could account for the lack of statistical significance (see Figure 3). One possible explanation for the variability in the results is the limited number of participants in the study. Another factor to consider is the findings of Clemente et al. (2017), which suggest that stimulation frequencies above 400 Hz can be perceived as sound. As a result, the change in sensation from tactile-only to tactile and audio could contribute to the increased variability observed in the results. The obtained PT achieved for invasive bone conduction (Clemente et al., 2017) which is a mean PT of $[0.2, 0.1, 0.47]$ N compared to the results obtained in this study being $[0.01, 0.45, 0.20]$ N for *SA* and $[0.01, 0.21, 0.25]$ N for *ST* at f=$[100, 400, 750]$ Hz. A smaller perception threshold at 100 Hz and 750 Hz for all three sites has been achieved for both user groups for non-invasive bone conduction feedback. The obtained PT at 400 Hz is higher than in Clemente et al. (2017) for all three sites.

TABLE 5 The *p*-values of the Friedman for SPLIR comparing the three different physiological sites L1, L2, and L3 at all frequencies and amplitudes is given.

	Frequency						
	100 Hz	200 Hz	400 Hz	750 Hz	1,500 Hz	3,000 Hz	6,000 Hz
L1 vs. L2 vs. L3	0.581	0.460	0.867	0.104	0.081	0.704	0.103

Significance level is $p < 0.05$. *Indicates statistically significance.

Note that a lower perception threshold is the desired performance. Performing better with respect to PT means a lower perception threshold was obtained, allowing to use a bigger force range and therefore a larger bandwidth for the feedback information is available. It also allows the use of smaller transducers, as investigated in Mayer et al. (2020a), and therefore reduced energy consumption for battery powered prosthesis. Furthermore, lower stimulation force reduces the resulting noise and therefore increases the likelihood of the acceptance within the prosthetic field.

For JND_a, no statistically significant difference between different sites at the three different frequencies was obtained. As a result, each of the three sites is equally sensitive.

For JND_f, a statistically significant difference between different sites at [0.1 V, 400 Hz] as well as for [0.3 V, 750 Hz] was found. No statistical difference was found for all other stimulation permutations. In combination with the significantly lower PT, L1 has the biggest bandwidth for providing sensory feedback.

For SPLIR, no statistically significant difference between the different sites at the different frequencies was obtained, meaning each stimulation on each site can be located equally well. As reported previously in preliminary studies in Mayer et al. (2020c), SPLIR drops to at chance level above 1,500 Hz. Such a drop suggests that the site identification is superior for tactile perception, which is prevalent below 750 Hz (Mayer et al., 2019), and the stimulation location can not be perceived auditory perception. The stimulation in the case of auditory perception is conducted *via* the bones to the auditory pathway. Stimulating on three different independent sites on the elbow will ultimately still lead to stimulation of the same auditory pathway and hence not allow the subject to distinguish the stimulation site.

4.2. Subject groups

Only qualitative discussion is performed in the comparison of subject groups, due to the small number of ST subjects available for the study. For perception threshold, subjects with trans-radial amputation qualitative show a lower PT than able-bodied subjects and therefore are more sensitive to stimulation. This allows the use of a wider force range / larger bandwidth for the feedback information, and the use of smaller transducers for reduced energy consumption. Furthermore, the subjects with trans-radial amputation achieve similar performance for PT using non invasive bone conduction compared to the subjects with invasive bone conduction studied in Clemente et al. (2017). For JND_a, similar to PT a slightly better performance was obtained for *ST* compared to *SA*. A smaller JND_a means a higher resolution of the feedback interface is feasible and therefore more detailed sensory feedback can be provided.

For JND_f, a slightly worse performance was obtained for *ST* compared to *SA*. A higher JND_f means a coarser resolution of the feedback interface necessary and therefore less detailed sensory feedback can be provided.

For SPLIR, similar performance for *ST* compared to *SA* was obtained. Both subject groups SPLIR drops to at chance level above 1,500 Hz, suggesting that the site identification is superior for tactile perception for both subject groups.

4.2.1. Established interface parameters

The results obtained in this study suggest a usable bandwidth for bone conduction as a sensory feedback from 100 to 750 Hz when multiple transducers are used on multiple stimulation sites. The perception threshold is as low as 0.01 N at 100 Hz and increases to 0.2 N at 750 Hz. This range of force perception and frequency bandwidth suggest that commercially available transducers used in audiology could be used for bone conduction sensory feedback. Furthermore, the perception threshold for non-invasive bone conduction was found to be comparable to results obtained with invasive bone conduction techniques (Clemente et al., 2017). The study also revealed that frequency resolution was more distinguishable than amplitude. This finding could have implications for the design of future bone conduction feedback systems, as it suggests that greater attention may need to be paid to the frequency content of the feedback signals.

It should be mentioned that sensory feedback bone conduction is not applicable for subjects with diseases affecting the perception of such stimulation e.g., a potential subject in this study had to be excluded due to the inability to perceive stimulation likely caused by rheumatoid arthritis.

5. Conclusion

This study has evaluated the temporal and spatial parameters of the non-invasive vibrotactile feedback on the bony landmarks of the elbow. The parameters are investigated on three different physiological sites over two user groups (able bodies and subjects with transradial amputation). The paper reports the effective operating range of frequencies and amplitudes and the resolutions that can be perceived generally by the human users.

The perception threshold on the ulnar olecranon (L1) is most sensitive for able-bodied subjects compared to the medial and lateral epicondylus. The perception threshold is lower and therefore

more sensitive for subjects with trans-radial amputation compared to able-bodied subjects. A qualitatively smaller, and therefore more sensitive, perception threshold has been obtained compared to invasive bone conduction.

Previous research (Clemente et al., 2017) showed that osseoperception, caused by mechanical vibrations through a bone-anchored (osseointegrated) prostheses, allows for a richer feedback and therefore was believed to play an important role in the sense of ownership of a prosthesis and the improvement of quality of live of people living with limb loss. The equivalent sensitivity achieved in non-invasive bone-conduction within this study highlights the potential of such an interface for conventional socket-based prostheses to not only provide richer feedback and functionality but also to enhance the sense of ownership of a prosthesis.

The resolution in amplitude and frequency of all three sites, as well as for able-bodied subject vs. subjects with trans-radial amputation, showed comparable performance. The detection of the stimulation site was not different between different sites as well as the two investigated user groups.

Data availability statement

The raw data supporting the conclusions of this article will be made available by the authors, without undue reservation.

Ethics statement

The studies involving human participants were reviewed and approved by Engineering Human Ethics Advisory Group at the University of Melbourne. The patients/participants provided their written informed consent to participate in this study.

Author contributions

RM, AM, YT, and DO: literature, experiment, data, analysis, and paper. GA and PC: paper design, experiment design, and paper review. All authors contributed to the article and approved the submitted version.

Funding

The project was funded by the Valma Angliss Trust.

Conflict of interest

The authors declare that the research was conducted in the absence of any commercial or financial relationships that could be construed as a potential conflict of interest.

Publisher's note

All claims expressed in this article are solely those of the authors and do not necessarily represent those of their affiliated organizations, or those of the publisher, the editors and the reviewers. Any product that may be evaluated in this article, or claim that may be made by its manufacturer, is not guaranteed or endorsed by the publisher.

References

Antfolk, C., D'alonzo, M., Rosén, B., Lundborg, G., Sebelius, F., and Cipriani, C. (2013). Sensory feedback in upper limb prosthetics. *Expert. Rev. Med. Devices* 10, 45–54. doi: 10.1586/erd.12.68

Augurelle, A. S., Smith, A. M., Lejeune, T., and Thonnard, J. L. (2003). Importance of cutaneous feedback in maintaining a secure grip during manipulation of hand-held objects. *J. Neurophysiol.* 89, 665–671. doi: 10.1152/jn.00249.2002

Canzoneri, E., Marzolla, M., Amoresano, A., Verni, G., and Serino, A. (2013). Amputation and prosthesis implantation shape body and peripersonal space representations. *Sci. Rep.* 3, 2844. doi: 10.1038/srep02844

Childress, D. S. (1980). Closed-loop control in prosthetic systems: historical perspective. *Ann. Biomed. Eng.* 8, 293–303. doi: 10.1007/BF02363433

Clemente, F., D'Alonzo, M., Controzzi, M., Edin, B. B., and Cipriani, C. (2016). Non-Invasive, temporally discrete feedback of object contact and release improves grasp control of closed-loop myoelectric transradial prostheses. *IEEE Trans. Neural Syst. Rehabil. Eng.* 24, 1314–1322. doi: 10.1109/TNSRE.2015.2500586

Clemente, F., Håkansson, B., Cipriani, C., Wessberg, J., Kulbacka-Ortiz, K., Brånemark, R., et al. (2017). Touch and hearing mediate osseoperception. *Sci. Rep.* 7, 45363. doi: 10.1038/srep45363

Cordella, F., Ciancio, A. L., Sacchetti, R., Davalli, A., Cutti, A. G., Guglielmelli, E., et al. (2016). Literature review on needs of upper limb prosthesis users. *Front. Neurosci.* 10, 209. doi: 10.3389/fnins.2016.00209

Dahiya, R., Metta, G., Valle, M., and Sandini, G. (2010). Tactile sensing–from humans to humanoids. *IEEE Trans. Rob.* 26, 1–20. doi: 10.1109/TRO.2009.2033627

Daniel, W. (1990). *Applied Nonparametric Statistics, 2nd Edn*. Boston, MA: PWS-KENT.

Dietrich, C., Walter-Walsh, K., Preißler, S., Hofmann, G. O., Witte, O. W., Miltner, W. H., et al. (2012). Sensory feedback prosthesis reduces phantom limb pain: proof of a principle. *Neurosci. Lett.* 507, 97–100. doi: 10.1016/j.neulet.2011.10.068

Dosen, S., Ninu, A., Yakimovich, T., Dietl, H., and Farina, D. (2016). A novel method to generate amplitude-frequency modulated vibrotactile stimulation. *IEEE Trans. Haptics* 9, 3–12. doi: 10.1109/TOH.2015.2497229

Farina, D., and Amsüss, S. (2016). Reflections on the present and future of upper limb prostheses. *Expert. Rev. Med. Devices* 13, 321–324. doi: 10.1586/17434440.2016.1159511

Farina, D., Vujaklija, I., Brånemark, R., Bull, A. M. J., Dietl, H., Graimann, B., et al. (2021). Toward higher-performance bionic limbs for wider clinical use. *Nat. Biomed. Eng.* 1–13. doi: 10.1038/s41551-021-00732-x

Goodrich, M. A., and Schultz, A. C. (2007). Human-robot interaction: a survey. *Foundat. Trends Human Comput. Interact.* 1, 203–275. doi: 10.1561/1100000005

Johansson, R., and Westling, G. (1987). Signals in tactile afferents from the fingers eliciting adaptive motor responses during precision grip. *Exp. Brain Res.* 66:141–154. doi: 10.1007/BF00236210

Kaernbach, C. (1990). A single-interval adjustment-matrix (SIAM) procedure for unbiased adaptive testing. *J. Acoust. Soc. Am.* 88, 2645–2655. doi: 10.1121/1.399985

Markovic, M., Schweisfurth, M. A., Engels, L. F., Farina, D., and Dosen, S. (2018). Myocontrol is closed-loop control: incidental feedback is sufficient for scaling the prosthesis force in routine grasping. *J. Neuroeng. Rehabil.* 15, 81. doi: 10.1186/s12984-018-0422-7

Mayer, R. M., Chen, S., Li, Z., Mohammadi, A., Tan, Y., Alici, G., et al. (2020a). "Investigation of vibrotactile transducers for a bone conduction sensory feedback system," in *5th International Conference on NeuroRehabilitation (ICNR2020)* (Virtual).

Mayer, R. M., Garcia-Rosas, R., Mohammadi, A., Tan, Y., Alici, G., Choong, P., et al. (2020b). Tactile feedback in closed-loop control of myoelectric hand grasping: conveying information of multiple sensors simultaneously via a single feedback channel. *Front. Neurosci.* 14, 348. doi: 10.3389/fnins.2020.00348

Mayer, R. M., Mohammadi, A., Alici, G., Choong, P., and Oetomo, D. (2018). "Static force dependency of bone conduction transducer as sensory feedback for stump-socket based prosthesis," in *ACRA 2018 Proceedings* (Dearborn, MI: Lincoln).

Mayer, R. M., Mohammadi, A., Alici, G., Choong, P., and Oetomo, D. (2019). "Bone conduction as sensory feedback interface: a preliminary study," in *41st Annual International Conference of the IEEE Engineering in Medicine and Biology Society (EMBC)* (Berlin: IEEE), 5322–5325.

Mayer, R. M., Mohammadi, A., Tan, Y., Alici, G., Choong, P., and Oetomo, D. (2020c). "Psychometric evaluation of multi-point tactile stimulation via bone conduction," in *8th International Conference on Biomedical Robotics and Biomechatronics (BIOROB2020)* (New York, NY).

Paterno, L., Ibrahimi, M., Gruppioni, E., Menciassi, A., and Ricotti, L. (2018). Sockets for limb prostheses: a review of existing technologies and open challenges. *IEEE Trans. Biomed. Eng.* 65, 1996–2010. doi: 10.1109/TBME.2017.2775100

Richard, G., Pietrzak, T., Argelaguet, F., Lécuyer, A., and Casiez, G. (2021). Studying the role of haptic feedback on virtual embodiment in a drawing task. *Front. Virtual Reality* 1, 573167. doi: 10.3389/frvir.2020.573167

Sanders, J. E., Allyn, K. J., Harrison, D. S., Myers, T. R., Ciol, M. A., and Tsai, E. C. (2012). Preliminary investigation of residual-limb fluid volume changes within one day. *J. Rehabil. Res. Dev.* 49, 10. doi: 10.1682/JRRD.2011.12.0236

Saunders, I., and Vijayakumar, S. (2011). The role of feed-forward and feedback processes for closed-loop prosthesis control. *J. Neuroeng. Rehabil.* 8, 1–12. doi: 10.1186/1743-0003-8-60

Schofield, J. S., Evans, K. R., Carey, J. P., and Hebert, J. S. (2014). Applications of sensory feedback in motorized upper extremity prosthesis: a review. *Expert. Rev. Med. Devices* 11, 499–511. doi: 10.1586/17434440.2014.929496

Sensinger, J. W., and Dosen, S. (2020). A review of sensory feedback in upper-limb prostheses from the perspective of human motor control. *Front. Neurosci.* 14, 345. doi: 10.3389/fnins.2020.00345

Shehata, A. W., Rehani, M., Jassat, Z. E., and Hebert, J. S. (2020). Mechanotactile sensory feedback improves embodiment of a prosthetic hand during active use. *Front. Neurosci.* 14, 263. doi: 10.3389/fnins.2020.00263

Stephens-Fripp, B., Alici, G., and Mutlu, R. (2018). A Review of Non-Invasive Sensory Feedback Methods for Transradial Prosthetic Hands. *IEEE Access* 6:6878–6899. doi: 10.1109/ACCESS.2018.2791583

Svensson, P., Wijk, U., Björkman, A., and Antfolk, C. (2017). A review of invasive and non-invasive sensory feedback in upper limb prostheses. *Expert Rev. Med. Devices* 14, 439–447. doi: 10.1080/17434440.2017.1332989

Tahir, A. M., Iqbal, J., and Aized, T. (2018). Human machine interface: robotizing the instinctive living. *Int. Rob. Automat. J.* 4, 1–0. doi: 10.15406/iratj.2018.04.00142

Westling, G., and Johansson, R. (1984). Factors influencing the force control during precision grip. *Exp. Brain Res.* 53, 277–284. doi: 10.1007/BF00238156

Wilcoxon, F. (1945). Individual comparisons by ranking methods. *Biometr. Bull.* 1, 80–83. doi: 10.2307/3001968

Frontiers in Neuroscience

Provides a holistic understanding of brain function from genes to behavior

Part of the most cited neuroscience journal series which explores the brain - from the new eras of causation and anatomical neurosciences to neuroeconomics and neuroenergetics.

Discover the latest Research Topics

See more →

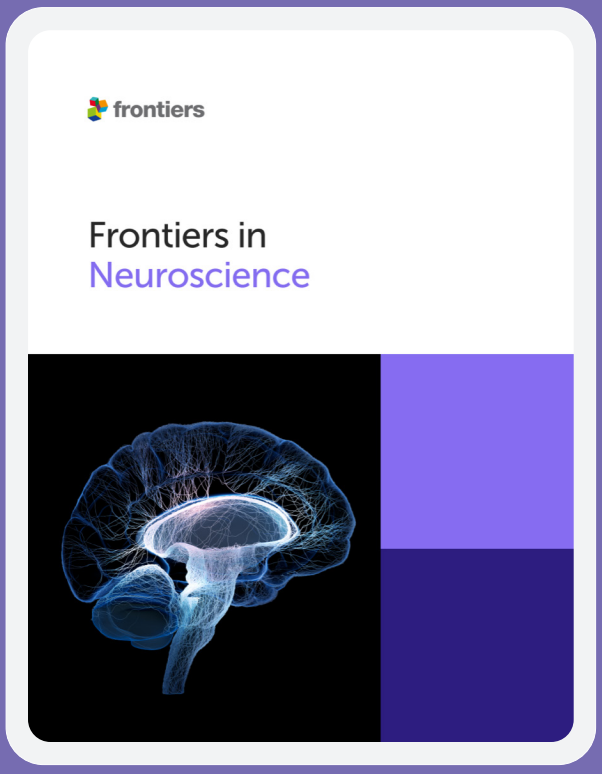

Frontiers

Avenue du Tribunal-Fédéral 34
1005 Lausanne, Switzerland
frontiersin.org

Contact us

+41 (0)21 510 17 00
frontiersin.org/about/contact